Mechanism of Phospholamban Activation by HAX-1 and their Roles in the Regulation of the SR Calcium-ATPase

A Dissertation

SUBMITTED TO THE FACULTY OF
THE UNIVERSITY OF MINNESOTA
BY

Erik Keith Larsen

IN PARTIAL FULFILLMENT OF THE REQUIREMENTS
FOR THE DEGREE OF
DOCTOR OF PHILOSOPHY

Advisor

Dr. Jiali Gao

April 2021

Abstract

The Ca^{2+} transient of the cardiomyocyte is key to the contractility of the heart. Its dysregulation has been associated with heart disease, leading to investigation of the regulation of Ca^{2+} for potential drug targets. The Sarcoplasmic Endo-Reticulum Ca^{2+} ATP-ase (SERCA) pump and its main inhibitor in heart tissue, phospholamban (PLN), are two promising targets that are under β-adrenergic control via phosphorylation of PLN by Protein Kinase A (PKA). Phosphorylation of Ser16 on the cytoplasmic domain of PLN results in decreased inhibition of SERCA. Recently, an additional member of the SERCA interactome has been discovered called Hematopoietic lineage cell-specific protein 1 (HCLS1) Associated Protein X-1 (HAX-1). Contrasting PLN phosphorylation, the interaction of HAX-1 and PLN increases the inhibition of PLN for SERCA, adding another layer of complexity to SERCA regulation and a potential new drug target. This thesis aims to investigate the structure-function relationship of the ternary complex, SERCA/PLN/HAX-1 using NMR spectroscopy as the primary technique.

Table of Contents

List of Tables

List of Figures

List of Abbreviations

Shannon Measurement of Information	SMI
Phospholamban	PLN
Sarco/endoplasmic reticulum calcium ATPase	SERCA
Hematopoietic lineage cell-specific protein – associated protein X-1	HAX-1
Heat Shock Protein 90	HSP90
Intrinsically Disordered Protein	IDP
Phosphatidylglycerol	PG
Phosphatidic acid	PA
Phosphatidylserine	PS
Phosphatidylcholine	PC
Phosphatidylinositol	PI
Endoplasmic reticulum	ER
Reactive oxygen species	ROS
Molecular recognition features	MORFs
Excitation-contraction coupling	ECC
Heart failure	HF
Angiotensin-converting-enzyme	ACE
G-coupled protein receptor	GCPR
cyclic-AMP	cAMP
Protein-Protein Interactions	PPI
Sarcolipin	SLN
Protein kinase A	PKA
Ca^{2+}/calmodulin-dependent protein kinase II	CAMKII
Maltose binding protein	MBP
Transmembrane	TM
Dipolar Assisted Rotational Resonance	DARR
Transferred Echo DOuble Resonance	TEDOR
Multiple acquisitions via sequential transfer of orphan spin polarization	MAeSTOSO
Multiple ExperIments via Orphan SpIn operatorS	MEIOSIS
Radio Frequency	RF
Cross Polarization	CP
Polarization Optimized Experiments	POE
Dual acquisition MAS spectroscopy	DUMAS
Double Quantum Single Quantum	DQSQ
Nuclear Magnetic Resonance	NMR
Solid-state NMR	ssNMR
Oriented-sample solid-state NMR	OS-ssNMR
Magic angle spinning solid-state NMR	MAS-ssNMR
refocused Insensitive Nuclei Enhanced by Polarization Transfer	rINEPT
Carbonyl Carbon Label Selective	CCLS
Dual Carbon Label Selective	DCLS
Residual Dipolar Coupling	RDC
Paramagnetic Relaxation Enhancement	PRE

Free induction decay	FID
Chemical shift anisotropy	CSA
Dipolar coupling	DC
Cryogenic electron microscopy	cryo-EM
Separated local field	SLF
Polarization Inversion Spin Exchange at the Magic Angle	PISEMA
Polarity indexed slant angle	PISA
Dipolar-coupling chemical-shift correlation	DIPSHIFT
INEPT-TOtal through Bond correlation SpectroscopY	TOBSY
Chemical shift perturbation	CSP
Chemical shift index	CSI
Nuclear Overhauser effects	NOEs
Heteronuclear single quantum correlation	HSQC
^{13}C-ethylmethanethiosulfonate	^{13}C-EMTS
Critical micelle concentration	CMC
Small Phase Incremental Alternation	SPINAL
Two Pulse Phase Modulated	TPPM

Chapter 1 Introduction

1.1 Entropy and information

Transmission of biochemical signals that are received and elicit functional responses results in the manifestation of life; the malfunction of which often results in disease. Biochemical signals are described as a flow of information, a concept that is central in life sciences. To quantify the amount of information contained within a system, an introduction of Entropy, a term coined by Rudolph Clausius, and its relation to Shannon Measurement of Information (SMI) is required.

Entropy was born from the realization that the change in Energy (U) was not sufficient to describe the direction of a spontaneous process; exothermicity is not required for spontaneity. There is a balance between minimizing the energy of a system as well as maximizing the number of possible states occupied. A state function to complement that of internal energy (U) was derived such that:

$$dS = \frac{dq_{rev}}{T}$$

for a spontaneous process [6]. Boltzmann defined the entropy of a typical system at the molecular level:

$$S = k_B \ln W(a_j)$$

Where k_B is the Boltzmann constant and $W(a_j) = \frac{A!}{\prod_j a_j!}$, the possible configurations where A is the number of systems in an ensemble and $a_j \in A$ is the number of

systems in a possible state j. If all possible configurations are equally probable (p_{ja}=(1,…,$W(a_j)$), the probability of a macroscopic state *a* is [7]:

$$P(a) = W(a_j)p(a_j)$$

The above derivations assumed that in large ensembles there is no difference between the maximum entropy (most probable) and the mean value of entropy. Eliminating this assumption (and dropping k_B for simplicity):

$$\bar{S} = \sum_{a_j} P(a_j) \ln W(a_j)$$

or:

$$\bar{S} = -\sum_{a_j} P(a_j) \ln p(a_j) + \sum_{a_j} P(a_j) \ln P(a_j)$$

And considering all configurations are of equal probability:

$$\bar{S} = -\sum_{a_j} \sum_{p_{ja}=1}^{W(a_j)} p_{ja}(a_j) \ln p_{ja}(a_j) + \sum_{a_j} P(a_j) \ln P(a_j)$$

The first term in the above equation is of the same form as the solution that Shannon found in 1948 that induced interest in the field of information theory, SMI [7]:

$$H(P) = -K \sum_i p_i \log_2 p_i$$

Where K is a positive constant and $\log_2$ results in the unit of bits rather than using the natural log as is done for convenience in thermodynamics when working with Boltzmann factors. *H* is a measurement of uncertainty in a random variable and can be conceptualized as the amount of information contained within a probability distribution [8]. With the relationship between entropy and information content defined, we are equipped to apply these principles biophysically.

1.2 Lipid membranes

Entropy within cells is primarily decreased by self-assembled phospholipid bilayers called membranes. Membranes are essential to life, a statement justified by the thermodynamic expression for the change in entropy of a system [9]:

$$dS = \frac{dU}{T} + \frac{PdV}{T} - \frac{\mu dN}{T}$$

explicitly describing a decrease in entropy through a decrease in internal energy (dU), a decrease in volume (dV), or an increase in the flux of molecules across a barrier (dN). These amphipathic, semi-permeable surfaces corral ions, small molecules, and macromolecules while allowing diffusion of water, both decreasing explorable volume as well as increasing chemical potentials (μ) of small molecules [9-13].

At the molecular level, the phosphoglycerides that constitute cell membranes are diverse in charge (positive, negative or zwitterionic), aliphatic chain length (most commonly 14 to 18 carbons), as well as chain saturation

(typically at the Δ^9 position) [14]. Additionally, membranes are not uniform among species or even within the cell organelles. Furthermore, head group charge differentiates between the inner and outer leaflet of a single lipid bilayer based on the location of biosynthetic machinery [15]. This diversity contributes to the ideal functioning of membrane proteins, the machinery embedded in the membrane that allows for transportation of nutrients and waste or act as transmitters or receivers of information. For example, Gustavsson *et al.* discovered that a calcium transporter, the sarco-endoplasmic reticulum calcium ATPase (SERCA) has greater activity when in the presence of negatively charged headgroups such as phosphatidylserine (PS) and/or upon increasing the aliphatic chain length [16].

1.3 Membrane proteins

As alluded to in the previous section, the formation of concentration gradients and the uptake of nutrients or the release of waste is not possible without channels or pumps for which hydrophilic ions and organic material pass through the hydrophobic lipid membrane. From a bird's eye view of a lipid bilayer, one might imagine a sea of lipids with randomly dispersed membrane proteins "floating" within. Despite the importance of this fluid mosaic model of lipid and membrane protein interactions provided by Singer and Nicholson in 1972 [17] the next 50 years would prove this model was inaccurate.

Organisms express thousands of membrane proteins, and in eukaryotes, membrane proteins account for approximately 30% of the human proteome [18,

19]. These proteins often have an interaction energy greater than thermal energies, forming homo or heteromeric complexes [9]. This enables fine tuning of the concentration gradients of various ions and molecules. Additionally, the lipid membrane is home to several other organic molecules such as steroids, like cholesterol, vitamins, like vitamin D, and eicosanoids. Drugs like ibuprofen and acetaminophen inhibit the synthesis of eicosanoids to limit pain and inflammation [14]. Lastly, the fluid mosaic model lacks an understanding of the heterogeneity displayed within the lipid bilayer. Barriers created by fixed molecular assemblies such as the cytoskeleton of large protein complexes create partitions through which proteins cannot freely diffuse [20]. Furthermore, the controversial topic of lipid rafts, a transient bilayer domain resembling the liquid-ordered phase in which membrane proteins experience dampened dynamics, adds another layer of complexity left out by the fluid mosaic model [20].

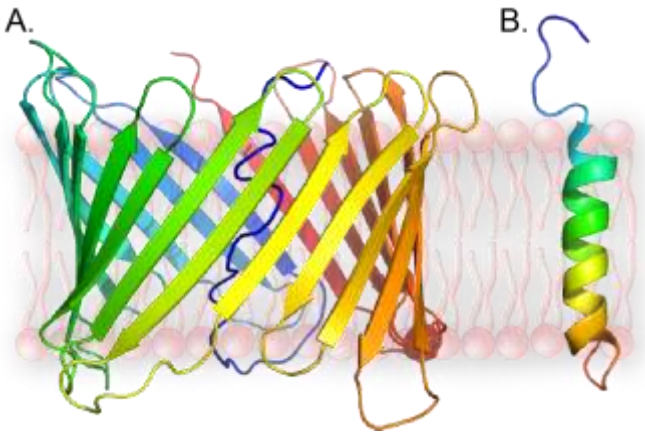

Figure 1.1: Secondary structure of transmembrane proteins

A. *An example of a β-barrel transmembrane protein: the voltage-gated anion channel (PDB: dK4T).* ***B.*** *An example of an α-helical transmembrane protein: sarcolipin.*

Ultimately, biophysical research is driven to understand how the machinery of the cell functions, how it malfunctions in disease, and to identify, site specifically within the machinery, drug targets that can be leveraged to restore normal

function. Half of all drug targets are membrane proteins [21] which can be classified as either integral membrane proteins or peripheral membrane proteins.

1.4 Integral membrane proteins

Integral membrane proteins are amphiphiles tightly bound to membranes by hydrophobic interactions [14]. Due to the amphiphilic nature, most integral membrane proteins span the entirety of the lipid bilayer (transmembrane proteins) interacting with the nonpolar carbon chains and the polar phosphate head groups. All membrane proteins contain some portion that is water soluble; no protein is known to be completely buried in a membrane [22]. Due to lipid membrane asymmetry and the location of peptide synthesis, membrane proteins orient asymmetrically as well [23]. Often, if the integral membrane protein is an ion channel or pump, orientational asymmetry results in a coordinated redistribution of ions in space, leading to changes in the chemical potential and a manifestation of a “flow of information” [24].

The transmembrane domains of integral membrane proteins may consist of two secondary structure motifs: an anti-parallel β barrel (**Fig. 1.1A.**) or an α-helix (**Fig. 1.1B.**). These two motifs have strong hydrogen bonding interactions that outcompete those of its surroundings [25]. α-helical membrane proteins can have a single transmembrane helix or bundle together with up to 20 total helices where changes in topology can lead to protein function [26]. Isoleucine, leucine, and valine are the most common amino acids found in transmembrane α-helices due

to their propensity to form hydrophobic interactions with the bilayer. β-barrel membrane proteins create a barrier between the hydrophobic lipid bilayer, often forming hydrophilic pores for which soluble biomolecules can diffuse called channels. To date, 3.6% of the protein data bank are transmembrane proteins with 80% of those being α-helical.

The difficulty of membrane protein structure determination is multifarious. Over-expression and purification can prove to be strenuous tasks as these proteins tend to aggregate or precipitate out of the solution without surfactants or lipid membrane mimetics. Additionally, the technology behind the techniques used to study these proteins are years behind those used for their soluble counterparts. Most importantly, creating a physiologically relevant lipid bilayer mimetic is difficult due to the heterogeneity of the lipid membrane. Nevertheless, with the field still in its infancy, these challenges present an opportunity for rapid growth.

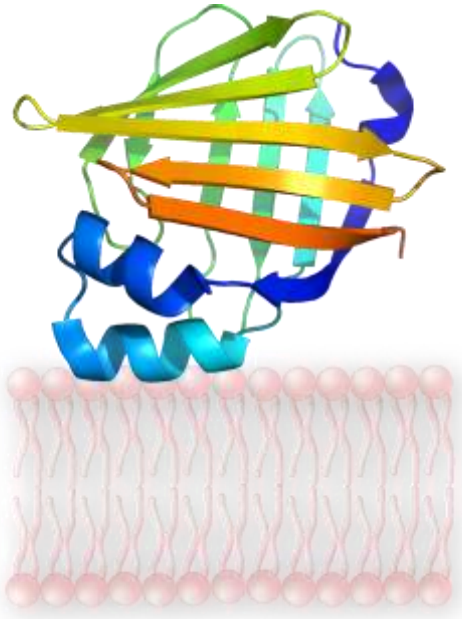

Figure 1.2: Surface proteins

An example of a peripheral membrane protein: Myelin protein 2.

1.5 Peripheral membrane proteins

Peripheral membrane proteins (**Fig. 1.2**) interact with the lipid bilayer transiently through electrostatic, hydrophobic and selective post-translational lipidations, making the conformational energy landscape complex. Contributing to the intricacy,

these interactions often occur in tandem: *e.g.*, long-range electrostatic interactions that contribute to the localization of peripheral membrane proteins to the bilayer followed by a folding upon binding driven by hydrophobic interactions.

Electrostatic interactions are primarily driven by the presence of negatively charged phospholipid headgroups such as phosphatidylglycerol (PG), phosphatidic acid (PA), phosphatidylserine (PS), and phosphatidylinositol (PI) [27]. Most peripheral proteins are cationic, however, ligand binding to an anionic peripheral protein can induce a conformational change exposing positively charged residues previously buried within the protein known as an “electrostatic switch” [28]. While electrostatic interactions are nonspecific, the specific headgroup profile of each membrane found within the cell (*e.g.* plasma membrane, endoplasmic reticulum (ER), mitochondrial membrane, *etc.*) or even of each leaflet can lead to recruitment of the necessary components for protein function at the membrane [27].

Hydrophobic interactions occur between residues I, L, V, G, P, A, W, F, or M and the lipid membrane. These interactions are used as an anchor to the membrane and can occur simply by a hydrophobic stretch in the primary amino acid sequence, or by induced conformational changes resulting in secondary structural moieties [29, 30]. Commonly, lipid binding requires interactions with the interfacial region of the bilayer (the ~15 Å region between the ~15 Å hydrocarbon core and the bulk water [31]) demanding a balance between hydrophobic and hydrophilic interactions.

The most abundant membrane surface induced secondary structural moiety is the amphipathic helix (**Fig. 1.3A.**). Amphipathic helices have been demonstrated to have functions beyond anchoring the protein to the membrane. They induce membrane deformation, fission and fusion, sense membrane curvature, coat lipid droplets, sense membrane composition, and can even be sensitive to stress conditions such as reactive oxygen species (ROS) [32]. This variety of function is derived from the degree to which the helix is coiled (α-helix, 3-10, 3-11, π), the length of the helix, and the primary amino acid sequence defining the interfacial properties of the amphipathic helix. Properties such as charge distribution and the basicity/acidity of the polar face, or the bulkiness of the sidechains can increase the specificity of the amphipathic helix to the biological function [32].

To quantify the amphiphilicity of a polypeptide to aid in amphipathic helix prediction, Eisenberg defined the mean helical hydrophobic moment in 1982 [33] as

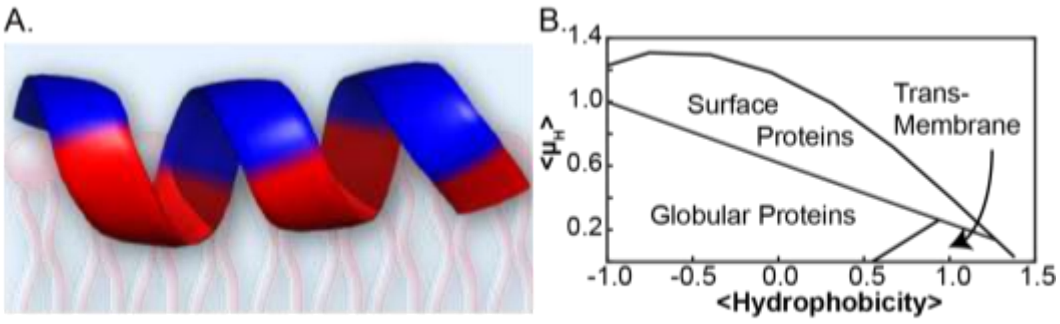

Figure 1.3: Amphipathic helices

A. *An example of an amphipathic helix with hydrophobic residues colored red and hydrophilic residues colored blue.* ***B.*** *An Eisenberg plot with each "phase" labeled based on the mean hydrophobicity and the mean hydrophobic moment.*

$$\langle \mu_H \rangle = \frac{\left| \sum_{i=1}^{N} \overrightarrow{H_i} \right|}{N}$$

where $\overrightarrow{H_i}$ is the vector representing the hydrophobicity of residue side chain i and N is the total number of residues. A large value of this mean vector sum of the hydrophobicities predicts that the helix is amphipathic and sits perpendicular to the membrane normal. Eisenberg developed a type of phase diagram for the prediction of globular, transmembrane, and peripheral proteins by relating the mean helical hydrophobic moment to the mean hydrophobicity (**Fig. 1.3B.**). The ability to predict these structures has seen a heightened importance in a recent push to study intrinsically disordered proteins (IDPs) which sample transient secondary structures or undergo disorder to order transitions upon ligand binding to promiscuously interact with many functionally diverse ligands.

1.6 Intrinsically disordered proteins

The transfer of information from DNA to RNA to a unique, well-defined protein structure resulting in a unique structure-function relationship has been, and often still is, the motivation behind biophysical protein research. However, until Huber discussed the possibility of conformational flexibility and the possible significance of “temperature factors” and “microstates” for protein function, many assumed proteins could only access one state. We now know that the missing electron density in X-ray crystallographic studies was a result of crystal packing effects [34], and that intrinsic disorder within proteins is a precursor for a protein to possess a

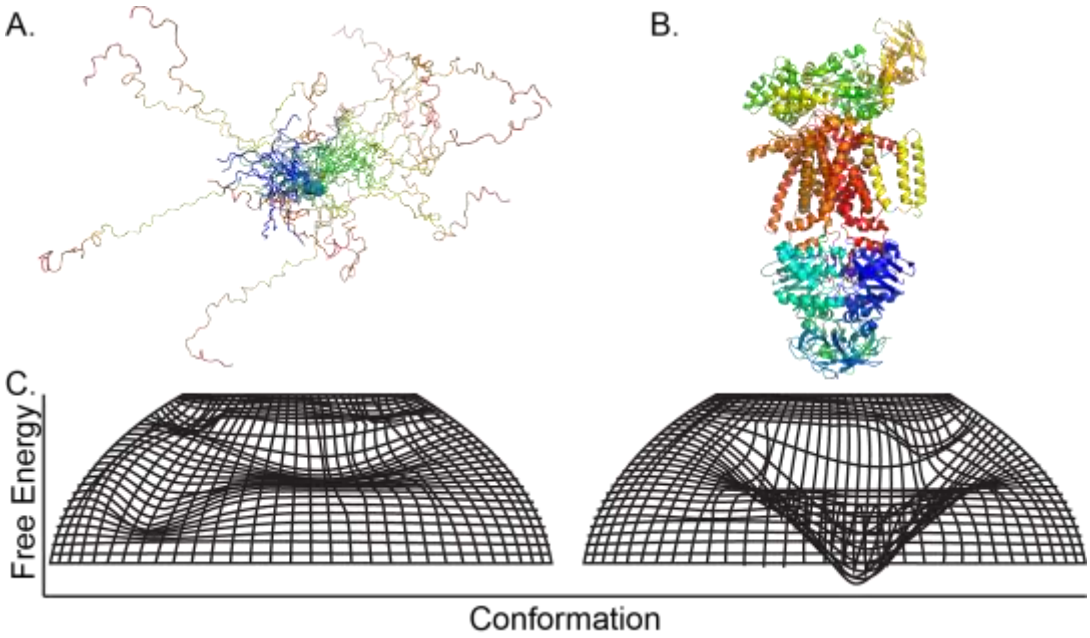

Figure 1.4: Energy landscapes of IDPs vs. well folded proteins

A. An example of an ensemble of structures for an intrinsically disordered protein: the spinach thylakoid soluble phosphoprotein (PDB: 2FFT). **B.** An example of a well folded protein: the E. coli maltose transporter (PDB: 2R6G). **C.** An example of an energy landscape for an intrinsically disordered protein (left) and a well folded protein (right). Well folded proteins have one primary location with low energy defining a fold, while IDPs have many shallow wells allowing for the protein to "hop" between conformations.

wide range of binding partners resulting in different biological functions [35]. With a turning point in the year 2000 when Uversky discussed "natively unfolded" proteins under physiologic conditions, IDPs slowly revealed themselves to scientific inquiry [36, 37]. The most recent predictions estimate that the level of disorder within an organisms proteome increases with organism complexity [38]; 55% of the human proteome is comprised of proteins with >30% predicted disorder [39].

IDPs differ from globular proteins beginning at the amino acid sequence. It is understood that charge, hydrophobicity, complexity and flexibility are unique to intrinsically disordered proteins selected by evolutionary pressure [35]. Initially, disordered regions in a protein were thought to simply be non-functional linkers between secondary structures, tethering the folded, functional domains spatially. For well-folded proteins, biological function is preserved evolutionarily by conserved amino acid sequences. The specific location of one of the 20 naturally occurring amino acids is identical through generations by natural selection. The entropy of one specific site in the primary amino acid sequence is therefore decreased and the information content of the molecule is increased (positional information) [24]. For IDPs, information content can also be evolutionarily maintained through conservation of chemical properties such as charge, hydrophobicity or plasticity over 10s of amino acids despite significant alterations in primary amino acid sequence, high conformational entropy (**Fig. 1.4**) , or lacking the ability to fold post-ligand-binding [24, 40]. This discrepancy between how information content is preserved within well-folded and intrinsically disordered proteins appears polarizing, however in reality, all proteins are on a sliding scale of “ordered-ness”, where even the most folded proteins experience some amount of flexibility and conformational dynamics [35].

To be evolutionarily conserved, kinetic and/or thermodynamic advantages of ligand binding must exist. A theory of kinetic advantage called the fly-casting mechanism [41] suggests that disordered proteins possess increased capture radius due to conformational flexibility, however, this has been a contentious point

when thinking about kinetic advantages of IDPs and has proven difficult to observe experimentally. A more probable theory is the relief of steric hindrances and an increase in long-range electrostatic interactions contribute to an increase in the probability of “meaningful” interactions between the IDP and the ligand [42, 43] compensating for the additional kinetic bottle neck of protein folding [44].

Thermodynamically, the affinity and specificity of interactions with IDPs are often decoupled resulting in highly specific yet weak interactions [45] due to the entropic penalty paid upon protein folding. This seemingly paradoxical effect is ideal for signal regulation where interactions need to be switched off rapidly corresponding to cellular conditions. An example of the thermodynamic advantage of IDPs for ligand binding is the *polyelectrostatic* effect. This theory describes the decrease in the equilibrium dissociation constant by increasing the number of discrete charges throughout an entire IDP [46]. Rather than considering specific protein-ligand interactions, this theory accounts for multiple transient conformations and their global effect on minimizing the free energy of binding. Molecular recognition features (MoRFs) are mostly disordered until bound to a ligand subsequently undergoing secondary structural rearrangement. These interactions result in transient, micromolar affinity complexes [47] and have been divided into subsets based on the induced secondary structural element: α- (alpha helical), β- (forms beta-sheets or strands), and *i*-(irregular hydrogen bonding patterns). MoRFs have defining characteristics that can help lead to their prediction and discovery, such as enrichment in I F,W,L, M and Y residues. Continuing with the alpha-helix as an example, α-MoRFs are enriched in I,F,L, and M residues [48].

Thus, the potential kinetic advantages and decoupling of specificity and affinity allow for a hypersensitivity to changes in the physiological environment.

1.7 Cardiophysiology

An adept model for signal transduction through membranes can be found within the cardiomyocyte. The heart controls the flow of matter to various parts of the body and vice versa. Cardiomyocytes, which make up contractile chambers of the heart, work in unison to pump blood throughout the cardiovascular system carrying nutrients such as O_2. Synergistic contraction of cardiomyocytes is dictated through myogenic electrical signaling called *excitation-contraction coupling (ECC)* [49]. The signal originates from the sinoatrial node and while they are not reliant on the nervous system for conception, they are strongly influenced by the autonomic nervous system [49]. The electrical impulses, communicated between cardiomyocytes by gap junctions during systole, coordinate the contraction mechanism throughout the chamber.

To understand how information is transmitted during ECC, a schematic of the structure of the heart is required (**Fig. 1.5**). The sarcolemma is the lipid membrane creating the barrier between extracellular and intracellular space. Membrane proteins that act as pumps, channels and transporters are located within this membrane. These membrane proteins control the flow of ions. Within the cell an important organelle called the sarcoplasmic reticulum (SR) resides in the cytoplasm. The electrical signal that “transmits information” is the flow of Ca^{2+}, Na^{+},

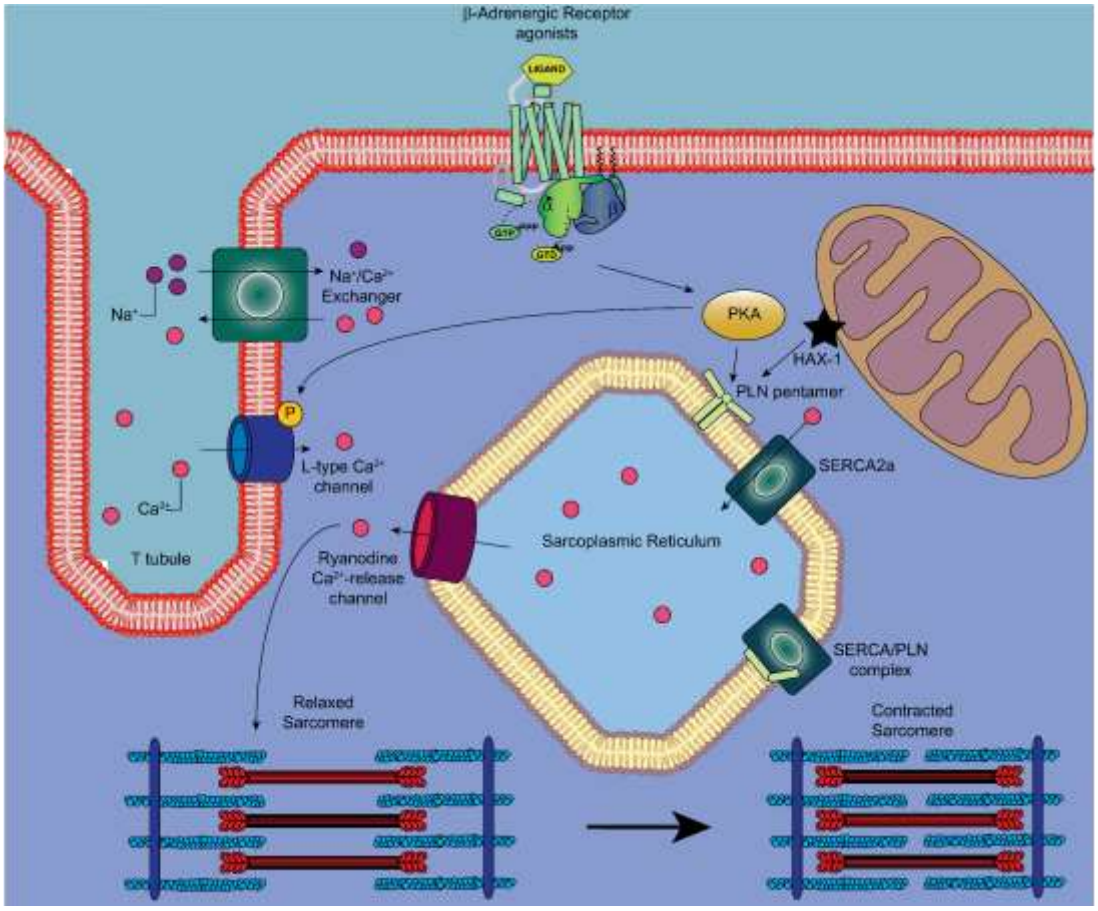

Figure 1.5: ECC: Calcium regulation in the cardiomyocyte action potential

Ca^{2+} leak through the L-type Ca^{2+} channel induces Ca^{2+} release from SR via RYR. Binding of Ca^{2+} to the sarcomere initiates contraction. SERCA Ca^{2+} reuptake into the SR initiates relaxation which is regulated by PLN, PKA and HAX-1.

and K^+ ions between the extracellular space, intracellular space, and sarcoplasmic reticulum called the *action potential*. This coordinated flow of ions is controlled by the opening and closing of the membrane proteins starting with a resting membrane potential of ~-90mV. This takes place during muscle relaxation, or diastole, and is known as phase 4 of the action potential cycle. The membrane potential at this phase is primarily preserved by K^+ ions permeating the membrane

with assistance from membrane channels such as the sodium-potassium pump or the sodium-calcium exchanger. Na^+ and Ca^{2+} can also leak through gap junctions via an action potential from a neighboring cell, increasing the resting membrane potential from -90mV to -70mV. Once a threshold membrane potential of ~-70mV is achieved, phase 0 begins where voltage gated Na^+ channels rapidly open allowing Na^+ into the cell through the sarcolemma to drive the membrane potential up to ~+20mV. In phase 1, new voltage gated K^+ channels are opened secondary to the rapid depolarization leading to a slight repolarization of the membrane potential to ~+5mV. At this point, the main trigger of contraction, Ca^{2+}, flows into the cytosol of the cell through voltage gated Ca^{2+} channels which leads to the plateauing of the membrane potential at +5mV throughout phase 2. The introduction of Ca^{2+} here initiates Ca^{2+} induced Ca^{2+} release of Ca^{2+} from the SR via channels called ryanodine receptors which triggers muscle contraction, or systole. The release of Ca^{2+} from the SR decreases the difference between SR and cytosol $[Ca^{2+}]$ from a 3 orders of magnitude difference during diastole, (100nM in cytosole, 100μM in SR) to a 1 order of magnitude difference during systole. The Ca^{2+} channels then close just as suddenly as they opened driving repolarization to ~-90mV. Additionally, the Sarcoendoplasmic Reticulum Ca^{2+} ATPase (SERCA) pumps Ca^{2+} across the SR membrane, reducing cytosolic $[Ca^{2+}]$ and beginning relaxation of the cardiomyocyte. This process, known as phase 3, results in the voltage gated K^+ channels shutting and brings the cycle full circle back at the starting position of phase 4, ready to repeat [50].

1.8 Therapeutic targets for heart failure

As of 2017, 5.7 million people in the U.S. alone suffered from heart failure (HF), and by 2030, greater than 8 million people are projected to be afflicted [51]. Current treatments of HF include β-adrenergic blockers, angiotensin-converting-enzyme (ACE) inhibitors, and gene therapeutics [52, 53]. To mitigate the effects of HF, several studies have shown that increasing SERCA2a activity can restore cardiac muscle function [54] and Hulot *et al.* have progressed the gene therapy approach to human clinical trials [55].

As mentioned in section 1.7, SERCA is involved in the sequestering of Ca^{2+} ions to the SR. SERCA makes use of thermodynamic force (difference in chemical potentials between two different states) by using the concentration gradient of protons (chemical potential) and the energy released from ATP hydrolysis to transport [Ca^{2+}] against a concentration gradient through the process of free energy transduction. This process initiates diastole. SERCA is a 110 kDa P-type ATPase comprised of 4 domains: the transmembrane domain formed by 10 helical segments, and the cytoplasmic domains called the actuator (A) domain, the phosphorylation (P) domain and the nucleotide binding (N) domain [56]. The two Ca^{2+} binding sites are located in the transmembrane domain incorporating residues E^{309} for binding site II and D^{800} for binding site I [57]. Ca^{2+} binding is a cooperative process in which binding of site I increases the affinity of site II for Ca^{2+}. The binding of Ca^{2+} distinguishes the two main states of SERCA, E1 and E2, where the former is Ca^{2+} bound and the latter is Ca^{2+} free.

Various SERCA isoforms are found within the body [58]. In vertebrates, SERCA is encoded by three genes producing more than ten isoforms located uniquely throughout muscle tissue. SERCA1 is found in fast-twitch skeletal muscle. SERCA 2 is ubiquitously expressed and found in cardiomyocytes (2a/2c) smooth muscle, non-muscle cells (2b), as well as human skeletal muscle (2d). SERCA 3 is found in endothelial and epithelial cells. SERCA expression is also developmentally regulated. The age-related decline in cardiomyocyte contractility is predicted to be linked with changes in SR function and studies have demonstrated that neural input or disease influence the pattern of SERCA expression [59]. Finally, the effect of electrical stimulation modulates SERCA expression as seen by Pette *et al.* [60-63]. Following 30 days of chronic low-frequency stimulation (CLFR), SERCA2a was upregulated and SERCA1a protein was downregulated. CLFR ultimately resulted in partial inactivation of SERCA in

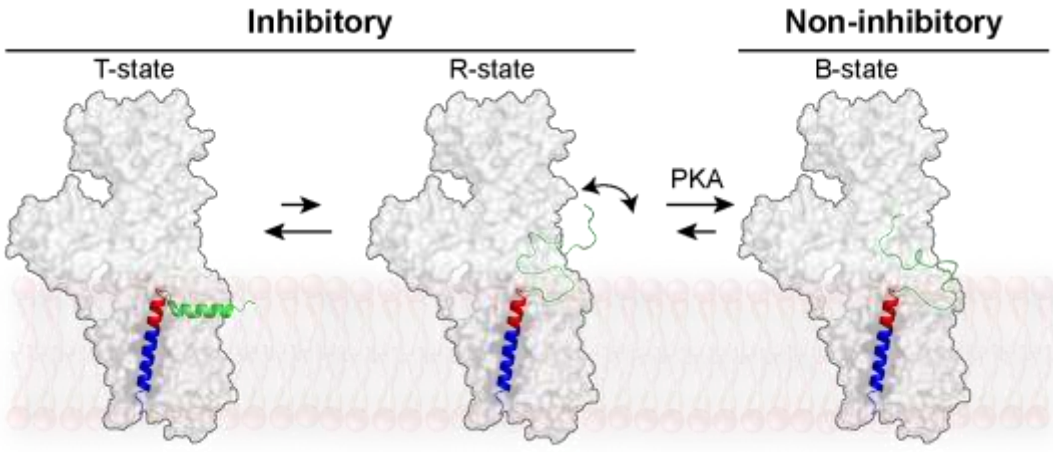

Figure 1.6: PLN conformational equilibrium

PLN Conformational Equilibrium. PLN interconverts between inhibitory T- and R-states. PKA conformationally selects the R-state to phosphorylate at Ser16 driving the equilibrium to the non-inhibitory SERCA bound B-state.

the SR and a net decrease in SR Ca^{2+} transport. In addition to the therapeutics discussed above, small molecule activators and inhibitors are currently under investigation for the SERCA pump [56, 64-69].

Interestingly, CLFR upregulated the expression of a small 52 amino acid peptide that has been found to bind SERCA2a throughout its enzymatic cycle called phospholamban (PLN). PLN is another potential therapeutic target. PLN disease mutations have been identified for both gain- and loss-of inhibitory function [70-74]. The function of PLN is to inhibit SERCA and fine tune Ca^{2+} regulation within the cardiomyocyte. Additionally, PLN is under β-adrenergic control; hormones such as adrenaline and small molecule ligands such as caffeine bind the G-coupled protein receptor (GPCR) which initiates a cascade of signals for the formation of cyclic-AMP (cAMP) by the adenylate cyclase [75]. cAMP activates the cAMP-dependent protein kinase A (PKA), which phosphorylates several substrates altering the function of these key cardiac proteins. One of the proteins that is reversibly phosphorylated is PLN. Monomeric PLN is in conformational equilibrium between the dominant T-state and the minor R-state. In the T-state, the cytoplasmic domain of PLN is alpha-helical and lipid bound, while in the R-state, the cytoplasmic domain is random coil and free in solution. PKA conformationally selects the R-state and phosphorylates Ser16, driving the equilibrium towards a non-inhibitory SERCA bound B-state. Phosphorylation results in a relief of inhibition of SERCA2a (**Fig. 1.6**).

Evidence suggests that phosphorylation levels of PLN at Ser16 and the Ca^{2+}/calmodulin-dependent protein kinase II (CaMKII) phosphorylated Thr17 are decreased in human failing hearts. There are several potential therapeutic approaches that target PLN to increase SERCA2a activity. Down-regulation of PLN expression via short hairpin RNA has shown success in animal models [76-78]. Moreover, inhibition of protein phosphatase inhibitor-1, the enzyme responsible for the decreased phosphorylation levels in failing human hearts [79-82] has shown encouraging results for ameliorating the effects of heart disease [83-87].

Recently, HCLS1-associated protein X-1 (HAX-1) has been shown to be a regulator of cardiac contractility via interaction with PLN and SERCA [88-96]. Originally found to interact with hematopoietic lineage cell-specific protein-1 (HCLS1), a substrate of receptor-coupled tyrosine kinases that has been shown to signal for both clonal expansion and deletion in lymphoid cells, HAX-1 was predicted to have cell survival functions [97]. This was mainly due to the predicted weak structural similarity to NIP3 and distribution within cells similar to the Bcl-2 family members: HAX-1 is ubiquitously expressed and mainly localized to the mitochondria, while also found at the endoplasmic reticulum (ER) and the nuclear envelope. Structurally, HAX-1 has no homologous proteins [97]. This has caused sparse literature pertaining to structural characterization. There has been evidence that HAX-1 is primarily disordered and adopts secondary structure via Ca^{2+} binding [98]. Additionally computational methods have predicted a primarily disordered structure based on the primary amino acid sequence [99]. A putative membrane

binding alpha helix is located from amino acids 261-273 [100]. Heat shock protein 90 (HSP90) has been discovered as a chaperone that interacts with HAX-1 suggesting that this interaction plays a role in HAX-1 protein folding [92, 94].

The localization of HAX-1 to the mitochondria provided insight towards its protective mechanism [94]. Involved mainly in Ischemia/reperfusion injury that is characterized by a decrease in [ATP], increase in glycolysis, increase in [lactic], increase in cytosolic [Na^+], and an increase in cytosolic [Ca^{2+}] [101], HAX-1 was initially found to activate Caspase 3 and Caspase 9 [102]. These two proteins are integral in the initiation of an extrinsic apoptotic pathway where death receptors on the cell surface trigger a cascade of caspase activation ultimately resulting in permeabilization of the mitochondrial membrane [103-106]. HAX-1 interaction with Pro-caspase 9 deactivates caspase 9 blocking the cascade of signals to death effector caspases 3, 6 and 7 preventing apoptosis. This has led to decades of cancer research centered around HAX-1 [94, 107-127]. Therapeutic studies suggest that the cardiac protective mechanism of action for pravastatin may be maintaining the mitochondrial expression of HAX-1 [108]. Additionally, chemoresistance is associated with the overexpression of HAX-1, which when knocked down, resensitizes the previously drug-resistant breast cancer cells to chemotherapy [128]. Additionally, HAX-1 has been found to bind microRNAs (miRNAs) which are essential tumorigenesis and chemoresistance regulators implicated in the resensitization of breast cancer cells to the chemotherapy drugs such as doxorubicin as well as cisplatin [129, 130]. Suppression of HAX-1 induced by miRNAs are emerging as an encouraging therapeutic for resensitization beyond

breast cancer cells now studied in esophageal squamous cell carcinoma, colorectal cancer cells as well as bladder cancer cells [131-133].

Kranias *et al.* have pioneered the research driven towards understanding the role of HAX-1 in Ca^{2+} regulation [71, 72, 82, 84, 85, 87-96]. HAX-1 has been found to interact with both SERCA2a as well as PLN [88, 90]. The minimum binding region of HAX-1 for PLN is located at amino acids 203-245 while the minimum binding region of PLN for HAX-1 is located at amino acids 16-22. Knock out mice have demonstrated that HAX-1 only localizes to the SR membrane in the presence of PLN. Upon phosphorylation of PLN, the HAX-1 inhibitory affects were abolished [91]. HAX-1 interaction with PLN accounts for roughly half of the inhibition originally thought to be solely due to PLN [95]. Most recently, HSP-90 has been discovered as a quaternary member of the SERCA/PLN/HAX-1 complex by Kranias *et al.* and SERCA2a's interactome has expanded once again thanks to her efforts [92, 94]. Interestingly, mitochondrial Ca^{2+} uptake can account for cardiomyocyte relaxation when the sarcolemmal mechanisms are inhibiting, suggesting HAX-1 may play a role at the membrane of each organelle for Ca^{2+} regulation within cardiomyocytes [134].

1.9 Objectives

It has been proposed that HAX-1 increases SERCA inhibition via disruption of PLN pentamers, however the structural changes of HAX-1 associating to the membrane and binding monomeric PLN leading to increased inhibition of SERCA are not yet understood. *I hypothesized that HAX-1 associates with the membrane*

as well as with PLN codependently to alter PLN dynamics. To test this hypothesis, I used NMR spectroscopy in conjunction with other biophysical and biochemical techniques to probe HAX-1, PLN, SERCA and the SERCA/PLN/HAX-1 complex. Specifically, I aimed to answer the following questions:

- How can HAX-1 be expressed, purified, and functionally assayed for *in vitro* biophysical characterization?
- What is the structure of HAX-1 in solution and in the presence of lipid membranes?
- How is SERCA function and PLN regulation affected by HAX-1 and how can a SERCA/PLN/HAX-1 complex be formed to perform NMR studies under fully functional conditions?

The answers to these questions would increase the understanding of the molecular basis of regulation of SERCA by the PLN/HAX-1 complex. This would contribute to the overall goal of the lab to understand the structural basis of muscle relaxation via Ca^{2+} regulation and could provide important information to target the SERCA/PLN/HAX-1 complex in the treatment of heart failure.

1.10 NMR spectroscopy

While X-ray crystallography or cryo-electron microscopy can provide atomic resolution structures of proteins both alone and in complex with various binding partners, for such a dynamic protein like HAX-1, tag free structural data is most readily available via nuclear magnetic resonance (NMR). To understand the

molecular basis of regulation of SERCA by the PLN/HAX-1 complex, both solution- and solid-state NMR are the ideal techniques to probe the conformational plasticity of HAX-1 both bound to membranes and in solution.

1.10.1 Basics of NMR

The elementary description of spectroscopy hinges upon the notion that a molecule sits at a particular energy state, labelled by the quantum numbers that define the allowed quantized energy states of a particular physical property, and hops between this initial state and excited states of higher energy upon absorbing electromagnetic energy equal to the energy difference between the excited state and the initial state [135, 136]. While it is true that this is what is observed upon making a measurement, in reality the molecule can exist in a superposition of any number of these states prior to measurement.

The NMR technique observes the spectrum produced by energy states of an intrinsic quantity of atomic nuclei, called spin, upon excitation with an electromagnetic field of radio wave frequency [135]. Spin, like mass or charge, is an inherent property of the nuclei determined by the subatomic particles that make up the atom and is closely related to the quantity angular momentum that is possessed by a rotating object [136]. The difference being that angular momentum requires an object to be rotating, while origination of spin does not; spin simply exists confirmed through experimental evidence [137]

Classically, the total angular momentum of a rotating diatomic molecule is defined by quantum number J in integer values:

$$L_{tot} = (J(J+1))^{\frac{1}{2}}\hbar$$

and gives some idea as to how fast the molecule is rotating [136]. The rotational energy of each state, (E_J) is proportional to the square of L_{tot}:

$$E_J = BJ(J+1)$$

where B is the rotational constant that is small for large masses and vice versa. While the above equations provide information about how fast the molecule is rotating, the azimuthal quantum number *M* gives an idea about the angle and direction of the rotation:

$$M_J = -J, -J+1, \ldots, J$$

These definitions remain the same for spin, but introduce a new variable to differentiate the two physical phenomena:

$$Spin = (S(S+1))^{\frac{1}{2}}\hbar$$

While particles with integer S are “allowed” by quantum mechanical treatment of the angular momentum of an atom (the eigenvalues of spherical harmonics always result in integer values describing the spatial form of the hydrogen atom orbitals), another experimentally proven phenomenon, lacking any physical framework, exists: certain atoms can have half integer quantum numbers.

This discovery was first made by Enrico Fermi and follows Fermi-Dirac statistics, hence particles with spin ½ integer are named fermions [138]. The competing theory of Bose-Einstein statistics follows integer spin values, hence particles with integer spin values are called bosons. The fundamental particles that compose a particle determine whether it is a fermion or a boson. There are three types of particles that make up the universe: leptons, quarks, and force particles. Leptons are low mass particles coming in six different flavors, electrons being one of them. Quarks are relatively heavy, also coming in 6 varieties and are spin ½. Force particles mediate the action of the different particles with each other. The most widely known force particle is the photon. Atomic nuclei are made up of neutrons and protons which are composed of 3 quarks each resulting in a net spin ½ (2 quarks with spin +1/2, one with spin -1/2). The combination of these fermions in parallel ($^{+}1/2+^{+}1/2$) or antiparallel ($^{-}1/2+^{+}1/2$) configurations ultimately determines the net spin of the atomic nuclei. Fortunately, for NMR, the Pauli exclusion principle means the electron angular momentum almost always cancels out so the total angular momentum is a result of

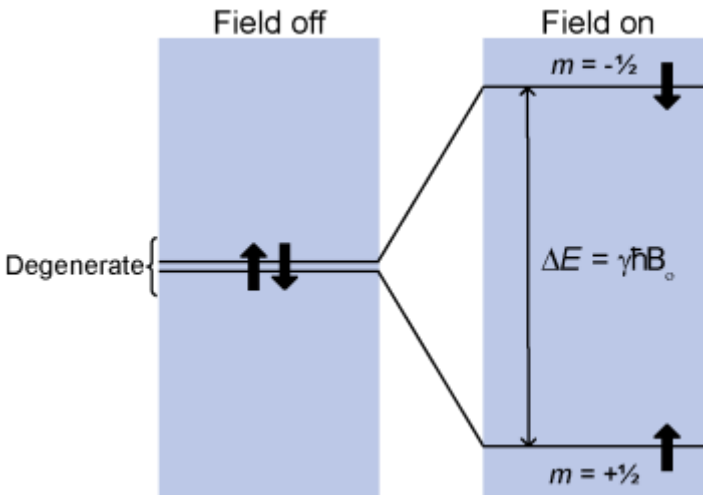

Figure 1.7: Spin degeneracy

Spin ½ states without a magnetic field applied (left) and Zeeman splitting with a magnetic field applied (right).

molecular rotation and nuclear spins.

A spin state is (2*I*+1)-fold degenerate. Because each spin state (or angular momentum quantum state) has a magnetic moment associated with it, to break this degeneracy a magnetic field is applied. This provides the spectrum of observable states. Consideration of only the allowed states (whether it is a boson or a fermion, there are discrete, quantized energy levels) is adequate for other forms of spectroscopy such as IR or UV spectroscopy. Because these spectroscopies observe vibrational or electronic energies, the rapid and frequent collisions that occur within solution cause mixed states lifetimes to be very short [135]. Additionally, manipulating mixed states requiring higher energy electromagnetic fields (compared to radio waves used in NMR) such as IR (vibrations) and UV (rotations and vibrations) requires very short, intense pulses. These pulses, while possible, are not always conducive to temperature sensitive samples such as those found in the body [135]. Because these mixed states can be manipulated in a time-dependent manner in NMR, there consists a unique library of experiments.

While a full quantum mechanical treatment of the mixed states is required for complete understanding of NMR, the vector model provides a way to visualize the superposition of states vital to the understanding of NMR experiments. Because magnetic energy depends on the interaction between the magnetic moment ($\vec{\mu}$) and the magnetic field ($\vec{B}$) we can visualize the lowest energy arrangement when $\vec{\mu}||\vec{B}$. Spin and magnetism are very closely linked

$$\hat{\mu} = \gamma \hat{s}$$

where γ is the gyromagnetic ratio and $\hat{s}$ is the angular momentum of spin s. Because spins have angular momentum and a magnetic moment, rather than aligning parallel with the magnetic field, they precess around the magnetic field according to

$$\omega_0 = -\gamma B_0$$

where ω^0 is the larmor frequency in radians/s. The precessing magnetic moment vector can be visualized in cartesian coordinates where B_0 is along the z-axis. The magnetic moment can be manipulated by R.F. pulses along any of the three axes at any angle representing mixtures of quantum states.

Relaxation from excited spin states does not occur through rotations and collisions of molecules. The precession of nuclei about $\overrightarrow{B_0}$ is affected, however, through other sources of magnetism (electric currents, magnetic moments of electrons, and magnetic moments of other nuclei). The circulation of electrons within an orbital create electric currents that generate magnetic fields and affect the precession of the spin. The effect from these small fluctuating magnetic fields is small (changes the tilt angle by 10^{-4} degrees in a 500 MHz spectrometer), however, leads to $\vec{\mu}$ sampling its entire range of motion. While sampling, there is a bias towards aligning with $\overrightarrow{B_0}$. This effect on an excited spin state whose magnetization has been rotated 90 degrees by an R.F. pulse to the x-y plane results in relaxation to the ground state (precessing around the z-axis). While precession of nuclei is on the order of ns, this transverse relaxation process

requires timescales on the order of s and is the source for most of the spectrometer time required for experimentation and is represented by:

$$M_z^{nuc} = M_{eq}^{nuc}(1 - e^{-\frac{t}{T1}})$$

Returning to the excited spin state of a 90-degree rotation of the nuclei, a second relaxation phenomena must be considered. Once the R.F. pulse is switched off, the nuclei precesses in the usual way in the x-y plane [139].

$$M_y^{nuc} = M_{eq}^{nuc}\cos(\omega_0 t)e^{-t/T_2}$$

$$M_x^{nuc} = M_{eq}^{nuc}\sin(\omega_0 t)e^{-t/T_2}$$

Since each nuclei experiences a slightly different local magnetic field due to the chemical environment, the precession of each individual nuclei begins to precess out of phase leading to transverse relaxation. For small molecules in solution, T_1 ~T_2. For large molecules like proteins or for solids, T_2 can be on the order of ms.

Rotating magnetic moments generate rotating magnetic fields that allow for observation of nuclear spins in a sample. Through Maxwell's equations it is known that changing a magnetic field is associated with an electric field [136].

$$\nabla \times E = -\frac{\partial B}{\partial t}$$

If a coil is placed near the sample, the electric field sets the electrons in motion as an electrical current. The analogue signal generated by the spins is called a free induction decay (FID) and is downconverted (the raw signal oscillated too fast

for ADCs) and digitized by comparing it to a reference signal of a known frequency chosen by the spectroscopist. The FID has the form

$$s_{FID} = \cos(\omega_0 t)\, e^{-t/T_2}$$

Comparing the raw signal to the reference signal results in

$$\cos\left(\left(\omega_0 - \omega_{ref}\right)t\right) e^{-t/T_2}$$

A complication now arises as the cosine function does not differentiate between positive and negative values of the differences in frequencies. To solve this issue the receiver out puts two signals (real and imaginary components):

$$s_A(t) \sim \cos\left(\left(\omega_0 - \omega_{ref}\right)t\right) e^{-t/T_2}$$

$$s_B(t) \sim \sin\left(\left(\omega_0 - \omega_{ref}\right)t\right) e^{-t/T_2}$$

where

$$s(t) = s_A + \mathrm{i}s_B$$

Each output is connected to its own ADC which measures the voltage level repeating at varying time points. For solid samples, the sampling bandwidth is around 250 ns, where for molecules in solution, the sampling bandwidth is around 4 μs. The digitized signal is then Fourier transformed to the frequency domain to obtain the spectrum of the spins in the sample.

Beyond the vector model, NMR spectra hold information only interpretable when considering the quantum mechanics of a nuclear spin. This requires solving

the time-dependent-Schrödinger equation. For NMR, the motions of the electrons and their interactions (magnetic and electrical influences) are averaged out under the assumption that spin energies are assumed to be too small to effect electronic motions. The orientation dependence of the energy of a spin in an electromagnetic field while rotating is described by the Hamiltonian:

$$\widehat{H}_j = \widehat{H}_j^{\text{elec}} + \widehat{H}_j^{\text{mag}}$$

Where $\widehat{H}_j^{elec}$is the nuclear electric energy and $\widehat{H}_j^{mag}$is the nuclear magnetic energy. For nuclei, there is no electric dipole moment and for spin ½, all electric multipole moments vanish:

$$\widehat{H}_j^{\text{elec}} = 0$$

The nuclear magnetic energy is manipulated by the surrounding magnetic field. If a 3-dimensional field is considered at the site of the spin:

$$\widehat{\boldsymbol{\mu}}_j = \gamma_j \hat{\mathbf{I}}_j$$

$$\widehat{H}_j^{\text{mag}} = \widehat{\boldsymbol{\mu}}_j \cdot \mathbf{B}$$

The magnetic field that the spin experiences is influenced by external and internal spin interactions. The external fields are B_0 described by $\widehat{H}_j^{static}$ and the applied R.F. fields described by $\widehat{H}_j^{RF}(t)$ throughout the pulse sequence as well as a gradient field that depends on the spatial position $\widehat{H}_j^{\text{grad}}(\mathbf{r}, t)$:

$$\widehat{H}_j^{\text{static}} = -\gamma B_0 \hat{I}_{jz}$$

$$\hat{H}_j^{\mathrm{RF}}(t) \cong \begin{cases} -\omega_{\mathrm{nut}}^j\{\cos(\omega_{\mathrm{ref}}t + \varphi_{\mathrm{p}})\hat{I}_{jx} + \sin(\omega_{\mathrm{ref}}t + \varphi_{\mathrm{p}})\hat{I}_{jy}\} & \text{during r. f. pulse} \\ 0 & \text{otherwise} \end{cases}$$

where $\omega_{\mathrm{nut}}^j = \left|\frac{1}{2}\gamma_j B_{\mathrm{RF}} \sin\theta_{\mathrm{RF}}\right|$ is the nutation frequency.

The internal spin Hamiltonian of spin ½ nuclei consists of purely magnetic interactions (quadrupolar electronic interactions exist only for spin>½) much weaker than the external interactions. Chemical shift, direct dipole-dipole couplings, J-couplings and spin-rotation interactions are classes of interactions that make up the internal spin Hamiltonian.

1.10.2 Chemical shift

The chemical shift is the indirect magnetic interaction between B_0 and the nuclei mediated by electrons. The external field induces electronic currents in the electron clouds surrounding atomic nuclei which in turn generates a local magnetic field that is typically four orders of magnitude weaker than B_0 (**Fig. 1.8**):

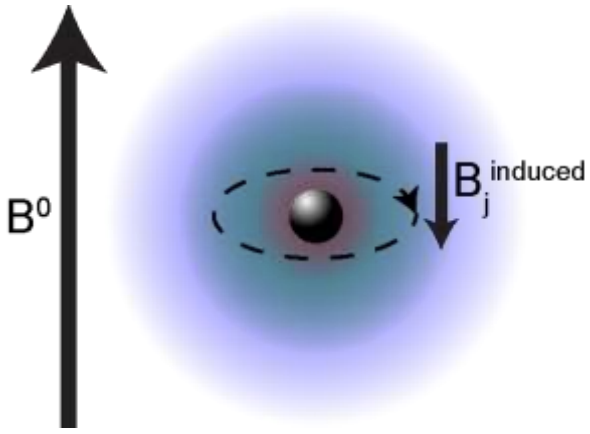

Figure 1.8: Chemical shift

The magnetic field (B^0) induces a current in the electrons creating an induced magnetic field $B_j^{induced}$.

$$\mathbf{B}_j^{\mathrm{loc}} = \mathbf{B_0} + \mathbf{B}_j^{\mathrm{induced}}$$

where

$$\mathbf{B}_j^{\mathrm{induced}} = \boldsymbol{\delta}^j \cdot \mathbf{B_0}$$

and $\boldsymbol{\delta}^j$ is a 3x3 matrix that takes into account that the induced field is

typically in a different direction than B_0. For each nuclei there exists a principal set of axes at which the external field can be applied where the induced field is parallel to the external field. The average of the diagonal principal values along the principal axes is the isotropic chemical shift:

$$\delta_j^{\text{iso}} = \frac{1}{3}\left(\delta_{XX}^j + \delta_{YY}^j + \delta_{ZZ}^j\right)$$

which determines the frequency at which peaks appear in solution NMR. If all three principal values are equivalent, the chemical shift tensor is isotropic and is a sphere. If two of the values are equivalent the tensor is uniaxial and if all three differ the tensor is biaxial and resemble an ellipsoid. Chemical shift anisotropy quantifies the deviation from the isotropic chemical shift:

$$\delta_j^{\text{aniso}} = \delta_{ZZ}^j - \delta_j^{\text{iso}}$$

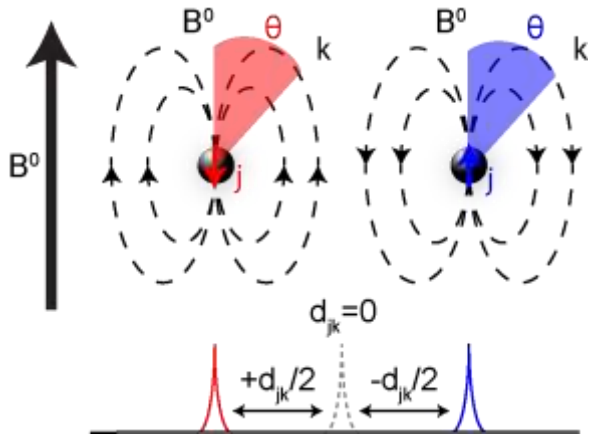

Figure 1.9: Direct dipole-dipole coupling

Spin j coupled to spin k and its orientational dependence (θ) results in splitting of the signal equal to the magnitude of d_{jk} (adapted from R.R. Gil, et al.).

where δ_{ZZ}^j is the principal value that deviates the most from δ_j^{iso}. Most likely, B_0 does not align with the principal axes values:

$$\hat{H}_j^{\text{CS}} \cong -\gamma_j \overline{\delta_{ZZ}^J(\theta)} B_0 \hat{I}_{jz}$$

under the secular approximation where δ_{ZZ}^j depends on the molecular orientation (θ). In solids, the

molecular orientation does not sample uniformly, but instead is more probable to have a specific orientation so the motional averaged $\overline{\delta_{ZZ}^{J}(\theta)}$:

$$\overline{\delta_{ZZ}^{J}(\theta)} = \int \mathrm{d}\theta \delta_{ZZ}^{j}(\theta)\, \mathrm{p}(\theta)$$

where $\mathrm{p}(\theta)$ is the probability of the molecule to be found in the range of θ and $\mathrm{d}\theta$.

1.10.3 Direct dipole-dipole coupling

The second class of internal magnetic interactions is direct dipole-dipole coupling. This is the direct magnetic interactions of nuclear spins with each other:

$$\widehat{H}_{jk}^{DD} = b_{jk}\left(3\left(\hat{I}_j \cdot e_{kj}\right)\left(\hat{I}_k \cdot e_{jk}\right) - \hat{I}_j \cdot \hat{I}_k\right)$$

where $b_{jk} = -\frac{\mu_0}{4\pi}\frac{\gamma_j \gamma_k \hbar}{r_{jk}^3}$ which is the magnitude of the vector between the two spins depending on the distance, r. Considering the secular approximation and defining the orientation with respect to B_0 in spherical coordinates [140] the magnitude depends on the angle between the vector joining the nuclei and B_0, θ_{jk} (**Fig. 1.9**, [141]):

$$d_{jk} = b_{jk}\frac{1}{2}\left(3\cos^2\theta_{jk} - 1\right)$$

when $3\cos^2\theta_{jk} - 1 = 0$, secular dipolar coupling vanishes. In solid-state NMR this is known as the magic angle (54.74°). In isotropic liquids, secular dipolar coupling averages to zero:

$$\int_0^{\pi} \mathrm{d}\theta_{jk} \sin\theta_{jk} \left(3\cos^2\theta_{jk} - 1\right) = 0$$

where $\sin\theta_{jk}$ gives all orientations equal probability.

1.10.4 J-coupling

The third class of internal magnetic interactions is indirect dipole-dipole coupling, or J-coupling, which persists in isotropic liquids. This interaction is similar to the chemical shift in that it is mediated by electrons, however, instead of providing a local magnetic field from the electron environment, J-coupling, provides a local magnetic field from electrons circulating through the chemical bond itself:

$$\widehat{H}_{jk}^{\mathrm{iso}} = 2\pi J_{jk} \hat{I}_j \cdot \hat{I}_k$$

where J_{jk} is a 3x3 matrix describing the scaler coupling (the average of the diagonal elements of the J-coupling tensor. Unlike the chemical shift, J-coupling is independent of magnetic field and anisotropic J-coupling is small enough to be ignored.

1.10.5 Spin rotation

The rotation of a molecule can generate circulating electric charges due to the charged nuclei and electrons. This generates a magnetic field, however, the secular component averages to zero. The non-secular part can be found to have an impact by causing relaxation in liquids.

1.10.6 Signal detection

$|\alpha\rangle$ and $|\beta\rangle$ are eigenstates of the z-component of the angular momentum for spin ½ and so are well defined. However, measuring the x- or y-component of the angular momentum leads to unpredictable measurements due to the quantum nature of reality. The measurement results in $|\alpha\rangle$ or $|\beta\rangle$ with a probability of 50%. The spin, however is not restricted to only $|\alpha\rangle$ or $|\beta\rangle$. It can occupy a superposition of states in which

$$|\psi\rangle = c_\alpha|\alpha\rangle + c_\beta|\beta\rangle$$

Where c_α and c_β are the complex superposition coefficients. These coefficients have the restriction

$$\langle\psi|\psi\rangle = 1$$

How these states evolve with respect to time comprises the field of spin dynamics. This requires a treatment of the wavefunction via the time-dependent Schrödinger equation:

$$\frac{\mathrm{d}}{\mathrm{dt}} = |\psi\rangle(t) = -\mathrm{i}\hat{H}|\psi\rangle(t)$$

And the equation of motion of a spin in an external field is

$$\frac{\mathrm{d}}{\mathrm{dt}}|\psi\rangle(t) = -\mathrm{i}\omega_0\tau\hat{I}_z|\psi\rangle(t)$$

a simple differential equation with the solution

$$|\psi\rangle(t_b) = e^{-\mathrm{i}\omega_0\tau\hat{I}_z}\,|\psi\rangle(t_a)$$

Where $e^{-\mathrm{i}\omega_0\tau\hat{I}_z} = \hat{R}_z(\omega_0\tau) = \hat{R}_z(\phi)$, the rotation operator. Throughout spin dynamics, the eigenstates remain the same except for a phase factor, while the superposition of states change with time.

To quantifiably predict, via the expectation value of a given operator $\hat{Q}$, the time evolution of the superposition of states, or coherences, the spin density operator formalism is employed. This treatment begins with the realization that the expectation value results in a quadratic equation

$$\langle\psi|Q|\psi\rangle = c_\alpha c_\alpha^* Q_{\alpha\alpha} + c_\alpha c_\beta^* Q_{\alpha\beta} + c_\beta c_\alpha^* Q_{\beta\alpha+} c_\beta c_\beta^* Q_{\beta\beta}$$

This enables a matrix representation of populations and coherences:

$$|\psi\rangle\langle\psi| = \begin{pmatrix} c_\alpha \\ c_\beta \end{pmatrix}\begin{pmatrix} c_\alpha^* & c_\beta^* \end{pmatrix}\begin{pmatrix} c_\alpha c_\alpha^* & c_\alpha c_\beta^* \\ c_\beta c_\alpha^* & c_\beta c_\beta^* \end{pmatrix}$$

where the diagonal elements represent the population of $|\alpha\rangle$ or $|\beta\rangle$ and the off-diagonal elements are coherences. If we would like to measure Q for multiple spins occupying different states, the most likely result is given by

$$\langle\psi|\hat{Q}|\psi\rangle = \langle\hat{Q}\rangle = \mathrm{Tr}\{|\psi\rangle\langle\psi|\hat{Q}\}$$

However, summing $|\psi\rangle\langle\psi|$ for every spin is impractical, so the density operator is defined

$$\hat{\rho} = \overline{|\psi\rangle\langle\psi|}$$

and

$$\langle Q \rangle = \mathrm{Tr}\{\hat{\rho}\hat{Q}\}$$

The coherences represent the transverse spin magnetization. Because coherences are complex numbers, they have a phase and an amplitude. The thermal equilibrium distribution between $|\alpha\rangle$ and $|\beta\rangle$ can be reliably guessed via the Boltzmann distribution, allowing for the prediction of the ensemble of spins at any given time after. If R.F. pulses are applied, it is a simple treatment of the density matrix with the appropriate sandwich rotation matrices.

1.10.7 Relaxation

Diminishment of the FID requires a treatment for the prediction of the relaxation of the magnetization back to thermal equilibrium. Contributing factors to the relaxation rate constants are dipolar, chemical shift anisotropy and quadrupolar interactions and vary with molecular rotational tumbling rates (τ_m). The origin of nuclear spin dynamics begins with the quantum mechanical master equation:

$$\frac{\mathrm{d}}{\mathrm{d}t}\sigma(t) = -\mathrm{i}[\mathrm{H}^s, \sigma(t)] - \hat{\hat{\Gamma}}\{\sigma(t) - \sigma_0\}$$

where H^s is the spin Hamiltonian and $\sigma(t)$ is the reduced density operator. $\sigma(t)$ is used to find the expectation values of a set of operators that only interact with nuclear spins. $\sigma(t)$ is a matrix consisting of diagonal elements (populations) and off diagonal elements (coherences). $\hat{\hat{\Gamma}}$ is the relaxation super-operator that drives the density operator towards its equilibrium value by accounting for dissipative interactions with the lattice; an operator that accounts for the interactions ignored

by the selected set of spin operators [142]. $\hat{\hat{I}}$ is an operator that operates on operators and subsequently requires a transformation from Hilbert space, spanned by state functions, to the Liouville space, spanned by the corresponding linear operators. For example, consider the commutator superoperator $\hat{\hat{\mathrm{H}}}$. The eigenvalues for $\hat{\mathrm{H}}$ ($\boldsymbol{\varepsilon}_r$) are equal to the energy states of the system; therefore, the eigenvalues for $\hat{\hat{\mathrm{H}}}$ are

$$\omega_{rs} = \varepsilon_r - \varepsilon_s$$

containing the differences between energy states of the system [142]. Defining the relaxation superoperator can be done phenomenologically through the Bloch equations:

$$\frac{\mathrm{d}}{\mathrm{d}t}\mathbf{M}_j(t) = \gamma\mathbf{M}(t) \times \mathbf{B}(t) - \mathbf{R}_j\{\mathbf{M}(t) - \mathbf{M}_0\}$$

where $\mathbf{B}(t)$ is the external magnetic field and $\mathbf{M}_j$ is the bulk magnetization of the sample and **R** is the relaxation matrix.

$$\mathbf{R} = \begin{pmatrix} \frac{\mathbf{1}}{\mathbf{T_2}} & \mathbf{0} & \mathbf{0} \\ \mathbf{0} & \frac{\mathbf{1}}{\mathbf{T_2}} & \mathbf{0} \\ \mathbf{0} & \mathbf{0} & \frac{\mathbf{1}}{\mathbf{T_1}} \end{pmatrix}$$

However, this description is limited to systems without spin-spin coupling. Semi-classical relaxation theory accounts for the spin-lattice interactions by attributing

random process operators into the interaction Hamiltonian to describe lattice dynamics ($F^{(q)}(t)$):

$$\mathrm{H}_1^{\mathrm{T}}(t) = \sum_q F^{(q)}(t) A^{(q)}$$

where $A^{(q)}$ are operators that act exclusively on the spin system. A correlation function characterizes these random processes:

$$\mathrm{g}^{(q,q')}(\tau) = \overline{F^{(q)}(t) F^{(q')*}(t+\tau)}$$

Experimentally, the autocorrelation function forms the basis for the relaxation of nuclei:

$$\mathbb{G}(t) = \langle B_x(t) B_x(t+\tau) \rangle = \langle B_x^2 \rangle \mathrm{e}^{-|\tau|/\tau_c}$$

defining the fluctuation of the local field (B_x) for a time (τ) that decays based on the correlation time (τ_c) [136]. Two times the Fourier transform of the correlation function defines the frequency at which the local field fluctuates (spectral density) which the Lipari-Szabo model defines as

$$\mathbb{J}(\omega) = 2 \int_0^\infty C(t) \cos \omega t \, \mathrm{d}t$$

where *C*(t) is the correlation function defined by the product of the overall motion ($C_O(t)$) and internal motion ($C_I(t)$). The internal motion is defined by the timescale of the motions, called the effective correlation time (τ_e), and the order parameter:

$$C_{\mathrm{I}}(t) = O^2 + (1 - O^2) e^{-t/\tau_e}$$

For isotropic motion

$$C_{\mathrm{O}}(t) = \frac{1}{5} e^{-t/\tau_{\mathrm{M}}}$$

where τ_{M} is the molecular correlation time leaving the spectral density function as

$$\mathbb{J}(\omega) = \frac{2}{5}\left[\frac{O^2\tau_M}{1+(\omega\tau_M)^2} + \frac{(1-O^2)\tau}{1+(\omega\tau)^2}\right]$$

where $\tau = \tau_e + \tau_{\mathrm{M}}$ [143]. Through Maxwell's relations, the free energy derived from the experimentally determined partition function through the relaxation of atomic nuclei can then be used to find any thermodynamic parameter of the system [6].

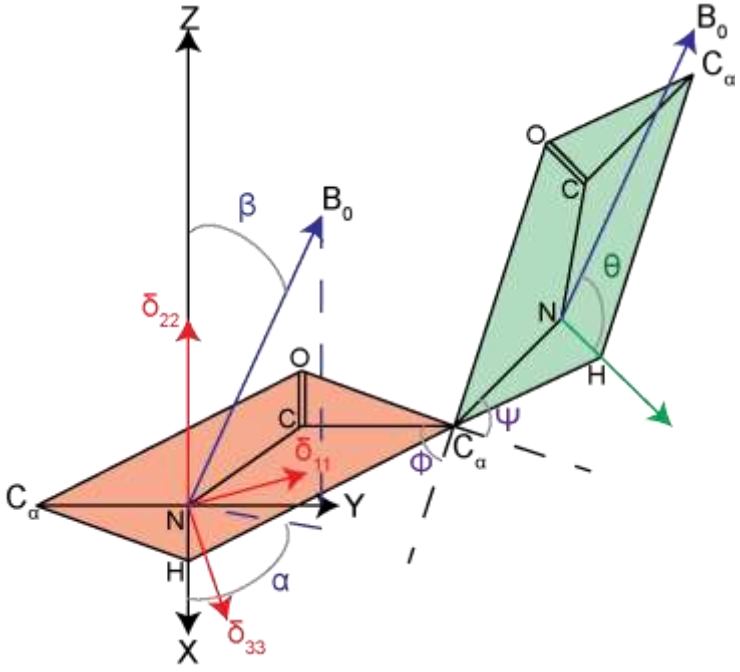

Figure 1.10: Tensor diagram for O-ssNMR

Pictorial representation of the chemical shift principle components with respect to the orientation of the amid plane. (adapted from Gustavsson et al.).

1.10.8 Solid state NMR

The isotropic tumbling of molecules in solution resulting in rapid molecular reorientation corresponding to rotational correlation times on the ns timescale are essential for the narrow linewidths of solution-state NMR. Even detergent-

solubilized membrane proteins are isotropic in solution allowing for solution-state NMR experimentation. Narrow linewidths produce high resolution spectra to easily observe atomic resolution, site specific information. The source comes from the motionally averaged dipolar couplings averaging to zero. The addition of lipid vesicles increases correlation times 1,000 fold to several μs [144], leading to broad powder patterns representing all possible orientations of the molecule. This limits solution-state NMR experimentation with lipid mimetics to detergent micelles only.

Solid-state NMR (ssNMR) is the gold standard for NMR on membrane proteins in the presence of lipid bilayers. ssNMR consists of two main techniques: oriented ssNMR (O-ssNMR) and magic angle spinning (MAS) ssNMR. O-ssNMR magnetically aligns all the molecules in the sample using the spectrometers magnetic field. This removes the powder pattern and results in each nucleus giving rise to only one peak. Each peak is orientation dependent. The lipid bilayer mimetic that orients the sample is called a bicelle which is composed of short chain and long chain lipids forming a liquid crystalline phase that spontaneously align. The alignment of a sample provides information otherwise unobservable by solution-state NMR. For example, the physical description of the amide nitrogen chemical shift is as follows:

$$\delta_I = (\delta_{33} - \delta_{11})\sin^2\beta\cos^2(\alpha - 17) + (\delta_{11} - \delta_{22})\sin^2\beta + \delta_{22}$$

Where α and β are defined according to **Fig. 1.10** and the principal values of the chemical shift tensor are 64 ppm, 77 ppm, and 217 ppm respectively [145].

Correlating the chemical shift anisotropy defined above, with N-H dipolar couplings defined as

$$D_{IS} = -\frac{\mu_0 \gamma_H \gamma_N \hbar}{4\pi r_{HN}^3}\left(\frac{3\cos^2\theta_{HN} - 1}{2}\right)$$

Where $\Theta_{HN}$is the angle between the N-H bond vector and the magnetic field, B_0, and r_{HN} is the distance from the amid nitrogen to the amid proton, produces a two-dimensional spectrum acquired by separated local field (SLF) experiments [140]. One such experiment is the Polarization Inversion Spin Exchange at the Magic Angle (PISEMA) experiment, in which the expected 3.6 residues per αhelical turn can be observed in a wheel like pattern called the polarity indexed slant angle (PISA) wheel [146, 147]. The size and location of the wheel are correlated to the angle between the helical axis and the normal of the bilayer. In conjunction with the location of the resonances in the helical wheel provide topological information on tilt angle and rotation angle of a transmembrane helix. MAS gets its name from the removal of dipolar couplings via mechanical orientation of the sample at an angle of 54.7°, as mentioned in section 1.7.3, and spinning at rates up to 120 kHz. Because the dipolar coupling term depends on

$$D_{IS} \propto \frac{3\cos^2\theta_{HN} - 1}{2}$$

Which is equal to zero when

$$\theta_{HN} = 54.7°$$

Averaging the secular contributions of the dipolar coupling by spinning the sample around θ_{HN} at high rates removes the dipolar coupling creating narrow linewidths in solid-state spectra [140].

Chapter 2 Solid-state NMR of membrane proteins in lipid bilayers: to spin or not to spin?

T. Gopinath, Daniel Weber, Songlin Wang, Erik Larsen, and Gianluigi Veglia

Departments of Biochemistry, Molecular Biology & Biophysics and Chemistry,

University of Minnesota, Minneapolis, MN 55455

Reprinted with permission from Accounts of Chemical Research [148].

KEYWORDS: Membrane Proteins, Solid-state NMR, Oriented samples, Magic Angle Spinning.

Abstract

Membrane proteins mediate a plethora of cellular functions and represent important targets for drug development. Unlike soluble proteins, membrane proteins require native-like environments to fold correctly and be active. Therefore, modern structural biology techniques have aimed to determine the structure and dynamics of these membrane proteins at physiological temperature and in liquid crystalline lipid bilayers. With the flourishing of new NMR methodologies and improvements in sample preparations, magic angle spinning (MAS) and oriented sample solid-state NMR (OS-ssNMR) spectroscopy of membrane proteins is experiencing a new renaissance. Born as antagonistic approaches, these techniques nowadays offer complementary information on the structural topology and dynamics of membrane proteins reconstituted in lipid membranes. By spinning biosolid samples at the magic angle (θ = 54.7^{o}), MAS NMR experiments remove the intrinsic anisotropy of the NMR interactions, increasing spectral resolution. Internuclear spin interactions (spin exchange) is reintroduced by RF pulses, providing distances and torsion angles to determine secondary, tertiary as well as quaternary structures of membrane proteins. OS-ssNMR, on the other hand, directly detects anisotropic NMR parameters such as dipolar couplings (DC) and anisotropic chemical shifts (CS), providing orientational constraints to determine the architecture (*i.e.*, topology) of membrane proteins relative to the lipid membrane. Defining the orientation of membrane proteins and their interactions with lipid membranes is of paramount importance since lipid-protein interactions

can shape membrane protein conformations and ultimately define their functional states. In this Accounts, we report selected studies from my group integrating MAS and OS-ssNMR techniques to give a comprehensive view of the biological processes occurring at cellular membranes. We focus on the main experiments for both techniques, with an emphasis on new implementation to increase both sensitivity and spectral resolution. We also describe how the structural constraints derived from both isotropic and anisotropic NMR parameters are integrated into dynamic structural modeling using replica-averaged orientational-restrained molecular dynamics simulations (RAOR-MD). We showcase small membrane proteins that are involved in Ca^{2+} transport and regulate cardiac and skeletal muscle contractility: phospholamban (PLN, 6 kDa), sarcolipin (SLN, 4 kDa), and DWORF (4 kDa). We summarize our results for the structures of these polypeptides free and in complex with the sarcoplasmic reticulum (SR) Ca^{2+}-ATPase (SERCA, 110 kDa). Additionally, we illustrate the progress toward the determination of the structural topology of a six transmembrane protein associated with succinate and acetate transport (SaTP, hexamer 120 kDa). From these examples, the integrated MAS and OS-ssNMR approach, in combination with modern computational methods, emerges as a way to overcome the challenges posed by studying large membrane protein systems.

2.1 Introduction

Membrane proteins are involved in vital cellular events, mediating intra- and inter-cellular communication.[149] Their structure and function are regulated by diverse lipid membranes that constitute various cellular compartments. The heterogeneous membrane environment is a significant barrier for classical structural biology methods, and the characterization of membrane proteins at atomic resolution remains an outstanding challenge. Currently, X-ray crystallography is the method of choice for determining the structural features of membrane proteins in their ground states. The majority of membrane protein structures deposited in the protein data bank (PDB) have been determined by X-ray in detergent preparations. However, detergents are a rough approximation of native membranes and are somewhat problematic, as they introduce structural distortions and deviations from a proteins' native state.[150, 151] The outstanding progress in cryogenic electron microscopy (cryo-EM) has facilitated the structure determination of membrane proteins in nearly native-like states.[152] However, both X-ray and cryo-EM fall short in the characterization of lipid-protein interactions as well as in the determination of membrane protein orientation relative to the lipid membranes (i.e., topology). More importantly, these methods cannot probe the timescale of the functional dynamics of membrane proteins.

Solid-state NMR (ssNMR) methods are now reaching a level of sophistication, enabling the characterization of membrane proteins' structure, dynamics, and interactions.[153] In the past, ssNMR of membrane proteins relied on two distinct techniques: magic angle spinning (MAS)[154] and oriented sample (OS)[155]

ssNMR. While the first approach removes the anisotropy from the NMR physical observable by spinning at the magic angle to obtain high-resolution spectra,[156] the latter exploits anisotropic NMR parameters to obtain the orientation of membrane proteins' helical or β-sheet domains.[157] While MAS NMR techniques are ideal for measuring distances and torsion angles of a protein's backbone, OS-ssNMR directly measures the orientation of amide groups relative to the membrane bilayers. Specifically, this method provides tilt and rotation angles of membrane protein domains with respect to the bilayer normal. A significant advantage of ssNMR spectroscopy over X-ray and cryo-EM is the site-specific characterization of a protein's motion, including the timescale at which these motions occur, as well as the depiction of the different energetic and functional states. Following in the footsteps of solution-state NMR,[158] ssNMR is emerging as an atomic resolution technique uniquely suited for detecting conformationally excited states,[159-161] high-energy conformations that exemplify intermediates of protein folding reactions, active and inactive states, or alternate conformations, which could be targeted by more specific allosteric drugs.

In the following synopsis, we describe the milestones that our group has reached in the past decade. By all means, this survey is not exhaustive and does not cover many breakthroughs achieved by other research groups in the study of membrane proteins.

2.2 Membrane mimetic systems for high-resolution ssNMR spectroscopy

The functional reconstitution of membrane proteins in membrane mimetic systems is an essential step for the structural and functional characterization by ssNMR. Detailed protocols have been outlined by Das *et al*.[162] For MAS, we reconstitute recombinant membrane proteins in lipid vesicles via detergent-mediated preparations. For OS-ssNMR studies, we have been using two main procedures, involving either mechanically or magnetically aligned membrane preparations.[162] Both reconstitution protocols have their merits and limitations. Mechanically aligned systems are prepared by spreading the lipid-protein mixtures on solid supports (typically glass plates), and with iterative hydration/dehydration cycles, both lipids and proteins align in a *lasagna-like* stacking of phospholipid and protein layers. These preparations are detergent-free and can be obtained using mixed lipid compositions to approximate native membranes. Magnetically oriented preparations include lipid bicelles,[163] and more recently, nano- and macro-discs.[164] Lipid bicelles were among the first systems to be utilized for magnetic alignment of membrane proteins.[165] Bicelles are formed by one or more lipid types (long-chain component) and a detergent that solubilize the lipids (short-chain component). Depending on the ratio between the long- and short-chain components, anisotropic bicelles adopt a discoidal shape or a *Swiss cheese* phase.[166] Unlike mechanically aligned membrane systems, the composition of bicelles has more restrictions as many lipids prevent the formation of stably aligned phases for NMR measurements.[167] Also, the presence of proteins modifies the

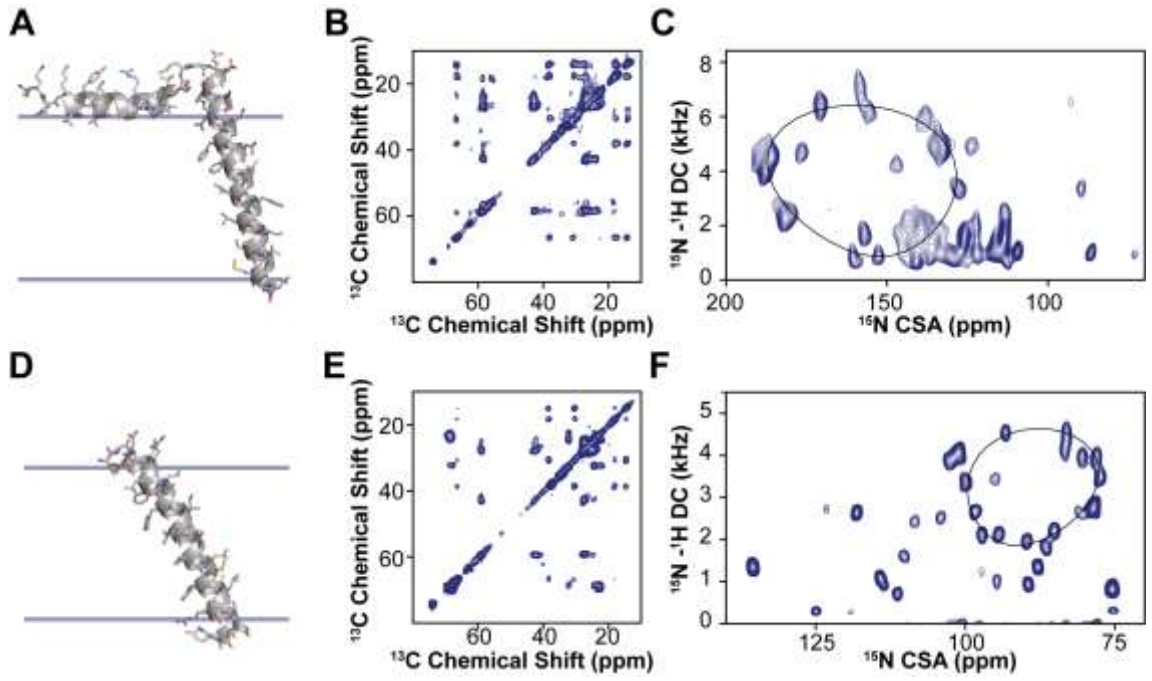

Figure 2.1: MAS and OS-ssNMR studies of single pass membrane proteins PLN and SLN

A. *Structure and membrane orientation of PLN obtained from a combination of isotropic and anisotropic restraints.* ***B.*** *^{13}C,^{13}C-DARR spectrum of PLN in lipid vesicles.* ***C.*** *SE-SAMPI4 spectrum of PLN in oriented lipid bicelles.* ***D.*** *Structure and orientation of SLN in lipid membranes calculated using both MAS and OS-ssNMR data.* ***E.*** *^{13}C,^{13}C-DARR spectrum of SLN in lipid vesicles.* ***F.*** *SE-SAMPI4 spectrum of PLN in oriented lipid bicelles. Note that the oriented spectrum of SLN was obtained using paramagnetic doping and in the absence of Yb^{3+} (unflipped bicelles).*

phase diagram of bicelles, and the conditions to obtain uniform orientation are often very narrow.

Another hurdle is represented by detergents (*e.g.*, 1,2-dihexanoyl-sn-glycero-3-phosphocholine, DHPC) that may interact with membrane proteins competing out lipids and causing the disruption of the bicellar phase.[151] Nonetheless, membrane proteins reconstituted in bicelle preparations possess more favorable conditions for ssNMR spectroscopic analysis.[168] The dynamics of bicelles

lengthen the transverse spin relaxation (T_2) of proteins, resulting in sharper and more intense resonances. As a consequence, it is possible to obtain highly-resolved two-dimensional (2D) separated local field (SLF) spectra. More importantly, membrane proteins reconstituted in bicellar preparations make possible the acquisition of 3D SLF experiments, *i.e.*, polarization inversion spin exchange at the magic angle (PISEMA) and SAMPI4, and residue-specific sequential assignments via proton driven spin diffusion (PDSD).

2.3 To spin or not to spin?

Since its incipit, ssNMR of membrane proteins has been carried out using MAS techniques.[169] OS-ssNMR has been relegated to an ancillary role due to the more demanding sample preparations. However, the redundancy of the primary sequences of helical membrane proteins and the inherent conformational heterogeneity hampers the complete sequential assignments and structure determination. To date, the majority of the structures solved by NMR of membrane proteins are *backbone structures* of small and medium-sized membrane proteins obtained by OS-ssNMR.[153] A few research groups have pioneered the combination of the two techniques to determine distances, torsion angles as well as orientational restraints.[170-175] The marriage of these techniques, often performed in similar membrane preparations, is very powerful. Both isotropic and anisotropic parameters can be combined to describe the ‘gymnastics’ of

membrane proteins, hopping from one state to another (**Fig. 2.1**). MAS techniques easily capture changes in the secondary structures. However, topological changes are more difficult to identify using isotropic NMR parameters. Transmembrane (TM) helix signaling occurs via intramembrane topological changes of helical domains, such as translation, piston, pivot (tilting), or rotation motions.[176, 177] While translation or piston-like motions can be monitored using inter-helical distances, tilt and rotation motions are often silent to the MAS analysis, but can be easily mapped using OS-ssNMR techniques. An example is the effects of a single mutation on the TM helix of DWarf Open Reading Frame (DWORF) (**Fig. 2.2**). The proline to alanine mutation of this small protein affects not only the helical content, but also its tilt and rotation angles relative to the lipid membrane. These topological changes are silent to MAS techniques, but they can be readily characterized by SLF experiments (**Fig. 2.2**). Although

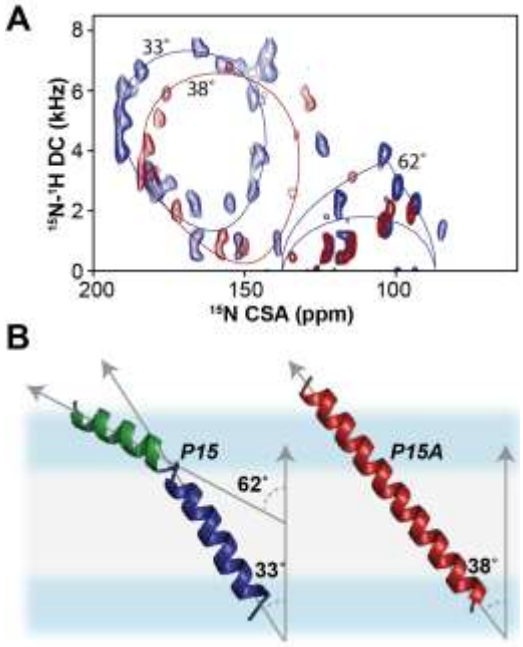

Figure 2.2: Effects of single mutation on the topology of DWORF in lipid membranes

A. *SE-SAMPI4 spectra of wild-type DWORF (blue) and P15A mutant (red) reconstituted into flipped 1,2-dimyristoyl-sn-glycero-3-phosphocholine (DMPC)/1-palmitoyl-2-oleoyl-glycero-3-phosphocholine (POPC) bicelles.* ***B.*** *Structural models of DWORF backbone obtained from replica-averaged orientational restrained molecular dynamics (RAOR-MD). Distinctive helical domains associated with the N-terminus (green) and C-terminus (blue) are fitted to PISA models.*

rotationally aligned MAS experiments for determining the topology of membrane proteins have been developed, they require fast rotational diffusion of proteins within lipid membranes and are often challenging for membrane proteins interacting strongly with lipids.[178, 179]

2.4 Advanced MAS and OS-ssNMR techniques

In the past decades, there have been several breakthroughs in MAS of membrane proteins. The first and most significant advancement involves the use of dynamic nuclear polarization (DNP)[180], which enhances the nuclear polarization via dipolar interactions with unpaired spin electrons, giving rise to high sensitivity spectra. In a few cases, this technique has dramatically improved the NMR spectra, and for selected membrane proteins, DNP has accessed information that was difficult to achieve using classical spectroscopic methods.[181] Also, protein perdeuteration[182] and paramagnetic doping[183] have contributed to speeding up NMR data acquisition. Our contribution has been in the development of novel pulse sequences with higher sensitivity for both MAS and OS-ssNMR.[184, 185] Our strategy is to recover *orphan spin operators* that are discarded during the execution of conventional pulse programs. We called these experiments *POE* for *P*olarization *O*ptimized *E*xperiments (**Fig. 2.3**).[185] The essential element of POE is the simultaneous cross-polarization (SIM-CP) that enables the transfer of polarization from the ^{1}H bath to two (or more) heteronuclei ^{13}C and ^{15}N. Dual acquisition MAS spectroscopy (DUMAS)[186, 187] was the first implementation of POE. In the DUMAS scheme, ^{13}C- and ^{15}N-edited 2D (or 3D)

experiments are simultaneously registered in a single experiment using two ^{13}C acquisition periods per scan. In our laboratory, 2D CC and NC correlation spectra are routinely acquired using DUMAS-based CXCX-NCA and Double Quantum Single Quantum (DQSQ)-NCO pulse sequences. After an initial analysis of CC and NC fingerprints, one can move on to more robust sequential assignment protocols, *e.g.*, a 3D DUMAS NCACX-CANCO experiment.

The sequential walk of carbonyl chemical shifts is obtained by matching the NCA planes of NCACX and CANCO data sets. In 3D DUMAS, a *bidirectional* SPECFIC-CP enables the polarization transfer from ^{15}N to $^{13}C_{\alpha}$ and vice versa. For selecting the NC bidirectional transfer, we use a four-step phase cycle on ^{15}N (+x, -x, +x, -x) and ^{13}C (+x, +x, -x, -x) radio frequency (RF) spin-locks.[188] This phase cycle selects the N to C_{α} or C to N transferred polarization and eliminates the ^{13}C and ^{15}N residual polarization pathways. To recover both *transferred* and *residual* polarization pathways of SPECIFIC-CP, we have developed the Multiple ExperIments via Orphan SpIn operatorS (MEIOSIS) approach that records four 2D spectra using two acquisitions per scan. The RF phases of SPECIFIC-CP spin-lock pulses are Hadamard-encoded, which enables the decoding of both transferred and residual polarization pathways leading to simultaneous acquisition of four multidimensional spectra. Similarly, a 3D MEIOSIS pulse sequence was developed for acquiring 3D CCC or CA(N)COCX correlation together with two other 3D spectra, NCACB and NCOCX, as shown for succinate and acetate transport membrane protein (SatP) (**Fig. 2.3**). We have also exploited residual polarization to concatenate up to eight two-dimensional experiments using Multiple

acquisitions via sequential transfer of orphan spin polarization (MAeSTOSO) approach. The MAeSTOSO approach can be very useful for acquiring 2D CXCX and N(C)C spectra with Dipolar Assisted Rotational Resonance (DARR) mixing periods for both long- and short-range correlations. All of these pulse sequences were tested with both crystalline preparations of globular proteins and single and/or multi-span membrane proteins such as sarcolipin (SLN), phospholamban (PLN), and SatP.[189] POE can also take advantage of the *afterglow* phenomenon, introduced by Traaseth and co-workers,[190] which can be incorporated into Transferred Echo DOuble Resonance (TEDOR)-NCX-based pulse sequences.[189] The 3D version of TEDOR-NCACX-NCOCX enables the simultaneous measurement of CC DARR restraints in the 1st acquisition and the

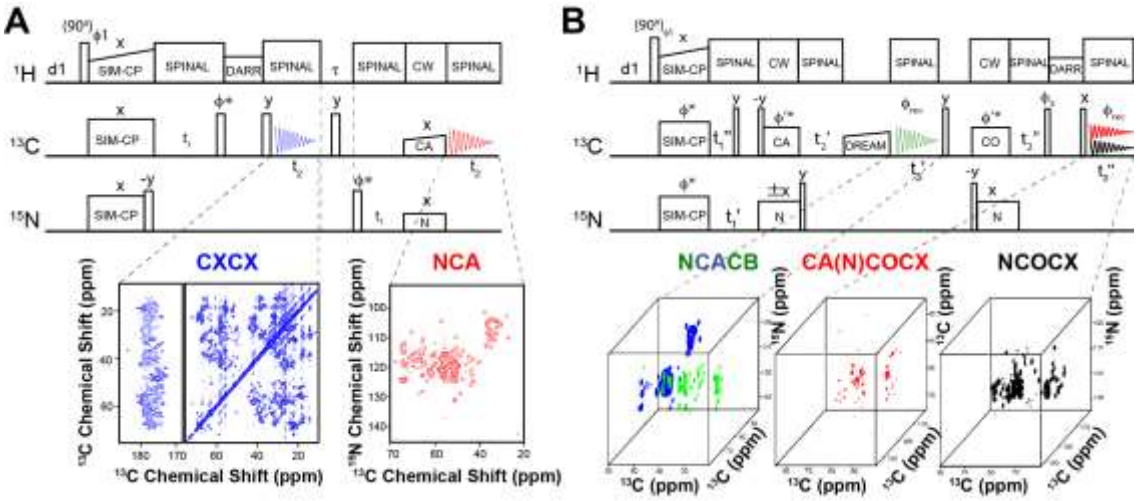

Figure 2.3: MAS Polarization Optimized Experiments (POE) on the six transmembrane SaTP protein transporter reconstituted in lipid membranes

A. *2D DUMAS experiments for the simultaneous acquisition of DARR (200 ms) and NCA experiments.* ***B.*** *MEIOSIS experiment with the simultaneous acquisition of three 3D experiments: NCACB, CA(N)COCX, and NCOCX.*

TEDOR NC distance restrains in the 2nd acquisition. This subtype of POE enables

one to record two different experiments, the first for resonance assignment and the second for distance measurements. More recently, POE were developed to include fast MAS experiments for the acquisition of ten experiments simultaneously.[191, 192]

Parallel to the improvements of MAS spectroscopy, our group has developed sensitivity enhancement (SE) SLF and heteronuclear correlation (HETCOR) experiments.[184] SE-SLF experiments increase the signal-to-noise ratio (S/N) by $\sqrt{2}$.[193, 194] We routinely use SE-SLF for 2D experiments to determine the topology of membrane proteins' backbones with respect to the bilayer normal. Recently, our laboratory has utilized paramagnetic relaxation enhancement (PRE) for the fast acquisition of SE-SLF experiments. By doping bicelles with 5% 1,2-dimyristoyl-sn-glycero-3-phosphoethanolamine-N-diethylenetriaminepentaacetic acid copper salt lipid (Cu^{2+}-DMPE-DTPA), we found that it is possible to accelerate the acquisition of multidimensional SE-SLF

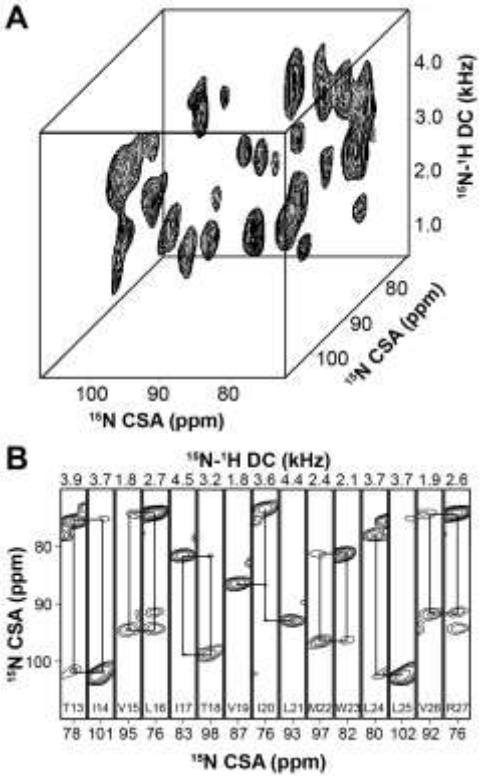

Figure 2.4: Example of 3D SLF experiments performed on SLN aligned in lipid bicelles

A. *3D SE-SAMPI4-PDSD spectrum of [U-^{15}N]-SLN in bicelles doped with 5% Cu^{2+}-chelated lipids.* ***B.*** *3D strip plots at specific dipolar coupling values from the 3D SE-SAMPI4-PDSD spectrum. The solid lines indicate [i, i+1] cross peaks.*

experiments up to 3 times. The improvements in sample stability combined with SE techniques and PRE made it possible to acquire 3D experiments for sequential residues assignments in magnetically oriented bicelle samples (**Fig. 2.4**).[195] A significant drawback of the application of paramagnetic doping to multidimensional SE-SLF pulse sequences is the temperature variations during the experiments, which is due to to the relatively short pulse delay (~ 1 s). These temperature oscillations not only affect the thermal stability of membrane proteins, but also disturb the magnetic alignment of the bicellar system. To address this issue, we designed heat-compensated SE-SLF pulse sequences (hcSE-SLF).[196] By removing the heterogeneity of the resonances in the spectra, the hcSE-SLF pulse sequences provide approximately 20% increase in sensitivity relative to SE-SLF experiments. The use of PRE is now being combined with Dual Acquisition orIented ssNMR spectroscopy (DAISY), a technique that records 2D SLF and SLF-Proton Driven Spin Diffusion (PDSD) OS-ssNMR spectra, simultaneously [188].

2.5 Structure calculations using ssNMR restraints

There are several approaches to implement isotropic and orientational restraints in the structure determination of membrane proteins. MAS experiments provide structural restraints, primarily isotropic chemical shifts and distances derived from DARR (or PDSD), chemical shift perturbation (CSP), and PREs, similarly to solution-state NMR. In most of the calculation protocols distances, angles, and chemical shift index (CSI) are implemented as harmonic restraints.[197] However, distances and angular restraints for membrane proteins are often very sparse and

may result in ill-defined structures, with the register of TM helices poorly defined. This problem is common to solution NMR structures of membrane proteins in detergent micelles.[150] For OS-ssNMR, Opella and Nevzorov introduced structural fitting procedures that would offer the best fit of chemical shift anisotropy (CSA) and dipolar coupling (DC) to calculate backbone orientations.[198] A more efficient procedure was introduced by Marassi and co-workers,[199] where the orientational restraints were treated as harmonic restraints and minimized using a simulated annealing algorithm. Together with the Cross, Marassi, Opella, and Hong groups, we recognized the importance of using a hybrid approach that would include not only the physical parameters obtained by MAS or solution NMR, but also orientation dependent parameters obtained by OS-ssNMR.[172, 200] In our original calculations, we included in the force field a *depth of insertion* potential developed by DeGrado's group that restrains the conformational freedom of membrane proteins within a low dielectric slab. This limits their conformational space to more physical minima defined by the hydrophobicity and electrostatics of membrane proteins. Using this protocol, we were able to determine the high-resolution structures of SLN and PLN (monomeric and pentameric assembly).[172, 174, 175, 200] Later on, we implemented distance, angular, and orientational restraints in a simulation system with explicit water and lipid environments.[201, 202] The explicit environment provides an improved description and a more accurate search of the membrane protein conformational phase space.[201, 202] Restrained molecular dynamics samplings have been shown to be applicable to a many biological systems, ranging from relatively rigid structural states to

heterogeneous conformational ensembles of proteins, including those adopting multiple topological states. Given the ensemble-averaged nature of the experimental ssNMR data, the latter case is accounted for by imposing the structural restraints as an average over independent simulations (replicas) evolving simultaneously in the so-called replica-averaged approach. These restrained simulations are able to give a view on the collective protein backbone motions at picosecond-to-millisecond timescales. To this extent, we were able to accurately describe the heterogeneous conformational ensembles of PLN both in its monomeric[201] and pentameric[202] states. The conformational equilibrium of PLN matched with the distinct states that were observed by both MAS and OS-ssNMR.

2.6 Topological allostery: transmembrane signaling via dynamic interactions

Unlike their soluble counterparts, membrane proteins are embedded in lipid bilayers where hydrophobicity is no longer a dominant force stabilizing ternary and quaternary structure.[203] Concomitant with the allostery occurring throughout an extensive network of interactions, signal transduction throughout TM domains must be communicated throughout a structure held together by weaker van der Waals forces, side-chain packing motifs (*i.e.*, leucine zippers), specific interactions with lipids and physical constraints imposed by the dimensions of lipid bilayers.[204, 205] Indeed, hydrogen bonding plays a significant role in stabilizing larger α-helical bundles,[25] but how external signals are transduced throughout

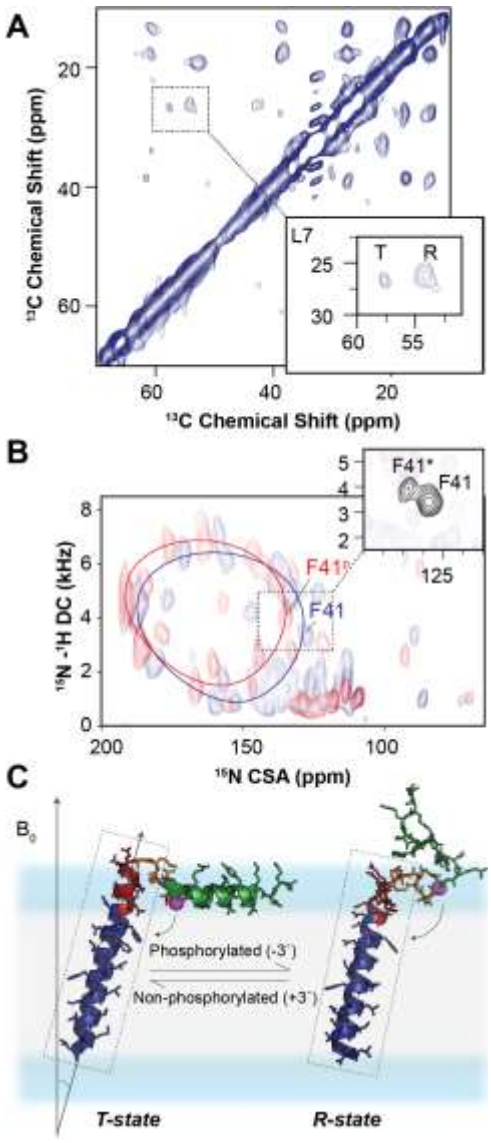

Figure 2.5: Two-state topological equilibrium of monomeric PLN

A. *Observation by MAS of two conformational states of PLN: the ground T-state and the excited R-state.* ***B.*** *2D [^{15}N-^{1}H] SE-SAMPI4 spectrum of PLN^{AFA} with (blue) and without (red) phosphorylation in flipped DMPC/POPC bicelles. The insets show the two-state equilibrium for a selective ^{15}N-Phe labeled PLN^{AFA}.* ***C.*** *T-state (PDB 2KB7) and R-state (PDB 2LPF) of PLN^{AFA}.*

transmembrane helices is still unknown. As mentioned above, rigid-body motions of the helical domains (*i.e.*, topological changes) are among the possible structural transitions that characterize TM dynamic signaling. In the current literature, there are many examples of rigid-body transitions such as those occurring in mechanosensitive channels, G protein-coupled receptors (GPCRs), *etc.*[203] Distance and angular restraints are insufficient to define these global topological changes. In contrast, SLF experiments are extremely sensitive to small TM changes in rotation and tilt that propagate from one to the opposite leaflet of the lipid membranes. Among the most outstanding examples are the topological changes mapped by Traaseth and co-workers for EmrE using OS-ssNMR.[206] In this case, the topological changes of EmrE were so pronounced to enable the detection of exchanging topologies in the SLF spectra. Another example is the topological

transitions of PLN in lipid membranes. (**Fig. 2.5**) PLN possesses two major regions: a hydrophobic TM domain that inhibits the sarcoplasmic reticulum Ca^{2+}-ATPase (SERCA), and a cytoplasmic domain that tunes the extent of inhibition via phosphorylation by protein kinase A (PKA) and calmodulin-dependent protein kinase II (CaMKII).[207] Our original topology of monomeric and pentameric PLN were obtained in mechanically aligned lipid bilayers.[172, 200] Under these conditions, the backbone resonances in the SLF spectra were so broad that we could not fully appreciate the presence of two different populations of resonances for the TM domain. In contrast, the spectra in lipid bicelles display a major and a minor population with slightly different tilt and rotation angles (**Fig. 2.5**), mirroring the two populations (R and T states) identified for the cytoplasmic region by MAS spectroscopy (**Fig. 2.5A.**).

Upon phosphorylation of Ser16 by PKA, we observed a shift of the ground population toward the lowest populated

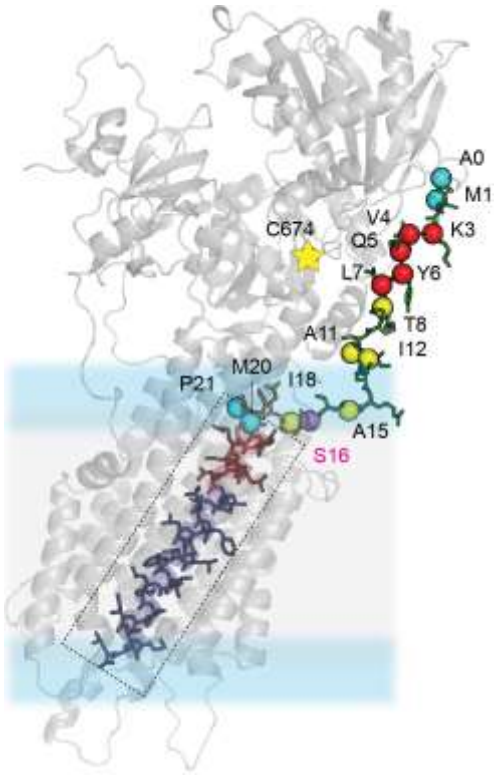

Figure 2.6: Structural determination of the SERCA-PLN complex by ssNMR

Mapping the binding between the dynamic N-terminus was achieved previously by PRE experiments followed by MAS [^{13}C-^{1}H] rINEPT and [^{13}C-^{13}C] DARR measurements (adapted from PNAS 2013). Residues marked by red spheres were found to experience unambiguous PRE-induced line broadening, yellow spheres ambiguous and blue sphere unambiguously no-PRE quenched.

state, which becomes the dominating state. These changes are very pronounced for Asn30 and Asn34, whose hydrogen bond interactions stabilize the E2 (Ca^{2+}-free) state of SERCA. Since the inhibition of SERCA by PLN occurs via allosteric interactions between the TM domain of the regulator and the Ca^{2+} binding site of the ATPase (**Fig. 2.6**), the topological changes of the TM domain allosterically modulate the extent of inhibition of the enzyme (*topological allostery*).[208] It is possible that different SERCA modulators expressed in non-cardiac cells, *i.e.*, regulins, might display different topologies reflecting their various biological activities. Therefore, the topological and allosteric diversity in regulins may modulate the ATPase affinity for Ca^{2+} ions, thereby differentially affecting calcium cycling.[209]

2.7 Characterization of motions via ssNMR

The characterization of the site-specific motions and more importantly the timescale of conformational changes are among the most important contributions of NMR to structural biology.[210] However, the analysis of the dynamics of membrane proteins in lipid bilayers is still a significant challenge. Hong and co-workers are using the dipolar-coupling chemical-shift correlation (DIPSHIFT) as a means to determine the dynamics of proteins and peptides.[169] Although it is possible to characterize the backbone dynamics for a few selected cases, the heterogeneity of membrane proteins spectra represents a significant hurdle. Our group has been relying on a semi-quantitative analysis of the segmental motions using a combination of CP and refocused Insensitive Nuclei Enhanced by

Polarization Transfer (rINEPT) experiments.[159] Since the intensity of polarization obtained from these experiments depends on the dynamics of the proteins, the comparison of these spectra gives an overall view of the complex motions of membrane proteins. In particular, the membrane-associated protein domains are mapped via CP based experiments that rely on DCs, whereas the dynamic residues that undergo fast dynamics average out anisotropic interactions and retain longer T_2 relaxation properties, which enables the mapping of these residues via J-coupling based INEPT transfer experiments.[211] We typically start with 1D ^{15}N CP and rINEPT experiments to look at the extent of dynamics by comparing the backbone spectral intensities. Due to the presence of intense lipid signals, 1D ^{13}C rINEPT experiments are usually less informative for a semi-quantitative analysis of mobile residues. However, a more detailed characterization can be made by using

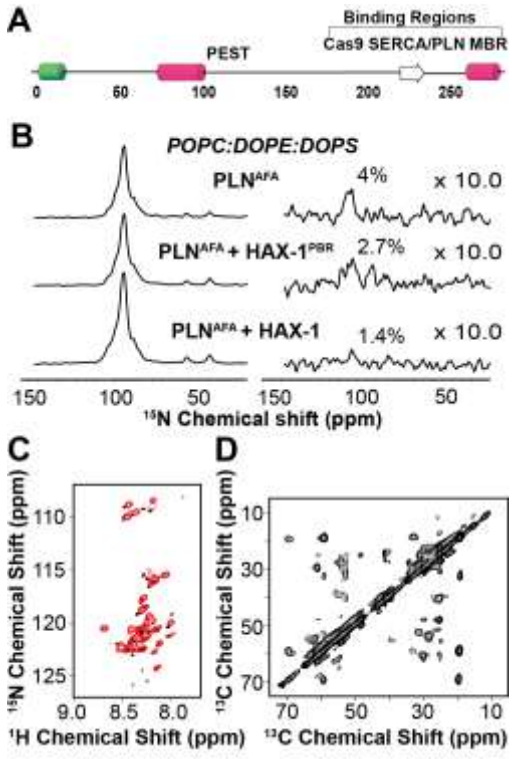

Figure 2.7: MAS ssNMR experiments on HAX-1, an intrinsically disordered protein of 279 amino acids

A. *Schematic of the predicted structural and functional domains of HAX-1.* ***B.*** *rINEPT spectra (right) normalized to CP spectra (left) of PLN^{AFA} in complex with HAX-1$^{203-245}$, the PLN binding region (PBR) of HAX-1 and full length HAX-1.* ***C.*** *Overlay of IDP HAX-1 spectra, obtained from MAS RI-HSQC (red), and solution NMR [^{1}H,^{15}N]-HSQC (black).* ***D.*** *^{13}C-^{13}C DARR experiments of HAX-1 in lipid vesicles.*

^{13}C-detected 2D ^{13}C-^{13}C DARR and INEPT-TOtal through Bond correlation SpectroscopY (TOBSY) experiments that map immobile and dynamic residues, respectively. To these experiments, we recently added ^{1}H-detected sensitivity enhanced refocused INEPT heteronuclear single quantum correlation (RI-HSQC) experiments for probing sparse conformational states with populations as low as 1%.[212] These experiments can be hybridized into new pulse sequences to map rigid and dynamic domains simultaneously.[213]

2.8 Interactions of intrinsically disordered proteins (IDPs) with lipid membranes

Although both MAS and OS-ssNMR have been extensively used to study dynamic small peptides interacting with membranes, studies on the interactions between IDPs and the membrane bilayer are still limited. In collaboration with the De Simone laboratory, our group has carried out a series of studies on the interactions between α-synuclein (α-Syn) and membrane model systems.[202, 214, 215] α-Syn in solution exists as a disordered polypeptide, adopting a random coil ensemble of conformers. Upon interactions with lipid membranes, α-Syn adopts a helical conformation.[216] However, the membrane-binding region has been virtually invisible to solution-state NMR analysis. We used INEPT-based experiments to image the ‘dark side’ of α-Syn and identify the residues directly involved with the membrane interactions and possibly responsible for the pre-fibrillar aggregates that have been hypothesized to constitute the toxic species. More recently, we used a combination of CP and rINEPT experiments to determine

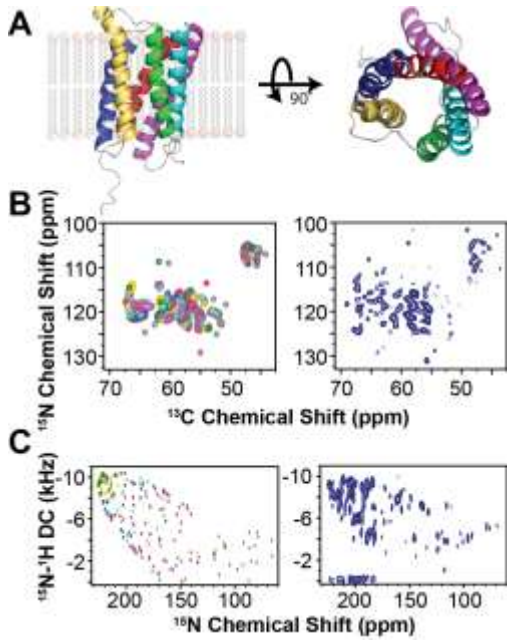

Figure 2.8: Integrated MAS and OS-ssNMR spectroscopy of SaTP in lipid membranes

A. *X-ray structure of SaTP (PDB 5ZUG)[1].* ***B.*** *Predicted MAS NCA spectrum (left) using the ShiftX2 Server[3] versus experimental NCA spectrum (right).* ***C.*** *Predicted SE-PISEMA spectrum obtained from MD simulation versus experimental SE-PISEMA spectrum (right).*

the interaction of hematopoietic-substrate-1 associated protein X-1 or HAX-1 with PLN (**Fig. 2.7**).[100] HAX-1 is a 279 amino acid intrinsically disordered protein (IDP) that is thought to interact with PLN, modulating the inhibition of SERCA. Indeed, our data confirm this hypothesis, but further suggest these interactions occur via an amphipathic helix located on the C-terminus of HAX-1 that interacts with lipid membranes (**Fig. 2.7**). This helix may be crucial for localizing HAX-1 near the SERCA/PLN complex as well as promoting a rigid, more inhibitory state of PLN.

2.9 Conclusions and perspectives

As for the entire field of structural biology,[217, 218] NMR is relying on multiple approaches to fully characterize the structure and dynamics of membrane proteins. Neither MAS nor OS-ssNMR possess the silver bullet; instead, the synergistic nature of these different approaches is emerging. Both MAS and OS-ssNMR are compatible with lipid compositions and ratios similar to physiological membranes

in liquid crystalline phases, which represents a significant advantage over the other structural biology approaches. Under these conditions, membrane proteins, if properly reconstituted, are active and undergo conformational transitions that mimic their cellular function. From a spectroscopic viewpoint, MAS NMR methods are progressing rapidly. However, multidimensional spectroscopy of OS-ssNMR is still in its infancy. Our group is able to run double resonance 2D and 3D [^{1}H,^{15}N] experiments routinely on selected samples. The quantum leap will be possible when triple resonance 3D [^{1}H,^{13}C,^{15}N] experiments will become available for the unambiguous assignments of membrane proteins. The next frontier is the conjugation of these ssNMR methodologies to determine the structure of multi-span membrane proteins. **Fig. 2.8** shows the application of MAS and OS-ssNMR to a six TM protein (SaTP) involved in the transport of succinate and acetate. Both the simulated spectra and the experimental fingerprints for both MAS and OS-ssNMR are rather promising, and the sensitivity of these experiments supports the feasibility of the structure determination. These results suggest that the future of ssNMR is bright. Although improvements in sample preparations, hardware, and pulse sequences must be in place, critical information on challenging biological systems can be obtained for the time being.

2.10 Biographical information

Gianluigi Veglia obtained his Ph.D. in Chemistry from the University of Rome, La Sapienza, under the direction of Prof. M. Delfini and Prof. A. Di Nola. In 1993, he was a visiting fellow at SUNY Stonybrook, NY, under the supervision of Prof.

M. Eisenberg and Prof. G. Prestwich. In 1995, he joined the laboratory of Prof. S. Opella as a Postdoctoral Associate. In 2000, he joined the University of Minnesota and is currently a Professor of Chemistry and Biochemistry. His research interests span from the structural characterization of soluble and membrane-associated proteins using both solution and solid-state NMR methods.

Daniel Weber is an American Heart Association Postdoctoral Fellow at the University of Minnesota, Minneapolis. He received his B.Sc. (Hons.) degree in Chemistry from James Cook University, Australia, and his Ph.D. in Chemistry from the University of Melbourne under the supervision of Prof. Frances Separovic. Daniel was a scientist at IBM Research before joining the Veglia Lab in 2017. His research interests include the application and development of solid-state NMR and computational modeling approaches for studying the structure and dynamics of membrane proteins.

Songlin Wang received his B.Sc. degree in Chemistry from Peking University, China, and his Ph.D. in Chemistry from the University of Illinois at Chicago under the direction of Prof. Yoshitaka Ishii. In 2016, he joined the laboratory of Prof. Gianluigi Veglia at the University of Minnesota as a postdoctoral associate. His research interests include characterizing the structures and interactions of the membrane proteins and developing novel NMR methodology.

Erik Larsen received his undergraduate degree in Chemistry from the University of Minnesota, Twin Cities, in 2015. Currently, he is graduate student the University of Minnesota, Twin Cities, working under the direction of Prof. Jiali Gao in the

Department of Chemistry. His current research focuses on calcium cycling regulation in cardiomyocytes towards drug development for heart disease.

T. Gopinath is a solid-state NMR scientist at Minnesota NMR Center, University of Minnesota, Minneapolis. In 2007, he received his Ph.D. in NMR Quantum Computing from the Indian Institute of Science, Bangalore, India, under the supervision of Prof. Anil Kumar. From 2008-2012, he worked as a postdoctoral scientist in the Veglia group and contributed to novel solid-state NMR methodological developments to speed-up the data collection using multi-acquisition polarization experiments. His current research focuses on further developments and applications of ssNMR methods to various biomacromolecules.

Footnores

*Corresponding Author: Phone (612) 625 0758. E-mail: vegli001@umn.edu

Orcid

Gianluigi Veglia: 0000-0002-2795-6964

Funding

This work is supported by the National Institute of Health to G.V. (GM64742 and HL 144130).

Chapter 3 Probing protein-protein interactions using asymmetric labeling and carbonyl-carbon selective heteronuclear NMR spectroscopy

Erik K. Larsen[1], Cristina Olivieri[2], Caitlin Walker[2], Manu V.S., Jiali Gao[1], David A. Bernlohr[2], Marco Tonelli[3], John L. Markley[4], and Gianluigi Veglia[1,2a]

[1]Department of Chemistry, University of Minnesota, Minneapolis, MN 55455

[2]Department of Biochemistry, Molecular Biology, and Biophysics, University of Minnesota, Minneapolis, MN 55455

[3]National Magnetic Resonance Facility at Madison, Madison, WI 53706

[4]Department of Biochemistry, University of Wisconsin-Madison, Madison, WI, 53706

Reprinted with permission from MDPI [219]

[a]**Corresponding Author:**
Gianluigi Veglia
Department of Chemistry and Department of Biochemistry,
Molecular Biology, and Biophysics,
312 Church St. SE, Minneapolis, MN 55455
Telephone: (612) 625-0758
Fax: (612) 625-5780
E-mail: vegli001@umn.edu.

Keywords

Protein-Protein Interactions (PPI); Nuclear Magnetic Resonance (NMR); Carbonyl Carbon Label Selective (CCLS); Dual Carbon Label Selective (DCLS); Residual Dipolar Coupling (RDC); Paramagnetic Relaxation Enhancement (PRE).

Abstract

Protein-protein interactions (PPIs) regulate a plethora of cellular processes and NMR spectroscopy has been a leading technique to characterize them at the atomic resolution. Technically, however, PPIs characterization has been challenging due to multiple samples required to characterize the hot spots at the protein interface. Here, we review our recently developed methods that greatly simplify PPI studies, minimizing the number of samples required to fully characterize residues involved in the protein-protein binding interface. This original strategy combines asymmetric labeling of two binding partners and the carbonyl-carbon label selective (CCLS) pulse sequence element implemented into heteronuclear single quantum correlation (^{1}H-^{15}N HSQC) spectra. The CCLS scheme removes signals of the J-coupled ^{15}N-^{13}C resonances, recording simultaneously two individual amide fingerprints for each binding partner. We show the application to the measurements of chemical shift correlations, residual dipolar couplings (RDCs) as well as paramagnetic relaxation enhancements (PRE). These experiments open an avenue for further modifications of existing experiments facilitating the NMR analysis of PPIs.

3.1 Introduction

Biological processes rely primarily on protein-protein interactions (PPIs) to mediate cellular function [220]. Historically biochemical techniques (co-immunoprecipitation, yeast-two hybrid, pull-down assays, etc.) measuring parameters intrinsic to the whole complex have been used to characterize these PPIs [221, 222]. Recently, advances in nuclear magnetic resonance (NMR) spectroscopy have provided the means to characterize PPIs at atomic resolution, offering fine details of individual macromolecules participating within the complex [223-225]. In addition to allowing the characterization of these complexes at atomic resolution, NMR is well suited for studying dynamic, transient (~100 μM K_D), and lowly populated states of complexes [226-228].

The mapping of PPIs using several observables such as chemical shift perturbation (CSP), residual dipolar couplings (RDC), intra- and inter-molecular as well as solvent paramagnetic relaxation enhancement (PRE) [229-231], cross-saturation (CS), and nuclear Overhauser effects (NOEs) has been well established [224]. These methods nevertheless fall short when studying large complexes due to the inherent attenuation of transverse relaxation times (T_2) resulting in a reduction of both signal intensity and resolution. Despite methods such as TROSY [232], deuteration [233, 234], and selective labeling [235, 236] addressing these concerns, multiple samples are still required to distinguish one species from another. Recently, several new NMR experiments based on simultaneous, interleaved detection of up to three NMR active species with distinct isotopic labeling have provided the opportunity to map the effect of PPIs on individual

components within a macromolecular complex. While there are outstanding reviews on protein-protein interactions [237-243], here we focus on our recently developed method that exploits spin-echo filtering-based experiments with strategic protein labeling schemes to characterize protein-protein complexes.

3.2 Results

3.2.1 Mapping two binding partners fingerprints simultaneously

Traditional approaches to map PPIs at an atomic level involve repeat experiments with reverse labeling patterns such that the interaction is probed from both binding partners. Prior to the introduction of the spin-echo filtering experiment by Bax *et al. [244]*, three-bond homonuclear ^{1}H-^{1}H *J* couplings had been used to derive backbone and side-chain conformational restraints [245-250]. This new experiment relied on measuring the magnetization loss due to unresolved *J* coupling and utilized an interleaved detection method, where two spectra are recorded simultaneously, but differ by 180° pulse positions on the ^{15}N channel. The spin-echo filtered experiment introduced by Bax is the building block for the Carbonyl Carbon Label Selective (CCLS) ^{1}H-^{15}N HSQC pulse sequence [251], which requires specific isotopic labeling to simultaneously map the chemical shift perturbations from two binding partners. The CCLS ^{1}H-^{15}N HSQC pulse sequence utilizes spin-echo filtering with a short magnetization transfer period between ^{15}N and ^{13}C' in order to detect ^{1}H-^{15}N correlations adjacent to the NMR inactive (^{12}C') carbonyl groups (**Fig. 3.1A.**). Building on the constant time (CT) HSQC, the CCLS ^{1}H-^{15}N HSQC necessitates the acquisition of two spectra, a reference spectrum

and a suppression spectrum, in an interleaved manner. The reference spectrum is acquired using the pulse sequence reported in **Fig 3.1A.**, with the 180° pulse on ^{13}C' during the ^{15}N CT evolution period applied at position *a* as proposed by Vuister *et.al*. [244], allowing for the removal of ^{13}C'-^{15}N coupling. The suppression spectrum is acquired with the 180° ^{13}C' pulse at position *b*, leaving ^{13}C-^{15}N *J* coupling active and converting the transverse in-phase magnetization of ^{15}N spins linked to ^{13}C' to antiphase magnetization. This antiphase magnetization contains components in both the *x*- and *y*-direction. The π ^{1}H and ^{13}C pulses applied at the end of the ^{15}N evolution convert the *y*-component, $4H_zN_yC'_z$, to an unobservable multiple quantum coherence, $4H_yN_zC'_y$, while the *x*-component, $4H_yN_zC'_y$, is dephased by the G2 gradient (**Fig. 3.1A.**). As a result, signals from ^{1}H-^{15}N groups coupled to ^{13}C' are suppressed, while signals from ^{1}H-^{15}N groups coupled to ^{12}C' are unaffected. The suppression spectrum can then be subtracted from the reference spectrum leaving the U-^{15}N, ^{13}C species observable (**Fig. 3.1B.**).

We tested the sensitivity of the CCLS method by comparing a reference CCLS-HSQC spectrum and a conventional HNCO spectrum of the 20-kDa protein U-^{13}C, ^{15}N-Ubiquitin at 10, 20, 30, and 40°C corresponding to average T_2 values of 27, 33, 40, and 47 ms, respectively [251]. The slower tumbling rates at lower temperatures lead to longer rotational correlation times (τ_C) and faster relaxation resulting in broader linewidths. We found the reference CCLS-HSQC experiment was more sensitive compared to the HNCO experiment for lower temperatures, demonstrating that the shorter time delay (T_{NC}) allows for increased sensitivity for large proteins or protein-protein complexes. The sensitivity enhancement gained

from optimal T_{NC} values compensates for the decrease in S/N observed upon subtraction of the suppression spectrum from the reference spectrum.

Furthermore, we applied this technique to resolve assignment ambiguities on the 41 kDa catalytic subunit of cAMP-dependent protein kinase A (PKA-C) [252, 253]. PKA-C is the prototypical Ser/Thr kinase and, until relatively recently, had remained unexplored by NMR due to its size and presence of conformational exchange effects on the μs-ms timescale [254-257]. Advances in pulse sequence design and sample preparation have since made it possible to investigate this system using NMR [258-261]. We successfully implemented the CCLS-HSQC pulse sequence to assist in the assignment of multiple catalytically relevant residues of PKA-C. Furthermore, recent work from our group demonstrates the ability of this pulse sequence to simultaneously detect PKA-C in complex with an endogenous inhibitor, the heat-stable protein kinase A inhibitor (PKIα) [253, 262], giving the possibility to detect the mutual effect of PKA-C and PKIα interaction (**Fig. 3.1C. -** unpublished data). Together these applications underscore the ability of CCLS to simultaneously detect PPIs and emphasizes the performance of this pulse sequence with high molecular weight systems.

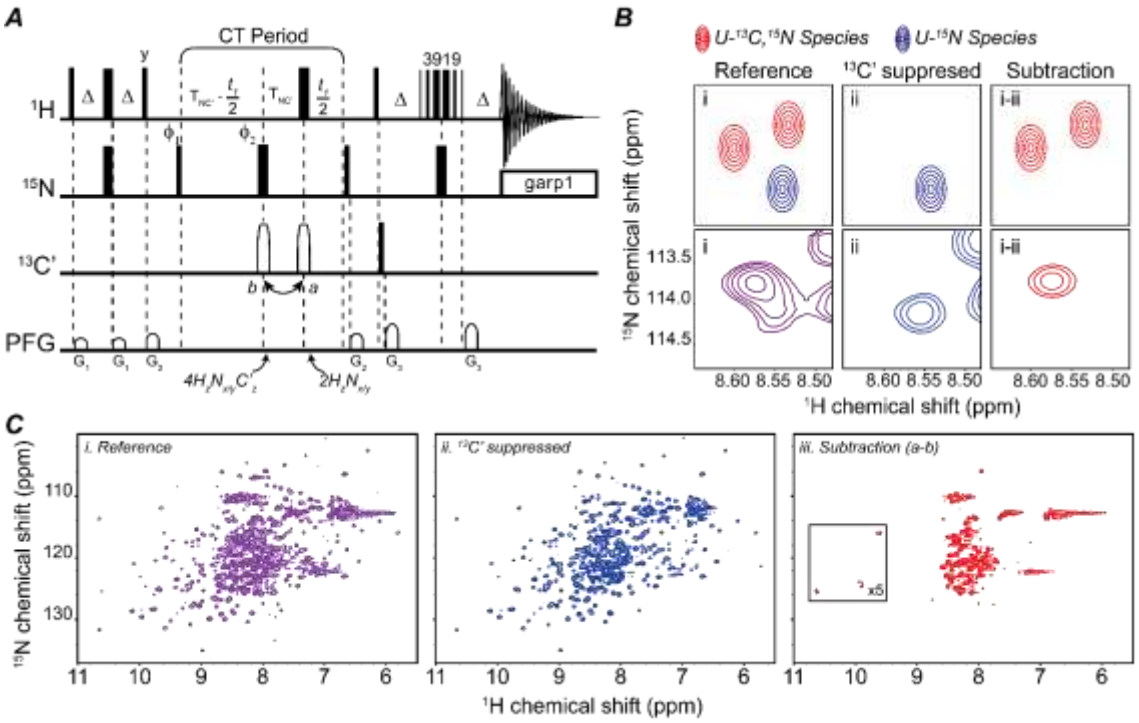

Figure 3.1: CCLS pulse sequence

A. *Schematic of the CCLS-HSQC pulse sequence. It can be assumed unless otherwise indicated that all rectangular pulses are applied along the x-axis. 90° and 180° flip angles are represented by narrow bars and wide bars, respectively. The carrier frequency for ^{1}H is set on resonance with water at 4.77 ppm; the carrier frequency for ^{15}N is set in the center of the amide region at 121.8 ppm; the ^{13}C offset is set to 174.8 for the C' region. The reference spectrum is recorded with the shaped pulse for $^{13}C'$ (open rectangle) at position a while the suppression spectrum is recorded with this pulse in position b. A 3-9-19 watergate pulse scheme is used in the reverse INEPT transfer. GARP1 decoupling with a field strength of 1kHz is used during acquisition of ^{15}N. Delay durations: Δ = 2.4 ms; δ = 0.11 ms; $T_{NC'}$ = 16.5 ms. Phase cycling: φ_1 = x,-x, φ_2 = x,x,-x,-x, φ_{rec} = x,-x. A second FID is acquired for each increment by changing the φ_1 phase to y,-y in order to accomplish States quadrature detection for the ^{15}N indirect dimension. The φ_1 and φ_{rec} phases are also incremented by 180° every other ^{15}N increment for States-TPPI acquisition. The gradients use the Wurst shaped z-axis gradients of 1 ms. Gradient strengths (G/cm): G1: 5, G2: 7, G3: 17. The CCLS-HSQC pulse sequence is based on the fast HSQC experiment [263] to preserve water magnetization.*

B. *Example spectra representing the reference spectrum, the suppression spectrum, and the resulting subtraction spectrum followed by insets from the PKA-C/PKIα complex displaying the separation of resonances from each species. The*

blue and red species are present in the reference CCLS-HSQC, while the suppression spectrum contains only red species. Subtraction of the suppression from the reference spectrum results in a third spectrum containing only the blue species.

C. *CCLS-HSQC experiment on the 50 kDa PKA-C/PKIα complex. The reference spectrum (left, purple) displays resonances from both U-^{15}N labeled PKA-C as well as U-^{15}N, ^{13}C labeled PKIα (S/N = 40). The suppression spectrum (middle, blue) suppresses signal from the ^{13}C' labeled PKIα showing only peaks from ^{12}C' labeled PKA-C (S/N = 50). Upon subtraction of the suppression spectrum from the reference spectrum, a subspectrum is obtained containing only peaks from PKIα (right, red) (S/N = 15).*

3.2.2 Fingerprinting three binding partners using one sample

Masterson *et al.* applied the CCLS pulse sequence element to deconvolute PPIs in a ternary mixture simultaneously [264].The dual carbon label selective (DCLS) ^{1}H-^{15}N HSQC experiment requires three labeled binding partners, with the first species U-^{15}N labeled, the second ^{15}N, ^{13}C' labeled, and the third U-^{13}C, ^{15}N labeled. The deconvolution of these spectra follows the same spin-echo filtering theory as CCLS, with additional filtering of Cα coupled spins (**Fig. 3.2A.**). Cα suppression requires a longer $T_{NC\alpha}$ delay due to both inter- and intra-residue ^{1}H-^{13}Cα J coupling [265]. Increasing the $T_{NC\alpha}$ delay nullifies protein backbone conformation dependency of $^{1}J_{NC\alpha}$ and $^{2}J_{NC\alpha}$ as it completely suppresses signal from $^{1}J_{NC\alpha}$ while inverting the residual signal intensities of $^{2}J_{NC\alpha}$.

This and the previously introduced pulse sequence rely on selective labeling of individual binding partners. Asymmetric selective labeling schemes to study PPIs in a multiple component sample are increasing in popularity [266-269] both for solution and solid-state NMR spectroscopy. For instance, Anglister and coworkers

have demonstrated the application of asymmetric deuteration in combination with transferred nuclear Overhauser spectroscopy to study intermolecular nuclear Overhauser effects (NOEs) of large, fast exchanging protein complexes [270-272]. With respect to CCLS and DCLS, selective labeling of ^{13}C' can be accomplished in recombinant proteins using either ^{15}N- and ^{13}C'-labeled amino acids or 1-^{13}C pyruvate and ^{13}C-labeled $NaHCO_3$ as the sole carbon sources [273-277]. Selective ^{13}Cα labeling is achieved by using 2-^{13}C glucose as the sole carbon source [274].

The DCLS experiment requires the acquisition of three interleaved experiments in parallel (**Fig. 3.2B.**). A reference data set is collected observing all three species simultaneously, followed by the first suppression data set where amide resonances adjacent to ^{13}C' are undetected, identical to the CCLS suppression spectrum. Lastly, a second suppression data set is collected where amide resonances coupled to ^{13}Cα are not detected. Deconvolution of the spectra is obtained by a linear combination of the data set. Subtraction of the second suppression spectrum from the reference spectrum provides a subspectrum containing only resonances from the U-^{13}C, ^{15}N labeled species. The subtraction of the first suppression spectrum from the second suppression spectrum provides an additional subspectrum containing only resonances from the U-^{15}N, ^{13}C' labeled species. In this manner, subspectra are obtained from a single sample for each individual component of the ternary mixture and all resonances can be resolved. As a proof of concept Masterson *et al.* applied this labeling scheme and pulse sequence to three non-interacting proteins, maltose binding protein (MBP), Kemptide, and ubiquitin. By applying DCLS, the authors obtained subspectra corresponding to

each individual component of the ternary mixture displaying the potential of this approach to study protein-protein interactions with a single sample.

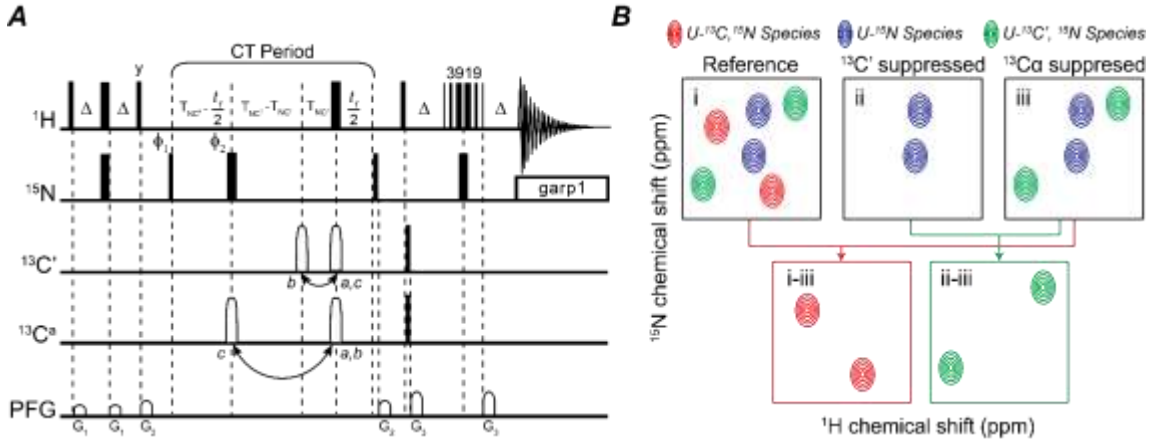

Figure 3.2: DCLS pulse sequence

A. *Schematic of the DCLS-HSQC pulse sequence. It can be assumed unless otherwise indicated that all pulses are applied along the x-axis. 90° and 180° flip angles are represented by narrow bars and wide bars, respectively. The reference spectrum is recorded with the shaped pulse for ^{13}C (open rectangle) at position a while the $^{13}C'$ suppression spectrum is recorded with this pulse in position b and the $^{13}C_{\alpha}$ suppression spectrum is recorded with the $^{13}C_{\alpha}$ shaped pulse in position c. A 3-9-19 watergate pulse scheme is used in the reverse INEPT transfer. GARP1 decoupling with a field strength of 1kHz is used during acquisition of ^{15}N. The carrier frequency for ^{1}H is set on resonance with water at 4.7 ppm; the carrier frequency for ^{15}N is set in the center of the amide region at 120 ppm; the ^{13}C offset is set to 56 ppm. Selective $^{13}C'$ ($^{13}C_{\alpha}$) sine shaped pulses are centered at 174 (56 ppm) and a null 113 ppm away. Delay durations: Δ = 2.4 ms; δ = 0.11 ms; $T_{NC'}$ = 16.4 ms; $T_{NC\alpha}$ = 24.5 ms. Phase cycling: φ_1 = x,-x, φ_2 = x,x,-x,-x, φ_{rec} = x,-x. A second FID is acquired for each increment by changing the φ_1 phase to y,-y in order to accomplish States quadrature detection for the ^{15}N indirect dimension. The φ_1 and φ_{rec} phases are also incremented by 180° every other ^{15}N increment for States-TPPI acquisition. The gradients use the Wurst shaped z-axis gradients of 1 ms. Gradient strengths (G/cm): G1: 5, G2: 7, G3: 17.*

B. *Example spectra representing the reference spectrum, the two suppression spectra, and the resulting subtraction spectra. The red, green and blue species are present in the reference DCLS-HSQC (i), while the first suppression spectrum (ii)*

contains resonances from the red species and the second suppression spectrum (iii) contains resonances from the red and green species. Subtracting spectrum iii from i results in only resonances from the blue species and subtracting spectrum iii from ii yields only resonances from the green species. This linear subtraction scheme results in spectra with each component in the mixture isolated

3.2.3 Measuring Residual Dipolar Coupling (RDC) of complexes using one sample

Residual dipolar coupling (RDC) allows orientation specific data to be derived via dipole-dipole interactions. The orientation restraints provided by RDC have proven useful in protein structure determination, nucleic acid structure, domain orientation, and more recently PPIs [278, 279]. We implemented CCLS and DCLS to sensitivity-enhanced TROSY or anti-TROSY spin-state selection to record the simultaneous measurement of RDCs [278, 280-283] for the relative orientations of multiple proteins within a single sample (**Fig. 3.3A.-B.**). RDC measurements are susceptible to experimental condition variations, which alter alignment tensors making difficult the direct correlations of orientational constraints obtained from different samples. Our approach, together with specific isotopic labeling, eliminates the need for multiple samples thus removing errors associated with sample inconsistencies [278].

Similar to DCLS (**Fig. 3.3C.**), we applied this pulse sequence to a non-interacting mixture of U-^{2}H, ^{15}N MBP, ^{15}N-Ser^{5}, ^{13}C'-Ala^{4} Kemptide, and, U-^{13}C, ^{15}N ubiquitin [284]. Following the same linear subtraction scheme reported for DCLS, we were

able to measure RDCs for each individual component in a ternary mixture. Importantly, these RDC values were in agreement with back calculated values determined from already solved crystal structures of MBP [285] and ubiquitin [286], confirming that the backbone conformational space of these proteins, along with their relative alignment tensors, were sufficiently defined.

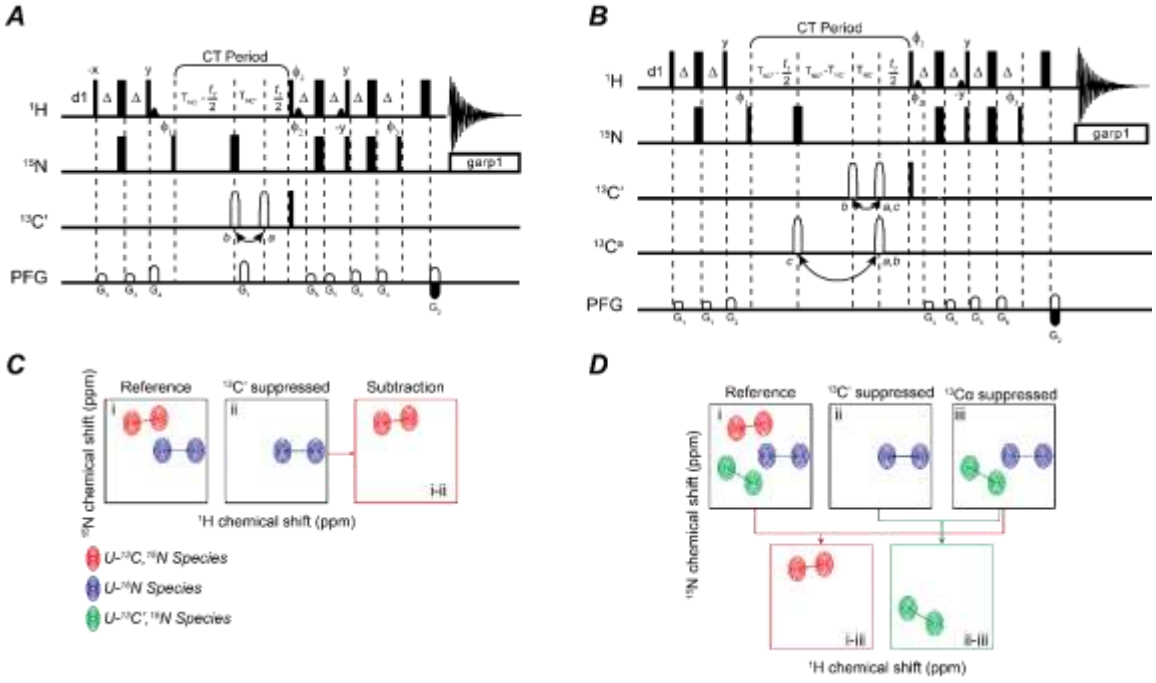

Figure 3.3: CCLS/DCLS RDC

A. *and* ***B.*** *Schematic of the gradient-selected TROSY-based pulse sequence for binary* ***A.*** *or ternary* ***B.*** *mixtures of proteins. It can be assumed unless otherwise indicated that all pulses are applied along the x-axis. 90° and 180° flip angles are represented by narrow bars and wide bars respectfully. The reference spectrum is recorded with the shaped pulse for ^{13}C (open rectangle) at position a while the $^{13}C'$ suppression spectrum is recorded with this pulse in position b and the $^{13}C_\alpha$ suppression spectrum is recorded with the $^{13}C_\alpha$ shaped pulse in position c. The carrier frequency for ^{1}H is set on resonance with water at 4.77 ppm; the carrier frequency for ^{15}N is set in the center of the amide region at 121.8 ppm; the ^{13}C offset is set to 56 ppm. Selective $^{13}C'$ ($^{13}C_\alpha$) sine shaped pulses are centered at 174.8 ppm (56 ppm). Delay durations: Δ = 2.4 ms; δ_1 = 1.5 s; $T_{NC'}$ = 16.5 ms; $T_{NC\alpha}$ = 23.5 ms. Phase cycling: φ_1 = x,-x, φ_2 = -x, φ_3 = -y, φ_{rec} = x,-x. Gradient strengths must be adjusted following the relationship $G_2 = G_1 \cdot (\gamma_N/\gamma_H)$, where γ_N and γ_H are the gyromagnetic ratios of ^{15}N and ^{1}H, respectively. A second FID is collected for*

each increment by changing the φ_2 and φ_3 to x and y respectively and by inverting the sign of the G_2 gradient in order to accomplish States quadrature detection for the ^{15}N indirect dimension. The φ_1 and φ_{rec} phases are also incremented by 180° every other ^{15}N increment for States-TPPI acquisition. The gradients use the Wurst shaped z-axis gradients of 1 ms. Gradient strengths (G/cm): G_3: 3, G_4: 13, G_5: 4, G_6: 5. To measure $^1J_{HN}$ coupling and NH RDC (in aligned media), a second spectrum, featuring the anti-TROSY component, is acquired by changing the φ_3 phase to y.

C. *Example spectra representing the reference spectrum, the suppression spectrum, and the resulting subtraction spectrum. The blue and red species are present in the reference CCLS-HSQC, while the suppression spectrum contains only red species. Subtraction of the suppression from the reference spectrum results in a third spectrum containing only the blue species.*

D. *Example spectra representing the reference spectrum, the two suppression spectra, and the resulting subtraction spectra. The red, green and blue species are present in the reference DCLS-HSQC i, while the first suppression spectrum ii contains resonances from the red species and the second suppression spectrum iii contains resonances from the red and green species. Subtracting spectrum iii from i results in only resonances from the blue species and subtracting spectrum iii from ii yields only resonances from the green species. This linear subtraction scheme results in spectra with each component in the mixture isolated.*

3.2.4 Measuring long-range distances and transient complexes using CCLS for Paramagnetic Relaxation Enhancements (PRE)

Paramagnetic relaxation enhancements (PRE) have been used extensively to obtain long-distance restraints for structure calculation and to study PPIs for both stable and transient complexes [287-292]. In the standard PRE experiment that involves two interacting proteins, the intra- or inter-molecular effects of a paramagnetic center are detected for only one of the binding partners in each independent NMR experiment (**Fig. 3.4A.i.**). To accurately probe these interactions, a minimum of four samples with differing spin label positions as well as reversed labeling schemes are required. Recently, we incorporated the CCLS

pulse sequence in the traditional $^{1}H_N$-Γ_2 ($^{1}H_N$-Γ_2-CCLS) [289] that, together with an asymmetric labeling scheme, enables the detection of both intra- and inter-molecular paramagnetic relaxation enhancements (PREs) simultaneously using only one sample [229] (**Fig. 3.4B.**). In this newly proposed strategy, one of the two binding partners must be U-^{15}N labeled and the second U-^{15}N, ^{13}C labeled (**Fig. 3.4A.ii.**). We also tested the proposed pulse sequence on the non-covalent, transient dimerization of ubiquitin. Specifically, we studied the complex formed between U-^{15}N, ^{13}C wild-type ubiquitin and the U-^{15}N-spin labeled K48C mutant. We were able to discriminate intra- and inter-molecular interactions detecting the structural and dynamics changes intrinsic to ubiquitin upon dimerization (**Fig. 3.4C.**). The Γ_2 rates obtained with the new pulse sequence were confirmed to be identical to standard experiments. This work demonstrates that the Γ_2-CCLS PRE experiment is suitable for identifying structural changes occurring in both binding partners upon formation of transient and permanent interactions using a reduced number of samples.

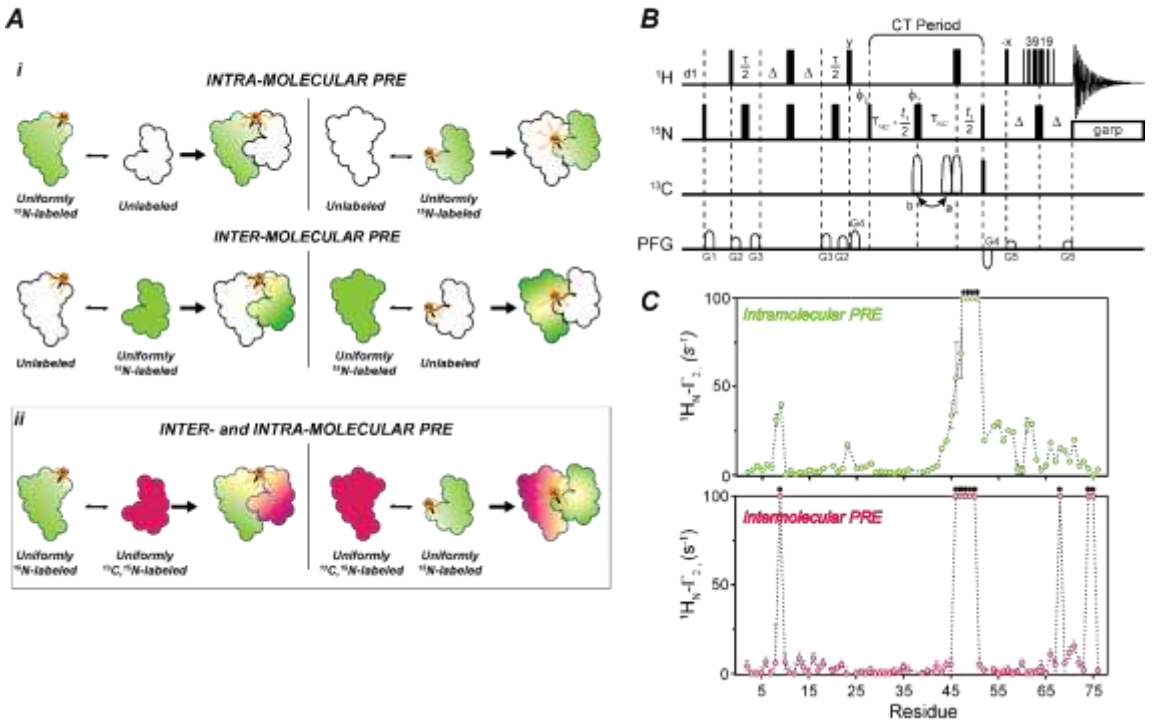

Figure 3.4: CCLS-PRE

A. *Schematic of the standard experiment for the detection of intra- and inter-molecular PRE. In this case four different samples are needed. The first sample for the intra-molecular PRE is prepared with an asymmetric labeling scheme using the first binding partner uniformly ^{15}N labeled with a conjugated spin label (SL) and the second is NMR silent (unlabeled). A sample with a reversed labeling scheme is necessary to detect the intra-molecular PRE for the second binding partner (top panel A). For the inter-molecular PRE, two additional samples are required: one NMR silent with the conjugated SL and a second NMR active (e.g., ^{15}N or ^{13}C labeled) (lower panel A). Simultaneous detection of inter- and intra-molecular PRE using $^{1}H_N$-Γ_2-CCLS experiment. One species is uniformly ^{15}N labeled while the other is ^{13}C and ^{15}N labeled (b) and this allows the simultaneous detection of intra- and inter-molecular PREs. As reported before, reverse positioning of the SL is required for obtaining a complete characterization of the complex.*

B. *The ^{1}H-Γ_2-CCLS pulse sequence for PRE Γ_2 measurements. The narrow and wide bars represent 90° and 180° hard pulses, respectively. The three ^{13}C 180° shaped pulses are 256 μs long Q3 pulse, the first two and the last one shaped pulses are applied to $^{13}C'$ and ^{13}CA, respectively. The $^{13}C'$ 180° shaped pulse may be at either position a or b. When it is at position a, the $^{1}J_{NC'}$ is decoupled and reference spectra are acquired. When it is at position b, the $^{1}J_{NC'}$ is present and $^{13}C'$-suppressed spectra are acquired. The flipping angles and phases of the pulses in 3919 are 20.8°$_x$, 62.2°$_x$, 131.6°$_x$, 131.6°$_{-x}$, 62.2°$_{-x}$, and 20.8°$_{-x}$,*

respectively, and the interval between pulses is 188 μs (= 1/d, d is the distance in Hz between center and next null). T = 16.5 ms, Δ = 2.6 ms. G1=(1 ms, 25.0 G/cm), G2=(0.3 ms, 5.0 G/cm), G3=(0.3 ms, 8.0 G/cm), G4=(1 ms, 15.0 G/cm), G5=(1 ms, 10.0 G/cm). Phase cycling scheme is φ1= (x, -x), φ2=(x, x, -x, -x), φ3=4(x), 4(-x), φ_{rec}=(x, -x, x, -x, -x, x, -x, x). The quadrature detections in t_1 dimension are acquired via States-TPPI of φ1. Constant time mode is used to measure Γ_2, that is $\Gamma_2 = ln\,(S_1/S_2)/(\tau_2 - \tau_1)$, where S_1 and S_2 are signal intensities of a peak measured with $\tau = \tau_1$ and $\tau = \tau_2$, respectively. 2×2 spectra are acquired in an interleave mode via changing relaxation delay τ (minimum 2 ms) and changing the $^{13}C'$ 180° shaped pulse from position a to b, respectively

***C.** Intra- and inter-molecular PRE measurements of ^{15}N-Ubi^{K48C} obtained with the ^{1}H-Γ_2-CCLS experiment. ^1H_N-Γ_2 rate plot calculated for K48C mutant conjugate with MTSL in presence of Ubi^{WT} (upper panel C). ^1H_N-Γ_2 rate plot calculated for WT ubiquitin in presence of Ubi^{K48C}-MTSL (lower panel C).*

3.2.5 Improving sensitivity with the G5 pulse

Advances in NMR methodology (TROSY, deuteration, selective labeling) have allowed for studies of protein-protein complexes approaching 1 MDa [293, 294]; however, these studies lack the ability to distinguish one species from another without the preparation of multiple samples. A recent technological advance that can improve nearly any pulse sequence is the universal triply compensated π pulses for high field spectrometers [295, 296], which we have incorporated into the CCLS pulse sequence (**Fig. 3.5**). All inversion and refocusing pulses in the ^{1}H and ^{15}N channel were replaced with G5 pulses except the ^{15}N refocusing pulse in middle of 3-9-19 water suppression. We were able to improve the signal intensity from 6% to 23% compared to the regular CCLS version. These experiments were performed on the Bruker 900 MHz AVIII spectrometer at 298K, and this enhancement will only be more significant in GHz spectrometers.

3.3 Conclusion and perspectives

Here, we demonstrate the CCLS/DCLS pulse sequences enable the study of PPIs through simultaneous inter-leaved detection of all components in a single sample. As we have illustrated, the CCLS and DCLS pulse sequence blocks can be applied to a multitude of well-established experiments (RDC and PRE). Extrapolating from this integration into existing NMR experiments, could NOESY be the next step? The possibility of observing multiple species in a single sample for NOESY experimentation is viable as Anglister *et al.[270]* has reviewed difference spectroscopy and its application to 2D NOESY experiments. However, the pulse sequences are long thereby limiting sensitivity which the CCLS/DCLS pulse blocks show promise toward combating. Thus, reflecting upon the versatility of the CCLS/DCLS pulse block and the associated advantages afforded, we envisage the insertion into other existing NMR experiments to study a wide range of multicomponent systems.

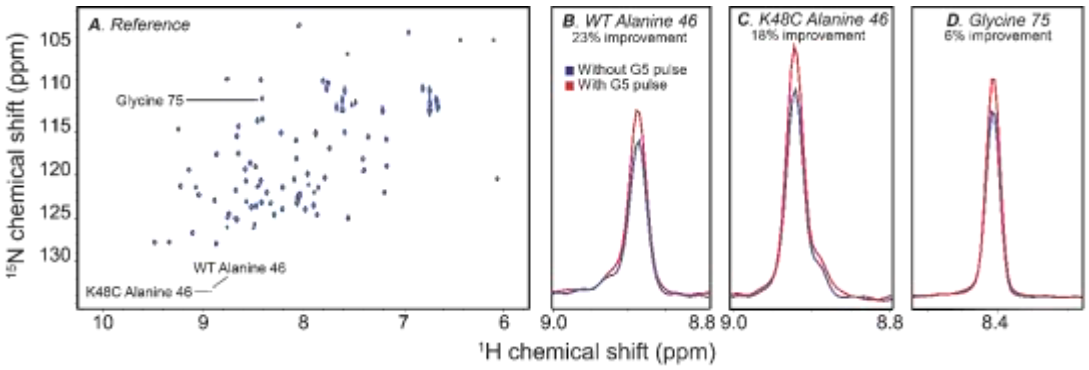

Figure 3.5: CCLS G5 pulse implementation

A. *CCLS ^{1}H-^{15}N HSQC reference spectrum of ^{15}N, ^{13}C Ubi^{WT} and U-^{15}N Ubi^{K48C} mutant.* ***B.*** *Overlay spectra of the Ubi^{WT} alanine 46 peak demonstrating a 23% signal intensity improvement with the G5 pulse.* ***C.*** *Overlay spectra of the Ubi^{K48C} alanine 46 peak demonstrating an 18% signal intensity improvement with the G5*

pulse. ***D.*** *Overlay spectra of the glycine 75 peak demonstrating a 6% improvement with the G5 pulse.*

3.4 Acknowledgements

This work is supported by the NIH (GM100310 to GV and P41 GM103399 to JLM). NMR experiments were carried out at the National Magnetic Resonance Facility at Madison and the Minnesota Nuclear Magnetic Resonance Center.

Chapter 4 Cysteine-ethylation of tissue-extracted membrane proteins as a tool to detect conformational states by solid-state NMR spectroscopy

Daniel K. Weber[†], Taysir Bader[‡], Erik K. Larsen[‡], Songlin Wang[†], Tata Gopinath[†], Mark Distefano[‡] and Gianluigi Veglia[†,‡,1]

[†] Department of Biochemistry, Molecular Biology, and Biophysics, University of Minnesota, Minneapolis, MN 55455, USA

[‡] Department of Chemistry, University of Minnesota, Minneapolis, MN 55455, USA

[1] Corresponding author: e-mail address: vegli001@umn.edu

Reprinted from Methods in Enzymology, 621, Daniel K. Weber, Taysir Bader, Erik K. Larsen, Songlin Wang, Tata Gopinath, Mark Distefano and Gianluigi Veglia, Cysteine-ethylation of tissue-extracted membrane proteins as a tool to detect conformational states by solid-state NMR spectroscopy, 281-304, © 2019*, with permission from Elsevier [297].*

* To whom correspondence should be addressed:

Gianluigi Veglia,

Department of Biochemistry, Molecular Biology & Biophysics,

University of Minnesota, 6-155 Jackson Hall, MN 55455.

Telephone: (612) 625-0758.

Fax: (612) 625-2163.

E-mail: vegli001@umn.edu

Abstract

Solid-state NMR (ssNMR) is an ideal tool to study structure and dynamics of membrane proteins in their native lipid environment. In principle, ssNMR has no size limitations. However, this feature is rarely exploited as large membrane proteins display severe resonance overlap. In addition, dismal yields in recombinant bacterial expression systems limit severely spectroscopic characterization of membrane proteins. For very large mammalian membrane proteins, extraction from the original organism remains the most viable approach. In this case, NMR-observable nuclei must be introduced post-translationally, but the approaches developed so far are rather scarce. Here, we detail the synthesis and engineering of a reactive ^{13}C-ethylmethanethiosulfonate (^{13}C-EMTS) reagent for the post-translational alkylation of cysteine sidechains of a 110 kDa sarcoplasmic reticulum Ca^{2+}-ATPase (SERCA) extracted from rabbit skeletal muscle tissue. When reconstituted into liposomes, it is possible to resolve the resonances of the engineered ethyl groups by magic-angle spinning (MAS) 2D [^{13}C,^{13}C]-DARR experiments. Notably, the ethyl-group modification does not perturb the function of SERCA, yielding well-resolved ^{13}C-^{13}C fingerprints that are used to image its structural states in the catalytic cycle and filtering out overwhelming naturally-abundant ^{13}C nuclei signals arising from the enzyme and lipids. We anticipate that this approach will be used together with ^{19}F NMR to monitor conformational transition of enzymes and proteins that are difficult to express recombinantly.

4.1 Introduction

Solid-state NMR (ssNMR) is a powerful technique for investigating structure and dynamics of membrane proteins, which unlike solution NMR, does not rely on perturbing detergents for their functional reconstitution [298]. With no upper size limit, ssNMR is accessible to the largest membrane proteins embedded in their native lipid-bilayer environment, but poorer resolution, combined with unique signal arising from hundreds to thousands of amino acids, produce spectra far too overlapped for meaningful interpretation. Furthermore, large membrane proteins may be extraordinarily difficult to obtain by heterologous expression from *E. coli*, or other common hosts, in a correctly folded state and in milligram quantities required for ssNMR. Although a few successful attempts have been reported for cell-free expression and yeast expression systems, the extraction from the host organism often remain the only viable option. In such cases, sparse, selective and segmental labelling methods built on recombinant expression to reduce spectral overlap [219, 236, 299-303] are inapplicable and NMR-observable nuclei must be introduced post-translationally. Fortunately, there is an extensive toolbox for post-translational modification of proteins, exploiting the chemistry of residues such as cysteine, lysine, tyrosine, arginine, glutamate, aspartate, serine, threonine, methionine, histidine, tryptophan as well as N- and C-termini [304, 305]. However, only a few to date have been utilized by the ssNMR community.

In this chapter, we detail protocols for the synthesis of a ^{13}C-ethylmethanethiosulfonate (^{13}C-EMTS) reagent [306] and its use for ethylating cysteines of a 110 kDa sarcoplasmic reticulum Ca^{2+}-ATPase (SERCA)

transmembrane enzyme isolated from rabbit skeletal muscle tissue. The ^{13}C-EMTS reagent is analogous to the methylating reagent methylmethanethiosulfonate (^{13}C-MMTS) introduced by Kay and co-workers [307], but does not require deuterated recombinant proteins to increase signal intensity. Importantly, this approach eliminates the background from lipids and naturally-abundant ^{13}C-nuclei in ^{1}H-^{13}C correlation spectra. Instead, the ^{13}C-^{13}C dipolar coupling of ethyl-tagged cysteines (Cys-S-$^{13}CH_2$-$^{13}CH_3$) provides a double-quantum filter previously demonstrated to yield background-free and well-resolved solid-state ^{13}C-^{13}C Dipolar-Assisted Rotational Resonance (DARR) experiments [306, 308]. This reagent reacts with cysteine (**Fig. 4.1A.**) by well-known chemistry between nucleophilic thiols and alkyl alkanethiosulfonates, which is appealing for its applicability under mild reaction conditions, i.e., aqueous solutions and physiological pH. EMTS reagent enables fast reaction times, stoichiometric conversion of cysteine without requiring excess reagent, and reversibility upon addition of common thiol reagents such as dithiothreitol and β-mercaptoethanol [309]. More importantly, it does not perturb the enzyme's function.

SERCA has 24 cysteines, of which six solvent-exposed residues are preferentially labelled throughout both the cytoplasmic nucleotide-binding (N) and phosphorylation (P) domains (**Fig. 4.1B.**). When using a five-fold molar excess of ^{13}C-EMTS, the ATPase activity is fully retained [306] and the ^{13}C-^{13}C DARR spectra give compelling fingerprints of the different structural states throughout the enzymatic cycle [310].

4.2 Protocols for using ^{13}C-EMTS

4.2.1 Synthesis and purification of the ^{13}C-EMTS reagent

The synthesis of ^{13}C-EMTS is described at 9.2 mmol scale, which accounting for a total yield of 75%, produces 35 mL of 200 mM stock–enough for over 18,000 NMR sample preparations using the protocol described in the following section. The scale was chosen to match the quantities of $^{13}C_2$-bromoethane available commercially, but can be significantly reduced. In our hands, we have successfully used this scheme at 0.7, 2, and 3.5 mmol scales to produce sufficient amounts for ssNMR studies. ^{13}C-EMTS is obtained by a nucleophilic SN_2 reaction between sodium methanethiosulfonate and

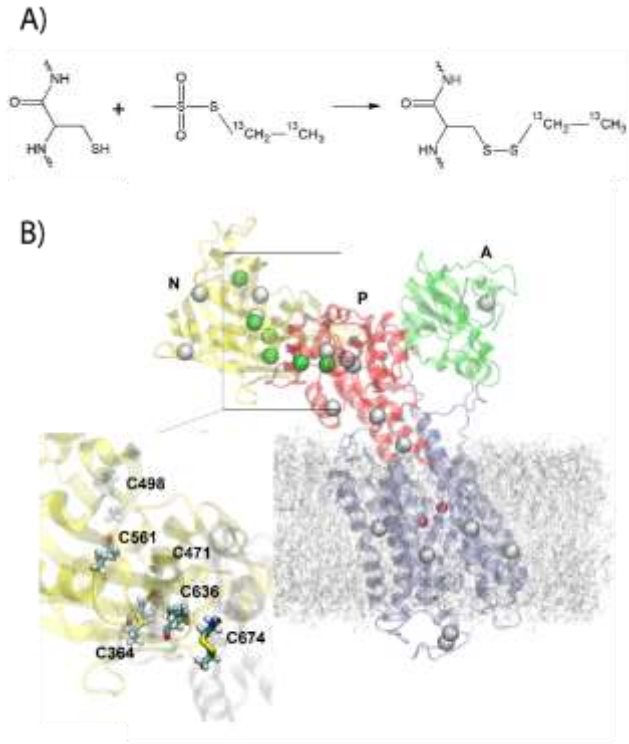

Figure 4.1

A. *Reaction scheme for ethylating cysteine with ^{13}C-EMTS reagent.* ***B.*** *Structural representation of ethylated cysteines (green spheres) and non-ethylated cysteines (white spheres) projected onto SERCA in the calcium-bound E1 state (E1·2Ca^{2+}, PDB 1SU4) [2]. Nucleotide-binding (N, yellow), phosphorylation (P, red) and actuator (A, green) domains are shown as well as Ca^{2+} sites (red spheres). Expanded region shows ethyl-modified cysteines (patch to convert cysteine to ethyl-cysteine for CHARMM molecular dynamics simulation are available on request). System was built using the CHARMM-GUI webserver [4, 5] and includes 400 POPC lipids.*

$^{13}C_2$-bromoethane (Error! Reference source not found.**A.**) as shown previously ADDIN EN.CITE <EndNote><Cite><Author>Vostrikov</Author><Year>2016</Year><RecNum>79</RecNum><DisplayText>[306]</DisplayText><record><rec-number>79</rec-number><foreign-keys><key app="EN" db-id="trszaapxg0wpfceztvgpxxsp9p5padxeasw0" timestamp="1562601751">79</key></foreign-keys><ref-type name="Journal Article">17</ref-type><contributors><authors><author>Vostrikov, Vitaly V.</author><author>Gustavsson, Martin</author><author>Gopinath, Tata</author><author>Mullen, Dan</author><author>Dicke, Alysha A.</author><author>Truong, Vincent</author><author>Veglia, Gianluigi</author></authors></contributors><titles><title>Ca(2+) ATPase Conformational Transitions in Lipid Bilayers Mapped by Site-directed Ethylation and Solid-State NMR</title><secondary-title>ACS chemical biology</secondary-title></titles><pages>329-34</pages><volume>11</volume><number>2</number><dates><year>2016</year></dates><urls><related-urls><url>http://pubs.acs.org/doi/abs/10.1021/acschembio.5b00953</url><url>http://www.ncbi.nlm.nih.gov/pubmed/26650884</url><url>http://www.pubmedcentral.nih.gov/articlerender.fcgi?artid=PMC4993155</url></related-urls><pdf-urls><url>file:///C:/Users/Weber/AppData/Local/Mendeley Ltd./Mendeley Desktop/Downloaded/Vostrikov et al. - 2016 - Ca(2) ATPase Conformational Transitions in Lipid Bilayers Mapped by Site-directed Ethylation and Solid-State

N.pdf</url></pdf-urls></urls><electronic-resource-num>10.1021/acschembio.5b00953</electronic-resource-num></record></Cite></EndNote>[306], but with several improvements described here to make the protocol more efficient.

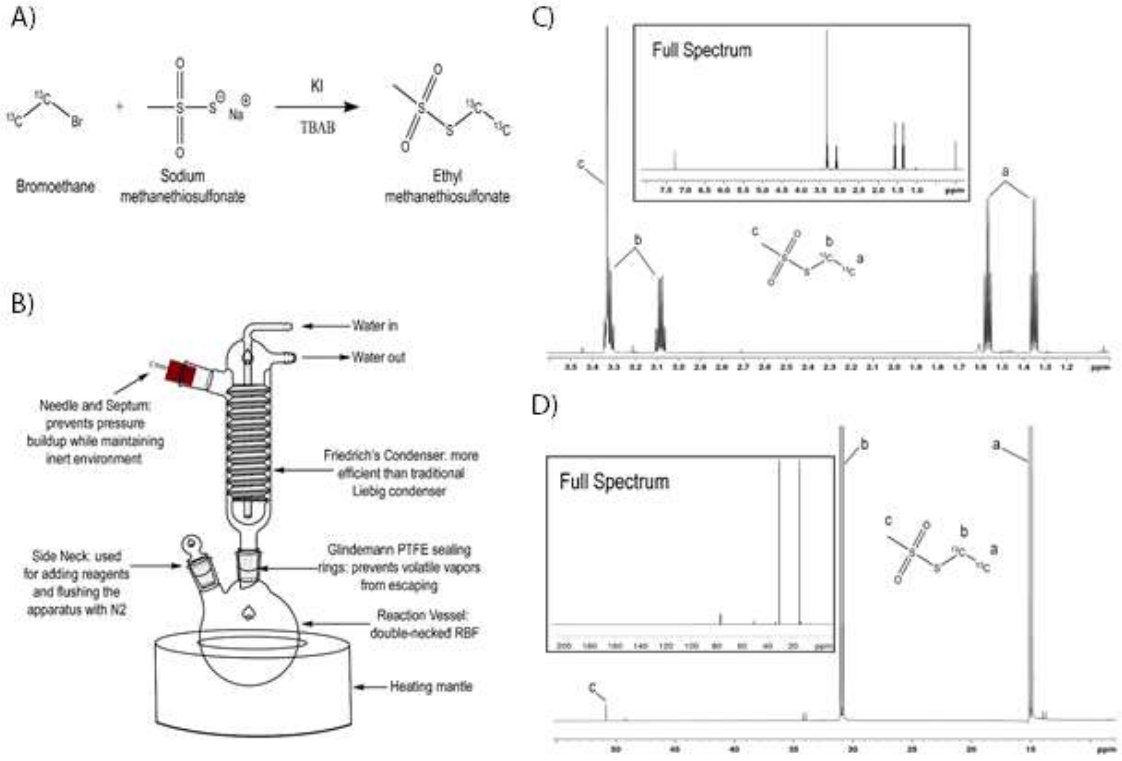

Figure 4.2

A. *Reaction scheme and* ***B.*** *apparatus for synthesis of* ^{13}*C-EMTS. synthesis.* ***C.*** ^{1}*H and* ***D.*** ^{13}*C NMR spectrum of* ^{13}*C-EMTS in* $CDCl_3$ *acquired in a Varian 600 MHz spectrometer at 298°K.* ^{1}*H spectrum was acquired using 8 scans and 30° pulses.* ^{13}*C spectrum was collected using 512 scans with power-gated decoupling.*

First, additional care must be taken to ensure the reaction is carried out under anhydrous conditions as bromoethane's C-Br bond is hydrolysable to ethanol and HBr in the presence water. Therefore, better yields were obtained using dry solvent and avoiding atmospheric exposure. Older reports of this

reaction, however, compromise yields by using 5% water for dissolving sodium methanethiosulfonate [311-313]. To circumvent this issue, a phase transfer catalyst that shuttles ionic sodium methanethiosulfonate into the organic phase can be used. In our protocol, we use tetra-n-butyl ammonium bromide (TBAB). Second, the solvent of choice has a dramatic effect on the final yield of the reaction. Highest yields were obtained using CH_3CN as a solvent. CH_3CN is a polar aprotic solvent and is favorable for SN_2 reactions as it increases the strength of the nucleophile due to weak solvation. Higher yields were also obtained when a catalytic amount of KI was added to the reaction. Iodide generated from KI displaces the bromine in bromoethane, which results in a better leaving group. Lastly, several phase-separated extractions were used to purify the final product from ionic by-products. Using the apparatus depicted in **Fig. 4.2B.** as a guide, the reaction protocol is as follows:

1. Combine dry reagents sodium methanethiosulfonate (1354 mg, 10.1 mmol), TBAB (10 mg, 0.03 mmol), and potassium iodide (10 mg, 0.06 mmol) in a two-necked 50 mL round-bottomed flask (RBF).
2. Attach a condenser column to the RBF. A standard Liebig condenser would be sufficient, but a higher efficiency condenser, such as a Friedrichs or a Jacketed Coil condenser, is recommended. Cheaper and more-common Dimroth or Davies condensers may also be acceptable.
3. Seal joints with Glindemann polytetrafluoroethylene (PTFE) rings to prevent volatile ^{13}C-bromomethane from escaping the reaction apparatus. Vacuum

grease may also be used, but risks contamination especially after prolonged heating.

4. Plug the top of the condenser with a rubber septum and insert a syringe needle through it (**Fig. 4.2B.**). The septum will serve to minimize the amount of volatile $^{13}C_2$-bromoethane escaping and keep the reaction vessel remains mostly under nitrogen, while the needle will prevent pressure build-up. Attach a tubing adapter to the side neck and fasten with a keck clip. Flush the apparatus with dry nitrogen for 5 minutes. Notice that there's no need to continuously flush nitrogen during the reaction. The reaction can also be run using a nitrogen reflux apparatus, but sufficient results were obtained with the described method.
5. De-gas anhydrous CH_3CN (15 mL) either by bath-sonication for 20 min or sparging with dry nitrogen for at least 5 min, then use it to dilute $^{13}C_2$-bromoethane (680 µL, 9.18 mmol) and add to reaction vessel via the side neck. The reaction mixture should appear as a cloudy white suspension.
6. Cap the side neck with a ground-glass stopper, PTFE joint seal and Keck clip.
7. Start a slow flow of water through the condenser (just faster than dripping) and turn on the heating mantle with a low setting. Reflux for at least 20 hours. The suspension will remain cloudy due to unreacted starting materials and formation of inorganic salts.
8. NMR may be used to confirm completion of the reaction. This may be done by briefly opening the side neck and drawing 100 µL of the reaction with a glass syringe and transferring to an NMR tube. Dilute to 700 µL with $CDCl_3$ containing

TMS standard and acquire 1D ^{1}H and ^{13}C NMR spectra. Example ^{1}H and ^{13}C-spectra of pure ^{13}C-EMTS are depicted in **Fig. 4.2C.** and **Fig. 4.2D.**, respectively. Chemical shifts of unreacted $^{13}C2$-bromoethane and ^{13}C-EMTS product are summarized in Table 4.1.

9. Filter the solution using medium ground glass filter, then wash the solids in filter with 20 mL of $CHCl_3$. Collect the filtrate and transfer to a separatory funnel.
10. Add 75 mL of 1 M $MgSO_4$ (in water) to convert any $CHCl_3$-soluble I_2 formed to water-soluble I_3^-. The organic layer stays on the bottom and the aqueous rises to the top. Collect the organic layer and repeat the extraction a total of three times using fresh 75 mL 1M $MgSO_4$ each time. Combine the aqueous layers and back extract with 20 mL $CHCl_3$.

Table 4.1: Chemical shifts of unreacted $^{13}C_2$-bromoethane and ^{13}C-EMTS product

Chemical shifts were referenced to a tetramethylsilane (TMS) standard. Note that doublet ^{1}H signals arise from $^{1}J_{CH}$ coupling with ^{13}C carbons.

Nuclei	^{1}H δ (ppm)	Multiplicity	^{13}C δ (ppm)	Multiplicity
$^{13}C_2$-bromoethane				
$^{13}CH_2$	3.33 and 3.58	Doublet of quartets	19.32	Doublet
$^{13}CH_3$	1.59 and 1.80	Doublet of triplets	28.02	Doublet
^{13}C-EMTS				
$^{13}CH_2$	3.08 and 3.32	Doublet of quartets	14.99	Doublet
$^{13}CH_3$	1.35 and 1.57	Doublet of triplets	30.93	Doublet
CH_3	3.33	Singlet	50.86 (small)	Singlet

11. Combine organic extractions and dry by adding anhydrous $MgSO_4$ powder until no clumping is observed. No more than 10 g should be required. Filter through a medium-glass filter directly into a pre-weighed 100 mL RBF. Rinse the remaining product from solid powder with 5 mL of anhydrous $CHCl_3$.
12. Remove organic solvent using a rotary evaporator with low heat (~30 °C). High heat may risk decomposition of ^{13}C-EMTS. The remaining product will be a colorless oil but may also be slightly yellow due to trace amounts of I_2 remaining. Trace I_2 impurity should not impede the ethylation reaction but could affect the activity of some enzymes. If this is an issue, then these traces may be removed by more phase-separated extractions in step 11.
13. Once all solvent is removed acquire 1D ^{1}H and ^{13}C NMR spectra in 0.7 mL $CDCl_3$. No CH_3CN solvent should remain, which will produce a singlet at 2.10 ppm ^{1}H spectra; and singlets at 116.43 ppm and 1.89 ppm in ^{13}C spectra [314]. The lack of CH_3CN peaks will also indicate that $CHCl_3$ was removed as it has a lower boiling point.
14. Weigh RBF flask and calculate the net mass of ^{13}C-EMTS and yield (MW of 142.003 g/mol). At this scale, the theoretical yield is 1303.59 mg, but expect an actual yield of around 75%.
15. Dissolve ^{13}C-EMTS into DMSO, quantitatively transfer to a 50 mL conical tube and dilute to 200 mM with DMSO using the graduations on the tube. Store at -20 °C. Aliquoting into smaller (polypropylene) tubes is recommended to limit repeated freeze-thawing of the main stock. The lifetime of the reagent has not been determined but has been stable for months in storage in our experience.

4.2.2 Ethylation and reconstitution of membrane proteins into lipid bilayers

The details regarding the purification of the SERCA are highly specific to this system and outside the scope of this review but may be briefly described in two stages. Firstly, skeletal muscle was dissected from a freshly euthanized rabbit and crude sarcoplasmic reticulum (SR) extracted by several rounds of blending and centrifugation [315], then stored in sucrose buffer at -80°C in sucrose buffer (20 mM MOPS, 0.3 M sucrose, 1 mM NaN_3, pH 7.0). Secondly, aliquots of crude SR were thawed, SERCA solubilized from the SR membrane into $C_{12}E_8$ detergent and purified in a single step by affinity to a Reactive Red resin [316]. Purified SERCA was then stored in aliquots of elution buffer (0.5 mg/mL SERCA, 0.1% $C_{12}E_8$, 1 mM $CaCl_2$, 1 mM $MgCl_2$, 20 mM MOPS, 20% glycerol, 8 mM ADP, pH 7.00, 0.25 mM) at -80°C and thawed again at 4°C prior to use. Activity was confirmed by coupled-enzyme assay as a function of calcium concentration [317]. The following steps may be more generalizable to any membrane protein and scaled to pack into a thin-walled 3.2 mm Varian MAS rotor (see **Fig. 4.3A.**):

1. Dialyze 7.5 mg of SERCA (15 mL) twice into 1 L of dialysis buffer (20 mM HEPES, 100 mM KCl, 5 mM $CaCl_2$, 1 mM $MgCl_2$, 1 mM NaN_3, 5% glycerol, 0.25 mM $C_{12}E_8$, pH 7.0). The first dialysis is done over 3 hrs and the second overnight, both at 4°C using 6-8 kDa MWCO dialysis tubing (Fisher Scientific). DTT must be removed as much as possible to avoid consumption of the ^{13}C-EMTS reagent. $C_{12}E_8$ detergent is included above its critical micelle

concentration (CMC) of 0.1 mM [318] to prevent SERCA denaturation during dialysis. Ca^{2+} and Mg^{2+} are included to stabilize SERCA in the Ca^{2+}-bound E1 state.

2. Transfer dialyzed SERCA to a 50 mL conical centrifuge tube with a small magnetic stirrer, dilute to 30 mL with dialysis buffer and bring to room temperature.
3. Add ^{13}C-EMTS reagent (200 mM) at a 5:1 molar excess of SERCA and incubate for 2 hrs at room temperature. The molar ratio of the reagent used must by optimized to the tolerance of the protein of interest. For SERCA, this ratio has been previously determined at small scale by analyzing activity over various molar excesses of ^{13}C-EMTS reagent by enzyme-coupled ATPase assays [317]. At 5:1, there is no loss in SERCA activity with solvent-exposed

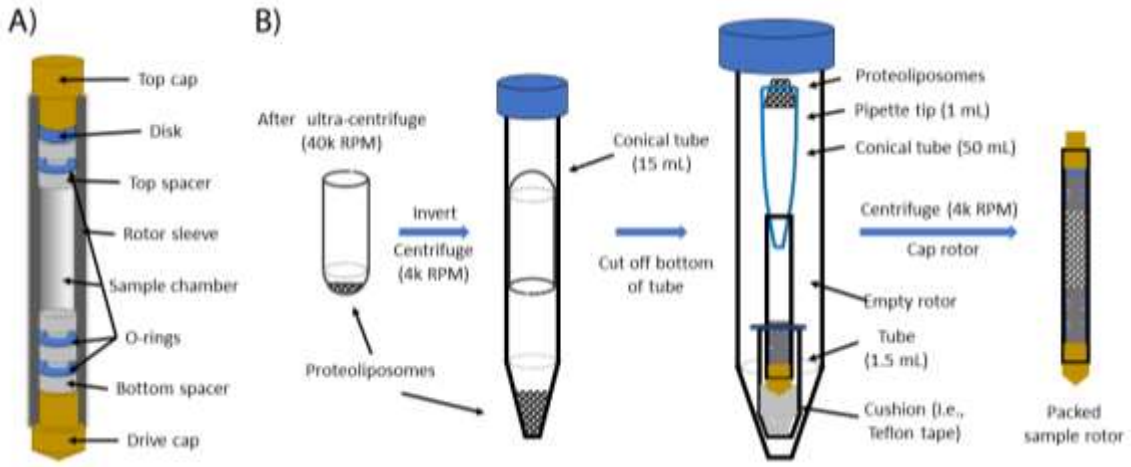

Figure 4.3

A. *Rotor schematic.* ***B.*** *Sample packing scheme for MAS-ssNMR*

cysteines 364, 471, 498, 561, 636 and 674 the most susceptible to ethylation. At this stage, a trypsin digest followed with liquid-chromatography electrospray

ionization tandem mass spectrometry (LC-ESI-MS/MS) may be used to identify labelled residues.

4. Solubilize 9 mg d_{54}-DMPC (1,2-dimyristoyl-sn-glycero-3-phosphocholine) into 1 mL of dialysis buffer and 20 mg of $C_{12}E_8$ detergent (i.e., 80 µL of aqueous 25% w/v stock purchased from Anatrace), add to ethylated SERCA and incubate 30 min at room temperature with stirring. Vortex and bath-sonicate to fully solubilize lipids and cool on ice if mixture becomes too viscous to transfer by pipette. Deuterated lipids are recommended to suppress long-relaxing signal from dynamic methyl groups that will create noise along the indirect dimension of DARR spectra.
5. Remove detergent by adding 1.5 g of Bio-Beads SM-2 (Bio-Rad) over amounts of 0.25 g, 0.25 g, 0.5 g and 0.5 g, with 30-minute intervals of stirring at room temperate after each addition. Bio-Beads have an absorptive capacity for $C_{12}E_8$ of 190 mg/g, for which it is recommended that they are added in successive amounts to allow smooth passage through the micelle to vesical transition and minimize losses of lipid [319]. The sample will become turbid due to formation of proteoliposomes.

4.2.3 Rotor packing

The following describes a simple method to pack sample into a thin-walled 3.2 mm Varian MAS rotor. This protocol may be substituted for one that utilizes specialized rotor packing equipment from commercial suppliers.

1. Aspirate proteoliposomes (from Section 2.2, Step 5) from Bio-Beads by syringe with a 25 G needle and transfer to a 40 mL centrifuge tube. Centrifuge at 12,000 rpm for 30 min at 4°C using a Beckman JA-25.50 rotor.
2. Discard supernatant and resuspend pellet into 2 mL of sample buffer (20 mM HEPES, 100 mM KCl, 5 mM $CaCl_2$, 1 mM $MgCl_2$, 1 mM NaN_3, 2.5% glycerol, pH 7.0).
3. Transfer to a centrifuge tube (compatible for a Beckman TLA-100.3 rotor) and centrifuge at 40,000 rpm for 30 min at 4°C.
4. Discard supernatant and remove as much residual buffer as possible by tapping the tube inverted over a paper towel.
5. Nest the inverted tube inside a 15 mL conical centrifuge tube (**Fig. 4.3B.**) and centrifuge 4,000 RPM for 20 min at room temperature using a Beckman SX4400 swinging-bucket rotor.
6. Very carefully, cut off the bottom of the tube as close to possible to the pellet using a sharp razor blade.
7. Fix the pellet inverted inside a 1 mL pipette tip inserted into the top of the rotor. Place the assembly inside a 50 mL conical tube and screw on lid (**Fig. 4.3B.**). If the 1 mL pipette tip does not fit the entrance of the rotor, then nesting the 1 mL tip inside a smaller 200 µL will work, but the top of the 1 mL pipette tip may have to be cut shorter to fit inside the 50 mL tube. The rotor should have a drive cap and bottom spacer already inserted.
8. centrifuge 4,000 RPM for 20 min at room temperature using a Beckman SX4400 swinging-bucket rotor.

9. Insert top spacer and seal rotor with top cap

4.3 Solid-state NMR spectroscopy

4.3.1 Hardware requirements

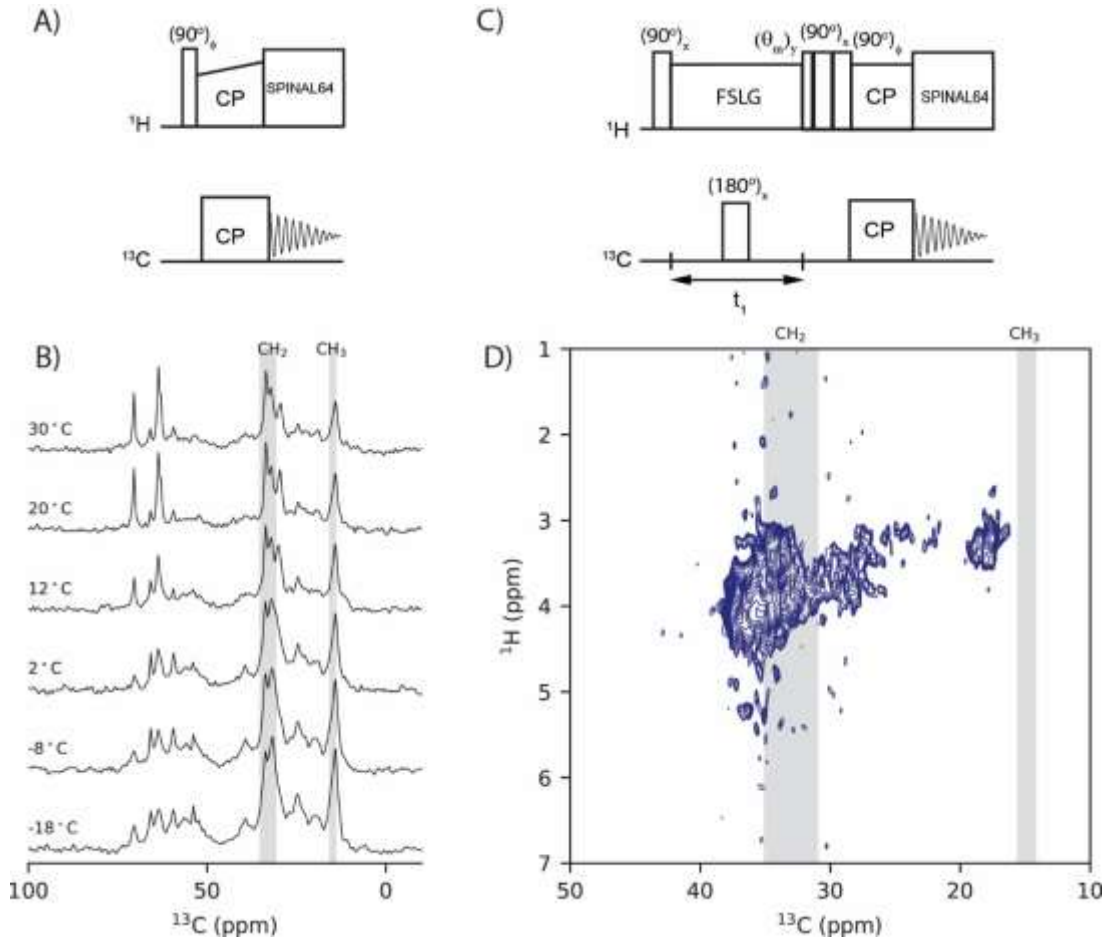

Figure 4.4

A. *Schematic of a standard 1D [^{13}C,^{1}H]-CP experiment.* ***B.*** *1D [^{13}C,^{1}H]-CP spectra of ^{13}C-cysteine-ethylated SERCA at variable temperatures. Spectra were acquired with 1000 scans (51 min per experiment); 3 sec recycle delays; 2.5 µs 90° pulse on ^{1}H; 2 ms CP contact time; CP field strength of 59 kHz on ^{1}H (with 80-100% linear ramp) and 35 kHz on ^{15}N; 100 kHz spectral width for ^{13}C; 100 kHz heteronuclear SPINAL decoupling applied over an acquisition time of 20 ms; and processed with 100 Hz exponential line broadening.* ***C.*** *Schematic of a 2D [^{13}C,^{1}H]-FSLG-HETCOR pulse sequence.* ***D.*** *2D [^{13}C,^{1}H]-FSLG-HETCOR spectrum acquired at 2°C and with parameters from 1D [^{13}C,^{1}H]-CP experiments, except*

*using 480 scans (26 hr experiment time); 100 µs CP contact time; 5207.66 Hz spectral width and 32 points for the indirect ^{1}H dimension; and FSLG ^{1}H homonuclear decoupling. Shaded regions in panel **B.** and **D.** specify expected signal from ^{13}C-ethylated cysteines.*

To further demonstrate the use of ^{13}C-EMTS labelling, we acquired MAS ssNMR spectra of tissue-extracted SERCA in the calcium-bound E1 state ($E1{\cdot}2Ca^{2+}$) prepared according to Section 2. Detection of ^{13}C-ethylated protein is achievable without the need of highly-specialized ssNMR equipment. For example, all spectra presented in this review were acquired on a simple setup including a 700 MHz Varian spectrometer equipped with a low-E Black Fox 3.2 mm HXY MAS (designed by Peter Gor'kov, National High Magnetic Field Laboratory, Tallahassee, FL) probe operating at a MAS rate of 12 kHz for all experiments. All spectra were externally refenced to adamantane [320] and processed using NMRPipe [321].

4.3.2 Cross-polarization and general considerations

Cross-polarization (CP) is a basic element in solid-state NMR pulse sequences and optimized here for detection of ^{13}C-ethyl-tagged cysteines by using standard 1D [^{13}C-^{1}H]-CP sequences (**Fig. 4.4A.**). The ethyl tag will produce distinguishable signals in the regions of 31-35 ppm (CH_2) and 14.5-15.5 ppm (CH_3) in CP spectra (**Fig. 4.4B.**). During the CP block, magnetization is transferred via dipolar couplings from the high-γ and highly-abundant ^{1}H nuclei to the low-γ ^{13}C nuclei during a Hartman-Hahn-matched spin-lock period on both nuclei–with the net result being an enhancement in signal on the directly-detected ^{13}C nuclei in

proportion to the ratio of gyromagnetic ratios (γ) γ_H/γ_C and faster recycle delays allowed as T_1 relaxation is driven by the faster-relaxing ^{1}H spin [322]. The Hartman-Hahn condition is optimized by varying the radio-frequency power levels (B_1) until nutation frequencies (ω) on ^{1}H and ^{13}C are equivalent or matched to a spinning sideband to achieve maximal ^{13}C signal. The optimal contact time must also be determined and depends on the rate of magnetization transfer, which is proportional to the strength of ^{13}C-^{1}H dipolar coupling in the sample; and decay of magnetization due to $T_1\rho$ relaxion, which is accelerated by molecular motions on timescale of ω [323]. The spin-lock field on one of the nuclei is generally ramped for better efficiency of magnetization transfer, where linear ramped-amplitude CP (RAMP-CP) [324] and adiabatic passage Hartmann-Hahn CP (APHH-CP) [325, 326] methods are common. High-power ^{1}H-decoupling is also applied to increase resolution during the acquisition period, and T_1 evolution periods for 2D experiments, as MAS at moderate spinning rates (< 25 kHz) are only partially eliminate line-broadening from dipolar coupling and chemical shift anisotropy (CSA). For this, Small Phase Incremental Alternation (SPINAL-64) [327] and Two Pulse Phase Modulated (TPPM) [328] methods are usually employed. Due to the high-power applied for decoupling, acquisition times are shortened as much as possible to reduce unnecessary wear on the probe and sample heating. Recycle delays between acquisitions are typically set on the order of 3 s and are limited to T_1 relaxation. Recycle delays of membrane-protein systems maybe reduced substantially with paramagnetic relaxation enhancement (PRE) by doping samples with paramagnetic ions [329] and lipid (Cu^{2+}-chelated) [195]. Note that high-power

^{1}H decoupling may cause probe damage and excessive sample heating. Faster MAS frequencies, however, will allow the use of low-power decoupling and recycle delays to be reduced as low as 0.1 ms for super-fast acquisition [330].

4.3.3 Sample temperature

Sample temperature must also be considered in early stages of optimization. Low temperatures preserve the sample integrity, enhancing magnetization and rigidifying the system. This will enhance the efficiency of the CP transfer via stronger dipolar coupling interactions but may also reduce resolution due to inhomogeneous exchange broadening from lipid and protein dynamics, particularly at temperatures below the gel-fluid phase transition of lipids. Higher temperatures may provide better resolution, however, the flexible nature of the ^{13}C-ethyl tag, especially when attached to dynamic domains, may risk complete loss of signal. When CP-based experiments become insensitive, INEPT-based (Insensitive Nuclei Enhanced by Polarization Transfer) [331] experiments may be used to detect highly dynamic regions [332, 333]. An array of 1D [^{13}C,^{1}H]-CP experiments (**Fig. 4.4B.**) show that signals arising from the ^{13}C-ethyl tag, are retained over a temperature range of -18°C to 30°C, but with no observable change in resolution. Therefore, ^{13}C-EMTS can be used to study enzyme dynamics across a broad temperature range.

4.3.4 Optimization and acquisition of [^{13}C,^{13}C]-DARR spectra

By visual inspection of **4.4A**, it is clear that the ^{13}C-ethyl tag is not the only signal observed in a simple 1D [^{13}C,^{1}H]-CP experiment. This is expected as the ethyl tag only introduces 10 to 12 ^{13}C-nuclei buried in the background of 4876 naturally-abundant (1.1% for ^{13}C) carbons of SERCA (110 kDa and 994 residues) plus carbons from endogenous lipids bound to enzyme. This is especially problematic for the [^{13}C,^{1}H]-Frequency-Switched Lee-Goldburg (FSLG) HETeronuclear CORrelation (HETCOR) experiment [334, 335] displayed in **Fig. 4.4C**. In **Fig. 4.4D.**, background noise entirely swamps the signals expected from the $^{13}CH_2$ groups of the ethyl tag, and the signal-to-noise ratio is too low to detect $^{13}CH_3$

groups in the background-free region of the spectrum. Subsequently, $^{13}CH_2$-$^{13}CH_3$ dipolar coupling within the ethyl tag may be exploited in a 2D [^{13}C,^{13}C]-DARR experiment (**Fig. 4.5A.**) to reduce this background by 100-fold. In this experiment, ^{13}C-^{13}C spins are recoupled under MAS conditions during a mixing time with ^{1}H RF field (DARR) at a multiple of the spinning rate applied to recover ^{13}C-^{1}H dipolar interactions driving polarization transfer [308]. Note that we found that [^{13}C,^{13}C]-DARR experiments were suitable under our moderate MAS rates, although, other homonuclear recoupling methods may also be applicable, including Proton-Driven Spin Diffusion (PDSD) [336], Phase-Altered Recoupling Irradiation Scheme (PARIS) [337] and Second-order Hamiltonian among Analogous Nuclei Generated by Heteronuclear Assistance Irradiation (SHANGHAI) [338]. Furthermore, Constant-Time-DARR (CT-DARR) experiments [339] may also be used to improve resolution in the directly-detected ^{13}C dimension, but in our experience this

experiment requires at least four times the acquisition time for sufficient signal-to-noise ratio.

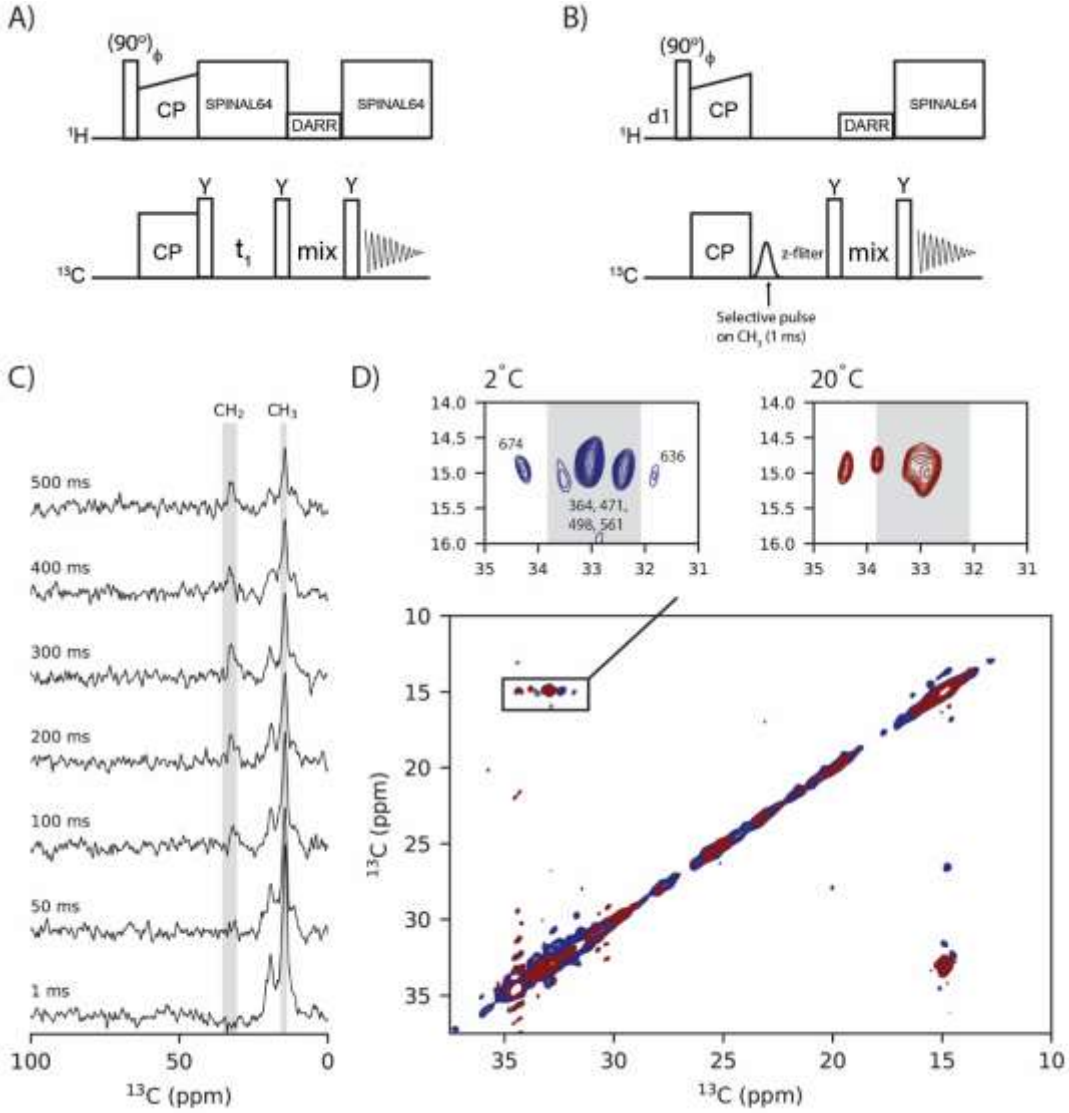

Figure 4.5

A. *Schematic of 2D [^{13}C,^{13}C]-DARR pulse and* ***B.*** *1D [^{13}C,^{13}C]-DARR pulse sequence highlighting a selective 1 ms Gaussian pulse on CH_3 carbons at 15 ppm.* ***C.*** *Array of selective 1D [^{13}C,^{13}C]-DARR spectra of ^{13}C-ethylated SERCA acquired at 20°C with variable DARR mixing times show build-up of intensity of CH_2 signal. Each 1D spectrum was acquired with parameters from 1D [^{13}C,^{1}H]-CP experiments detailed in the caption of* ***Figure 4.4****, but with a 12 kHz field on ^{1}H during DARR mixing and 5000 scans (4 hr each experiment). Spectra were processed with 100 Hz exponential line-broadening.* ***D.*** *2D [^{13}C,^{13}C]-DARR spectra acquired at 2°C (blue) and 20°C (red) with 300 ms DARR; 60 t_1 increments and 5*

kHz spectral width on the second ^{13}C dimension; and 1000 scans (52 hr experiment time for each spectrum). 2D spectra were processed with 20 Hz Lorentzian line-sharpening and 20 Hz Gaussian line-broadening. Shaded region highlights residues of the P-domain as previously assigned [306].

In addition to optimizing [^{13}C,^{1}H]-CP parameters as discussed in the previous section, the length of mixing times must also be optimized for 2D [^{13}C,^{13}C]-DARR experiments. Obviously, optimization by an array 2D experiments is expensive from an NMR time viewpoint. Therefore, similar to initial reports [308], we took advantage of the large separation of $^{13}CH_2$ and $^{13}CH_3$ shifts to optimize parameters using selective 1D [^{13}C,^{13}C]-DARR experiments (**Fig. 4.5B.**). The sequence differs to the 2D sequence (**Fig. 4.5A.**) in that the magnetization of $^{13}CH_3$ is selectively inverted after CP, the t_1 chemical shift evolution period is removed and build-up of $^{13}CH_2$ signal is observed over an array of DARR-mixing times. For our sample at 20°C, we found that 300 ms provided optimal cross-peak intensity using an array of 4 hr long 1D experiments (**Fig. 4.5C.**).

At the scale described in Section 2.2, with 7.5 mg of SERCA reconstituted into 9 mg of d_{54}-DMPC, a 2D [^{13}C,^{13}C]-DARR spectrum can be acquired overnight with good signal-to-noise ratio. In both spectra acquired at 2°C and 20°C over 2 days (**Fig. 4.5D.**), the filtering ability of the ^{13}C-ethyl tag is exemplified by the observation that only labeled carbons are observed in the off-diagonal regions and that separation of $^{13}CH_2$ and $^{13}CH_3$ resonance places cross-peaks well away from the intense diagonal. Furthermore, resolution is afforded mostly by the greater chemical shift dispersion of the $^{13}CH_2$ dimension. Five resolved signals are observed in spectra acquired at 2°C, while only four at 20°C, probably owing to

faster conformational dynamics. In our case, higher resolution is not observed at higher temperature, likely due to the need to apply line-broadening to increase signal-to-noise ratio and time-constraints to acquiring additional points along the indirect dimension.

4.3.5 Assignment of labeled cysteins

Since site-specific mutations are unfeasible, the assignment ^{13}C-ethylated cysteine resonances in DARR spectra is non-trivial task. The approach to be pursued will likely take advantage of chemical, structural and functional features unique to the protein of interest. At the very least, tryptic digests of ^{13}C-ethylated protein will help identify which cysteines have been labeled. Furthermore, as done previously [306], a large excess of iodoacetamide may be added following incubation with ^{13}C-EMTS to identify partially-reacted and non-reacted cysteines through detection of carbamidomethylated (CAM) peptides. Specific assignments may be made by well-informed PRE-experiments. For example, the ethylated-cysteines in the N-domain (nucleotide binding domain) of SERCA were unambiguously assigned previously [306] by selective quenching upon addition of a paramagnetic ADP-TEMPO ligand (ADP = adenosine diphosphate; TEMPO = 2,2,6,6-tetramethyl-1-piperidinyloxy) and selective spin-labelling of C674 with iodoacetamide TEMPO [340]; while ^{13}C-ethylated P-domain (phosphate-binding domain) cysteines closest the membrane are generally assigned by quenching by

a DOPE (1,2-dioleoyl-sn-glycero-3-phosphoethanolamine) lipid engineered with a TEMPO headgroup.

4.4. Conclusions and perspectives

In this chapter, we reported the protocols for utilizing ^{13}C-EMTS to post-translationally introduce ^{13}C-ethyl tags to the 110 kDa SERCA Ca^{2+}-pump, extracted from the skeletal muscle of rabbits, for ssNMR characterization in lipid membranes. Similar post-translational methods based on ^{13}C-methyl labelling have enabled solution NMR characterization of large systems including the 180 kDa α7 ring of the 20S proteasome [307], the 300 kDa ClpP protease [307], the 100 kDa ClC-ec1 chloride channel [341] and a 240 kDa NADPH-cytochrome P450 oxidoreductase-nanodisc complex [342]. ^{13}C-methyl labeling, however, requires extensive deuteration of the surrounding protein to enhance signal intensity of the label and eliminate background in 2D [^{1}H,^{13}C]-spectra [307], or deuteration of the label to filter out background using ^{2}H-^{13}C scalar coupling-edited experiments [343] that cannot be applied to ssNMR due to short coherence lifetimes. Furthermore, good resolution is required to resolve poorly-dispersed methyl peaks. For MAS-ssNMR, the use of ^{13}C-EMTS overcomes several major practical issues, including: 1) the use of ^{13}C-^{13}C dipolar coupling to eliminate background from naturally abundant ^{13}C nuclei in protein and lipid carried through from extraction; 2) wider chemical shift dispersion of $^{13}CH_2$ to provide much-needed additional resolution; and 3) not at any stage being limited to obtaining protein by heterologous

expression. This labelling strategy, therefore, enables the structural states of large membrane proteins, obtained directly from their host organism, to be fingerprinted by ssNMR. Furthermore, this ^{13}C-ethyl tag may also be adapted to other MAS experiments to extract additional structural and topological information [344].

The synthetic protocol described in Section 4.1 may also be modified to introduce other useful nuclei, such as ^{2}H and ^{19}F that have no issues with background in biological systems. These reaction schemes can be carried out using commercially available bromoalkane precursors. For example, order parameters extracted from ^{2}H quadrupolar couplings can report structure and dynamics of the target proteins [345, 346] and may also be introduced by post-translational site-selective protein α-deuteration [347]. ^{19}F also has a large γ providing greater sensitivity and ability to measure long-range distances between probes, but requires specialized probes either equipped high-power ^{1}H and ^{19}F channels, or fast-MAS to remove ^{1}H-^{19}F-dipolar interactions to improve resolution [348]. In solution NMR, post-translational modification with CF_3 tags has enabled the conformational dynamics of G protein-coupled receptors (GPCRs) to be studied [349]. Subsequently, a number reagents have been utilized in solution NMR to post-translationally modify cysteines with ^{19}F nuclei [350-354]. ^{19}F may also be introduced to tyrosine either electrochemically [355, 356] or chemically using acetyl hypofluorite [357]. Furthermore, glutamines may also be enzymatically modified with ^{19}F [358].

Another residue prone to post-translational methylation is lysine, which undergoes reductive methylation in the presence of ^{13}C-formaldehyde yielding a tertiary amine. Lysine has also been modified with ^{19}F-tags with reagents designed to preserve charge and hydrophilicity of the protein [359, 360]. Partial (monomethylation) or complete methylation (di-methylation) of lysines is possible by titrating the amount of ^{13}C-formaldehyde [361, 362]. Lysine methylation can yield tremendous insights into protein structure and dynamics [343, 363]. Lysines have high occurrence (6-7%) in soluble and solvent-exposed membrane proteins. Often, these residues are located nearby or within active sites and can report on protein function. In general, lysine methylation is structurally non-perturbing. However, when these residues participate to the chemistry of enzymes, capping their charged side chain may result in a significant reduction or loss of activity as it was found for SERCA (data not shown). Nonetheless, there are several reports on the successful application of reductive methylation of lysines [364-368] and efforts toward developing protocols for monoethylation have provided enhanced spectral quality and narrower line-widths [343]. This method, however, has had its largest utilization for liquid-state NMR spectroscopy, where the fast tumbling rates of globular proteins and their internal flexibility of solvent-exposed lysine enhance the sensitivity of the methyl groups [341]. For ssNMR, however, lysine methyl labelling is still limited as the resonances overlap with the ^{13}C natural abundance background.

4.5 Acknowledgments

This work was supported by the National Institute of Health (GM 64742 and HL 144130).

Chapter 5 Structural basis for allosteric control of the SERCA-phospholamban membrane complex by Ca^{2+} and phosphorylation

Daniel K. Weber[1], Máximo Sanz-Hernández[2], U. Venkateswara Reddy[1], Songlin Wang[1], Erik K. Larsen[3], Tata Gopinath[1], Martin Gustavsson[1], Razvan L. Cornea[1], David D. Thomas[1] Alfonso De Simone[2,4] and Gianluigi Veglia[1,3,]*

[1] Department of Biochemistry, Molecular Biology, and Biophysics, University of Minnesota, Minneapolis, MN 55455, USA

[2] Department of Life Sciences, Imperial College London, South Kensington, London, SW7 2AZ, UK

[3] Department of Chemistry, University of Minnesota, Minneapolis, MN 55455, USA

*[4] Department of Pharmacy, University of Naples "Federico II", Naples, Italy**

[208]

To whom correspondence should be addressed: Gianluigi Veglia,

Department of Biochemistry, Molecular Biology & Biophysics,

University of Minnesota, 6-155 Jackson Hall, MN 55455.

Telephone: (612) 625-0758.

Fax: (612) 625-2163.

E-mail: vegli001@umn.edu.

Keywords: *Topological Allostery, membrane proteins, allosteric coupling, oriented solid-state NMR, bicelles.*

Abstract

Phospholamban (PLN) is a mini-membrane protein that directly controls the cardiac Ca^{2+}-transport response to β-adrenergic stimulation, thus modulating cardiac output during the fight-or-flight response. In the sarcoplasmic reticulum membrane, PLN binds to the sarco(endo)plasmic reticulum Ca^{2+}-ATPase (SERCA), keeping this enzyme's function within a narrow physiological window. PLN phosphorylation by cAMP-dependent protein kinase A or increase in Ca^{2+} concentration reverses the inhibitory effects through an unknown mechanism. Using oriented-sample solid-state NMR spectroscopy and replica-averaged NMR-restrained structural refinement, we reveal that phosphorylation of PLN's cytoplasmic regulatory domain signals the disruption of several inhibitory contacts at the transmembrane binding interface of the SERCA-PLN complex that are propagated to the enzyme's active site, augmenting Ca^{2+} transport. Our findings address long-standing questions about SERCA regulation, epitomizing a signal transduction mechanism operated by posttranslational modified bitopic membrane proteins.

5.1 Introduction

Miniproteins are translated from small open reading frames of 100-300 nucleotides in length and constitute a neglected portion of the human proteome[369]. Most miniproteins are membrane-embedded and act as regulators or ancillary proteins to enzymes or receptors [370-372]. Among the most critical miniproteins is phospholamban (PLN), a bitopic membrane polypeptide that

regulates the function of the sarco(endo)plasmic reticulum Ca^{2+}-ATPase (SERCA) in cardiac muscle [373]. PLN directly controls cardiac output by maintaining SERCA's activity within a tight physiological window [374]. SERCA is a ten-transmembrane (TM) pump that promotes diastole by removing Ca^{2+} from the sarcoplasm and restoring high Ca^{2+} concentrations in the sarcoplasmic reticulum (SR) in preparation for the next systole [374]. As with other P-type ATPases, SERCA is fueled by ATP and cycles between two major conformational states *E*1 and *E*2, of high and low Ca^{2+}-affinity, respectively [375]. In cardiomyocytes, PLN is expressed in 4-fold molar excess of SERCA, suggesting that this endogenous regulator is permanently bound to the enzyme in a 1:1 stoichiometric ratio [376]. PLN binds the ATPase *via* intramembrane protein-protein interactions, lowering its apparent Ca^{2+} affinity and stabilizing the *E*2 state of the pump [374, 377]. SERCA/PLN inhibitory interactions are relieved upon β-adrenergic stimulation, which unleashes cAMP-dependent protein kinase A (PKA) to phosphorylate PLN's cytoplasmic domain at Ser16, enhancing Ca^{2+} transport by SERCA and augmenting heart muscle contractility [378]. Ablation, point mutations, or truncations of PLN have been linked to congenital heart disease[377]. Despite multiple crystal structures of SERCA alone[375] and several structural studies of PLN free and bound to SERCA [379-381], the inhibitory mechanisms of PLN and its reversal upon phosphorylation or Ca^{2+} increase are still unknown. Mutagenesis data and molecular modeling suggested that SERCA regulation occurs through electrostatic and hydrophobic interactions between the helical transmembrane (TM) region of PLN and the binding groove of the ATPase formed by TM2, TM6,

and TM9 [382]. Upon phosphorylation, or binding SERCA, however, the helical TM domain of PLN does not undergo significant changes in secondary structure [184, 383, 384]. As a result, X-ray crystallography [384] and other structural techniques (*e.g.*, EPR or NMR) have not offered significant mechanistic insights into the regulatory process.

Here, we reveal the elusive signal transduction mechanism responsible for phosphorylation-induced activation of the SERCA/PLN complex using a combination of oriented-sample solid-state NMR (OS-ssNMR) spectroscopy and dynamic structural refinement by replica-averaged orientational-restrained molecular dynamics simulations (RAOR-MD) [201, 385]. The analysis of anisotropic ^{15}N chemical shifts (CSs) and ^{15}N-^{1}H dipolar couplings (DCs) of PLN alone and in complex with SERCA in magnetically aligned lipid bicelles unveiled collective topological changes of PLN's inhibitory TM domain in response to Ser16 phosphorylation. Specifically, the local perturbations of phosphorylation were allosterically transmitted via an order-disorder transition of the juxtamembrane helical residues involved in several inhibitory interactions with SERCA. This intramembrane regulatory mechanism represents a potential paradigm of the structural basis of SERCA activity modulation by other regulins (*e.g.*, sarcolipin, myoregulin, DWORF, etc.) [370] in response to different physiological cues.

5.2 .Results

5.2.1 The TM domain of PLN undergoes a topological two-state equilibrium

In lipid membranes, PLN adopts an *L*-shaped conformation, with a membrane-adsorbed, amphipathic regulatory region (domain Ia, M1 to T17) connected by a short loop (Ile18 to Gln22) to a helical inhibitory region (domains Ib, Gln23 to Asn30; and domain II, Leu31 to Leu52), which crosses the SR membrane [386, 387]. In its storage form, PLN is pentameric [387-389] and de-oligomerizes into active *L-shape* monomers [386]. The dynamic cytoplasmic region undergoes an order-disorder transition between tense (*T*) and relaxed (*R*) states, with the latter promoted by Ser16 phosphorylation [184, 383, 390]. Upon binding SERCA, domain Ia transitions to a more-rigid and non-inhibitory bound (*B*) state, becoming more populated upon phosphorylation [184, 383]. How does Ser16 phosphorylation signal the reversal of inhibition to the TM region? Since the inhibitory TM region is ~ 45 Å away from Ser16 and ~ 20 Å from the SERCA's Ca^{2+} binding sites, we speculated that both phosphorylation (of PLN) and Ca^{2+} binding (to SERCA) must transmit conformational and topological changes across the membrane, thus allosterically modulating SERCA's function.

Residue-specific anisotropic NMR parameters such as CSs and DCs are exquisitely suited to describe topological transitions such as tilt, bend, and torque of TM proteins in lipid bilayers near-physiological conditions [391, 392]. Their analysis by OS-ssNMR requires that membrane-embedded proteins are uniformly oriented relative to the static magnetic field ($\mathbf{B_0}$). Therefore, we reconstituted PLN free and in complex with SERCA into magnetically aligned lipid bicelles [393].

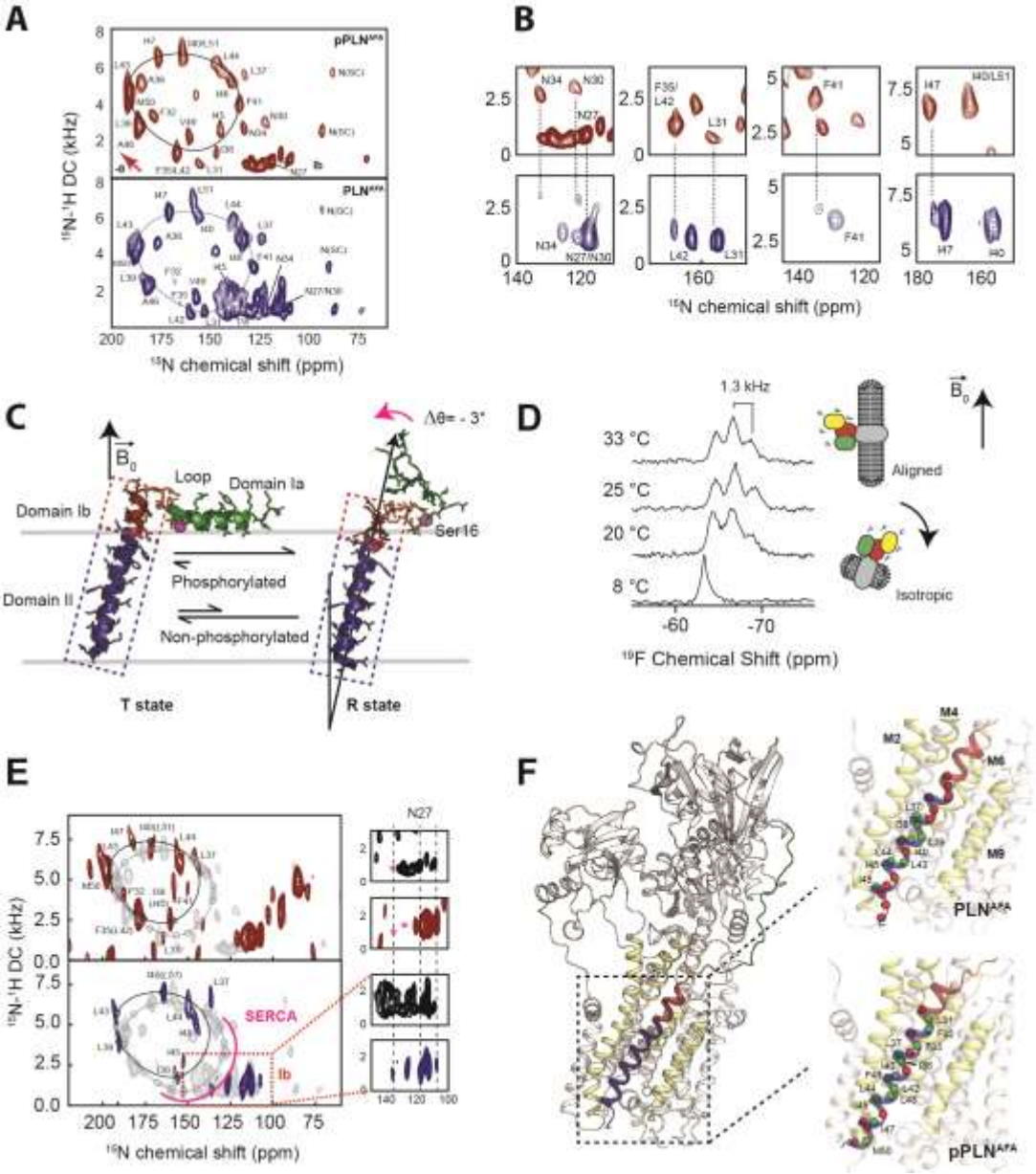

Figure 5.1: Topological equilibrium of PLN and pPLN free and bound to SERCA in lipid bilayers detected by OS-ssNMR

A. *2D [^{15}N-^{1}H] SE-SAMPI4 spectra of PLN^{AFA} and pPLN^{AFA} reconstituted into aligned lipid bicelles. The fitting of resonance patterns with PISA wheels for an ideal helix is superimposed.* ***B.*** *Expanded regions of PLN^{AFA} ^{15}N-labeled at N, L, F, or I residues (lower panel, blue contours) showing two populations. The upper panels (red) are the corresponding regions for the U-^{15}N labeled pPLN^{AFA}. U-^{15}N labelled spectra were acquired at higher signal-to-noise to observe the second population.* ***C.*** *Structures of the T (PDB 2KB7[386]) and R (PDB 2LPF[394]) states for PLN^{AFA}.* ***D.*** *^{19}F NMR spectra of TFMB-tagged SERCA reconstituted into anisotropic (q = 4) bicelles at variable temperatures.* ***E.*** *2D [^{15}N-^{1}H] SE-SAMPI4 spectra of uniformly ^{15}N labeled PLN^{AFA} (blue, lower panel) and pPLN^{AFA} (red,*

upper panel) bound to SERCA in the absence of Ca^{2+} (E2 state). Spectra are overlaid with PLN^{AFA} or $pPLN^{AFA}$ in their free forms (grey). PISA wheels are overlaid, showing assigned residues (black points) used to fit helical tilt and rotation angles. Ambiguous assignments are shown in parentheses. The region corresponding to domain Ib is expanded to show peak broadening (asterisk) following the transition of PLN's cytoplasmic region to the B state. ***F.*** *Selected structure of the SERCA/PLN^{AFA} complex. Expanded region shows visible (green spheres, labelled) and broadened (red spheres) residues mapped onto domain II of PLN^{AFA} (left) and $pPLN^{AFA}$ (right, form a structure of the SERCA/PLN^{AFA} complex).*

Since monomeric PLN is the functional form [395], we utilized a monomeric mutant of PLN devoid of TM cysteine residues [396]. Both unphosphorylated (PLN^{AFA}) and phosphorylated ($pPLN^{AFA}$) variants of PLN were expressed recombinantly, while SERCA was purified from mammalian tissues [397]. Since lipid bicelles orient spontaneously with the normal of the membrane ($\vec{n}$) perpendicular to $\mathbf{B_0}$, we doped the sample with Yb^{3+} ions to change the magnetic susceptibility and orient the lipid membranes with $\vec{n}$ parallel to $\mathbf{B_0}$. This expedient doubles the values of CSs and DCs and increases the resolution of the NMR spectra [398, 399]. **Fig. 5.1A.** shows the 2D [^{15}N-^{1}H] sensitivity-enhanced (SE)-SAMPI4 [400] separated local field (SLF) spectra of free PLN^{AFA} and $pPLN^{AFA}$. Due to PLN's intrinsic conformational dynamics, the SLF spectra visualize only its TM region. The spectra display the typical wheel-like pattern diagnostic of a helical conformation for both the TM domains of PLN^{AFA} and $pPLN^{AFA}$. Residue-specific assignments were carried out on free PLN^{AFA} using a combination of a 3D SE-SAMPI4-PDSD spectrum [401], selective ^{15}N labeled samples, and predictions from MD simulations [402] (**Table 5.1**; **Fig. 5.1–fig. supp. 5.1-3**). To obtain PLN's topology in lipid bilayer, the assigned resonances were fit to idealized *P*olar *I*ndex *S*lant *A*ngle (PISA) models extracting whole-body tilt (θ) and rotation or azimuthal (ρ) angles [145, 403], which

for free PLN^{AFA} was $\theta = 37.5 \pm 0.7°$ and $\rho_{L31} = 201 \pm 4°$, and for pPLN^{AFA} $\theta = 34.8 \pm 0.5°$ and $\rho_{L31} = 201 \pm 4°$, where ρ_{L31} is the rotation angle referenced to Leu31. Notably, the high resolution of the oriented SLF spectra of PLN^{AFA} show two distinct sets of peaks (**Figure 5.1B.**), with populations unevenly distributed. The average population of the minor state estimated from the normalized peak intensities is approximately 30 ± 9 %. Remarkably, the resonances of the minor population overlap almost entirely with those of pPLN^{AFA} (**Fig. 5.1B.**), revealing a topological equilibrium in which the TM region of PLN interconverts between two energetically different orientations. We previously showed that PLN phosphorylation shifts the conformational equilibrium toward the *R* state [184], releasing the interactions with the lipid membranes of domain Ia (**Fig 5.1C.**). Our OS-ssNMR data show that these phosphorylation-induced effects propagate to the TM domains, shifting the topological equilibrium toward the less populated state.

5.2.2 PLN phosphorylation by PKA signals a rearrangement of the SERCA/PLN binding interface

To investigate how Ser16 phosphorylation allosterically affects the inhibitory TM binding interface, we reconstituted the SERCA/PLN complex in lipid bicelles and studied it by OS-ssNMR. The alignment of mammalian SERCA in bicelles was confirmed by cross-linking the most reactive cysteines with a trifluoromethylbenzyl (TFMB)-methanethiosulfonate (MTS) tag to probe its alignment by ^{19}F NMR (**Fig. 5.1D.; Fig. 5.1–fig. supp. 4**). Five of the twenty-four cysteines of SERCA were

uniquely labeled as monitored by solution NMR in isotropic bicelles (q = 0.5). In anisotropic bicelles (q = 4.0) and at low temperature, the ssNMR spectrum of ^{19}F-SERCA consists of a single unresolved ^{19}F resonance due to the rapid reorientation of the enzyme in the isotropic phase. Upon increasing the temperature, the ^{19}F-SERCA/bicelle complex orients with $\vec{n}$ perpendicular to $\mathbf{B}_0$, and the ^{19}F resonance becomes anisotropic as a triplet with 1.3 kHz dipolar coupling [404]. **Fig.5.1E.** shows the 2D SLF spectra of PLN^{AFA} and pPLN^{AFA} in complex with SERCA. To maintain a functional and stable complex, we used a lipid-to-complex molar ratio of 2000:1, with PLN concentration 10 times less than in the SERCA free samples. Therefore, the signal-to-noise ratio in the oriented spectra is significantly reduced relative to the free forms. Nonetheless, the SLF spectra of both SERCA/PLN^{AFA} and SERCA/pPLN^{AFA} complexes show the wheel-like patterns typical of the α-helical domains with selective exchange broadening for resonances located at the protein-protein binding interface (**Fig. 5.1F.**). The assigned peaks associated with the helical domain II were fit to the ideal PISA model, yielding θ= 33.2 ± 1.2° and ρ_{L31} = 193 ± 7°. Therefore, upon binding SERCA, PLN^{AFA} requires a distinguishable -4.3 ± 1.4° change in tilt (p = 4.3 × 10^{-15}) and a less significant -8 ± 8° change in rotation (p = 0.00027). These error bounds factor the linewidths and variation associated with substituting ambiguous assignments into the PISA fitting (parentheses of **Figure 5.1E.**). Similarly, the PISA model for pPLN^{AFA} was fit to θ = 30.4 ± 1.1° and ρ_{L31} of 197 ± 4°, suggesting that the topology of the TM domain requires adjustments of -3.4 ± 1.2° (p = 2.9 × 10^{-14}) and -4 ± 6° (p = 0.0013) to form a complex with the ATPase.

Reductions in the TM helix tilt angle, which accompanied phosphorylation and complex formation, also coincided with a dramatic broadening of peaks in the cluster of isotropic resonances around 140 ppm (**Fig. 5.1E.**). These resonances are attributed to the dynamic domain Ib residues, and their disappearance is consistent with SERCA binding, which requires the unwinding of the juxtamembrane region, and a concomitant reduction of the tilt angle to re-establish hydrophobic matching with the thickness of the lipid bilayer [184, 381]. Therefore, for free and bound PLN, we find that communication between cytoplasmic and intramembrane environments is transduced via domain Ib dynamics. Analysis of the SLF spectra also shows that phosphorylation of PLN at Ser16 restores the intensities of most resonances except for those at the upper binding interface (*i.e.*, Asn30, Leu31, Asn34, and Phe41). These spectral changes suggest a reorganization of PLN-SERCA packing interactions, rather than a complete dissociation of the complex, consistent with prior MAS-ssNMR, EPR, and FRET measurements [184, 381, 405, 406].

5.2.3 Dynamic structural refinement of the SERCA-PLN complexes

To determine the structural ensembles of the SERCA/PLN^{AFA} and SERCA/pPLN^{AFA} complexes, we incorporated the data from our experimental measurements into RAOR-MD samplings [201, 385]. This dynamic refinement methodology employs full atomic MD simulations in explicit lipid membranes and water and utilizes restraints from sparse datasets to generate experimentally-

driven structural ensembles. As starting coordinates for our samplings, we used the X-ray structure of *E*2-SERCA/PLN, where a super-inhibitory mutant of PLN was used to stabilize the complex for crystallization **[384]**. We docked the TM domains of PLN^{AFA} using restraints obtained from chemical cross-linking experiments for both cytoplasmic and luminal sites [382, 407, 408] (**Fig. 5.2–fig. supp. 5.1A.**).

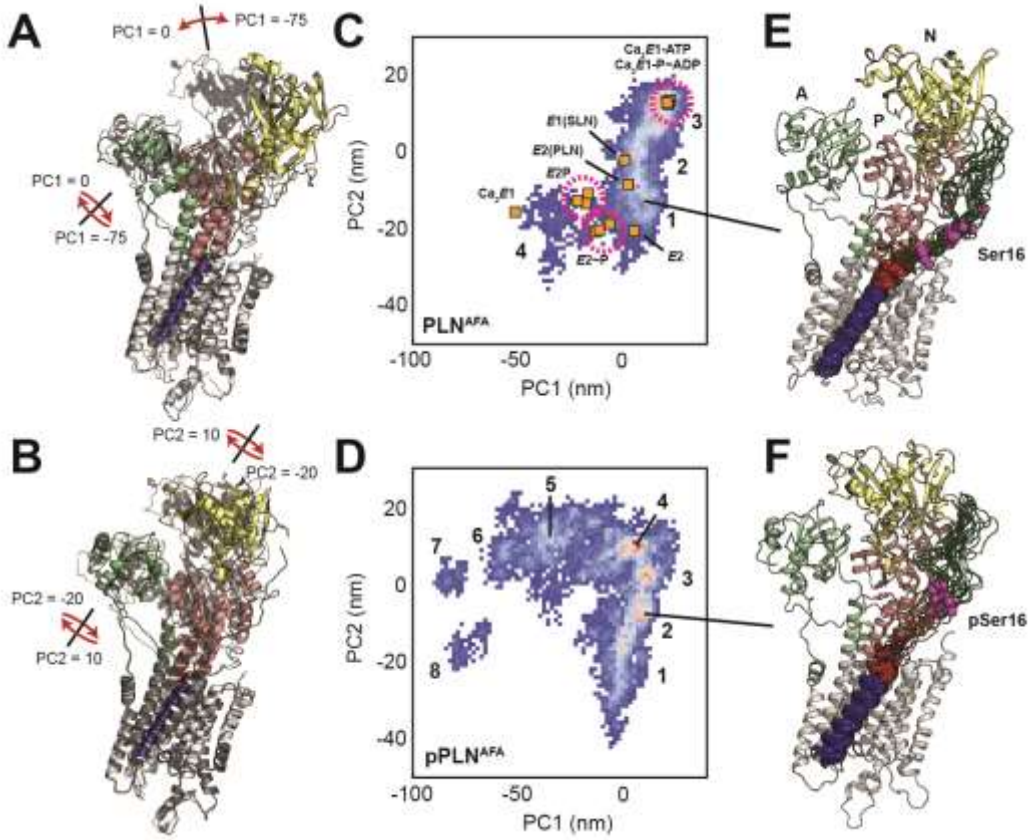

Figure 5.2: Conformational ensembles and energy landscapes of the SERCA/PLN^{AFA} and SERCA/pPLN^{AFA} complexes

A. *and* ***B.*** *Depiction of headpiece movements associated with the first* ***A.*** *and second* ***B.*** *principal components. Structures with the highest PC values are shown as transparent black.* ***(C, D)*** *PCA histograms of SERCA/PLN^{AFA}* ***C.*** *and SERCA/pPLN^{AFA}* ***D.*** *structural ensembles with projections of crystal structures in various states: Ca_2E1-ATP[409, 410], Ca_2E1~P-ADP[410-412], Ca_2E1[2], E1-SLN[413], E2-PLN[384], E2P[411, 414], E2~P[411, 414, 415], and E2[416]. Clusters are numbered.* ***E.*** *and* ***F.*** *Top 20 most representative structures of PLN^{AFA}*

*(**E.,** cluster 1) and pPLN^{AFA} (**F.**, cluster 2) bound to SERCA from the most representative state.*

The dynamic cytoplasmic region (loop and domain Ia), which was not resolved in the crystal structure, was held in proximity to the nucleotide-binding (N) and phosphorylation (P) domains of SERCA using upper boundary restraints from paramagnetic relaxation enhancements (PRE) obtained from MAS-ssNMR [184]. Additionally, CSs and DCs from OS-ssNMR were applied to the TM region as ensemble-averaged restraints across eight replicas. The resulting structural ensembles were in excellent agreement with all the available experimental data for both complexes. The overall profile of the average pairwise distances for residues in domain Ia and loop to the spin-label at Cys674 matches the PRE measurements, with the minimal distance (*i.e.,* maximum PRE effect) observed for PLN-Tyr6 (**Fig. 5.2–fig. supp. 5.1B., C.**). Similarly, back-calculated CS and DC values for PLN^{AFA} and pPLN^{AFA} were in excellent agreement with experiments (**Fig. 5.2–figure supp. 5.1D.**). Average back-calculated tilt angles of 32.8° and 30.4° for PLN^{AFA} and pPLN^{AFA}, respectively, matched PISA fits to experimental values (**Fig. 5.2–fig. supp. 5.1E., 2**). All pairwise distances between previously reported cross-linkable positions [382, 407, 408, 417] were distributed within acceptable ranges (**Fig. 5.2–fig. supp. 5.1F.**). Although not used as an initial docking restraint, cytoplasmic residues PLN Lys3 and SERCA Lys397 were also partially distributed within a distance consistent with previously reported cross-linking [418].

To assess the SERCA/PLN complexes' conformational landscape, we used principal component analysis (PCA). PCA identified a combined opening of the cytoplasmic headpiece involving a hinge-like displacement of the N domain and rotation of the A domain away from the P domain (PC1) and planar rotations separating the N and A domains (PC2) (**Fig. 5.2A., B.**; **Fig. 5.2–fig. supp. 5.3-5)**. These motions differentiate the *E*1 and *E*2 states of SERCA, as shown by the projections of crystal structures onto the PCA map (**Fig. 5.2C., D.**). The SERCA/PLN^{AFA} complex spans four distinct clusters, while the SERCA/pPLN^{AFA} complex spans eight (see **Fig. 5.2–figure supp. 5.6** for representative structures). When bound to PLN^{AFA}, SERCA mostly retains the compact *E*1-like headpiece present in the crystal structure and interconverts with equal frequency between a highly compact cluster (3) resembling nucleotide-bound *E*1 states and a cluster (1) intermediate toward the *E*2 states, which exhibits a partial opening of the A and N domains caused by breaking of the salt bridges involving Arg139-Asp426/Glu435 and Lys218-Asp422. Albeit biased along the *E*1 coordinate of PC2, similar states were present for pPLN^{AFA}, but the interaction of pSer16 with Arg604 weakens the Asp601-Thr357 and Arg604-Leu356 hydrogen bonds at the hinge of the N and P domains, leading to four additional open states (clusters 5 to 8). Separate clusters correspond to successive breakages of interdomain hydrogen bonds in the headpiece. Salt bridges between PLN-Ser16 to SERCA-Arg460 and PLN-Arg14 to SERCA-Glu392 were also found to stabilize these open states (**Fig. 5.2–fig. supp. 5.7**). These open states resemble off-pathway crystal structures solved for the Ca_2E1 state observed in the absence of nucleotide[2, 375, 419]. For all

clusters, the binding interactions near the Ser16 position were more persistent for pPLN^{AFA} than PLN^{AFA} (**Fig. 5.2E., F.**; **Fig. 5.2–fig. supp. 5.6**).

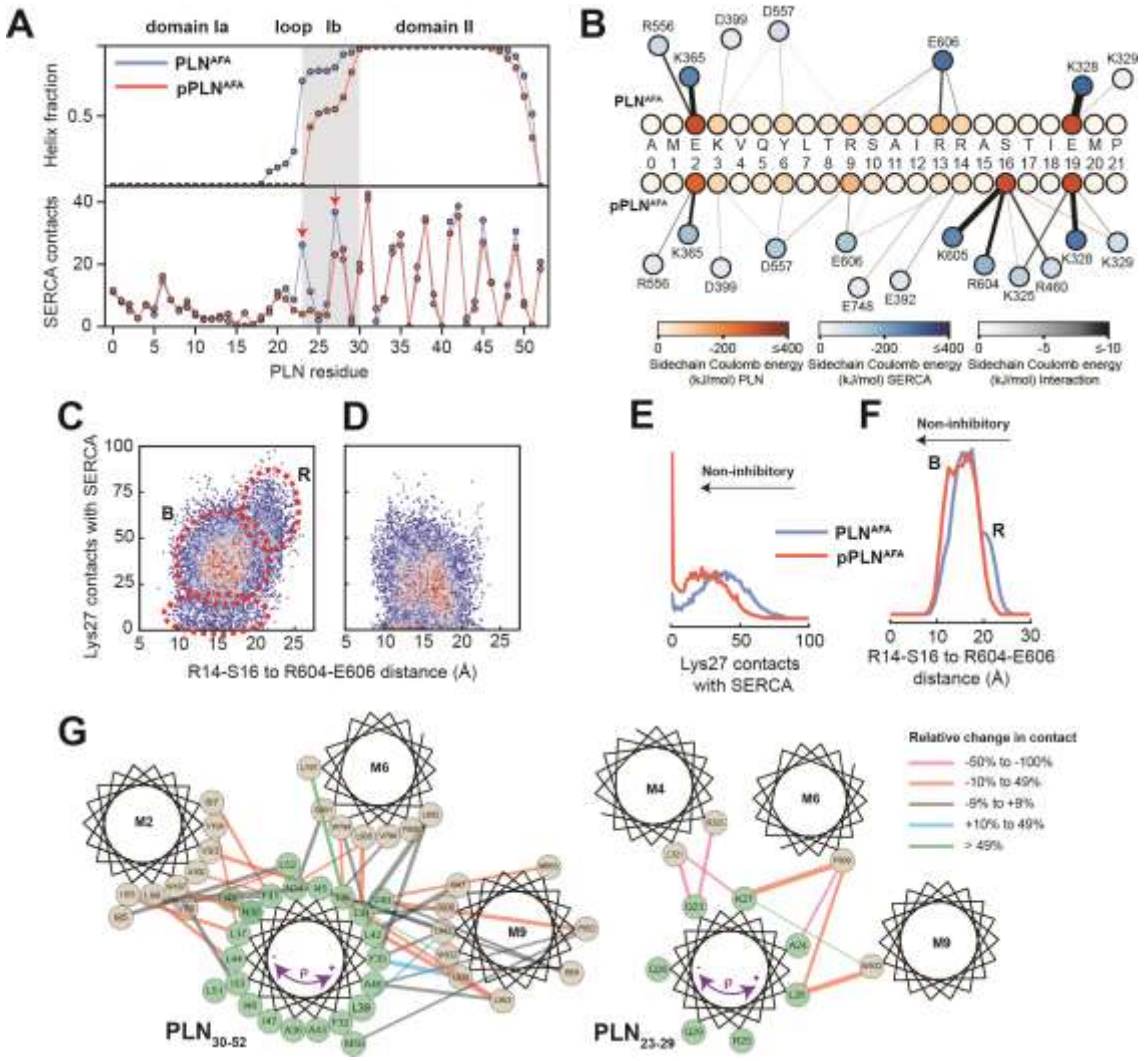

Figure 5.3: Mechanism for reversal of PLN inhibition by phosphorylation

A. *Ensemble-averaged per-residue structural analysis (upper panel) and intermolecular contact profiles (lower panel). A contact is defined when any PLN atom comes within 3.5 Å of any SERCA atom for any given frame.* ***B.*** *Spider plot of pairwise electrostatic interactions between cytoplasmic residues and SERCA in RAOR-MD conformational ensembles.* ***C.*** *and* ***D.*** *2D Histograms correlating the distances between the cytoplasmic binding interfaces, defined by the center of masses of Arg14 to Ser16 of PLN and Arg604 to Glu606 of SERCA, to the inhibitory intermolecular contacts of PLN Lys27 for the SERCA/PLN^{AFA}* ***C.*** *and SERCA/pPLN^{AFA}* ***D.*** *ensembles.* ***E.*** *and* ***F.*** *Corresponding 1D histograms for Lys27 contacts* ***E.*** *and binding of the cytoplasmic domain* ***F.****.* ***G.*** *Disruption of the inhibitory TM pairwise interactions detected in the RAOR-MD conformational ensembles.*

Linewidths of the interhelical contacts are scaled to average contacts per frame for the non-phosphorylated complex and colored by the relative change observed with phosphorylation. Directions of the purple arrows exemplify clockwise or counterclockwise rotations of the TM domain of PLN during the trajectories.

From the analysis of the structural ensembles of the two complexes, it emerges that the relief of inhibition (i.e., activation) occurs via a rearrangement of the intramembrane contacts between the TM region of $pPLN^{AFA}$ and SERCA, with a reconfiguration of electrostatic interactions near the phosphorylation site and a disruption of packing at the protein-protein interface (**Fig. 5.3A.**, **B.**). The interactions between the cytoplasmic regions are transient and highly dynamic, resembling the conformational ensembles of intrinsically disordered complexes [420]. For both complexes, we observe persistent interactions between PLN-Glu2 and SERCA-Lys365, PLN-Glu19, and SERCA-Lys328, and to a lesser extent PLN-Lys3 and SERCA-Asp399 and PLN-Tyr6 and SERCA-Asp557. For PLN^{AFA}, however, the arginine residues (Arg9, Arg13, and Arg14) interact transiently with SERCA-Glu606, while for $pPLN^{AFA}$, the phosphate group at Ser16 interacts strongly with SERCA-Arg604 and SERCA-Lys605. Interestingly, we detected the formation of intramolecular salt-bridges between the phosphate of Ser16 and PLN-Arg9, PLN-Arg13, and PLN-Arg14, causing domain Ia to adopt a compact conformation as previously suggested by fluorescence data [421, 422] (**Table 5.2**, **6.3**). These cytoplasmic protein-protein interactions destabilized PLN's domain Ib and consequently severed inhibitory intermolecular contacts with SERCA's TM helices involving Gln23-Leu321/Arg325 (M4), Lys27-Phe809 (M6) and Asn30-Trp107 (M2), while the intermolecular contacts involving domain II are mostly retained (**Fig. 5.3A** and **Fig. 5.3–fig. supp. 5.1**). In fact, hydrophobic substitutions

within domain Ib have been identified as hotspots for engineering super-inhibitory PLN mutants (*i.e.*, Asn/Lys27Ala and Asn30Cys), which exhibit stable helical structure well into the loop domain [384, 423, 424]. Importantly, these structural ensembles capture the order-disorder dynamics of domain Ib resonances observed in the OS-ssNMR spectra and suggested by previous NMR and EPR studies[425]. Destabilization and detachment of this region is consistent with the reappearance of exchange-broadened interfacial resonances of domain II paralleled by broadening of the resonances of the dynamic domain Ib in the SLF spectra of the SERCA/pPLN^{AFA} complex (**Fig. 5.1E.**). The interactions of domain Ia (Arg13-Ser16) and inhibitory contacts of domain Ib (at Lys27) with SERCA appear to be mutually exclusive (**Fig. 5.3C.-F.**). In both complexes, the electrostatic interactions of PLN-Arg13, PLN-Arg14, or PLN-pSer16 with the SERCA's Arg604-Glu606 stretch cause the detachment of PLN's domain Ib and the consequent weakening of the inhibitory interaction (**Fig. 5.3C.-G.**). This illustrates the regulatory role of the *B* state of PLN for relieving inhibition and the superinhibitory activity of domain Ia-truncated PLN [184].

5.2.4 Phosphorylation disrupts correlated motions between PLN^{AFA} and SERCA's Ca^{2+} binding sites

To assess the effects of PLN's phosphorylation on Ca^{2+} transport, we calculated the topological correlations of the TM's tilt angle fluctuations between PLN's and SERCA's TM helices (**Fig. 5.4A.-D.**). When PLN^{AFA} is bound to SERCA,

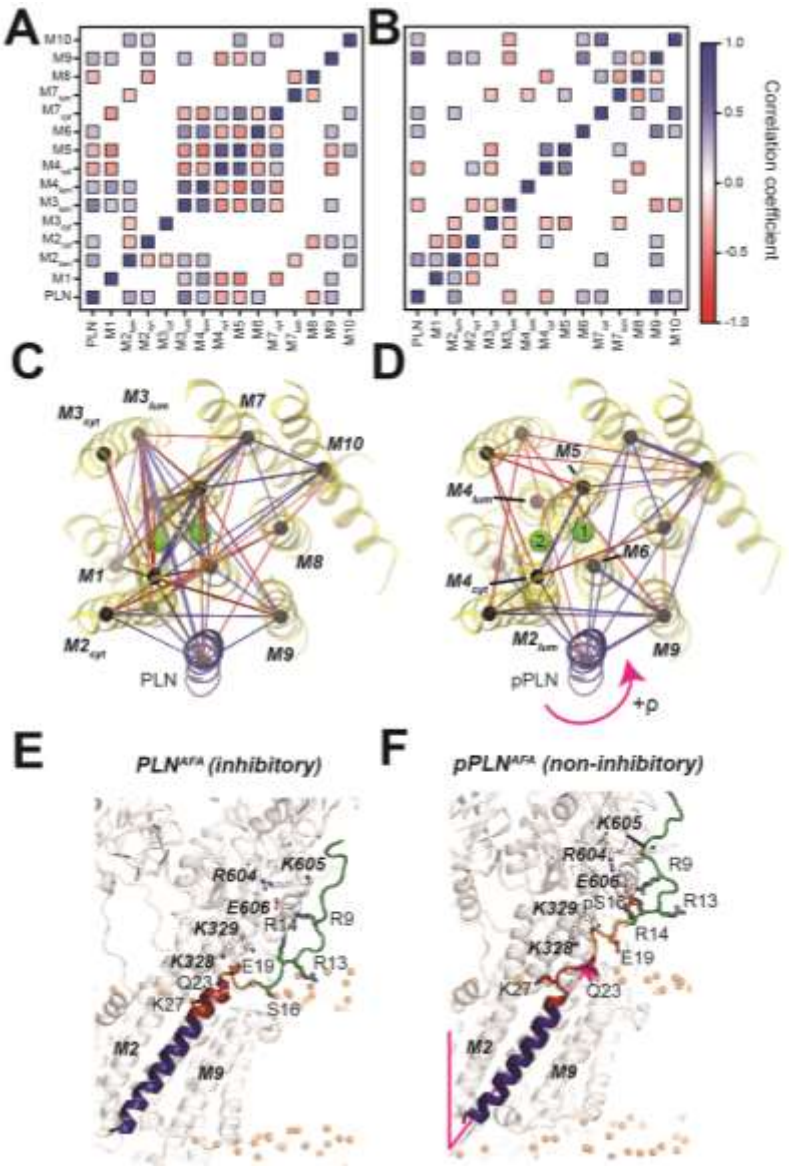

Figure 5.4: PLN topological transitions are allosterically coupled to SERCA's Ca^{2+} binding sites

A. *and* ***B.*** *Correlation maps of motions between the TM topology of PLN^{AFA}* ***A.*** *or pPLN^{AFA}* ***B.*** *with the topology of the 10 TM domains of SERCA.* ***C.*** *and* ***D.*** *Corresponding spider plots showing the density of correlations are displayed below. Green spheres mark positions of the calcium-binding sites.* ***E.*** *and* ***F.*** *Snapshots of the SERCA/PLN^{AFA}* ***E.*** *and SERCA/pPLN^{AFA}* ***F.*** *complexes highlighting the transient interactions with the cytoplasmic region and loosened interactions with the TM region of SERCA.*

we observe a dense network of correlated motions between PLN's TM region and the binding groove (TM2, TM6, and TM9), as well as a dense cluster of correlations involving TM3, TM4, TM5, TM6, and TM7. This allosteric coupling influences the Ca^{2+}

binding sites' geometry, possibly reducing SERCA's Ca^{2+} binding affinity. In contrast, the analysis of the trajectories of the SERCA/pPLN^{AFA} complex displays only correlated motions between the TM of pPLN^{AFA} and the most proximal SERCA helices, with only a sparse network of correlations involving TM4, TM5, TM6, and TM8. Phosphorylation of PLN at Ser16 increases the electrostatic interactions with the cytoplasmic domain of SERCA (*R* to *B* state transition, *i.e.*, disorder to order) [184], and simultaneously weakens intramembrane protein-protein interactions to uncouple the dynamic transitions of PLN from SERCA. The latter removes the structural hindrance of PLN's TM domain and augments Ca^{2+} transport (**Fig. 5.4E.**, **F.**).

5.2.5 Effects of Ca^{2+} ion binding to SERCA on PLN's topology

To assess the effects of Ca^{2+}, we performed SLF experiments on SERCA/PLN^{AFA} and SERCA/pPLN^{AFA} complexes in the *E*1 state (**Fig. 5.5A.**, **B.**). The addition of Ca^{2+} to the SERCA/PLN^{AFA} complex did not cause significant changes to the PLN topology (θ= 32.9 ± 1.4° and ρ_{L31} = 199 ± 4°; p = 0.29 and p = 0.0025 compared to the *E*2 complex). However, the reappearance (*i.e.*, sharpening) of several resonances in the spectra (*e.g.*, Phe32, Phe35/Leu42, and Ala36) indicates a rearrangement of the binding interface between the two proteins similar to phosphorylation's effect on the *E*2 complex. A small topological change, however, was observed for the SERCA/pPLN^{AFA} complex, for which Ca^{2+}-binding induced a decrease of both tilt and rotational angles of 1.8 ± 1.3° and 10 ± 7°,

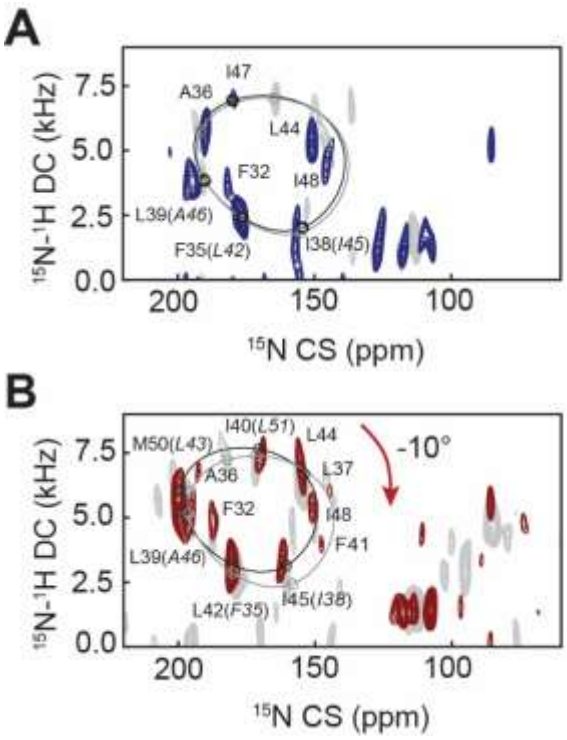

Figure 5.5: Effects of Ca^{2+} binding to SERCA on the topology of PLN and pPLN

A. *and* ***B.*** *2D [^{15}N-^{1}H] SE-SAMPI4 spectrum of PLN^{AFA}* ***A.*** *and $pPLN^{AFA}$* ***B.*** *bound to SERCA in the E1 form reconstituted into aligned lipid bicelles. PISA wheels for an ideal are superimposed. Equivalent spectra of the E2 form complexes are shown in grey.*

respectively (θ= 28.6 ± 0.7° and ρ_{L31} = 187 ± 6°, $p = 1.9 \times 10^{-6}$ and $p = 4.2 \times 10^{-7}$ compared to the *E*2 complex). Due to the lack of X-ray structures, we were unable to carry out dynamic modeling of these complexes. However, these experimental results agree with our *E*2-SERCA models suggesting that a loss of inhibition, either from phosphorylation or Ca^{2+} binding, does not require an extensive structural and topological reconfiguration of PLN's domain II or complete dissociation of the complex.

5.3 Discussion

OS-ssNMR spectroscopy revealed that the TM helix of PLN undergoes a topological equilibrium that is shifted upon phosphorylation, providing direct evidence of the allosteric coupling between the outer membrane regulatory and

TM inhibitory regions. Our dynamic modeling of the SERCA/PLN complexes using experimental restraints shows that the structural disorder of the juxtamembrane domain Ib following Ser16 phosphorylation of PLN signals a slight topological change in the TM region that is sufficient to relieve its inhibitory function. This event involves allosteric effects between the inhibitory interactions of domain II of PLN and SERCA's core helices harboring the Ca^{2+} binding sites. In addition to the localized disruption of PLN domain Ib interactions with SERCA, phosphorylation and Ca^{2+}-binding signal a collective switch of PLN's TM domain from an inhibitory to a non-inhibitory topology. The tilt angle reductions of PLN accompanying the relief of inhibition are easily identifiable from the OS-ssNMR spectra, while rotations are more subtle; nonetheless these topological changes are sufficient to disrupt critical inhibitory interactions.

Recent X-ray investigations and extensive computational studies showed that SERCA undergoes significant rocking motions throughout its enzymatic cycle [426-428]. These conformational transitions analyzed in the absence of PLN are highly concerted and cooperative, *i.e.*, the dynamics of the cytoplasmic headpiece of SERCA correlates with its TM domains [427, 428]. PLN (and other regulins) [370] wedges into the ATPase's binding groove and either correlate with the topological changes of SERCA's TM domains or interfere with its rocking motions leading to uncoupling of ATP hydrolysis and Ca^{2+} transport. PLN experiences significant changes in tilt angle (ranging from 28.6° to 37.5°), depending on both the conformational state of PLN and enzymatic state of SERCA. Therefore, these dynamic and topological transitions provide the mechanism to modulate TM

protein-protein interactions, which can be tuned by posttranslational phosphorylation, O-glycosylation [429], and binding of ancillary proteins [430, 431].

The structural and dynamic changes of PLN, detected by OS-ssNMR, resolves an ongoing controversy about the *subunit* vs. *dissociative* models proposed for SERCA regulation [377, 405, 406, 432, 433]. The latter model speculates that the reversal of the inhibitory function of PLN is due to a complete dissociation of this regulin from the ATPase; but this is not supported by spectroscopic data either *in vitro* or *in cell* [184, 381, 405, 406, 433]. On the other hand, the subunit model agrees well with all spectroscopic measurements, but it does not explain the reversal of inhibition caused by phosphorylation or the elevation of Ca^{2+} concentration. Our ssNMR-driven dynamic calculations clearly shows that topological and structural changes modify the interactions at the interface and are propagated to the distal Ca^{2+} binding sites.

Fig. 5.6 summarizes our proposed mechanistic model for allosteric control of SERCA by PLN's topological changes. We previously showed that PLN's cytoplasmic domain undergoes a three-state equilibrium (*T*, *R*, and *B*) in which the *T* and *R* states are inhibitory, while the *B* state is non-inhibitory.[184] Our new data show that, when bound to the *E*2-SERCA state, the TM region of PLN (domains Ib and II) remains locked into the ATPase's binding groove. An increase of Ca^{2+} concentration drives SERCA into the *E*1 state and reconfigures the intramembrane binding interface augmenting Ca^{2+} transport without significant topological changes to PLN. On the other hand, detectable topological changes occur upon

PLN's phosphorylation both at low and high Ca^{2+} concentrations, shifting the equilibrium toward the non-inhibitory *B* state of PLN [434] and transmitting changes across the SERCA/PLN interface that increase Ca^{2+} transport. In this framework, it is possible to explain how single-site disease mutations or deletion in domains Ia and Ib may lead to perturbations of the protein-protein electrostatic network of interactions, resulting in dysfunctional Ca^{2+} transport [423, 435, 436].

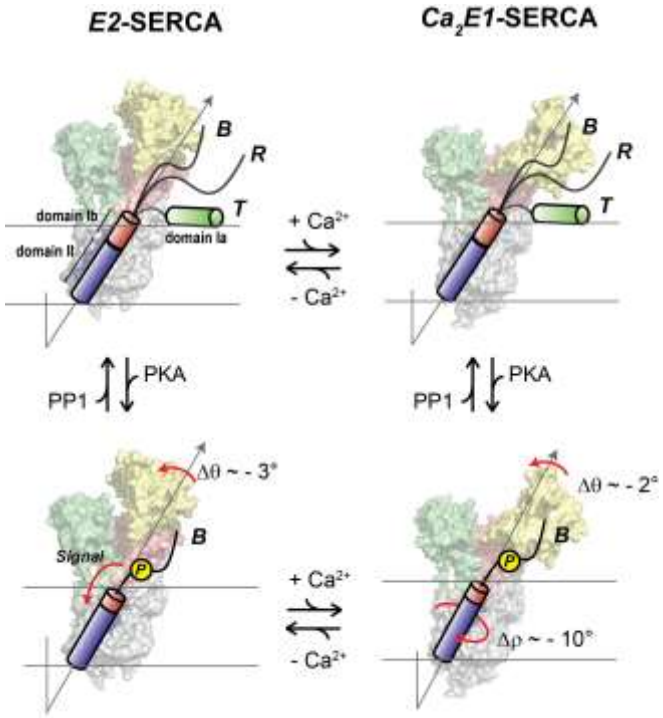

Figure 5.6: Regulatory model of SERCA by PLN's phosphorylation and Ca^{2+}

PLN's cytoplasmic domain exists in equilibrium between three distinct populations in the presence of SERCA. The increase of Ca^{2+} ions causes significant shifts SERCA's conformation toward the E1 state, while the topology of PLN is only slightly affected (top equilibrium). Phosphorylation of PLN at Ser16 signals more extensive topological changes with a reconfiguration of SERCA/PLN TM interactions both at low and high Ca^{2+} concentrations (bottom equilibrium), augmenting Ca^{2+} transport. Note that the T and R populations are not represented for clarity.

In conclusion, the structural dynamics and topological allostery identified for PLN may explain how bitopic miniproteins, despite their simple architecture, can fulfill diverse regulatory roles and how posttranslational modification at cytoplasmic sites may constitute switches for signal transduction across cellular membranes operated by single or multiple transmembrane domains [437]. Several mini-

membrane proteins regulate membrane-embedded enzymes or receptors [369]. In the heart, phospholemman [438-440], a member of the FXYD family, regulates the Na^+/K^+-ATPase interacting via its transmembrane domain, with its regulatory interactions modulated by protein kinases A and C. Several regulins have also been recently found to control SERCA's isoforms in other tissues [370] and share similar topologies to PLN. They all bind at distal locations from the active sites (*e.g.*, ATP or ion channels) of enzymes, revealing possible hotspots for allosteric control by small molecules. Therefore, the characterization of the topological allosteric control of SERCA by PLN represents a first step in understanding how and why evolution has preserved these small polypeptides as a means to regulate the function of ATPases [439, 441] or other membrane transporters [442].

5.4 Acknowledgments

This work was supported by the National Institute of Health grants R01 GM064742 and R01 HL144100 to G.V. and R01HL139065 and R37AG026160 to D.D.T. and R.L.C. D.W; and European Research Council (CoG - BioDisOrder - 819644) funding to A.D.S. was supported by an American Heart Association Postdoctoral Fellowship (19POST34420009).

5.5 Methods

5.5.1 Expression, purification, and phosphorylation of PLN^{AFA}

Uniformly ^{15}N-labelled PLN^{AFA} was expressed as a soluble fusion with maltose binding protein (MBP) as reported previously [443], with minor modifications. Freshly transformed *E. coli* Codon Plus (Invitrogen) cells were used to inoculate overnight LB cultures, which were subsequently centrifuged and resuspended into M9 minimal media ($^{15}NH_4Cl$ as the sole nitrogen source) at an OD_{600} of ~0.7. Cultures were grown at 30°C to OD_{600} 1.0 then induced with 1 mM IPTG over 20 h to a final OD_{600} of 5. Cells (~6 g/L of M9) were stored at -20 °C. Selectively ^{15}N-labelled PLN was expressed from M9 media (free of NH_4Cl) with 125 mg/L of the respective ^{15}N-amino acid, 300 mg/L of non-scrambling and 450 mg/L scrambling-prone ^{14}N-amino acids [444]. Reverse-labeled PLN was expressed in M9 minimal media ($^{15}NH_4Cl$) with 1 g/L of the respective ^{14}N-labeled amino acid. Induction times for selective and reverse labeling growths were reduced to 3 to 4 h to reduce scrambling.

For purification, cells were homogenized (Sorvall Omni Mixer) and lysed by sonification in 200 mL lysis buffer (20 mM sodium phosphate, 120 mM NaCl, 2 mM DTT, 1 mM EDTA, 0.1 mg/mL lysozyme, 0.5 % glycerol, 0.5% Tween 20 and protease inhibitors, pH 7.3). The lysate was centrifuged (17,500 rpm, JA25.50 rotor, 4□C, 40 min) and supernatant loaded onto 30 mL bed volume of amylose resin. The resin was washed with buffer (20 mM sodium phosphate, 120 mM NaCl, pH 7.3) and eluted into 100 mL buffer including 50 mM maltose. Elution volumes were concentrated to ~50 mL and dialyzed overnight against 3 L of cleavage buffer

(50 mM Tris-HCl, 2 mM β-mercaptoethanol, pH 7.3). All purification steps were done at 4°C and yielded up to 120 mg of fusion protein from 1 L M9 media.

To phosphorylate PLN^{AFA} at Ser16 ($pPLN^{AFA}$), the MBP fusion was dialyzed into 30 mM Tris-HCl, pH 7.5, followed by addition of 11x reaction buffer to reach 50 mM Tris-HCl, 10 mM $MgCl_2$, 0.05 mM PMSF, 1 mM NaN_3, 1 mM EDTA). The catalytic subunit of protein kinase A (PKA) was added at 1:1000 ratio to fusion protein, with 2 mM DTT, and the reaction started by addition of 2 mM ATP and incubation at 30°C for 3 h with gentle agitation.

MBP-PLN, either phosphorylated or non-phosphorylated, was cleaved with TEV protease and 2 mM DTT for 3 h at 30 °C to liberate insoluble PLN (**Fig. 5.7A.**), which was pelleted by centrifugation and dissolved into 10% SDS and 50 mM DTT at approximately 10 mg/mL then stored at -20 °C. PLN was further purified by HPLC using a Vydac 214TP10154 C4 column heated at 60 °C and eluted using H_2O/0.1% trifluoroacetic acid (TFA) and a linear gradient of isopropanol/0.1% TFA from 10 to 40% over 10 mins then to 80% over 50 min (2 mL/min flow rate). The protein was lyophilized. Complete phosphorylation of $pPLN^{AFA}$ was confirmed by MALDI-MS (**Fig. 5.7B.**). The inhibitory activity of PLN^{AFA} against SERCA, and relieved inhibition of $pPLN^{AFA}$, in the DMPC/POPC (4:1) lipid bilayer composition used for NMR studies, was confirmed by a coupled enzyme assay[317] (**Fig. 5.7C.**).

5.5.2 Preparation of oriented bicelle samples

Long-chain lipids DMPC (37.0 mg), POPC (10.4 mg) and PE-DTPA (0.9 mg; *i.e.*, 79.25:19.75:1.0 molar ratio) were aliquoted together from chloroform stocks (Avanti Polar Lipids), dried to a film with N_2 and residual solvent removed under high vacuum. The film was resuspended into 1 mL ddH_2O, freeze-thawed three times between liquid N_2 and a 40 °C water bath then lyophilized. DHPC (7.7 mg; 1:4 molar ratio, or q = 4, to long chain lipids) was prepared separately from a chloroform stock, dried and lyophilized from ddH_2O.

For bicelles containing only PLN, DHPC was dissolved into 250 μL sample buffer (20 mM HEPES, 100 mM KCl, 1 mM NaN_3, 2.5% glycerol, pH 7.0), then used to solubilize PLN (2.5 mg) by vortex. Separately, long-chain lipids were suspended into 250 μL of buffer. PLN in DHPC and long-chain lipids, both pre-chilled in ice, were combined and vortexed while allowing the sample to reach room temperature, then placed back on ice. The process was repeated at least three times to fully solubilize long-chain lipids, which produced a completely transparent liquid at cold temperature (micelle phase) and transparent solid gel at room temperature (bicelle phase). The sample was placed on ice, brought to pH 4.2 with KOH, then concentrated to ~180 μL using a 0.5 mL 10 kDa MWCO centrifugal filter (Amicon) at 4°C. The solubility of PLN^{AFA} and $pPLN^{AFA}$ was significantly diminished at higher pH. The sample was doped with 0.8 μL of 1 M $YbCl_3$, corrected back to pH 4.2 with KOH, then loaded into a 5 mm flat bottom sample cell (New Era).

For bicelles containing the SERCA/PLN^{AFA} complexes, SERCA1a was purified from rabbit skeletal muscle as previously described [397]. SERCA was eluted from Reactive Red affinity resin at ~0.5 mg/mL in SERCA, 0.1% $C_{12}E_8$, 1 mM $CaCl_2$, 1 mM $MgCl_2$, 20 mM MOPS, 20% glycerol, 8 mM ADP, 0.25 mM DTT, pH 7.00 and stored at -80°C. Protein concentration was determined by Pierce BCA Assay (Thermo Scientific) and activity confirmed by coupled-enzyme assays [317]. Immediately prior to use, SERCA (4 mg) was thawed at 4°C and combined with long-chain lipids (prepared as above, except with 1.5% molar PE-DTPA chelating lipid) solubilized into 1 mL of 4% $C_{12}E_8$ in sample buffer. The mixture was diluted to ~30 mL with sample buffer and stirred at 4°C for 30 min prior removal of $C_{12}E_8$ by adding 4 g of Bio-Beads SM-2 (Bio-Rad) in stages of 0.5, 0.5, 1 and 2 g with 15 min stirring between additions. Stirring continued overnight at 4°C. Bio-Beads were removed by a 25G syringe and the cloudy suspension of proteoliposomes centrifuged at (12,000 rpm, JA25.50 rotor, 4°C, 30 min). The pellet was resuspended into ~40 mL sample buffer and centrifuged once more to wash out residual elution buffer. The final pellet was resuspended with 250 μL sample buffer and fully solubilized by adding a 250 μL mixture of PLN^{AFA}, or pPLN^{AFA} (0.23 mg), in DHPC (adjusted to pH 7.0) with several cooling/heating cycles under vortex. The bicelle mixture (~1 mL) was centrifuged (13,400 rpm, Eppendorf F45-12-11 rotor, 4 °C, 30 sec) to remove insoluble debris and the supernatant concentrated to ~200 μL using a 0.5 mL 10 kDa MWCO centrifugal filter (Amicon) at 4 °C. The sample was doped with 1.6 μL of 1 M $YbCl_3$ in four stages, correcting pH back to 7.0 with KOH at each addition. Sample buffer included 20 mM HEPES, 100 mM KCl, 1 mM

NaN_3, 5 mM $MgCl_2$, 2 mM DTT, 2.5% glycerol, pH 7.0 with 4 mM EGTA or 5 mM $CaCl_2$ to stabilize *E*2 or *E*1 states, respectively. SDS-PAGE confirmed co-reconstitution of SERCA and PLN in the bicelles (**Fig. 5.7D.**).

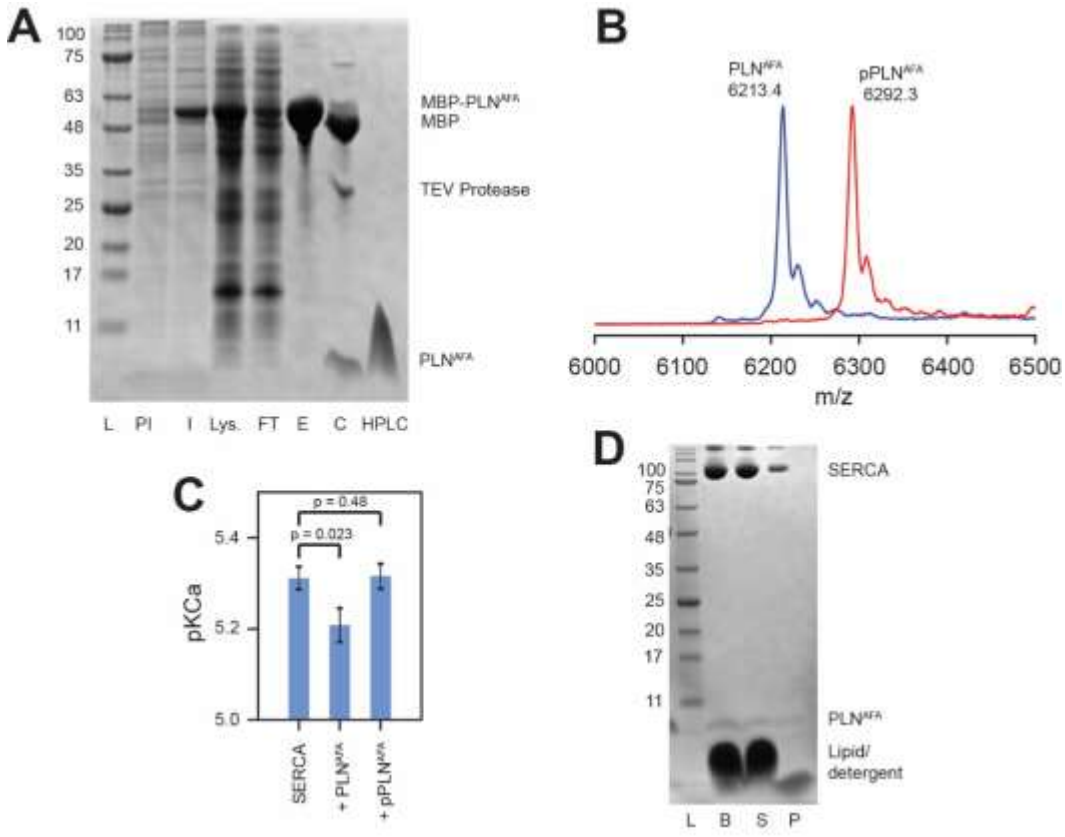

Figure 5.7: Activity and confirmation of PLN^{AFA}

A. *SDS-PAGE gel of the expression and purification of PLN^{AFA} as an MBP-fusion: ladder (L), pre-induced (PI) and induced (I) expression, lysate supernatant (Lys.), purified MBP-PLN^{AFA} eluted from amylose resin (E), MBP-PLN^{AFA} after cleavage with TEV protease (C),and HPLC-purified PLN^{AFA}.* ***B.*** *MALDI-MS spectra of HPLC-purified ^{15}N PLN^{AFA} and pPLN^{AFA}.* ***C.*** *Coupled-enzyme ATPase activity assays of SERCA reconstituted into DMPC/POPC (4:1; lipid-to-protein ratio of 700:1) liposomes with a 5-fold excess of either PLN^{AFA} or pPLN^{AFA}. Assays consisted of 50 mM HEPES, 100 mM KCl, 5 mM $MgCl_2$, 0.2 mM NADH, 0.5 mM PEP, 10 U/mL pyruvate kinase, 10 U/mL lactate dehydrogenase, and 7 µM calcium ionophore A23187 at pH 7.0. ATPase activity was measured by the rate of reduction in NADH absorbance at 340 nm at EGTA-buffered calcium concentrations between 10^{-7} and 10^{-4} M, initiated by addition of 0.5 mM ATP. Activity as a function of calcium concentration was fitted to a Hill function to extract the pKCa values (calcium concentration at half V_{max}) shown. Errors indicate the standard deviation from 3*

replicate measurements. Statistical significance was determined by unpaired t-test (Microsoft Excel 365 Version 2002). ***D.*** *SDS-PAGE gel of SERCA and PLN reconstituted into bicelles for OS-ssNMR: bicelle sample freshly solubilized by DHPC (B), supernatant after centrifugation (S) and pellet formed from a small non-solubilized component (P).*

5.5.3 Synthesis of TFMB and tagging of SERCA

Trifluoromethylbenzyl (TFMB)-methanethiosulfonate (MTS) was synthesized analogously to our method previously reported for synthesizing a ^{13}C-ethylmethanethiosulfonate tag[306, 445] with minor modifications. Briefly, 4-(trifluoromethyl)benzyl bromide (5 mmole), MTS (5 mmole) and KI (0.03 mmole) were dissolved into 2 mL of dimethylformamide and stirred under nitrogen for 16 h at 40°C.

For TFMB tagging, SERCA (8 mg) was thawed and dialyzed into 1 L of *E*1-state sample buffer (as above, but without DTT and including 0.25 mM $C_{12}E_8$) overnight at 4 °C. DMPC (25.2 mg) and POPC (7.1 mg), solubilized in 500 µL of 5% $C_{12}E_8$, was then added to dialyzed SERCA. Detergent was removed by stirring with 1 g Bio-Beads SM-2 for 1.5 h at 4°C and a further 30 min at room temperature. Proteoliposomes were removed from Bio-Beads with a 25G syringe and centrifuged (18,000 rpm, JA25.50 rotor, 4 °C, 40 min). The pellet was suspended into 120 µL buffer and solubilized by adding DHPC (q = 4 for oriented or q = 0.5 for isotropic bicelles). TFMB-MTS (200 mM in DMSO) was added to the bicelles at 5:1 molar excess and incubated at room temperature for 1 hour prior to concentrating to ~250 with a 0.5 mL 10 kDa MWCO centrifugal filter (Amicon) and loading into a Shigemi NMR tube for ^{19}F NMR measurement.

^{19}F NMR spectra of TFMB-tagged SERCA were acquired on a solution state Bruker 600 MHz Avance NEO spectrometer equipped with a TCI HCN cryoprobe. 1D single-pulse experiments were acquired using a 90° pulse of 12 µs and recycle delay of 0.4 s. Spectra in isotropic bicelles were acquired with 1 k scans and 4 k scans for oriented bicelles. Spectra were processed using NMRPipe [321].

5.5.4 Oriented solid-state NMR spectroscopy

All ^{15}N spectra were acquired on a Varian VNMRS spectrometer equipped with a low-*E* static bicelle probe[446] operating at a ^{1}H frequency of 700 MHz. 1D [^{1}H-^{15}N]-cross-polarization (CP)-based experiments used 90° pulse length of 5 µs, or 50 kHz radiofrequency (RF) field, on ^{1}H and ^{15}N channels; contact time of 500 µs with a 10% linear ramp on ^{1}H centered at 50 kHz; and an acquisition time of 10 ms under 50 kHz SPINAL64 heteronuclear proton decoupling [327]. For all experiments, ^{15}N was set to 166.3 ppm and externally referenced to $^{15}NH_4Cl$ at 39.3 ppm [447]; and detected using a spectral width of 100 kHz.

2D separated local field (SLF) spectra were collected using a signal-enhanced (SE)-SAMPI4 experiment [400, 448, 449]. The indirect dipolar dimension utilized complex points and a spectral width of 20.8 kHz. The t_1 evolution period utilized ^{1}H homonuclear decoupling with an RF field of 50 kHz and 48 µs dwell time, and a phase-switched spin-lock pulses on ^{1}H and ^{15}N of 62.5 kHz RF field. The sensitivity enhancement block used a τ delay of 75 µs and three cycles of phase-modulated Lee-Goldberg (PMLG) homonuclear decoupling [450] with an effective RF field of 80 kHz.

3D SE-SAMPI4-PDSD spectra [401] were acquired with 15 increments in both indirect dimensions; spectral widths of 20.8 kHz and 10 kHz in the dipolar coupling and indirect ^{15}N dimensions, respectively; and 3 s mixing time for ^{15}N-^{15}N diffusion [451]. Total acquisition times for PLN^{AFA} samples were typically 1 h for a 1D [^{1}H-^{15}N] CP spectra (1 k scans), 5 h for 1D [^{1}H-^{15}N] WE-CP spectra (5 k scans), 24 h for 1D [^{1}H-^{15}N] rINEPT spectra (25 k scans), 40 h for 2D SE-SAMPI4 spectra (1 k scans) and 2 weeks for 3D SE-SAMPI4-PDSD spectra (2 experiments added with 0.25 k scans each). For the SERCA/PLN^{AFA} complexes, 2D SE-SAMPI4 spectra were acquired over 4.5 days at 25 °C (4 k scans, 15 indirect points) and 1D [^{1}H-^{15}N] CP spectra for 4 h (4 k scans). A recycle delay of 3 sec was used for all experiments. All spectra were processed using NMRPipe [321] and analyzed using NMRFAM-SPARKY [452] and Nmrglue [453].

5.5.5 PISA wheel simulations and fitting

Polar Index Slant Angle (PISA) wheels [145, 403] were fitted to 2D SE-SAMPI4 spectra using the PISA-SPARKY plugin in the NMRFARM-SPARKY package [454]. Default parameters were used to describe ideal helix structure and ^{15}N chemical shift (CS) and ^{15}N-^{1}H dipolar coupling (DC) tensors. The Cα-N-H bond angle was modified from 116° to 119° to best fit PLN^{AFA} spectra. CSs and DCs were fit by exhaustively searching tilts (θ), rotations (ρ_{L31}, *i.e.*, referenced to residue Leu31) and order parameters (*S*) in increments of 0.1°, 1.0° and 0.01, respectively, for the lowest RMSD between calculated and experimental values [454]. The parameter *S*, which factors scaling due to rigid-body helical fluctuations

and imperfect alignment [455], was determined as 0.80 ± 0.05 and 0.81 ± 0.03 for PLN^{AFA} and $pPLN^{AFA}$, respectively, alone in bicelles. Due to the sparsity of peaks assigned for spectra of PLN in complex with SERCA, *S* was fixed to 0.80 to reduce fitting errors. Errors in tilt θ, ρ_{L31} and *S* were determined by repeating fitting 20 times with peak positions randomly adjusted at each iteration. Random adjustments were taken from a Gaussian distribution having a standard deviation equal to average FWHM peak linewidths (3 ppm for CS and 0.8 kHz for DC dimensions). The statistical significance of topological comparisons made throughout the text were determined using an unpaired *t*-test (Microsoft Excel 365 Version 2002) on tilt and azimuthal angles from the 20 repeat fits.

5.5.6 Unrestrained molecular dynamics

A simulation of truncated PLN^{AFA} (M20 to L52; PDB 2LPF [394]) in 97 DMPC and 32 POPC, 150 mM KCl and 4927 waters was constructed using the CHARMM-GUI webserver [4, 5] and CHARMM36 forcefield[456]. Production runs were done using the AMBER18 [457, 458] package at 10 Å cutoff and 8 Å force-based switching and default configuration files provided by the CHARMM-GUI webserver. For example, using the Langevin thermostat [459] (310 K), Monte Carlo barostat [460] (1 bar, semi-isotropic coupling) and the SHAKE algorithm [461] for constraining hydrogens. The simulation was run for 1 μs. The final 900 ns of trajectory was used to predict ^{15}N chemical shifts and ^{15}N-^{1}H dipolar couplings, as previously reported [402].

5.5.7 NMR-restrained refinement of the SERCA/PLN complex

The initial conformation of SERCA in the *E*2 state was obtained from the crystal structure of the SERCA/PLN complex (PDB 4Y3U) [384]. Missing loops in the structure of SERCA were introduced using MODELLER software [462]. The interface between SERCA and PLN^{AFA} (human sequence with a single Asn27Lys substitution) was then refined *in silico* by introducing information from our cross-linking data. Specifically, the transmembrane section of PLN^{AFA} was docked onto SERCA *in vacuo*, maintaining backbone positional restraints on the pump and restraining the dihedral angles of PLN^{AFA} to retain the helical structure. Docking was guided by cross-linking data [382, 407, 408], performing short MD runs (500 ps) with an harmonic upper wall potential applied to restrain the distances between cross-linked residues to below 5 Å. 100 such runs were performed starting from different orientations of PLN^{AFA}, and the resulting docked complexes were clustered according to the backbone RMSD of the proteins. The center of the most highly populated cluster was picked as the most representative structure and used to continue the modelling. The N-terminal segment of PLN^{AFA}, not present in the original structure, was built as a random coil detached from SERCA. Ser16 was modelled both with and without the phosphorylation, generating two different PLN^{AFA}/SERCA complexes.

The structures of the PLN^{AFA}/SERCA and $pPLN^{AFA}$/SERCA complexes were then embedded in DMPC:POPC bilayers, mimicking the experimental conditions, and solvated with TIP3P water [463]. The systems were equilibrated for 1 μs with positional restraints using the coarse-grained model MARTINI[464]

and then re-converted to full-atom descriptions using the Backward approach [465]. The full-atomic systems were equilibrated for 50 ns at 300 K and a further 50 ns after releasing the positional restraints. Eight equally spaced structures were extracted from the final 20 ns of sampling. These eight structures were used as starting points for ssNMR-restrained replica-averaged sampling (RAOR-MD). The final equilibrated box (of dimensions 10.8 x 10.8 x 15.9 nm^3) contains 247 DMPC lipids, 82 POPC molecules, 39,017 TIP3P waters and 23 Na^+ ions to neutralize the system (~174,000 atoms).

^{15}N chemical shift (CS) and ^{15}N-^{1}H dipolar coupling (DC) restraints were incorporated into the sampling using replica-averaged restrained MD, as previously described [201, 385] (code available at https://github.com/maximosanz/modelSSNMR), composed of eight replicas evolving simultaneously. The restraining forces were gradually incorporated during an initial equilibration phase of 20 ns, where the forces were linearly increased to a maximum of 50 J/(mol·ppm^2) and 800 J/(mol·kHz^2) for CSs and DCs, respectively.

In order to enhance the conformational sampling of the disordered domain Ia of PLN^{AFA}, we implemented a sampling based on annealing cycles, whereby the PLN^{AFA} N-terminus periodically binds and detaches from the SERCA surface. The experimental PRE measurements [184] were incorporated in order to drive each binding event. At the beginning of each cycle, the domain Ia of PLN^{AFA} is fully detached from SERCA by introducing a lower-wall harmonic potential that pushes

PLN^{AFA} residues away from SERCA residues present in the cytoplasmic domains of the pump. The lower wall potential pushes PLN^{AFA} residues 0 to 10 at least 50 Å away from Ile140 (SERCA A domain), Thr430 (SERCA N domain) and Cys674 (SERCA P domain). Residues 11 to 14 were pushed at least 25 ˚A away from those residues and in addition the interfacial SERCA residues Thr742, Ala327 and Leu119. The detachment occurs gradually, by linearly increasing the force of the lower-wall potential to a maximum of 5 J/(mol · nm^2) after 500 ps. During this time, the temperature is also linearly increased to 370 K to enhance the conformational sampling space of the disordered domain Ia. CS and DC force constants were linearly decreased to half their value to avoid instabilities during this high-energy phase of the cycle. This detachment step yields a fully detached PLN^{AFA} domain Ia with no SERCA contacts and enough surrounding free space to explore its unbound disordered conformational space. This step is followed by another 500 ps of sampling at 370 K, where the detached PLN^{AFA} domain Ia is allowed to fluctuate. Subsequently, a binding stage follows, whereby the lower-wall potential is linearly removed over 1 ns of sampling. The PRE-derived distance restraints were gradually incorporated over this time as an upper-wall potential at 30 Angstrom with a maximum force of 5 J/(mol·nm^2). During this step the force constants of CS and DC are also restored to their full value, and the temperature is linearly decreased to 300 K. After the binding phase, the PLN^{AFA} N-terminus adopts a SERCA-bound conformation. This step leads onto the sampling phase of the cycle, where the restraint forces and the temperature are kept constant for 2 ns. The structures sampled during these 2 ns are the ones included in the final

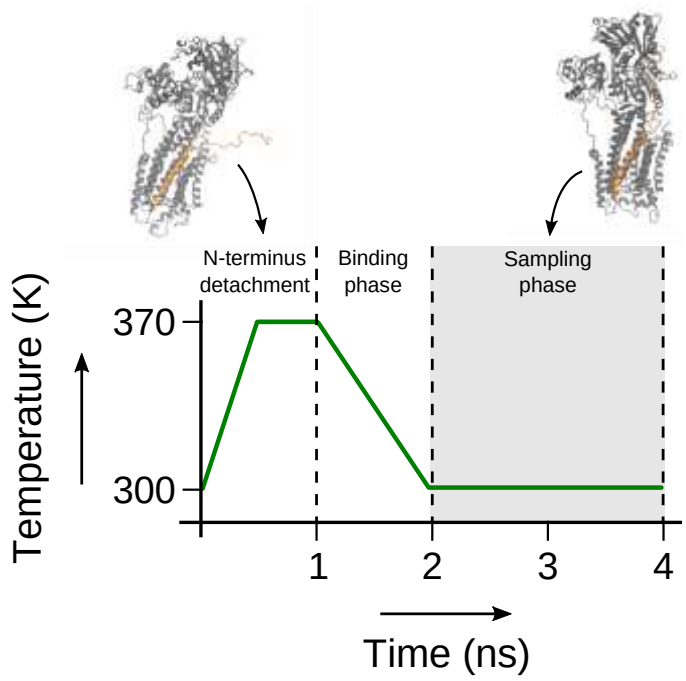

Figure 5.8: Annealing cycle used in the sampling of the SERCA/PLN^{AFA} complex

During the first nanosecond of the simulation, the N-terminus of PLN is detached from SERCA and the temperature is raised to 370 K to randomize its conformation. Then the system is cooled back down to 300 K over 1 ns, during which time the CS, DC and PRE restraints are re-introduced. The complex is sampled for 2 ns, after which the cycle restarts.

conformational ensembles of SERCA/PLN^{AFA}. This annealing cycle sampling approach is illustrated in **Fig. 5.8**.

We performed 25 annealing cycles per replica for both PLN^{AFA} and pPLN^{AFA}, resulting in a total simulation time of 0.8 µs for each ensemble. 10,000 equally separated structures (400 ns) in the sampling part of the cycles were extracted to perform the analyses described in the main text. All samplings were performed using a previously described version of GROMACS [466], modified to include the CS and DC restraints [385]. The CHARMM36 force field [456] was used. Temperature was coupled using the v-rescale algorithm [467] and pressure was coupled at 1 bar using the semi-isotropic Berendsen method[468]. All simulations were carried out under periodic boundary conditions. The integration timestep was set to 2 fs and the LINCS algorithm was used for constraints [469]. Electrostatic interactions were accounted for using the Particle Mesh Ewald method [470]. Ensembles were

analyzed using CPPTraj [471] for principle component analyses (PCA); VMD [472] for contact, hydrogen bond and distance measurements; custom Python scripts for computing helical tilt (θ) and rotation (ρ) angles; and GROMACS energy tool for electrostatic interactions.

5.6 Supplementary Figures

Table 5.1: O-ssNMR assignments

Summarized ^{15}N CS and ^{15}N-^{1}H DC assignments of PLN^{AFA} and pPLN^{AFA} reconstituted alone in bicelles or in complex with SERCA in either E2 (Ca^{2+}-free) or E1 (5 mM Ca^{2+}) states.

Res.	PLN^{AFA}		pSer16-PLN^{AFA}		PLN^{AFA} + SERCA (*E*2)		pSer16-PLN^{AFA} + SERCA (*E*2)		PLN^{AFA} + SERCA (*E*1)		pSer16-PLN^{AFA} + SERCA (*E*1)	
	CS	DC	CS	DC	CS	DC	CS	DC	CS	DC	CS	DC
N27	117.6*	1.19*	118.1	0.90	-	-	-	-	-	-	-	-
N30	117.6*	1.19*	121.5	3.10	-	-	-	-	-	-	-	-
L31	152.8	0.94	155.2	0.74	-	-	164.3	1.26	-	-	-	-
F32	167.7	2.46	177.9	3.38	-	-	187.6	4.07	181.6	3.78	186.6	4.56
N34	125.8	1.36	132.4	2.71	-	-	-	-	-	-	-	-
F35	164.7	1.17	166.2*	1.36*	-	-	179.1	2.86	176.4	2.30	-	-
A36	176.5	4.74	184.3	5.28	186.5	5.72	191.0	6.37	190.4	5.91	192.8	6.76
L37	123.9	4.89	132.2	5.71	136.5	6.66	146.0	6.57	146.1	4.73	151.7	5.87
I38	140.8	1.03	146.5	1.40	156.9	1.86	160.3	2.54	156.4	2.11	164.9	2.14
L39	181.7*	2.31*	185.7*	2.86*	190.3	3.88	194.4	3.99	194.5	3.76	198.5	4.75
I40	155.7	6.19	163.5*	6.88*	164.0	7.04	171.5	6.87	166.7	6.99	169.9	7.25
F41	127.8	3.39	134.6	4.19	-	-	150.0	4.46	-	-	148.4	4.33
L42	160.5	0.91	166.2*	1.36*	175.5	1.74	179.1	2.86	-	-	181.1	2.63
L43	187.5*	4.17*	190.9*	4.46*	192.8	5.77	198.3	5.76	196.5	5.89	-	-
L44	138.0	6.02	145.6	6.19	149.9	6.22	155.5	6.26	156.0	5.19	155.1	6.65
I45	139.2	1.80	144.5	2.64	152.7	2.74	160.3	2.54	-	-	162.1	3.57
A46	181.7*	2.31*	185.7*	2.86*	-	-	191.4	2.84	-	-	-	-
I47	170.5	6.35	175.9	6.65	-	-	181.8	7.23	179.5	6.74	181.9	7.99
I48	132.7	4.88	139.2	5.39	145.5	5.16	154.3	6.03	151.2	4.94	-	-
V49	157.1	1.75	160.1	2.26	-	-	-	-	-	-	-	-
M50	187.5*	4.17*	190.9*	4.46*	-	-	198.0	5.14	202.5	4.80	199.9	5.94
L51	158.3	7.06	163.5*	6.88*	-	-	-	-	-	-	-	-

* These peaks are overlapped.

Table 5.2: Pairwise inter- and intramolecular hydrogen bond summary for PLN^{AFA}/SERCA REMD PCA clusters

Parentheses report the average number hydrogen bonds to a charged residue of SERCA or PLN (bold font) observed over all frames assigned to the respective clusters. Hydrogen bonds were defined with a donor -acceptor distance less than 3 Å and a donor-H-acceptor angle less than 20°.

Cluster	Average hydrogen bonds per frame						
	E2	K3	R9	R13	R14	S16	E19
1	R556 (0.10) K365 (0.08) R638 (0.02)	-	E606 (0.05)	**E19 (0.01)**	E606 (0.01)	-	K328 (0.08) **R13 (0.01)**
2	R556 (0.10) K365 (0.04)	E644 (0.02) D557 (0.02)	D557 (0.01)	E606 (0.05) **E19 (0.04)**	E606 (0.02)	-	K328 (0.38) **R13 (0.04)**
3	K365 (0.11) R556 (0.09) R638 (0.01)	D399 (0.01)	E606 (0.02)	-	E606 (0.06)	-	K328 (0.15) R325 (0.04) K329 (0.03)
4	K397 (0.14) K365 (0.11) R638 (0.05)	D399 (0.24)	D557 (0.10) E392 (0.02) E606 (0.01)	D616 (0.06)	-	-	-

Table 5.3: Pairwise inter- and intramolecular hydrogen bond summary for pSer16-PLN^{AFA}/SERCA REMD PCA clusters

Hydrogen bonds were measured according to Table 2.

Cluster	Average hydrogen bonds per frame						
	E2	K3	R9	R13	R14	S16	E19
1	K365 (0.04) R556 (0.03) K397 (0.02)	D557 (0.01)	D557 (0.14) **S16 (0.13)** E392 (0.02)	**S16 (0.59)** E606 (0.02)	**S16 (0.72)** E606 (0.04)	**R14 (0.72)** **R13 (0.59)** R604 (0.54) K605 (0.30) **R9 (0.13)**	K328 (0.07) K329 (0.02)
2	K365 (0.07) R556 (0.03)	D399 (0.01)	**S16 (0.55)** E606 (0.03)	**S16 (0.21)** **E19 (0.06)** E748 (0.02) D616 (0.01)	**S16 (0.81)** E606 (0.06)	**R14 (0.81)** **R9 (0.55)** **R13 (0.21)** K605 (0.16) R604 (0.01)	K328 (0.10) **R13 (0.06)**
3	K365 (0.12) **K3 (0.02)** R556 (0.01)	D399 (0.03) D557 (0.02) **E2 (0.02)**	**S16 (0.82)** E606 (0.05)	**S16 (0.07)** E748 (0.03)	**S16 (0.85)** E606 (0.01)	**R14 (0.85)** **R9 (0.82)** **R13 (0.07)** K605 (0.05)	-
4	R556 (0.09) K365 (0.06) R560 (0.02) R638 (0.01) K400 (0.01)	D557 (0.03)	**S16 (0.28)** E606 (0.05)	**S16 (0.57)** **E19 (0.03)**	**S16 (0.86)** E606 (0.02)	**R14 (0.86)** **R13 (0.57)** **R9 (0.28)**	K328 (0.09) **R13 (0.03)** K329 (0.02)
5	R556 (0.07) K365 (0.05) **K3 (0.03)** K400 (0.03) R638 (0.03)	399 (0.04) **E2 (0.03)**	**S16 (0.16)** E606 (0.05)	**S16 (0.77)**	**S16 (0.77)**	**R13 (0.77)** **R14 (0.77)** **R9 (0.16)** K328 (0.03) K329 (0.02)	R325 (0.19) K328 (0.13) K464 (0.02)
6	R556 (0.06) **K3 (0.04)**	**E2 (0.04)**	D399 (0.08) E394 (0.05)	**S16 (0.84)**	**S16 (1.14)** E392 (0.25)	**R14 (1.14)** R460 (0.89) **R13 (0.84)** K464 (0.11) K329 (0.07) R325 (0.01)	K328 (0.21) K329 (0.04) K464 (0.03)
7	K365 (0.14)	-	**E19 (0.03)** D616 (0.02)	E748 (0.54) E606 (0.03)	**S16 (0.36)**	R325 (1.18) **R14 (0.36)** K329 (0.31) K328 (0.25)	**R9 (0.03)**
8	K397 (0.10) K400 (0.03)	E644 (0.01)	E394 (0.23)	**S16 (0.67)**	**S16 (1.22)** E392 (0.65)	**R14 (1.22)** **R13 (0.67)** R460 (1.35)	R325 (0.45) K328 (0.44) K329 (0.37)

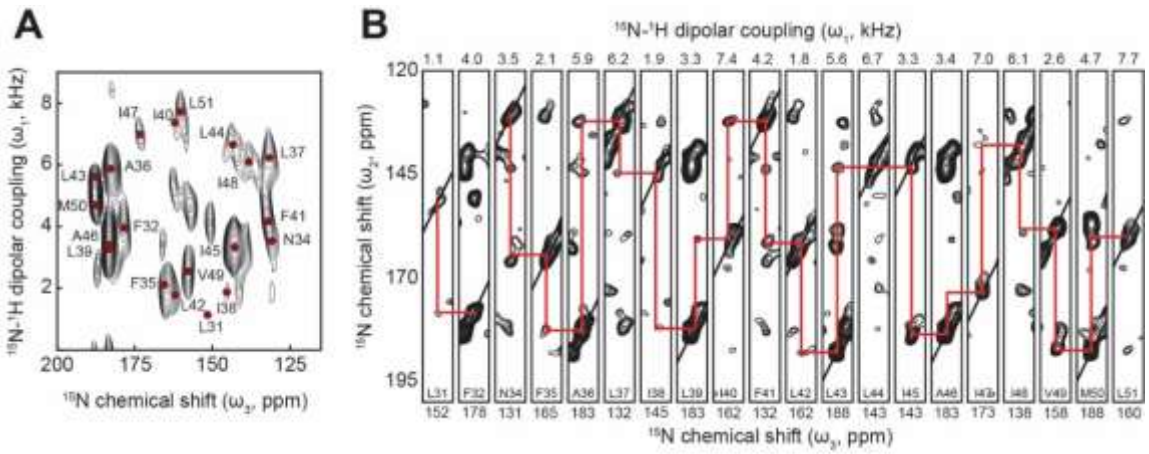

Figure 5.9: Figure 1 supplement 1. Assignment by 3D OS-ssNMR

A. *2D projection and* ***B.*** *strip plot of [^{15}N-^{15}N-^{1}H] 3D SE-SAMPI4-PDSD spectrum of pPLN^{AFA} in bicelles showing sequential ^{15}N-^{15}N correlations.*

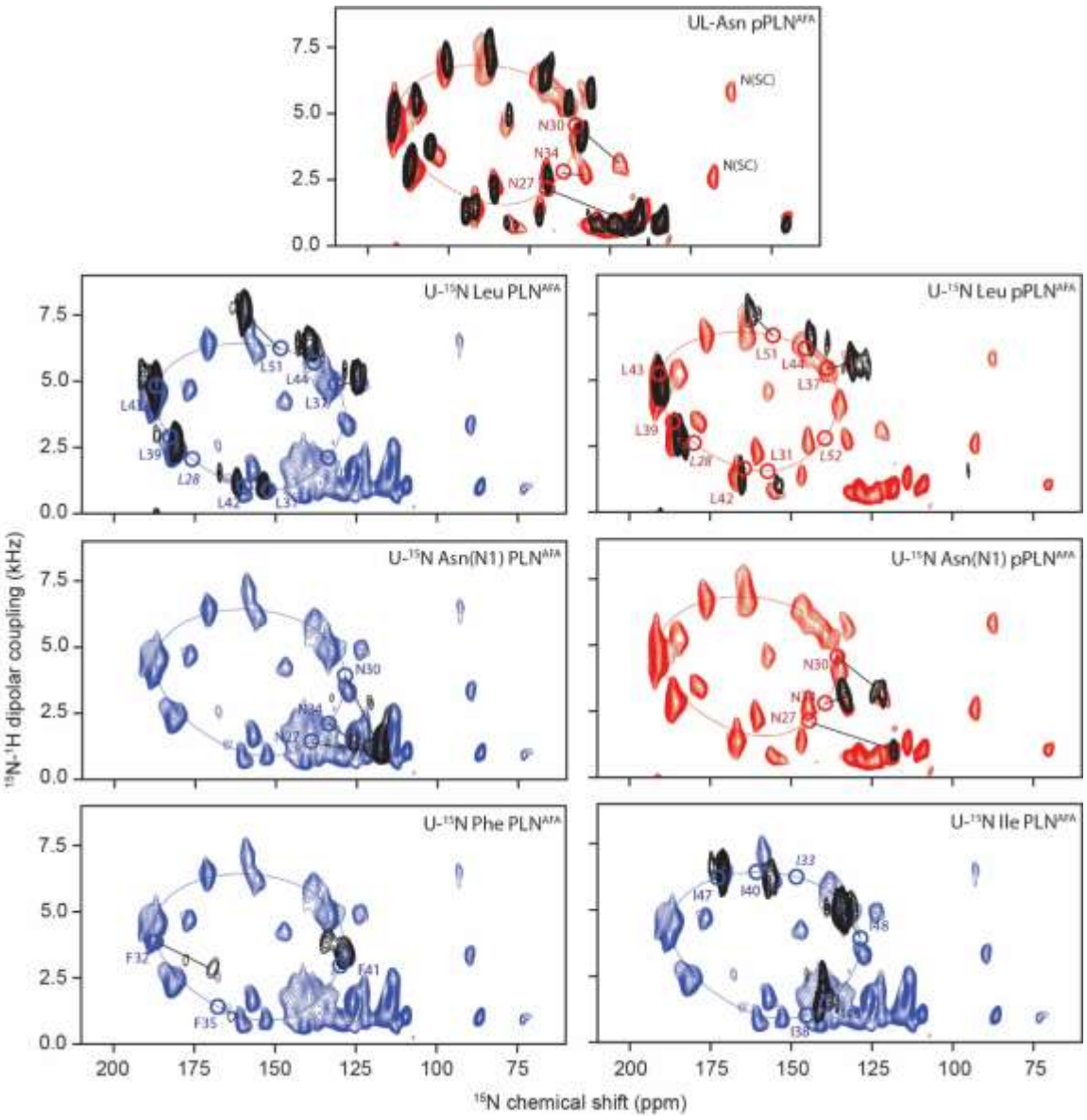

Figure 5.10: Figure 1 supplement 2. Assignment of OS-ssNMR spectra by selective labeling and un-labeling experiments

2D [^{15}N-^{1}H] SE-SAMPI4 spectra of uniformly ^{15}N-labelled PLN^{AFA} (blue) and pPLN^{AFA} (red) overlaid with recombinant residue-specific uniformly labeled (U) and uniformly unlabeled (UL) preparations (black). Circles indicate theoretical peak positions based on PISA fitting and labels in italics are residues missing from experimental spectra.

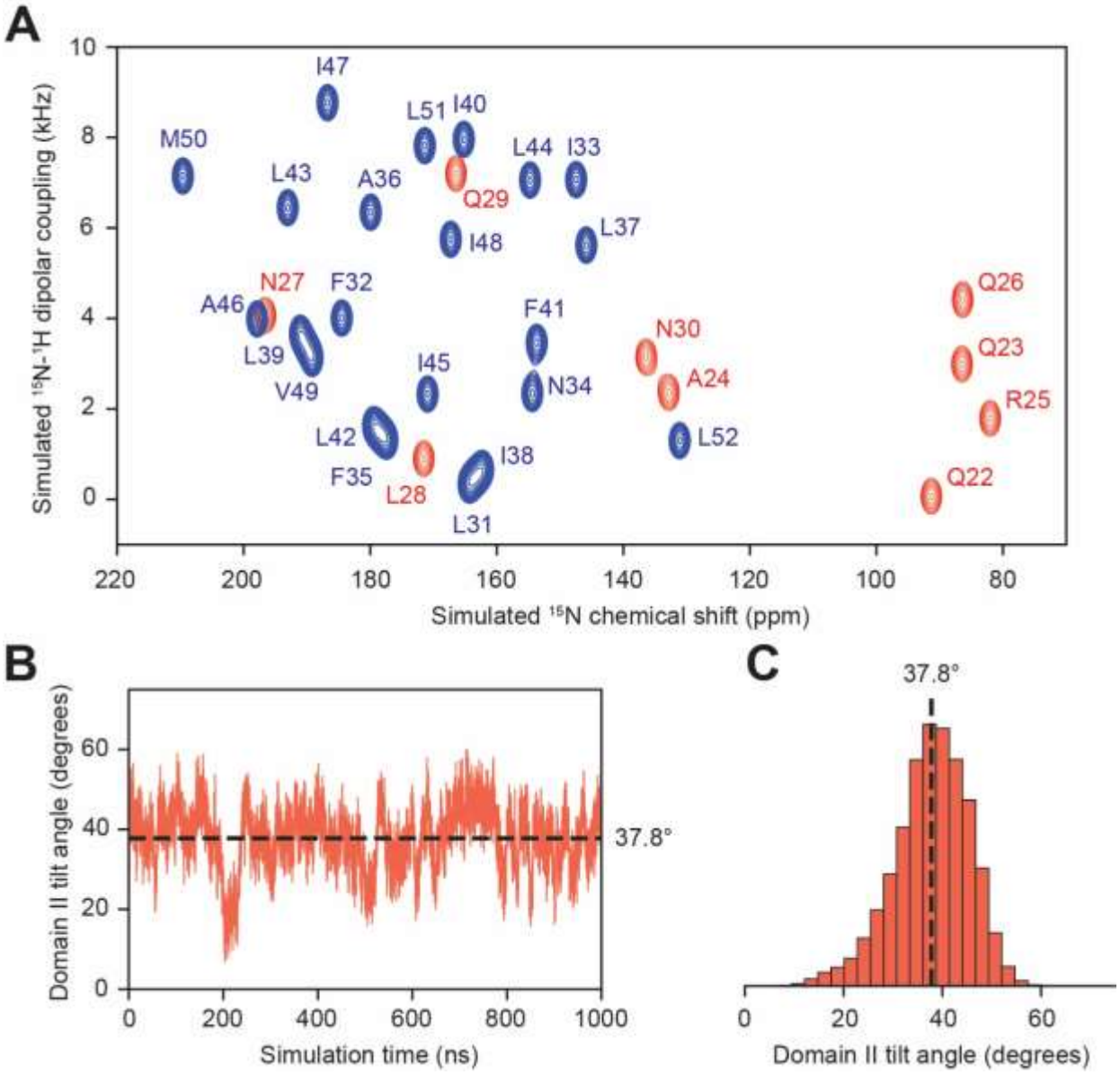

Figure 5.11: Figure 1 supplement 3. Prediction of assignments from unrestrained MD simulation of truncated PLN

A. *Back-calculated SLF spectrum of domain Ib (red) and II (blue) residues computed as previously described[402].* ***B.*** *PLN^{AFA} domain II tilt angle throughout the simulation and* ***C.*** *the corresponding histogram.*

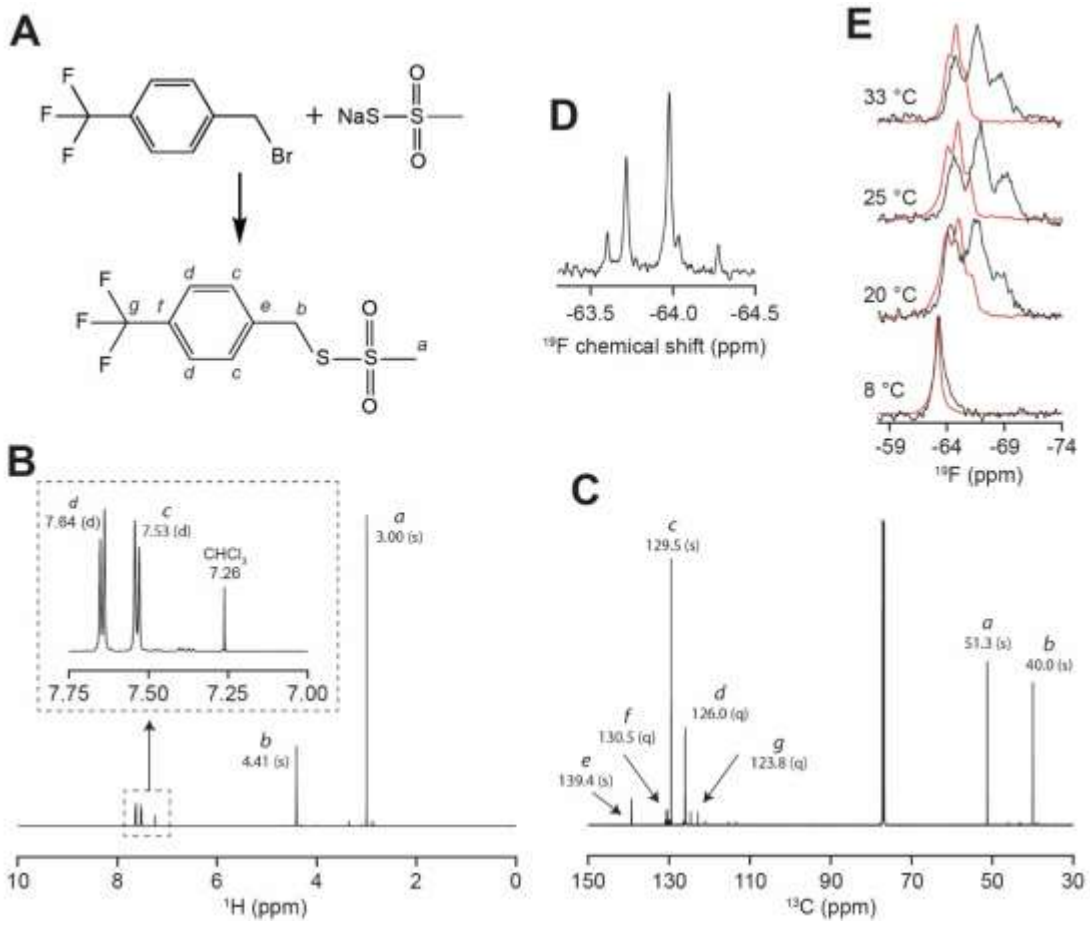

Figure 5.12: Figure 1 supplement 4. Synthesis and oriented NMR of the trifluoromethylbenzyl (TFMB)-methanethiosulfonate (MTS) tag

A. *Synthesis of the TFMB-MTS tag. Lettering specifies carbon and proton assignments in* ***B.*** *^{1}H and* ***C.*** *^{13}C NMR spectra of the tag in $CDCl_3$. Values in parenthesis specify peak multiplicity (s = singlet, d = doublet, q = quartet).* ***D.*** *^{19}F NMR of TFMB-tagged SERCA in isotropic bicelles.* ***E.*** *^{19}F NMR of TFMB-tagged SERCA (black) and free tag (red) in oriented bicelles. Spectra show that the tag partitions into bicelles, but with considerably reduced dipolar coupling compared to SERCA-reacted tag. This confirms that the dipolar triplet is not from unreacted tag.*

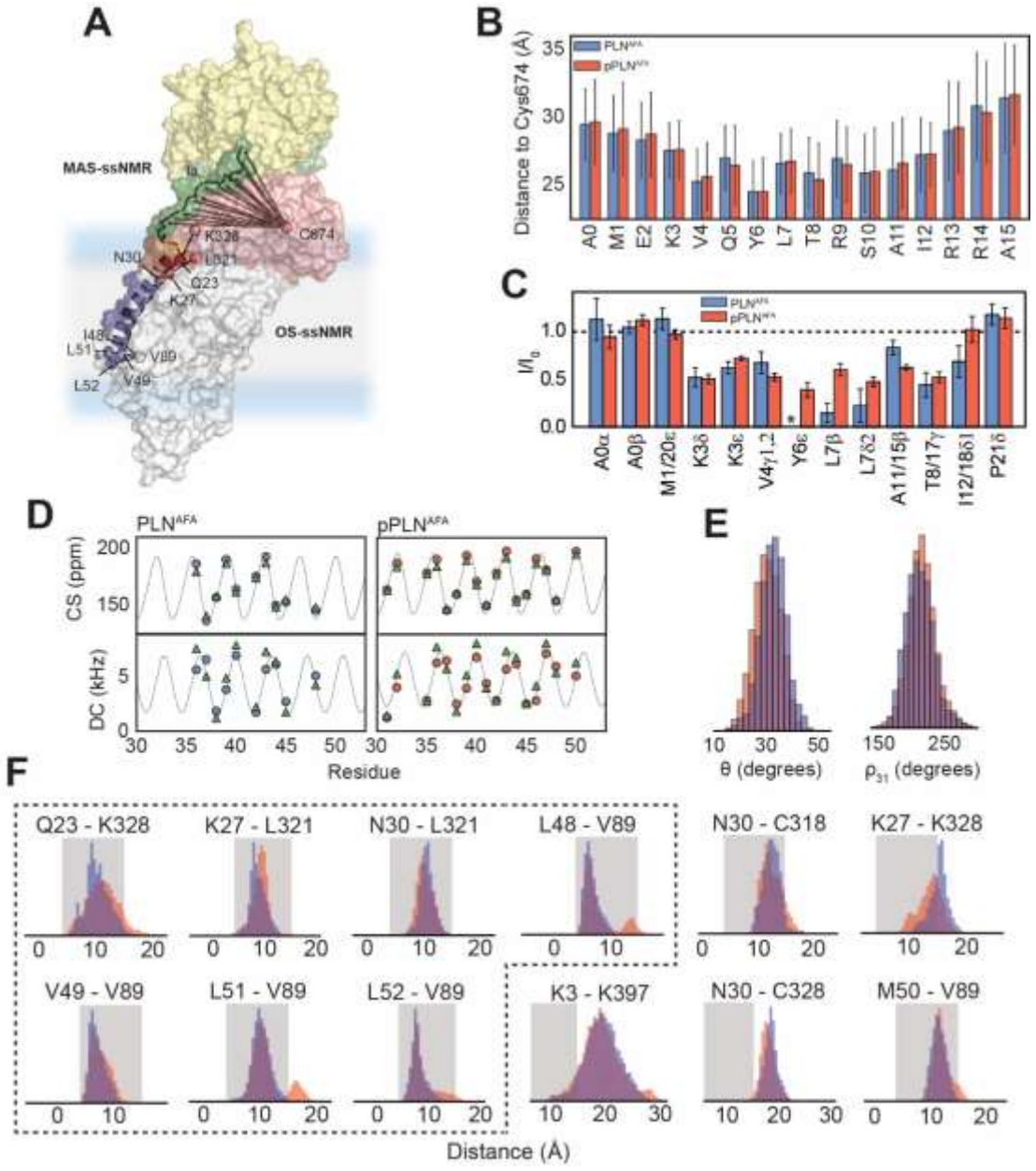

Figure 5.13: Figure 2 supplement 1. Restraints for RAOR-MD structural refinement

A. *Schematic of crosslinking restraints[382, 407, 408] used for docking and paramagnetic relaxation enhancements previously observed by MAS-ssNMR[184] between methanethiosulfonate spin-labeled (MTSSL) Cys674 and cytoplasmic residues of PLN^{AFA} and pPLN^{AFA}.* ***B.*** *Averaged pairwise distances between cytoplasmic residues (at Cβ) of PLN^{AFA} and Cys674-Sγ show qualitative agreement with* ***C.*** *prior [^{13}C-^{13}C] DARR MAS-ssNMR PRE measurements (reproduced with permission from [184]).* ***D.*** *Wave plots comparing ^{15}N chemical shifts and ^{15}N-^{1}H dipolar couplings obtained experimentally (blue or red circles)*

and back-calculated (green triangles) from RAOR-MD ensembles. Wave lines were taken from a PISA fits to the experimental points. ***E.*** *Tilt (θ) and azimuthal angles (ρ_{31}) back-calculated from RAOR-MD ensembles of PLN^{AFA} (blue) and $pPLN^{AFA}$ (red).* ***F.*** *REMD pairwise distance distributions (Cβ-Cβ) of crosslinking residues[382, 407, 408, 417, 418]. Histograms encased in dotted lines relate to residue-pairs restrained during initial docking. Shaded regions show a typical 4 to 15 Å crosslinking range. The residue pair Asn30 – Cys318, outside of this range, has optimal crosslinking with longer (15 Å) reagents[417].*

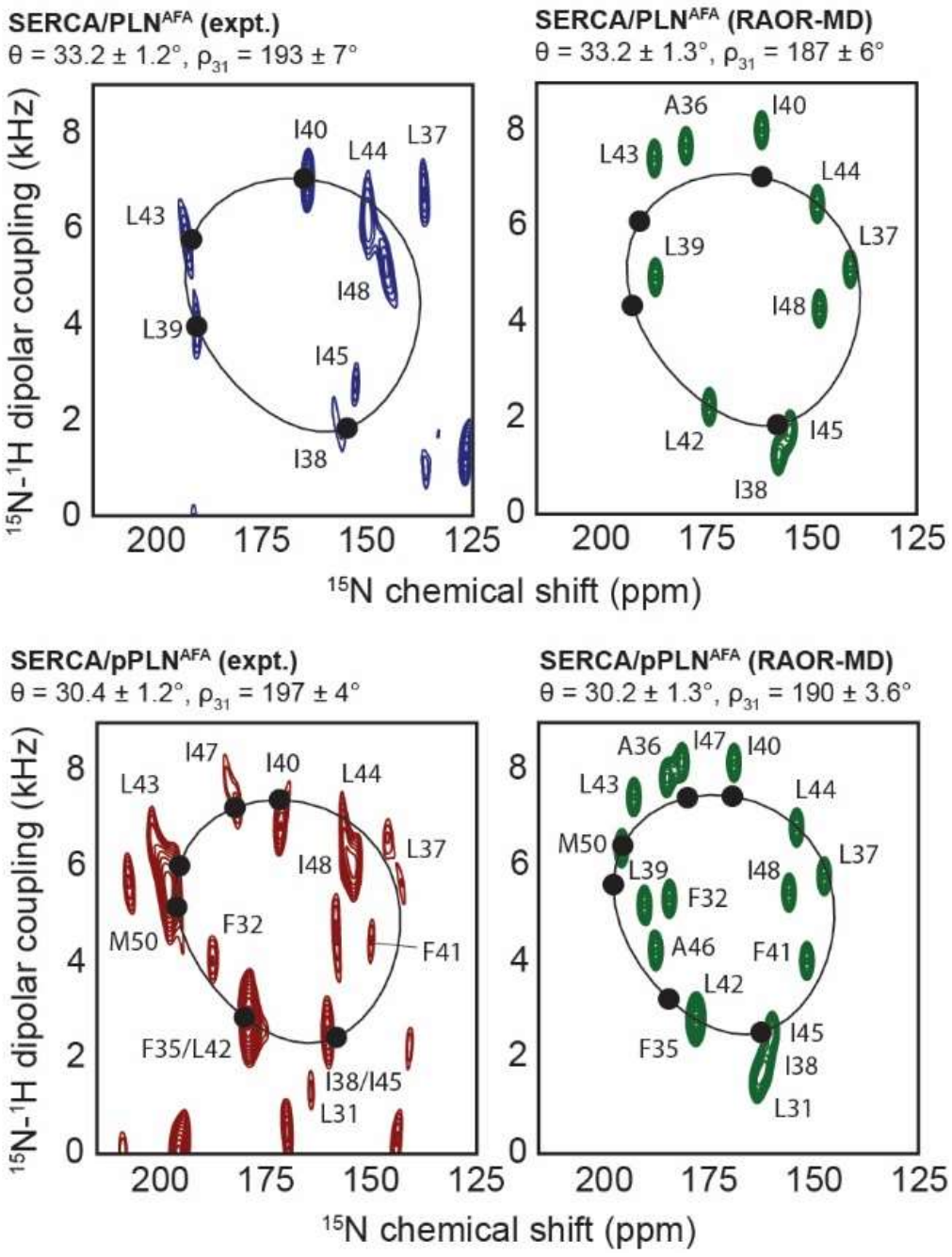

Figure 5.14: Figure 2 supplement 2. Experimental and back-calculated RAOR-MD SLF spectra of the PLN^{AFA}/SERCA complex

Comparison of cross-peak positions observed from experimental SE-SAMPI4 spectra (blue or red) and back-calculated from RAOR-MD ensembles (green; assumes 200 Hz and 800 Hz linewidths in CSA and DC dimensions, respectively). PISA fits were performed using only residues (solid circles) conforming closely to

ideal helicity in experimental spectra (i.e. Ile38, Leu39, Ile40 and Leu43 for PLN^{AFA}; and Phe35, Ile38, Ile40, Leu43, Ile47 and Met50 for pPLN^{AFA}).

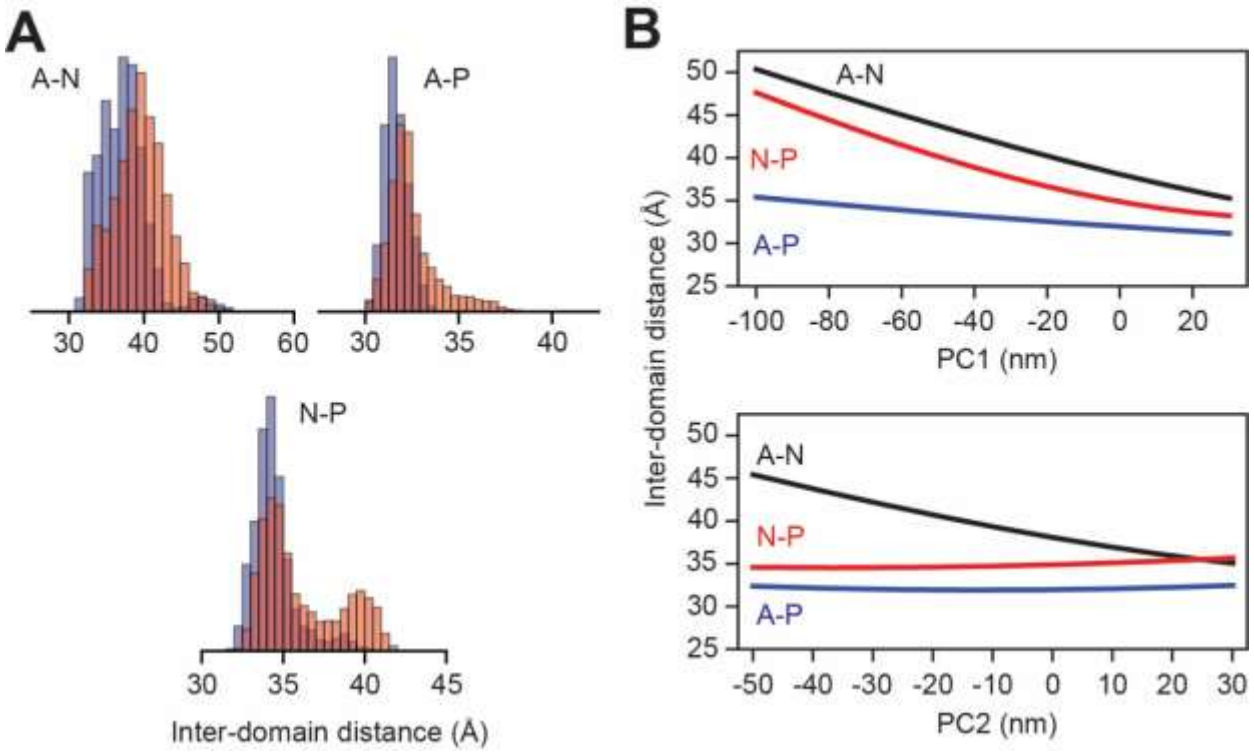

Figure 5.15: Figure 2 supplement 3. Headpiece dynamics of SERCA in RAOR-MD

A. *Inter-domain headpiece distances distributions from RAOR-MD of SERCA in complex with PLN^{AFA} (blue) and pPLN^{AFA} (red).* ***B.*** *SERCA headpiece distance as a function of the two largest components (PC1 and PC2) from Principal Component Analysis (PCA) of the two RAOR-MD calculations. Center of masses were determined using only backbone atoms with the Actuator (A) domain defined by residues 1 to 48 and 111 to 253, the Nucleotide-binding (N) domain by 360 to 602 and the Phosphorylation (P) domain by 314 to 359 and 602 to 757.*

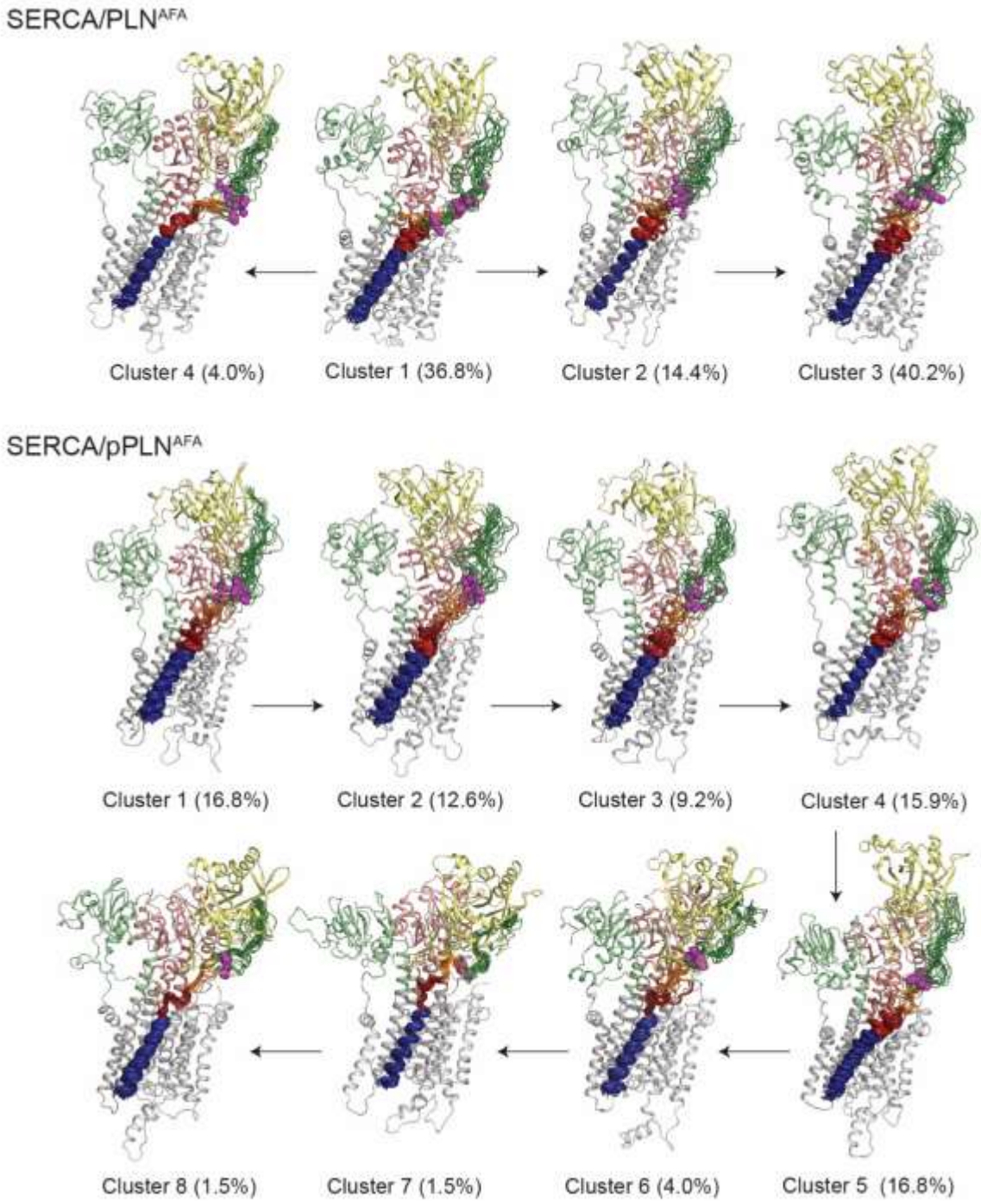

Figure 5.16: Figure 2 supplement 6. RAOR-MD clustering. Top 20 most representative structures of each cluster extracted from PCA

Structures were aligned by TM residues of SERCA. Only the most representative structure of SERCA is shown for each cluster.

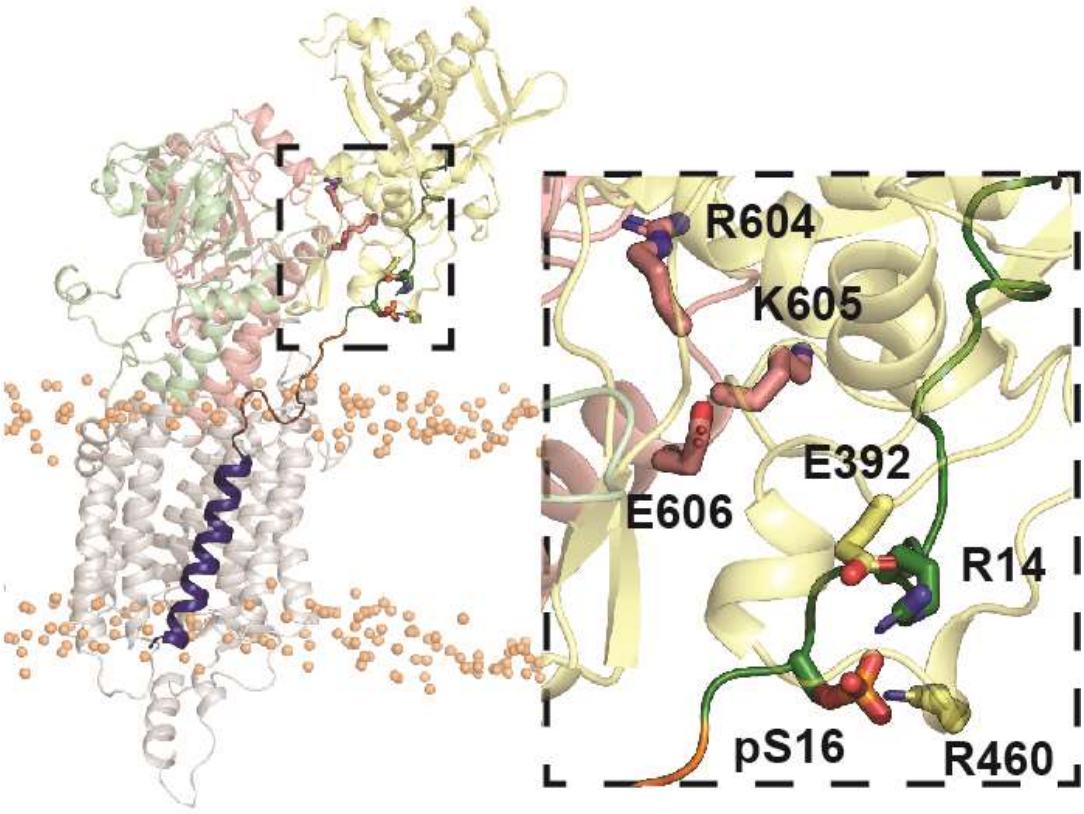

Figure 5.17: Figure 2 supplement 7

Example open state snapshot (PCA cluster 6) of SERCA stabilized by electrostatic interactions between pSer16 and the N domain.

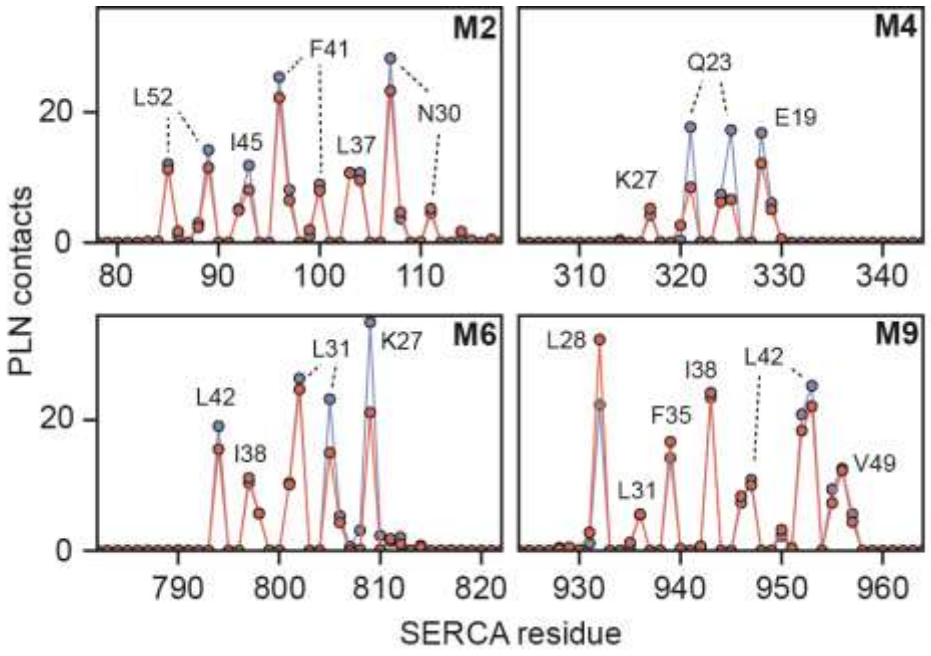

Figure 5.18: Figure 3 supplement 1. Summary of inhibitory TM contacts

Per-residue ensemble-averaged intermolecular contacts for TM helices of SERCA. A single contact by SERCA to PLN^{AFA} (blue) or pPLN^{AFA} (red) in RAOR-MD simulations is defined when any SERCA atom comes within 3.5 Å of any PLN atom for any given frame. PLN^{AFA} residues responsible for the most contacts are designated at local maxima.

Chapter 6 Intrinsically disordered HAX-1 regulates Ca^{2+} cycling by interacting with lipid membranes and the phospholamban cytoplasmic region

*Erik K. Larsen,[1] Daniel K. Weber,[2] Songlin Wang,[2] Tata Gopinath ,[2] Daniel J. Blackwell,[3] Michael P. Dalton,[3] Seth L. Robia,[3] Jiali Gao,[1,4] and Gianluigi Veglia[1,2]**

[1]*Department of Chemistry, University of Minnesota, Minneapolis, MN 55455.*

[2]*Department of Biochemistry, Molecular Biology, and Biophysics, University of Minnesota, Minneapolis, MN 55455*

[3]*Department of Physiology, Loyola University, Maywood, IL 60153, USA*

[4]*School of Chemical Biology and Technology, Beijing University Graduate School, Shenzhen 518055, China*

Reprinted with permission from BBA [100].

* To whom correspondence should be addressed:

Gianluigi Veglia,
Department of Biochemistry, Molecular Biology & Biophysics,
University of Minnesota, 6-155 Jackson Hall, MN 55455.
Telephone: (612) 625-0758.
Fax: (612) 625-2163.
E-mail: vegli001@umn.edu.

Keywords: HAX-1, Intrinsically Disordered Proteins, Phospholamban, Protein-membrane Interactions, NMR spectroscopy.

Abstract

Hematopoietic-substrate-1 associated protein X-1 (HAX-1) is a 279 amino acid protein expressed ubiquitously. In cardiac muscle, HAX-1 was found to modulate the sarcoendoplasmic reticulum calcium ATPase (SERCA) by shifting its apparent Ca^{2+} affinity (pCa). It has been hypothesized that HAX-1 binds phospholamban (PLN), enhancing its inhibitory function on SERCA. HAX-1 effects are reversed by cAMP-dependent protein kinase A that phosphorylates PLN at Ser16. To date, the molecular mechanisms for HAX-1 regulation of the SERCA/PLN complex are still unknown. Using enzymatic, *in cell* assays, circular dichroism, and NMR spectroscopy, we found that in the absence of a binding partner HAX-1 is essentially disordered and adopts a partial secondary structure upon interaction with lipid membranes. Also, HAX-1 interacts with the cytoplasmic region of monomeric and pentameric PLN as detected by NMR and *in cell* FRET assays, respectively. We propose that the regulation of the SERCA/PLN complex by HAX-1 is mediated by its interactions with lipid membranes, adding another layer of control in Ca^{2+} homeostatic balance in the heart muscle.

6.1 Introduction

The hematopoietic-substrate-1 associated protein X-1 (HAX-1) is a multifunctional, intracellular protein discovered over two decades ago [97]. HAX-1 is localized in many different tissues and regulates a variety of cellular targets [112]. Specifically, HAX-1 is involved in critical cellular functions such as apoptosis [104, 473-479], cell migration [107, 480, 481], endocytosis [482, 483], and mRNA transport [484-486], and interacts with several targets including viral proteins [102, 487-490], ABC-transporters [491] and potassium channels [479]. Aberrant expression of HAX-1 has been linked to severe diseases, including cancer, psoriasis, and congenital neutropenia (Kostmann syndrome) in addition to neurodevelopmental delays and abnormalities [112].

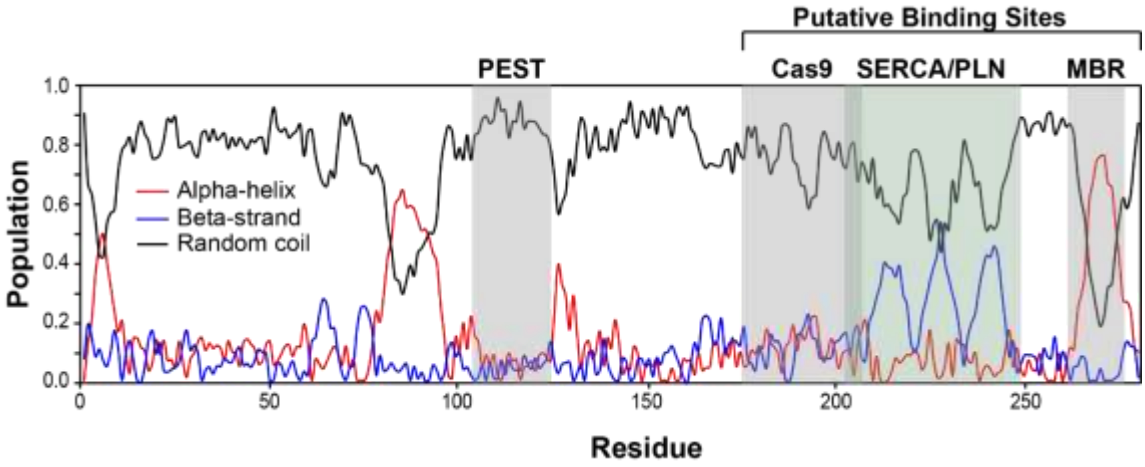

Figure 6.1: HAX-1 secondary structure predictions based on s2D software [492]

Random coil regions are indicated in black, alpha-helix in red, and beta-strand in blue. The domains that are responsible for the function of HAX-1 are indicated on top of the graph: PEST sequence [97], caspase 9 binding site [475], SERCA/PLN binding region [88, 90], and the putative membrane binding region [97].

Recently, HAX-1 was identified as a novel regulator of Ca^{2+} transport in cardiomyocytes [91]. Specifically, it was found that HAX-1 interacts with phospholamban (PLN), an endogenous inhibitor of the sarcoplasmic reticulum (SR) Ca^{2+}-ATPase (SERCA) [88]. SERCA is part of the primary signaling mechanism in cardiomyocytes as it transports Ca^{2+} from the cytosol into the SR, thereby controlling contraction and relaxation of the heart muscle [493]. Abnormalities in Ca^{2+} cycling are linked to the progression of heart failure [494-497]. The activity of SERCA is mainly regulated by PLN, a bitopic membrane protein embedded in the SR [498]. In the healthy heart, unphosphorylated PLN inhibits SERCA by reducing its apparent affinity for Ca^{2+}, while phosphorylated PLN at Ser16 reverses its inhibitory function in response to β-adrenergic stimulation [498]. A growing body of evidence indicates that HAX-1 binds SERCA either independently or in conjunction with PLN [88, 89, 91, 95, 96, 499]. To date, however, there are only sparse structural studies on HAX-1, limiting our understanding of the molecular mechanism and biological function of this protein. Theoretical predictions suggest that HAX-1 is likely to be intrinsically disordered (**Fig. 6.1**), which may explain its functional versatility. Cellular localization studies suggest that HAX-1 may also interact with lipid membranes as it chiefly interacts with proteins localized around organelle membranes [112].

To gain insights on the function and molecular mechanism of action, we studied full-length HAX-1 in its free form and in the presence of lipid membranes and PLN using a combination of enzymatic and in cell assays, circular dichroism (CD), and NMR spectroscopy. When free in solution, HAX-1 is mostly disordered and

becomes partially ordered upon interacting with lipid membranes. Our solid-state NMR (ssNMR) experiments show that HAX-1 interacts with the cytoplasmic region of monomeric PLN when both proteins are functionally reconstituted in lipid bilayers, while FRET measurements show that HAX-1 is able to interact with the cytoplasmic region of PLN in its pentameric assembly. Our results support the theoretical predictions on HAX-1 structure and demonstrate its ability to interact with both lipid membranes and PLN, confirming its role in Ca^{2+} cycling.

6.2 Methods

6.2.1 Expression and purification of HAX-1

The full length HAX-1 (279 amino acid) was expressed either as a fusion protein with a histidine-tagged maltose binding protein (MBP) for soluble, native expression or with a histidine-tagged SUMO protein for inclusion body expression in the BL21(DE3) strain of *E. coli*. For the SUMO fusion construct, we used a pE-SUMO vector, containing a T7 promoter and ampicillin resistance. The *E. coli* bacteria were grown at 24°C and overnight protein expression was induced at OD_{600} of 0.8. The cells were resuspended in 20 mM PBS, 150 mM NaCl, 0.5% Triton X-100, 0.5% glycerol, 75ug/mL EDTA, 1mM DTT, at pH 7.3 and lysed with a French press in the presence of lysozyme. After lysis, the suspension was centrifugated at 17,500 rpm for 45 minutes at 4°C with His-SUMO-HAX-1 contained in insoluble inclusion bodies in the resulting pellet. Inclusion bodies were homogenized using a Potter-Elvehjem pestle and glass tube in 20 mM PBS, 2% Triton X-100, at pH 7.3 with three plunging cycles. A final washing step without

detergent was used to remove excess Triton X-100. The inclusion bodies were solubilized in 10 mM Tris, 100 mM NaH_2PO_4, and 6M urea at pH 8.0. His-SUMO-HAX-1 was purified by affinity chromatography using Ni-NTA under denaturing conditions. Washing and elution steps were carried out at pH 7.0 and 4.0, respectively. His-SUMO-HAX-1 was then diluted in 20 mM PBS and 0.01% $C_{12}E_8$ 15 times and cleaved with ULP1 at 4°C. The cleavage reaction was dialyzed into ddH_2O allowing HAX-1 to precipitate from solution, which was collected by centrifugation at 17,500 RPM for 45 minutes. The resulting pellet was solubilized in 10% SDS prior to purification using reversed-phase high performance liquid chromatography (RP-HPLC). The purified protein was then lyophilized overnight to a white powder. The correct sequence was confirmed by trypsin digestion, where 6 fragments matched the expected result. One of the fragments showed a clear propensity for oxidation at M175 (**Figs. 6.11A.** and **B.**), a post-translational modification that may emphasize the anti-apoptotic role of HAX-1 in oxidative stress [94, 96, 478]. Note that to avoid oxidation of the purified HAX-1 we carried out the studies in the presence of DTT. The correct molecular weight was further confirmed by LC-MS, which detected peaks at M_w of 31620.52, 32018.52, and 33416.52 Da for unlabeled, ^{15}N-labeled, and ^{15}N-^{13}C-labeled HAX-1 (**Fig. 6.11C.**). Approximately 99% labelling efficiency was estimated for the subsequent NMR experiments.

We also expressed HAX-1 fused to Maltose Binding Protein (MBP) (**Fig. 6.12**). For the MBP fusion the *E. coli* bacteria were grown at 24°C with overnight protein expression induced with 0.5 mM IPTG once the OD_{600} reached 0.8. Harvested cell

pellets were stored at -20°C. For purification of HAX-1, cells were resuspended in 20 mM PBS, 150 mM NaCl, 0.5% Tween-20, 0.5% glycerol, 75ug/mL EDTA, 1mM DTT, at pH 7.3 and lysed by French press in the presence of lysozyme. After lysis, the suspension was centrifugated at 17,500 rpm for 45 minutes at 4°C and the fusion protein was purified from the resulting supernatant by affinity chromatography with amylose resin (New England Biolab). The fusion protein was then purified by size exclusion chromatography (SEC) with a superdex 75 column (GE Healthcare). Subsequent cleavage by the tobacco etch virus (TEV) protease required 0.1% Tween 20 for optimal cleavage. Finally, the cleavage mixture was purified by affinity once more with TALON resin (Takara) resulting in purified protein in detergent.

6.2.2 Expression and purification of PLN^{AFA}

Expression and purification of a monomeric, functional variant of PLN^{WT}, PLN^{AFA}, where the cysteines in the transmembrane domain (C36, C41, and C46) were mutated into alanine, phenylalanine, and alanine, respectively [396], was carried out as previously described [500]. Briefly, unlabeled and uniformly (U) ^{15}N-labeled PLN^{AFA} and U-^{13}C,^{15}N-labeled PLN^{AFA} was expressed in *E. coli* bacteria with maltose binding protein (MBP) as a fusion protein at 30°C with overnight induction. Cells were resuspended in 20 mM PBS, 150 mM NaCl, pH 7.3 and lysed by French press. Purification was performed using affinity chromatography using amylose resin. The purified fusion construct was cleaved using TEV protease over ~3 hours at 34°C. After the cleavage reaction was complete, MBP and uncleaved

fusion protein were removed from PLN^{AFA} via centrifugation at 17,500 RPM for 45 minutes at 4°C. The resulting pellet was resuspended in 10% SDS and further purified by reversed phase HPLC using water as buffer A and isopropanol as buffer B with 0.1% trifluoroacidic acid (TFA) in both buffers. The purified protein was then lyophilized overnight to a white powder.

6.2.3 SERCA isolation and purification

SERCA1a isoform was used in this study due to the robust purification protocol and high yields. Note SERCA1a has been proven structurally and functionally similar to SERCA2a (heart isoform) [501]. SERCA1a was extracted from rabbit skeletal muscle as previously described [502]. Briefly, skeletal muscle from a New Zealand white rabbit was harvested and the crude sarcoplasmic reticulum (SR) was extracted through centrifugation. The crude SR was stored in sucrose buffer at -80°C (20 mM MOPS, 0.3 M sucrose, 1 mM NaN_3, pH 7.0). The stored SR was then thawed, where SERCA was solubilized into octaethylene glycol monododecyl ether ($C_{12}E_8$) from the SR membrane and purified by affinity to Reactive Red resin. Purified SERCA was stored in aliquots of elution buffer (0.8 mg/mL SERCA, 0.1% $C_{12}E_8$, 1 mM $CaCl_2$, 1 mM $MgCl_2$, 20 mM MOPS, 20% glycerol, 8 mM ADP, pH 7.00) at -80°C. This preparation was thawed again at 4°C and activity was measured by ATP/NADH coupled enzymatic assays prior to use [503].

6.2.4 ATP/NADH coupled enzymatic assays

1,2-dioleoyl-sn-glycero-3-phosphocholine (DOPC) and 1,2-dioleoyl-sn-glycero-3-phosphoethanolamine (DOPE) were purchased from Avanti Polar Lipids. SERCA, HAX-1 and PLN^{AFA} were co-reconstituted in DOPC and DOPE (4:1) reaching a final ratio of 700:1:m:n lipid:SERCA:HAX-1:PLN^{AFA}, where m and n are the selected molar ratios for each experiment. Lipids solubilized in chloroform were dried under a flux of N_2 for ~30 minutes and kept under vacuum overnight. The lipid film was then resuspended into 0.1 mM KCl, 5 mM $MgCl_2$, 10% (v/v) glycerol, and $C_{12}E_8$ at 4:1 (w/w) $C_{12}E_8$:lipid ratio. 40 ng of SERCA1a was added to the mixture. The lipid/detergent mixed micelles were stirred in the presence of 30 mg of biobeads ® at 4°C for 3 hours to remove residual detergent and form proteoliposomes. The reconstituted system was then resuspended in sucrose buffer. SERCA activity was measured in a final buffer containing 5 mM ATP, Ca^{2+} (pCa 5.0 – 8.0 for a 12 point curve),100 mM MOPS, 200 mM KCl, 10 mM $MgCl_2$, 0.4 mM NADH, 1.0 mM phosphoenolpyruvic acid (PEP), 20 IU/mL lactate dehydrogenase (LDH), 20 IU/mL pyruvate kinase (PK), and 0.00712 mg/mL Ca^{2+} ionophore A23187(A.G. Scientific). Assays were incubated at 25°C prior to carrying out the ATP/NADH coupled enzyme assay as a function of [Ca^{2+}]. The rate of reaction (ATP hydrolysis) was monitored by the decrease of absorption at 340 nm due to the consumption of NADH by LDH to convert pyruvate into lactate. The data were recorded using a Spectramax 384 Plus and fit with the Hill equation:

$$V = V_{max} \frac{[Ca^{2+}]^n}{[Ca^{2+}]^n + {K_{Ca}}^n}$$

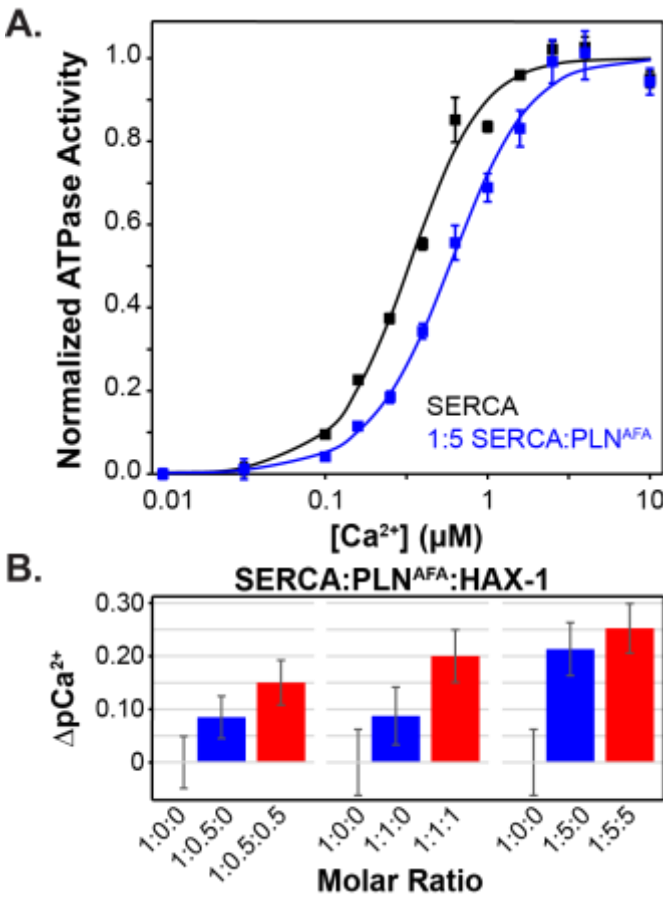

Figure 6.2: HAX-1 augments the inhibitory potency of PLN

A. *Normalized SERCA activity assays in the presence of PLN^{AFA} (blue) at a molar ratio of 1:5.* ***B.*** *Bar graph representing the changes in the apparent calcium affinity of SERCA alone and in complex with PLN^{AFA} and HAX-1 at varying molar ratios.*

Where V_{max} is maximum activity, n is the Hill coefficient, and $[Ca^{2+}]$ at half V_{max} is K_{Ca}.

6.2.5 Circular dichroism (CD)

For the CD measurements with different lipid mixtures, a solution of 5 μM HAX-1 was prepared in 20 mM KH_2PO_4 and 50 mM KCl (**Fig. 6.15**). For DMPC titrations, a 5 μM HAX-1 solution was prepared in 10 mM KH_2PO_4 at pH 7.0 (**Fig. 6.3**). Lipid suspensions in $CHCl_3$ were first dried under N_2 flux overnight and then resuspended in acqueous buffer. The lipid suspension was extruded 10 times through a 0.1 μm polycarbonate filter prior to addition of HAX-1 to reach a total lipid-to-protein ratio of 200:1 (**Fig. 6.15**). For the DMPC titrations, a series of lipid-to-protein ratios were used ranging from 10:1 to 800:1 (**Fig. 6.3**). The CD spectra were recorded on a Jasco J-815 spectropolarimeter.

The acquisition parameters are reported in **Table 3.1**. The partition constant, K_x, determining by fitting the decrease of the dichroic profile at 208 nm to a Langmuir isotherm using:

$$I_{208} = \frac{a}{1 + \left(\frac{K_x}{[DMPC]}\right) + c}$$

Where c is the y-intercept and the sum of a and c is the asymptote at saturation [504-506].

6.2.6 Solution-state NMR experiments

Lyophilized HAX-1 was prepared by solubilizing into 20 µL of 100 mM KOH. 140 µL of ddH_2O was then added and the sample placed on ice. 20 µL of 10x buffer (200 mM KH_2PO_4, 500 mM KCl, pH 6.20) was added to the solution and vortexed. The pH was adjusted to 7.0 and 19 µL of D_2O and 5 µM DSS were added for a total of 200 µL. Isotropic bicelles were prepared by mixing DMPC and DHPC at a *q*-ratio of 0.33 (5% w/v lipids) and added at a lipid-to-protein ratio of 240:1 in lyophilized powder form. The [^{1}H,^{15}N]-HSQC experiments were carried out on a 900 MHz Bruker spectrometer and performed at 45 °C, with the exception of urea denaturation at 25 °C, using 8 scans per 256 increments. The [^{1}H,^{15}N]-TRACT experiments were carried out on a 600 MHz spectrometer and performed at 25 °C. To record the relaxation of the α and β spins, 31 delay times were used. These data were fit with an exponential decay curve (SciPy library, Python 3.7) and τ_c was calculated using 160 ppm for the difference of the two principal components of the ^{15}N chemical shift tensor ($\Delta\delta_N$), 1.02 Å for the ^{15}N-^{1}H inter-nuclear distance

(r_{HN}) and 17° for the angle between the unique axis of ^{15}N chemical shift tensor and the ^{15}N-^{1}H bond (Θ) [507]. Spectra were processed with NMRPipe [508] and analyzed with NMRFAM-SPARKY [509].

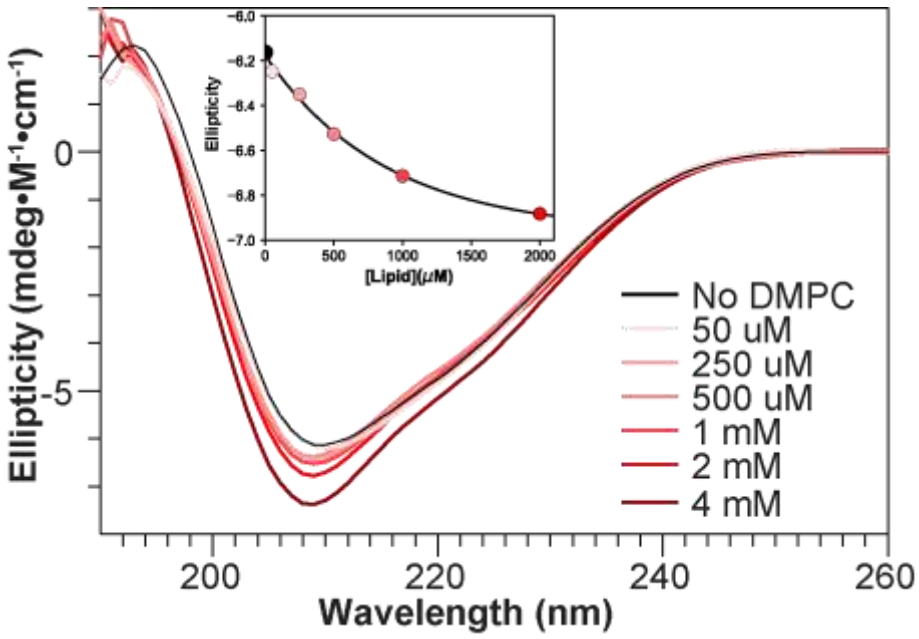

Figure 6.3: Circular dichroism spectroscopy shows that HAX-1 undergoes structural rearrangement upon interacting with DMPC LUVs

Wavelength circular dichroism spectra for increasing lipid:protein ratios of DMPC:HAX-1. The inset shows the exponential decay toward saturation in the increasingly negative values at the alpha-helical indicative 208 nm.

6.2.7 Solid-state NMR experiments

Magic angle spinning (MAS) solid-state NMR experiments were carried out on a 700 MHz spectrometer using a 3.2 mm probe. All spectra were acquired at 25°C with a MAS rate set to 10 or 12 kHz using a 15 ms acquisition time and 3 s recycle delay. For these samples, 0.5 mg U-^{15}N,^{13}C PLN^{AFA} was reconstituted in 12 mg

d_{54}-DMPC vesicles (L/P ratio = 100) in 20 mM HEPES, 100 mM KCl, 1 mM NaN_3, 1 mM Mg^{2+}, 2.5% glycerol, pH 7.0. For the HAX-1 sample, 2.5 mg HAX-1 was added to the same sample. The one-dimensional cross polarization (CP) and rINEPT spectra were acquired using 2,048 and 10,000 scans for HAX-1 and PLN/HAX-1 samples, respectively. 2D [^{13}C,^{13}C]-DARR experiments were recorded using 256 scans and 120 increments in the indirect dimension with a mixing time of 100 ms.

6.2.8 Fluorescence resonance energy transfer (FRET) experiments

Wild-type PLN labeled with N-terminal Cerulean (Cer) and yellow fluorescent protein (YFP) fusion tags were co-expressed in AAV-293 cells with or without HAX-1. Cells were cotransfected at a plasmid molar ratio of 1:5:10 for Cer-PLN:YFP-PLN:HAX-1. Intrapentameric FRET was quantified as previously described [73]. Briefly, FRET was quantified from acceptor sensitization by fluorescence microscopy. Images were acquired with a 40 × 0.75 NA objective, with 50 ms exposure time for Cer, YFP, and FRET (Cer excitation, YFP emission) imaging conditions. FRET efficiency was calculated according to $E = G/(G + 3.2 \times F_{Cer})$, where $G = F_{FRET} - a \times F_{YFP} - d \times F_{Cer}$ [510], where F_{FRET}, F_{YFP}, and F_{Cer} are the matching fluorescence intensity from FRET, YFP, and Cer images, respectively, and G represents FRET intensity corrected for the bleed-through of the channels. The parameters a and d are bleed-through constants calculated as $a = F_{FRET}/F_{Cer}$ for a control sample transfected with only YFP-SERCA and $d = F_{FRET}/F_{YFP}$ for a

control sample transfected with only Cer-SERCA. These values were determined to be *G*=4.74 *a*=0.075 and *b*=0.88. The FRET efficiency of each cell was compared to that cell's fluorescence intensity in the YFP channel, which was taken as an index of protein expression level. The relationship between FRET and protein expression ([PLN]) yielded estimates of PLN oligomerization affinity and the intrinsic FRET efficiency of the PLN pentamer. The data were analyzed with a hyperbolic fit of the form $FRET=(FRET_{max})([PLN])/(K_D+[PLN])$, where $FRET_{max}$ is the intrinsic FRET of the PLN pentamer ($FRET_{max}$) and K_D is the apparent dissociation constant of oligomerization [511].

6.3 Results

6.3.1 HAX-1 acts synergistically with PLN to increase SERCA inhibition

HAX-1 was expressed using His-MBP and His-SUMO fusion constructs and purified under native and denatured conditions, respectively. A similar strategy was used to assess the intrinsically disordered nature of α-synuclein [512]. Under both experimental conditions, HAX-1 was fully functional as established by SERCA inhibition assays. Expression as a His-SUMO fusion protein was preferred as the purification from inclusion bodies eliminated the need of Tween 20 and resulted in higher purity, avoiding degradation. **Fig. 6.10** shows the characterization of the recombinant HAX-1 using mass spectrometry. **Fig. 6.11** shows the expression gels and the superposition of the [^{1}H,^{15}N]-HSQC experiments of the amide regions of HAX-1 purified using both native and denatured conditions. The two NMR spectra of HAX-1 are essentially superimposable, showing that the protein behaves like an

IDP in both preparations [513]. As expected for disordered proteins, the chemical shift breadth of amide resonances is narrower than a globular protein. To assess the protein's monodispersity, we analyzed [^{1}H,^{15}N]-TRACT experiments [507]. From these relaxation data, we estimated a correlation time (τ_c) of 15.1 ± 0.9 ns (**Fig. 6.12**), confirming that HAX-1 in the NMR samples is monodispersed [514]. To determine the activity of HAX-1, we carried out ATP-coupled assays on SERCA in the presence and absence of PLN and with HAX-1 at various molar ratios. As previously reported [91, 95], HAX-1 augmented the inhibitory effects of PLN at SERCA:PLN:HAX-1 in a 1:1:1 ratio (**Fig. 6.2**). Note that at higher concentrations of HAX-1 the results are no longer reliable, probably due to protein aggregation.

6.3.2 HAX-1 is an intrinsically disordered protein

Previous studies suggested that truncated HAX-1 is intrinsically disordered and adopts a partial secondary structure only upon binding Ca^{2+} [98]. Additionally, using computational approaches, Balcerak *et al.* predicted that HAX-1 is largely disordered [99]. To confirm these predictions, we used a combination of CD and NMR spectroscopy. The CD spectra suggest that HAX-1 adopts partial secondary structures, with a dichroic profile containing less than 30% α-helical structures (**Fig. 6.3**) [515]. The NMR amide fingerprint from the [^{1}H,^{15}N]-HSQC experiments features a narrow dispersion in the ^{1}H chemical shifts that further confirmed the disordered nature of HAX-1 (**Fig. 6.4**). Upon chemical denaturation with urea (**Fig. 6.13**), the [^{1}H,^{15}N]-HSQC of HAX-1 displays sharper peaks in conjunction with a

few additional peaks. Also, the spectrum has a higher signal-to-noise (S/N) ratio, *i.e.*, 37 versus 141 for native and denatured conditions, respectively.

6.3.3 HAX-1 undergoes a partial ordering upon interaction with model lipids membranes

It has been hypothesized that HAX-1 exists as a membrane-associated protein with the C-terminal tail interacting with lipid bilayers [97, 473, 485, 516-518]. To determine whether HAX-1 undergoes structural transitions in the presence of membrane mimetic environments, we used a combination of CD and solution and ssNMR spectroscopy. The CD spectra of HAX-1 upon titration with DMPC large unilamellar vesicles (LUV) show that this protein undergoes a partial ordering upon interaction with this membrane mimetic system in a concentration-dependent manner (**Fig. 6.3**). Increasing the LUV concentration, the CD spectra show a sequential decrease of molar ellipticity at 208 nm, indicating an increase of the secondary structure content, which is modulated by the interaction with lipids (**Fig. 6.3**). Fitting the changes in molar ellipticity resulted in a partition constant K_x of 1.1 ± 0.2 mM, suggesting a weak interaction of this polypeptide with the DMPC LUV [504-506]. A higher effect was obtained by adding DHPC:DMPC mixtures in 3:1 molar ratios, which shows a significant increase in alpha-helical structure. More importantly, negatively charged lipids such as 1-palmitoyl-2-oleoyl-sn-glycero-3-phosphate (POPA) and 1-palmoitoyl-2-oleoyl-sn-glycero-3-phospho-L-serine (POPS) show more pronounced changes in HAX-1 secondary structure (**Fig. 6.14**.

The latter suggests that the nature of the lipid membrane modulates the secondary structure of HAX-1.

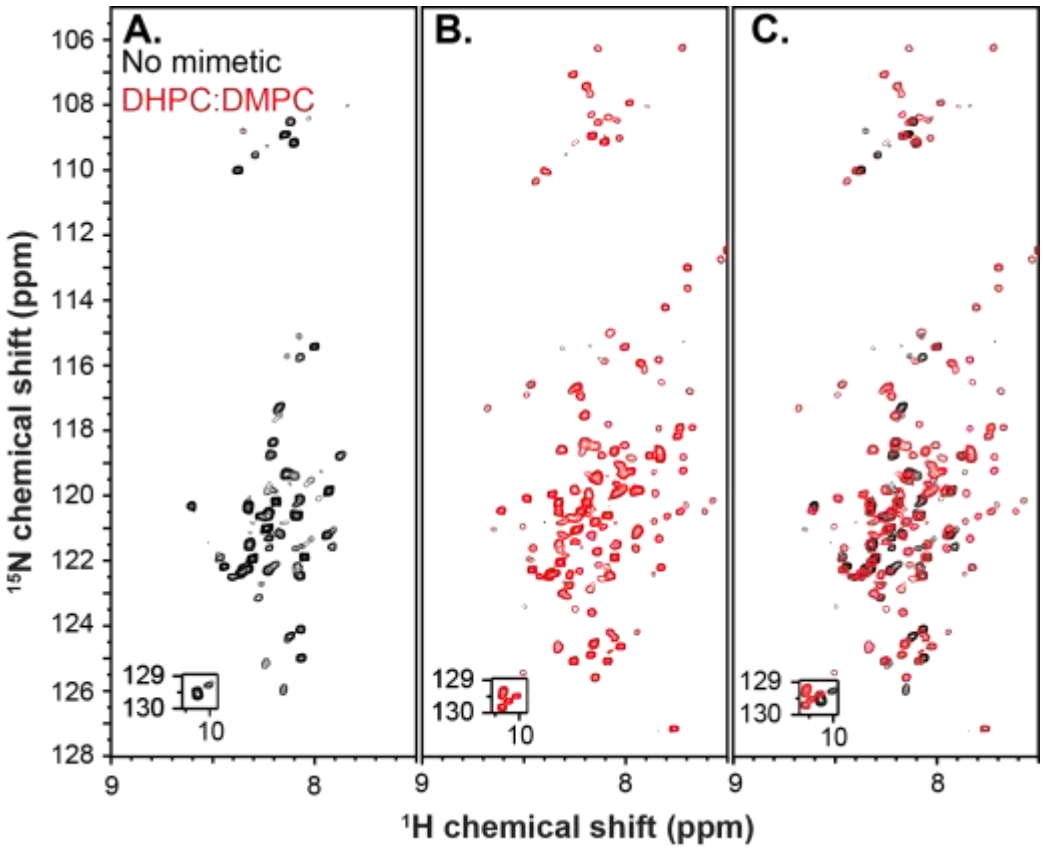

Figure 6.4: NMR fingerprinting of HAX-1 free and upon interactions with isotropic bicelles

A. *[^{1}H,^{15}N]-HSQC spectrum of HAX-1 in 50 mM KCl, 100 mM KH_2PO_4, pH 7.0.* ***B.*** *[^{1}H,^{15}N]-HSQC spectrum of HAX-1 in 50 mM KCl, 100 mM KH_2PO_4, pH 7.0 with DMPC/DHPC isotropic bicelle (q = 0.33).* ***C.*** *Overlay of* ***A.*** *and* ***B.***

Finally, we determined the effects of membrane mimetic systems on the structure of HAX-1 using both solution and solid-state NMR spectroscopy. In **Fig. 6.4**, we report the HAX-1 fingerprints in the absence and presence of DHPC:DMPC isotropic bicelles (3:1 molar ratio). It is apparent that upon addition of isotropic bicelles, the breadth of the ^{1}H chemical shift increases slightly and each resonance

in the spectra becomes significantly sharper and more resolved, an effect that is probably caused by the increase in the secondary structure content in accordance to the CD spectra. Since isotropic bicelles are a mere approximation of physiological lipid membranes [519], we carried out ssNMR spectroscopy on HAX-1 reconstituted with DMPC LUVs. We first performed CP-based experiments, which rely on polarization transfer via dipolar couplings to detect the most rigid domains of a protein [520]. For HAX-1, these experiments show an envelope of resonances corresponding to residues that interact with the lipid membranes (**Fig. 6.5A.**). In addition, the rINEPT experiments, whose polarization transfer occurs via through-bond J-couplings, revealed the presence of several resonances, corresponding to the most mobile residues of HAX-1 as well as those residues that do not interact with the membrane bilayer (**Fig. 6.5B.**). These data demonstrate that HAX-1 interacts with the membranes only partially and there is a significant portion of the protein that remains dynamic and does not interact with lipid membranes.

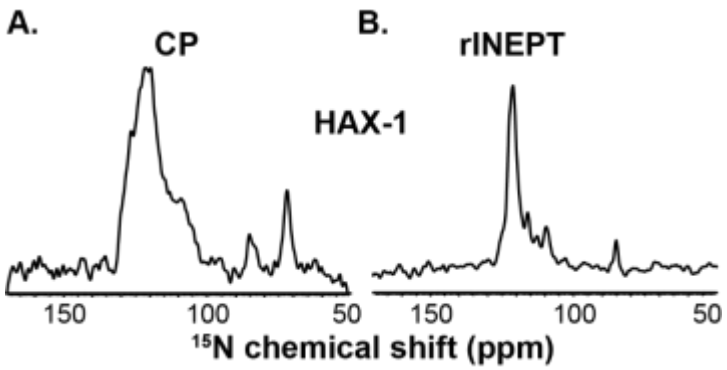

Figure 6.5: Interactions of HAX-1 with DMPC vesicles by ssNMR spectroscopy

***A.** CP and **B.** rINEPT spectra acquired on the same HAX-1 sample in DMPC LUVs.*

6.3.4 HAX-1 binds the cytoplasmic domain of monomeric PLN

Using yeast-two-hybrid analysis and pull down assays, it was found that HAX-1 interacts with the cytoplasmic region of PLN, increasing its inhibitory potency for SERCA [88-91, 95, 96]. In particular, these researchers found that residues 203-245 of HAX-1 constitute the minimal binding sequence targeting residues 16-22 of PLN, which include the two phosphorylation sites, Ser16 and Thr17, for protein kinase A and CaMKII, respectively [88]. To assess the physical interactions between these two proteins, we reconstituted U-^{13}C,^{15}N

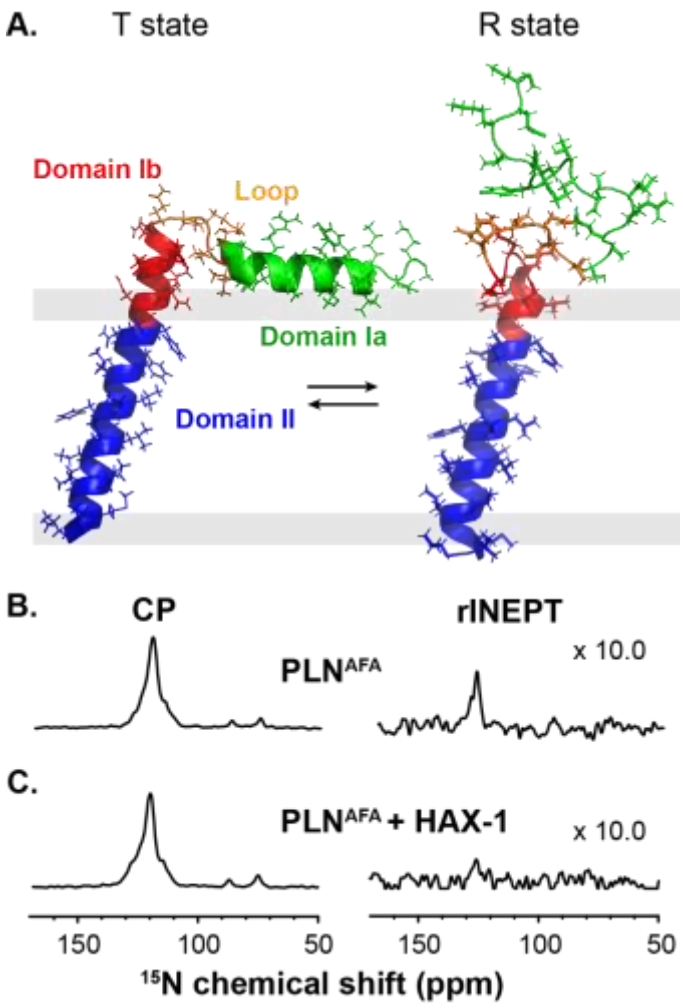

Figure 6.6: HAX-1 interacts with the cytoplasmic domain of PLN^{AFA}

A. *Structures of PLN in the T (left, Protein Data Bank (PDB) ID code 2KB7) and R (right, PDB ID code 2LPF) states. Each domain is color-coded with the more flexible domains (Ia and loop) in green and orange, respectively and the more rigid transmembrane domains (Ib and II) in red and blue, respectively.* ***B.*** *CP and rINEPT spectra of PLN^{AFA} in DMPC vesicles.* ***C.*** *CP and rINEPT spectra of PLN^{AFA}and HAX-1 in DMPC vesicles.*

PLN with unlabeled HAX-1 in DMPC lipid vesicles and carried out MAS ssNMR experiments.

Previously, we characterized the structure of PLN^{AFA} in lipid membranes and found that this bitopic membrane protein contains two regions (transmembrane and cytoplasmic) that can be divided into four dynamic domains: the N-terminal amphipathic helix (domain Ia), a mobile loop, a juxtamembrane helix (domain Ib), and a more rigid and hydrophobic helix embedded in the hydrocarbon region of the membrane (domain II) [172]. Also, our laboratory [16, 160, 207, 434, 521] and others [211, 522-525] discovered that PLN's cytoplasmic region exists in equilibrium between two inhibitory conformations: an ordered T (tense) state (helical and membrane bound) and a disordered R (relaxed) state (dynamic and membrane detached, **Fig. 6.6A.**), the latter of which is characterized by a flexible cytoplasmic domain available for a putative, non-inhibitory SERCA-bound B state [207]. The two inhibitory states, the R state and the T state, manifest as separate resonances in the [^{13}C,^{13}C]-DARR spectra for selected residues [160, 207] and can be discriminated using either CP or rINEPT experiments [159, 213]. **Fig. 6.6B.** and **C** show CP and rINEPT experiments for U-^{13}C,^{15}N PLN^{AFA} and U-^{13}C,^{15}N PLN^{AFA}/HAX-1 complex, respectively. The CP experiment shows an envelope of resonances corresponding to the most rigid residues of PLN^{AFA}, including the transmembrane domain (residue 34-52) and the juxtamembrane region (domain Ib, residues 21-33). In contrast, the rINEPT spectrum displays weaker peak intensities corresponding to the loop and domain Ia resonances, which are more dynamic. Moreover, the population of the dynamic region of PLN^{AFA} can be tuned

(*i.e.*, increased or decreased) by single-site mutations engineered in the dynamic loop [521]. The increase in the population of the R state shifts PLN toward the non-inhibitory B state, increasing Ca^{2+} transport [521]. These results were confirmed by analyzing the dynamics of naturally occurring mutations (R9C and R25C) in lipid membranes by ssNMR [74].

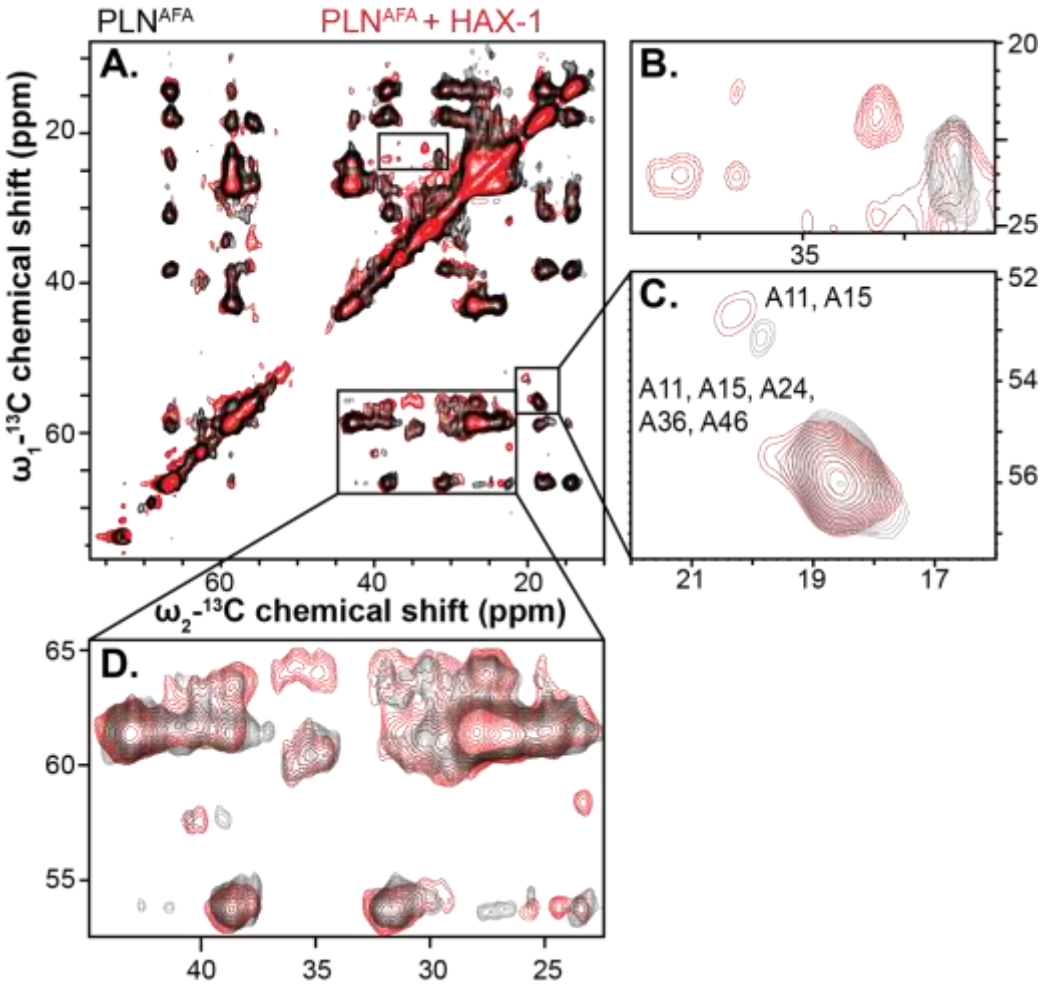

Figure 6.7: 2D [13C,13C]-DARR spectra of PLN in the presence and absence of HAX-1

A. *[^{13}C,^{13}C]-DARR overlay of PLN^{AFA} (black) and PLN^{AFA} with HAX-1 (red).* ***B.*** *inset of* ***A.*** *showing the most dramatic chemical shifts upon addition of HAX-1* ***C.*** *inset of A. demonstrating the A11/15 of PLN^{AFA} chemical shift in the presence of HAX-*

*1. **D.** Further confirmation of PLN^{AFA} interaction with HAX-1 with the appearance of peaks at 35 ppm in the ω_1 dimension and 65 ppm in the ω_2 dimension.*

In the rINEPT spectrum of the PLN^{AFA}/HAX-1 complex (**Fig. 6.6C.**), we observed a decrease of the dynamic population compared to PLN^{AFA} (~2%) (**Fig. 6.6B.**), which indicates that the cytoplasmic region of PLN^{AFA} is more rigid in the presence of HAX-1. The decreased dynamic population is comparable to the population of the R state present in PLN^{R9C} (~1%) [213]. We also registered a 2D [^{13}C,^{13}C]-DARR experiment of U-^{13}C,^{15}N PLN^{AFA} bound to HAX-1 (**Fig. 6.7**). As reporter for PLN^{AFA} conformational equilibrium, we selected the resonances of the Ala residues [160, 526]. The resonances of these residues are essentially overlapped; however, the ^{13}Cαchemical shifts of the resonances associated with the R state of Ala11 and Ala15 are resolved as they fall in the random coil region of the spectrum [160, 207]. Upon addition of HAX-1, there is a slight chemical shift change of the R state, and more importantly, a decrease of the population of the R state consistent with the rigidification of PLN (**Fig. 6.7C.**). The appearance of new resonances further confirms the interaction between HAX-1 and monomeric PLN^{AFA} (**Fig. 6.7B. and D.**). Taken together, these MAS ssNMR data support the physical interactions between monomeric PLN^{AFA} and HAX-1, which causes a shift in the conformational equilibrium of PLN from a dynamic to a rigid state.

6.3.5 HAX-1 binds the cytoplasmic domain of pentameric PLN

Finally, we investigated the interactions between HAX-1 and PLN in living cells. For these experiments, we utilized wild-type PLN that is in equilibrium between a pentameric assembly (storage) and monomeric form in cell membranes [527]. First, we quantified intra-pentameric FRET for PLN^{WT} labeled with genetically encoded fluorescent tags [511]. Co-expression of HAX-1 slightly decreased the intrinsic FRET of the pentamer ($FRET_{max}$) from 45.4 ± 0.9% to 38.2 ± 2.2%, consistent with a change in the overall architecture of the pentamer. Student's T-test comparison of 6 independent groups of 3 technical replicates yielded a *p*-value of 0.0003. Decreased intrinsic FRET indicates that the N-terminal fluorescent tags of PLN are more widely separated from one another, increasing the FRET distance (**Fig. 6.8**). These data indicate that HAX-1 binding to PLN increases the association of PLN cytoplasmic domains with the surface of the membrane, supporting the hypothesis that HAX-1 interacts with both PLN and the lipid membrane.

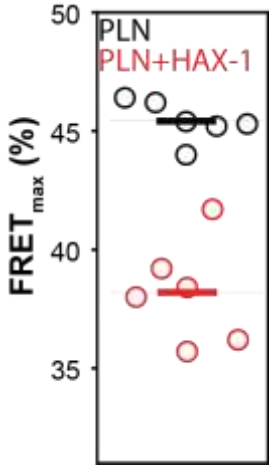

Figure 6.8: In cell FRET experiments show that HAX-1 changes the architecture of pentameric PLN^{WT}

Coexpression of a stoichiometric excess of HAX-1 decreases the intrinsic FRET ($FRET_{max}$) of the pentameric form of PLN, consistent with increasing fluorescent protein separation distance.

6.4 Discussion

HAX-1 belongs to a family of proteins that that are ubiquitously expressed and play various roles in health and disease [112]. Given their relatively small size and

remarkable biological importance, it is surprising that these proteins have not lured structural biologists. To date, there are only sparse structural reports on HAX-1, and they suggest that this protein is essentially disordered. Hirosaka *et al.* [98] expressed and labeled truncated HAX-1 for NMR studies. The amide signature of their construct as analyzed by [^{1}H,^{15}N]-HSQC experiments displays a poor chemical shift dispersion in the ^{1}H dimension, suggesting a relatively uniform chemical environment for each residue and supporting the unfolded nature of HAX-1. Furthermore, these authors showed that addition of Ca^{2+} slightly changes the amide chemical shifts, suggesting that HAX-1 can bind Ca^{2+} ions. Independently, Balcerak *et al.* [99] showed that HAX-1 is indeed able to bind Ca^{2+} ions and provided a computational model of the protein featuring ~40% of disordered domains.

Moreover, initial studies suggested that HAX-1 is a mitochondrial membrane protein with residues 261-273 in the C-terminal tail acting as a membrane anchor [97]. More recent studies have shown that HAX-1 isoform A localizes in the ER and lamellipodia, while isoform B has been found in the nuclear matrix with claims that HAX-1 is a cytosolic protein [528]. What is known, however, is that HAX-1 primarily interacts with proteins localizing around organelle membranes. Only recently, Kranias and co-workers reported the involvement of HAX-1 in the regulatory cycle of SERCA, suggesting a direct interaction with PLN [88]. To verify these predictions, we probed the interactions of HAX-1 with both lipid mimetic environments and PLN. We found that HAX-1 adopts partial folding upon binding to membranes and accentuated preference for negatively charged lipids. NMR

experiments in lipid membranes show that upon binding, HAX-1 restricts the motion of the cytosolic region of monomeric PLN, shifting its conformational equilibrium. In conjunction with decreasing $FRET_{max}$ measurements of pentameric PLN in the presence of HAX-1, these data might explain the function of HAX-1 which could 'sequester' the cytoplasmic region of PLN while simultaneously anchoring it to the membrane as seen in **Fig. 6.9**. Without the cytoplasmic region available to bind SERCA, only the inhibitory intramolecular interactions between the transmembrane domain of PLN and SERCA would be preserved. Our results are in agreement with the proposed model of allosteric regulation of SERCA, where the cytoplasmic region, upon binding the Ca^{2+}-ATPase, 'activates' its function (*i.e.*, PLN becomes less inhibitory) [207]. Under physiological conditions, PLN inhibits SERCA adopting three different states: the inhibitory T and R, where the inhibition is elicited via intramembrane interactions, and the non-inhibitory B state. Phosphorylation shifts the equilibrium toward the B state, 'activating' the enzyme, which increases its apparent affinity for Ca^{2+}. HAX-1 binding, on the other hand, shifts the equilibrium towards the inhibitory T state interacting with both membrane bilayers and PLN (**Fig. 6.9**). This model agrees with the activity assays reported in both this paper and carried out independently by Kranias and co-workers [95].

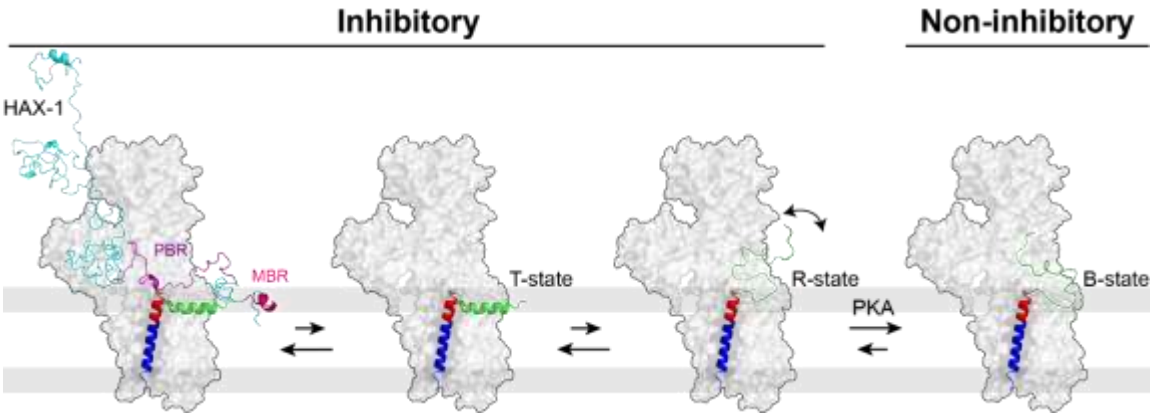

Figure 6.9: Proposed mechanism for HAX-1 synergistic inhibition of SERCA with PLN

PLN in complex with SERCA (PDB ID code 4Y3U) is in equilibrium between a T and R state. PKA recognizes and phosphorylates the R state preferentially, shifting the equilibrium toward a non-inhibitory state [434]. In contrast, HAX-1 (modeled by I-TASSER) traps the cytoplasmic domain of PLN in the T state and shifts the equilibrium toward a more inhibitory state (Figure adapted from Gustavsson et al.[207]).

6.5 Conclusions

In summary, our studies demonstrate that HAX-1 is an intrinsically disordered protein with the ability of interacting with model membranes to adopt a partially ordered structure. We showed that full-length HAX-1 is able to regulate the inhibitory potency of PLN by interacting with the cytoplasmic domain of PLN and shifting the conformational equilibrium toward a more inhibitory state. This adds a new level of control to Ca^{2+} transport and contractility of the heart muscle.

6.6 Acknowledgements

This work is supported by the National Institute of Health (GM 64742 to GV). We would like to thank Prof. Evangelia Kranias for critical reading of the manuscript and Changkon Park for his contributions to sample preparations.

6.7 Supplementary Figures

A.

MSLFDLFRGFFGFPGPRSHRDPFFGGMTRDEDDDEEEEEEEGGSWGRGNPRFHSPQHPPEE

FGFGFSFSPGGGIRFHDNFGFDDLVRDFNSIFSDMGAWTLPSHPPELPGPESETPGERLREG

QTLRDSMLKYPDSHQPRIFGGVLESDARSESPQPAPDWGSQRPFHRFDDVWPMDPHPRTR

EDNDLDSQVSQEGLGPVLQPQPKSYFKSISVTKITKPDGIVEERRTVVDSEGRTETTVTRHEA

DSSPRGDPESPRPPALDDAFSILDLFLGRWFRSR

B.

#	b mass	Seq	y mass
1	148.08	F	
2	263.32	D	1380.6
3	378.28	D	1265.57
4	477.46	V	1150.55
5	663.53	W	1051.48
6	760.74	P	866.06
7	907.37	M(+15.99)	768.38
8	1022.54	D	621.86
9	1119.45	P	506.57
10	1256.5	H	409.74
11	1353.56	P	272.38
12		R	175.12

C.

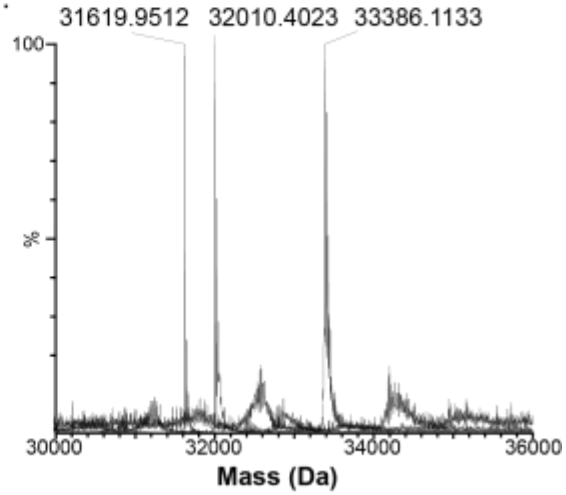

Figure 6.10: Figure S1. Mass spectrometry of recombinant HAX-1

A. *Trypsin digest peptide fragments matched to HAX-1 primary amino acid sequence with a -10log(P) score above 24. (Blue bars are matched peptides, Red O indicates an oxidized state for Met).* ***B.*** *MS/MS data derived from the oxidized matched peptide sequence.* ***C.*** *LC-MS spectra of unlabeled, U-^{15}N, and U-^{15}N,^{13}C HAX-1.*

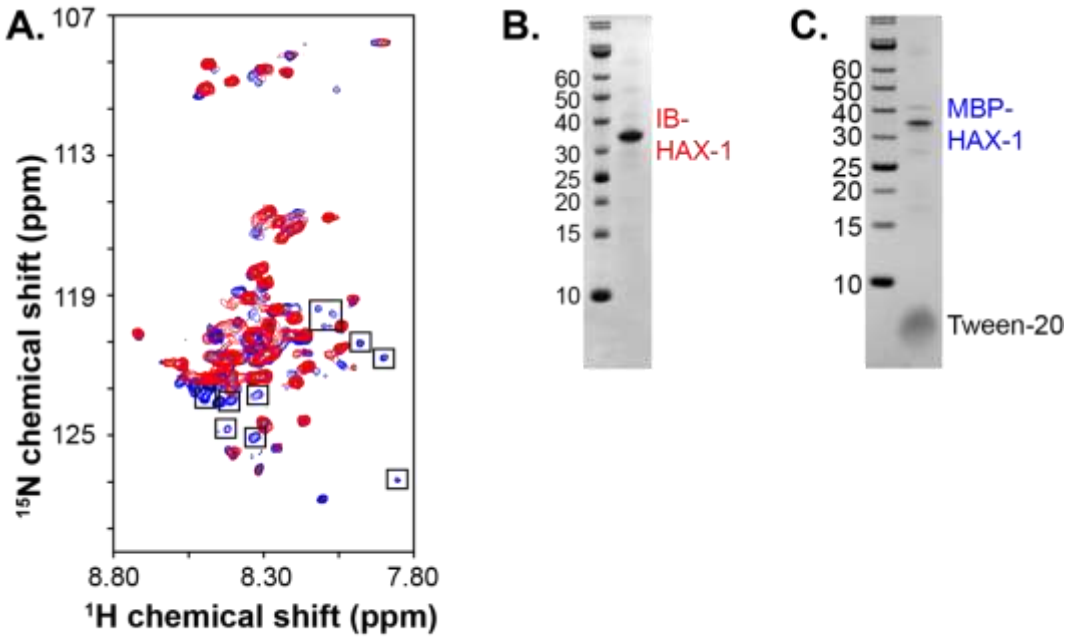

Figure 6.11: Figure S2. NMR spectra and corresponding SDS-PAGE gels of recombinant U-15N HAX-1 expressed in native conditions and in inclusion bodies

A. *Overlay of the [^{1}H,^{15}N]-HSQC spectra for MBP-HAX-1 fusion protein purification and SUMO-HAX-1 fusion inclusion body purification (IB-HAX-1). The MBP-fusion purified HAX-1 [^{1}H,^{15}N]-HSQC spectrum was recorded on a 900 MHz Bruker spectrometer. The sample consisted of 100 µM HAX-1, 50 mM KCl, 20 mM MOPS, 0.1% Tween 20. The number of scans was 16 for 128 increments. Temperature was held constant at 25 ^{o}C. The SUMO-fusion purified HAX-1 [^{1}H,^{15}N]-HSQC spectrum was recorded on a 900 MHz Bruker spectrometer. The sample consisted of 300 µM HAX-1, 50 mM KCl, 20 mM MOPS. The number of scans was 8 for 128 increments. The temperature was held at 25 ^{o}C. Boxed resonances of the blue spectrum appear in the spectra of samples purified from inclusion bodies recorded in isotropic bicelles and samples subject to higher temperatures.* ***B.*** *SDS-PAGE gel of purified HAX-1 from inclusion bodies.* ***C.*** *SDS-PAGE gel of purified HAX-1 from native conditions****.***

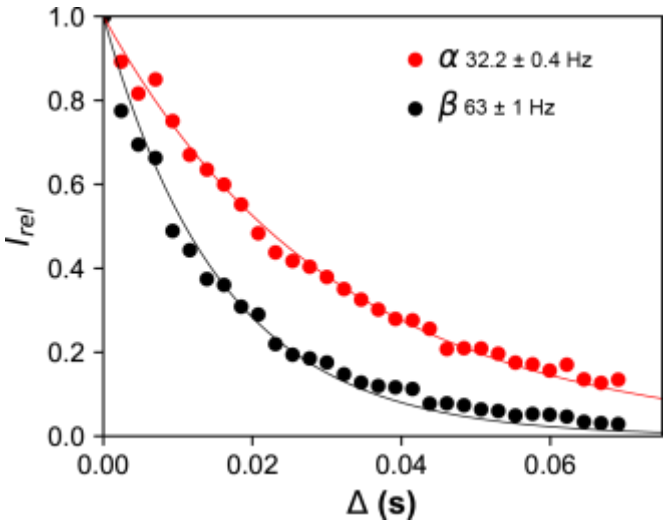

Figure 6.12: Figure S3. TRACT NMR data and corresponding exponential decay fits

An overlay of the relaxation data and the relaxation rates for the α- and β-spin states (R_α and R_β, respectively). 31 time points were recorded from 0 to 0.070 seconds (2.3 ms increments starting from 0.1 ms) for the relaxation period (Δ). Least-squares fitting with Monte Carlo error analysis was used for the estimation of R_α and R_β.

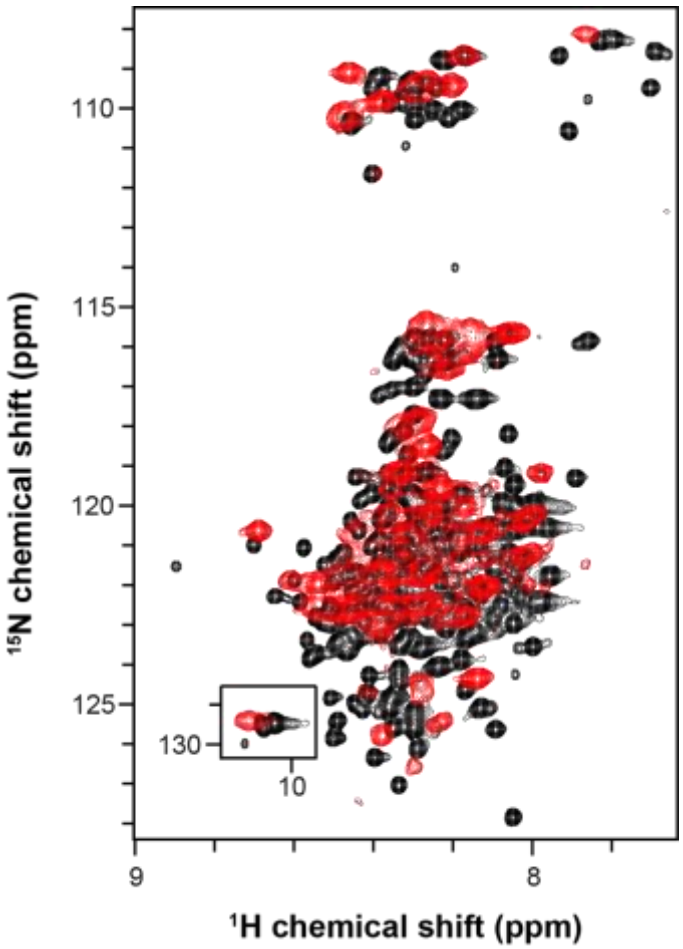

Figure 6.13: Figure S4. Amide fingerprints of HAX-1 under native and denaturing conditions

Superposition of [^{1}H,^{15}N]-HSQC spectra of HAX-1 in native solution conditions (red) and in 6M urea (black). The spectra were referenced with 4,4-dimethyl-4-silapentane-1-sulfonic acid (DSS).

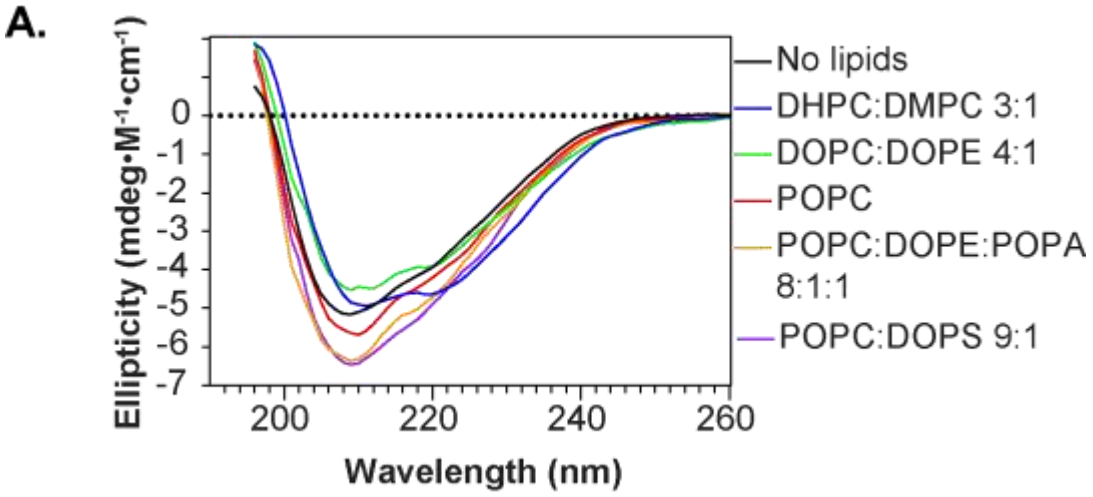

Figure 6.14: Figure S5. Circular Dichroism spectroscopy shows that HAX-1 undergoes structural rearrangement upon interacting with different membrane mimetics

CD spectra of HAX-1 interacting with various lipid mimetic compositions.

Table 6.1: Table S1 Circular Dichroism Collection Parameters

Circular Dichroism Parameters	
Data-collection parameters	
Instrument	Jasco-J815
Temperature (K)	298
Wavelengths	190 - 260 nm
[HAX-1]	5 μM
Digital Integration Time	2 seconds
Bandwidth	5 nm
Data pitch	1.0nm
Scanning mode	continuous
Scanning speed	50 nm/min
Accumulations	10

Conclusions and Perspectives

The preceding chapters (2 through 6) are the culmination of my work to answer the questions I posed for myself:

- How can HAX-1 be expressed, purified, and functionally assayed for *in vitro* biophysical characterization?
- What is the structure of HAX-1 in solution and in the presence of lipid membranes?
- How is SERCA function and PLN regulation affected by HAX-1 and how can a SERCA/PLN/HAX-1 complex be formed to perform NMR studies under fully functional conditions?

Chapter 2 is a reprint of a solid-state NMR review publication that I was a collaborator on. Aside from formatting and editing this publication, I contributed previously unpublished data on the effects of HAX-1 binding to the PLN cytoplasmic domain, as well as MAS RI-HSQC, HSQC, and MAS ^{13}C-^{13}C DARR data. This paper and these data highlight the idea of combining solution- and solid-state NMR (both MAS and OS) that was the backbone of my research on the peripheral membrane protein HAX-1.

Chapter 3 is a reprint of a review paper that I authored on the CCLS-HSQC pulse sequence. This was the first, first-author paper that I published and served as a tool to learn the NMR theory necessary to progress through my Ph.D. In addition, this pulse sequence was used to partially assign HAX-1 in the presence of isotropic bicelles; a strategy that we had previously not used before in the

assignment of solution-state spectra. The assignment proved necessary to determine the location of HAX-1 that associates with lipid membranes experimentally.

Chapter 4 is a reprint of a book chapter describing the methods for synthetic ethyl labeling of SERCA. I contributed to this paper primarily through the extraction of SERCA from New Zealand White Rabbit skeletal muscle. Aside from providing the technical skill for purification of SERCA used in activity assays and ssNMR experiments for question number three, tagging SERCA in this way is a future perspective for the HAX-1 project now that there is a foundational understanding of the HAX-1/PLN interaction. This tagging strategy will be used to study the structure function relationships of the ternary SERCA/PLN/HAX-1 complex.

Chapter 5 is a reprint of an eLife research paper describing the structure-function relationship of phosphorylated and unphosphorylated PLN binding to SERCA. My work on this paper consisted of reproducing each spectrum published to ensure not only that this work was correct, but that we could move forward with OS-ssNMR for the PLN/HAX-1 complex. From this work, we discovered that the interactions of domain Ib are essential for PLN binding of SERCA, setting the foundations for my research on HAX-1/PLN interactions.

Chapter 6 is a reprint of a BBA Biomembranes research paper describing the purification methods and structure of HAX-1 as an IDP; these data answered the first objective. HAX-1 interactions with lipid membranes as well as the PLN

cytoplasmic domain were explored, however with this initial paper, I felt I had only scratched the surface of the latter two objectives. My final research paper investigates the lipid/HAX-1 interactions and fully describes the effects HAX-1 binding has on not only the cytoplasmic domain of PLN, but the transmembrane domain as well. From this manuscript, we learn that HAX-1 interacts with the membrane via its C-terminal putative membrane binding region. Importantly, we discovered that HAX-1 does not only affect the cytoplasmic domain of PLN, but results in the stabilization of the SERCA binding residues of PLN. Through a collaboration with Seth Robia at Loyola, Chicago, we confirm this effect *in vivo*, demonstrating a decrease in K_d and a decrease in $FRET_{max}$. These data prove that HAX-1 increases PLN inhibition by increasing the stability of SERCA binding residues while pulling the cytoplasmic domain of PLN away from the non-inhibitory SERCA bound state.

In summary, we have developed a method with which to purify HAX-1 for *in vitro* studies. We have demonstrated that HAX-1 is an intrinsically disordered protein that interacts with lipid membranes via its C-terminal membrane binding domain. The membrane binding domain was found to be essential for binding the cytoplasmic domain of PLN and stabilizing the SERCA binding residues of PLN, thereby increasing the inhibition of PLN for SERCA.

Bibliography

1. Sun, P., et al., *Crystal structure of the bacterial acetate transporter SatP reveals that it forms a hexameric channel.* J Biol Chem, 2018. **293**(50): p. 19492-19500.
2. Toyoshima, C., et al., *Crystal structure of the calcium pump of sarcoplasmic reticulum at 2.6 A resolution.* Nature, 2000. **405**(6787): p. 647-655.
3. Han, B., et al., *SHIFTX2: significantly improved protein chemical shift prediction.* Journal of Biomolecular Nmr, 2011. **50**(1): p. 43-57.
4. Jo, S., et al., *CHARMM-GUI: A web-based graphical user interface for CHARMM.* Journal of Computational Chemistry, 2008. **29**(11): p. 1859-1865.
5. Wu, E.L., et al., *CHARMM-GUI Membrane Builder toward realistic biological membrane simulations.* Journal of Computational Chemistry, 2014. **35**(27): p. 1997-2004.
6. McQuarrie, D.A. and J.D. Simon, *Physical chemistry : a molecular approach*. 1997, Sausalito, Calif.: University Science Books. xxiii, 1270 p.
7. Zupanovic, P. and D. Kuic, *Relation between Boltzmann and Gibbs entropy and example with multinomial distribution.* Journal of Physics Communications, 2018. **2**(4).
8. Ben-Naim, A., *Entropy, Shannon's Measure of Information and Boltzmann's H-Theorem.* Entropy, 2017. **19**(2).
9. Davies, P.C., E. Rieper, and J.A. Tuszynski, *Self-organization and entropy reduction in a living cell.* Biosystems, 2013. **111**(1): p. 1-10.
10. Ayuyan, A.G. and F.S. Cohen, *The Chemical Potential of Plasma Membrane Cholesterol: Implications for Cell Biology.* Biophys J, 2018. **114**(4): p. 904-918.
11. Phillips, R., J. Kondev, and J. Theriot, *Physical biology of the cell*. 2009, New York: Garland Science. xxiv, 807 p.
12. Zhu, Q., et al., *Entropy and Polarity Control the Partition and Transportation of Drug-like Molecules in Biological Membrane.* Sci Rep, 2017. **7**(1): p. 17749.
13. Davies, J.A. and C.H. Chang, *Engineering kidneys from simple cell suspensions: an exercise in self-organization.* Pediatr Nephrol, 2014. **29**(4): p. 519-24.
14. Voet, D., J.G. Voet, and C.W. Pratt, *Fundamentals of biochemistry*. 1999, New York: Wiley. xxiii, 931 p.
15. Visco, I., S. Chiantia, and P. Schwille, *Asymmetric supported lipid bilayer formation via methyl-beta-cyclodextrin mediated lipid exchange: influence of asymmetry on lipid dynamics and phase behavior.* Langmuir, 2014. **30**(25): p. 7475-84.
16. Gustavsson, M., N.J. Traaseth, and G. Veglia, *Activating and deactivating roles of lipid bilayers on the Ca(2+)-ATPase/phospholamban complex.* Biochemistry, 2011. **50**(47): p. 10367-74.
17. Singer, S.J., *Fluid Lipid-Globular Protein Mosaic Model of Membrane Structure.* Annals of the New York Academy of Sciences, 1972. **195**(Jun20): p. 16-&.
18. Ahram, M., et al., *Estimation of membrane proteins in the human proteome.* In Silico Biol, 2006. **6**(5): p. 379-86.
19. Almen, M.S., et al., *Mapping the human membrane proteome: a majority of the human membrane proteins can be classified according to function and evolutionary origin.* BMC Biol, 2009. **7**: p. 50.
20. Sanders, C.R. and J.M. Hutchison, *Membrane properties that shape the evolution of membrane enzymes.* Current Opinion in Structural Biology, 2018. **51**: p. 80-91.

21. Hoffman, R., *Hematology : basic principles and practice*. 7th edition. ed. 2018, Philadelphia, PA: Elsevier. p.
22. V., w.E. *Membrane Transport Proteins.* Chemistry LibreTexts 2021; January 3, 2021.
23. Rothman, J.E. and J. Lenard, *Membrane asymmetry.* Science, 1977. **195**(4280): p. 743-53.
24. Pritisanac, I., et al., *Entropy and Information within Intrinsically Disordered Protein Regions.* Entropy, 2019. **21**(7).
25. Bowie, J.U., *Membrane protein folding: how important are hydrogen bonds?* Current Opinion in Structural Biology, 2011. **21**(1): p. 42-49.
26. von Heijne, G., *Membrane-protein topology.* Nat Rev Mol Cell Biol, 2006. **7**(12): p. 909-18.
27. Whited, A.M. and A. Johs, *The interactions of peripheral membrane proteins with biological membranes.* Chem Phys Lipids, 2015. **192**: p. 51-59.
28. Shao, X., et al., *Synaptotagmin-syntaxin interaction: the C2 domain as a Ca2+-dependent electrostatic switch.* Neuron, 1997. **18**(1): p. 133-42.
29. Dathe, M., et al., *Peptide helicity and membrane surface charge modulate the balance of electrostatic and hydrophobic interactions with lipid bilayers and biological membranes.* Biochemistry, 1996. **35**(38): p. 12612-22.
30. White, S.H. and W.C. Wimley, *Hydrophobic interactions of peptides with membrane interfaces.* Biochim Biophys Acta, 1998. **1376**(3): p. 339-52.
31. Cho, W. and R.V. Stahelin, *Membrane-protein interactions in cell signaling and membrane trafficking.* Annu Rev Biophys Biomol Struct, 2005. **34**: p. 119-51.
32. Gimenez-Andres, M., A. Copic, and B. Antonny, *The Many Faces of Amphipathic Helices.* Biomolecules, 2018. **8**(3).
33. Eisenberg, D., R.M. Weiss, and T.C. Terwilliger, *The helical hydrophobic moment: a measure of the amphiphilicity of a helix.* Nature, 1982. **299**(5881): p. 371-4.
34. Huber, R., *Conformational Flexibility and Its Functional-Significance in Some Protein Molecules.* Trends in Biochemical Sciences, 1979. **4**(12): p. 271-276.
35. Uversky, V.N., *Intrinsic Disorder, Protein-Protein Interactions, and Disease.* Adv Protein Chem Struct Biol, 2018. **110**: p. 85-121.
36. Uversky, V.N., J.R. Gillespie, and A.L. Fink, *Why are "natively unfolded" proteins unstructured under physiologic conditions?* Proteins, 2000. **41**(3): p. 415-27.
37. Dunker, A.K., et al., *Intrinsic protein disorder in complete genomes.* Genome Inform Ser Workshop Genome Inform, 2000. **11**: p. 161-71.
38. Peng, Z., et al., *Exceptionally abundant exceptions: comprehensive characterization of intrinsic disorder in all domains of life.* Cell Mol Life Sci, 2015. **72**(1): p. 137-51.
39. Deiana, A., et al., *Intrinsically disordered proteins and structured proteins with intrinsically disordered regions have different functional roles in the cell.* PLoS One, 2019. **14**(8): p. e0217889.
40. Narasumani, M. and P.M. Harrison, *Bioinformatical parsing of folding-on-binding proteins reveals their compositional and evolutionary sequence design.* Sci Rep, 2015. **5**: p. 18586.
41. Shoemaker, B.A., J.J. Portman, and P.G. Wolynes, *Speeding molecular recognition by using the folding funnel: the fly-casting mechanism.* Proc Natl Acad Sci U S A, 2000. **97**(16): p. 8868-73.
42. Mollica, L., et al., *Binding Mechanisms of Intrinsically Disordered Proteins: Theory Simulation, and Experiment.* Frontiers in Molecular Biosciences, 2016. **3**.

43. Ganguly, D., W.H. Zhang, and J.H. Chen, *Electrostatically Accelerated Encounter and Folding for Facile Recognition of Intrinsically Disordered Proteins.* Plos Computational Biology, 2013. **9**(11).
44. Kubelka, J., J. Hofrichter, and W.A. Eaton, *The protein folding 'speed limit'.* Current Opinion in Structural Biology, 2004. **14**(1): p. 76-88.
45. Mittag, T., et al., *Structure/function implications in a dynamic complex of the intrinsically disordered Sic1 with the Cdc4 subunit of an SCF ubiquitin ligase.* Structure, 2010. **18**(4): p. 494-506.
46. Borg, M., et al., *Polyelectrostatic interactions of disordered ligands suggest a physical basis for ultrasensitivity.* Proc Natl Acad Sci U S A, 2007. **104**(23): p. 9650-5.
47. Fuxreiter, M., P. Tompa, and I. Simon, *Local structural disorder imparts plasticity on linear motifs.* Bioinformatics, 2007. **23**(8): p. 950-6.
48. Vacic, V., et al., *Characterization of molecular recognition features, MoRFs, and their binding partners.* J Proteome Res, 2007. **6**(6): p. 2351-66.
49. Shiels, H.A., *Cardiomyocyte Morphology and Physiology.* Cardiovascular System: Morphology, Control and Function, 2017. **36**: p. 55-98.
50. Luo, C.H. and Y. Rudy, *A model of the ventricular cardiac action potential. Depolarization, repolarization, and their interaction.* Circ Res, 1991. **68**(6): p. 1501-26.
51. Savarese, G. and L.H. Lund, *Global Public Health Burden of Heart Failure.* Card Fail Rev, 2017. **3**(1): p. 7-11.
52. Hayward, C., et al., *The Current and Future Landscape of SERCA Gene Therapy for Heart Failure: A Clinical Perspective.* Hum Gene Ther, 2015. **26**(5): p. 293-304.
53. McMurray, J.J., et al., *Angiotensin-neprilysin inhibition versus enalapril in heart failure.* N Engl J Med, 2014. **371**(11): p. 993-1004.
54. Kairouz, V., et al., *Molecular targets in heart failure gene therapy: current controversies and translational perspectives.* Ann N Y Acad Sci, 2012. **1254**: p. 42-50.
55. Hulot, J.S., K. Ishikawa, and R.J. Hajjar, *Gene therapy for the treatment of heart failure: promise postponed.* Eur Heart J, 2016. **37**(21): p. 1651-8.
56. Tadini-Buoninsegni, F., et al., *Drug Interactions With the Ca(2+)-ATPase From Sarco(Endo)Plasmic Reticulum (SERCA).* Front Mol Biosci, 2018. **5**: p. 36.
57. Kekenes-Huskey, P.M., et al., *Calcium binding and allosteric signaling mechanisms for the sarcoplasmic reticulum Ca2+ATPase.* Protein Science, 2012. **21**(10): p. 1429-1443.
58. Periasamy, M. and A. Kalyanasundaram, *SERCA pump isoforms: their role in calcium transport and disease.* Muscle Nerve, 2007. **35**(4): p. 430-42.
59. Kaprielian, Z., E. Bandman, and D.M. Fambrough, *Expression of Ca2(+)-ATPase isoforms in denervated, regenerating, and dystrophic chicken skeletal muscle.* Dev Biol, 1991. **144**(1): p. 199-211.
60. Heilmann, C. and D. Pette, *Molecular transformations in sarcoplasmic reticulum of fast-twitch muscle by electro-stimulation.* Eur J Biochem, 1979. **93**(3): p. 437-46.
61. Heilmann, C., et al., *ATPase activities, Ca2+ transport and phosphoprotein formation in sarcoplasmic reticulum subfractions of fast and slow rabbit muscles.* Eur J Biochem, 1977. **81**(2): p. 211-22.

62. Leberer, E., et al., *Slow/cardiac sarcoplasmic reticulum Ca2+-ATPase and phospholamban mRNAs are expressed in chronically stimulated rabbit fast-twitch muscle.* Eur J Biochem, 1989. **185**(1): p. 51-4.
63. Pette, D. and G. Vrbova, *What does chronic electrical stimulation teach us about muscle plasticity?* Muscle & Nerve, 1999. **22**(6): p. 666-677.
64. Michelangeli, F. and J.M. East, *A diversity of SERCA Ca2+ pump inhibitors.* Biochemical Society Transactions, 2011. **39**: p. 789-797.
65. Li, H., et al., *Skeletal muscle non-shivering thermogenesis as an attractive strategy to combat obesity.* Life Sci, 2021. **269**: p. 119024.
66. Dahl, R., *A new target for Parkinson's disease: Small molecule SERCA activator CDN1163 ameliorates dyskinesia in 6-OHDA-lesioned rats.* Bioorg Med Chem, 2017. **25**(1): p. 53-57.
67. Qaisar, R., et al., *Restoration of Sarcoplasmic Reticulum Ca(2+) ATPase (SERCA) Activity Prevents Age-Related Muscle Atrophy and Weakness in Mice.* Int J Mol Sci, 2020. **22**(1).
68. Lee, Y., S. Chakraborty, and M. Muthuchamy, *Roles of sarcoplasmic reticulum Ca(2+) ATPase pump in the impairments of lymphatic contractile activity in a metabolic syndrome rat model.* Sci Rep, 2020. **10**(1): p. 12320.
69. Tong, X., et al., *SERCA2 Deficiency Impairs Pancreatic beta-Cell Function in Response to Diet-Induced Obesity.* Diabetes, 2016. **65**(10): p. 3039-52.
70. Medeiros, A., et al., *Mutations in the human phospholamban gene in patients with heart failure.* Am Heart J, 2011. **162**(6): p. 1088-1095 e1.
71. Haghighi, K., et al., *A mutation in the human phospholamban gene, deleting arginine 14, results in lethal, hereditary cardiomyopathy.* Proc Natl Acad Sci U S A, 2006. **103**(5): p. 1388-93.
72. Liu, G.S., et al., *A novel human R25C-phospholamban mutation is associated with super-inhibition of calcium cycling and ventricular arrhythmia.* Cardiovasc Res, 2015. **107**(1): p. 164-74.
73. Ha, K.N., et al., *Lethal Arg9Cys phospholamban mutation hinders Ca2+-ATPase regulation and phosphorylation by protein kinase A.* Proc Natl Acad Sci U S A, 2011. **108**(7): p. 2735-40.
74. Nelson, S.E.D., et al., *Effects of the Arg9Cys and Arg25Cys mutations on phospholamban's conformational equilibrium in membrane bilayers.* Biochim Biophys Acta Biomembr, 2018. **1860**(6): p. 1335-1341.
75. Levitzki, A., *From Epinephrine to Cyclic-Amp.* Science, 1988. **241**(4867): p. 800-806.
76. Eizema, K., et al., *Adenovirus-based phospholamban antisense expression as a novel approach to improve cardiac contractile dysfunction: comparison of a constitutive viral versus an endothelin-1-responsive cardiac promoter.* Circulation, 2000. **101**(18): p. 2193-9.
77. Fechner, H., et al., *Highly efficient and specific modulation of cardiac calcium homeostasis by adenovector-derived short hairpin RNA targeting phospholamban.* Gene Ther, 2007. **14**(3): p. 211-8.
78. Marín-García, J., A. Akhmedov, and G.W. Moe, *Post-genomic cardiology*. Second edition. ed. 2014, Amsterdam ; Boston: Elsevier/AP, Academic Press is an imprint of Elsevier. x, 924 pages.
79. Brixius, K., et al., *Ser16-, but not Thr17-phosphorylation of phospholamban influences frequency-dependent force generation in human myocardium.* Pflugers Arch, 2003. **447**(2): p. 150-7.

80. El-Armouche, A., et al., *Decreased protein and phosphorylation level of the protein phosphatase inhibitor-1 in failing human hearts.* Cardiovasc Res, 2004. **61**(1): p. 87-93.
81. Schwinger, R.H., et al., *Reduced Ca(2+)-sensitivity of SERCA 2a in failing human myocardium due to reduced serin-16 phospholamban phosphorylation.* J Mol Cell Cardiol, 1999. **31**(3): p. 479-91.
82. Carr, A.N., et al., *Type 1 phosphatase, a negative regulator of cardiac function.* Mol Cell Biol, 2002. **22**(12): p. 4124-35.
83. El-Armouche, A., et al., *Evidence for protein phosphatase inhibitor-1 playing an amplifier role in beta-adrenergic signaling in cardiac myocytes.* FASEB J, 2003. **17**(3): p. 437-9.
84. Vafiadaki, E., et al., *Identification of a protein phosphatase-1/phospholamban complex that is regulated by cAMP-dependent phosphorylation.* PLoS One, 2013. **8**(11): p. e80867.
85. Qian, J., et al., *Small heat shock protein 20 interacts with protein phosphatase-1 and enhances sarcoplasmic reticulum calcium cycling.* Circ Res, 2011. **108**(12): p. 1429-38.
86. El-Armouche, A., et al., *Phosphatase inhibitor-1-deficient mice are protected from catecholamine-induced arrhythmias and myocardial hypertrophy.* Cardiovasc Res, 2008. **80**(3): p. 396-406.
87. Pathak, A., et al., *Enhancement of cardiac function and suppression of heart failure progression by inhibition of protein phosphatase 1.* Circ Res, 2005. **96**(7): p. 756-66.
88. Vafiadaki, E., et al., *Phospholamban interacts with HAX-1, a mitochondrial protein with anti-apoptotic function.* J Mol Biol, 2007. **367**(1): p. 65-79.
89. Vafiadaki, E., et al., *The role of SERCA2a/PLN complex, Ca(2+) homeostasis, and anti-apoptotic proteins in determining cell fate.* Pflugers Arch, 2009. **457**(3): p. 687-700.
90. Vafiadaki, E., et al., *The anti-apoptotic protein HAX-1 interacts with SERCA2 and regulates its protein levels to promote cell survival.* Mol Biol Cell, 2009. **20**(1): p. 306-18.
91. Zhao, W., et al., *The anti-apoptotic protein HAX-1 is a regulator of cardiac function.* Proc Natl Acad Sci U S A, 2009. **106**(49): p. 20776-81.
92. Lam, C.K., et al., *Novel role of HAX-1 in ischemic injury protection involvement of heat shock protein 90.* Circ Res, 2013. **112**(1): p. 79-89.
93. Mattiazzi, A. and E.G. Kranias, *The role of CaMKII regulation of phospholamban activity in heart disease.* Front Pharmacol, 2014. **5**: p. 5.
94. Lam, C.K., et al., *HAX-1 regulates cyclophilin-D levels and mitochondria permeability transition pore in the heart.* Proc Natl Acad Sci U S A, 2015. **112**(47): p. E6466-75.
95. Bidwell, P.A., K. Haghighi, and E.G. Kranias, *The antiapoptotic protein HAX-1 mediates half of phospholamban's inhibitory activity on calcium cycling and contractility in the heart.* J Biol Chem, 2018. **293**(1): p. 359-367.
96. Bidwell, P.A., et al., *HAX-1 regulates SERCA2a oxidation and degradation.* J Mol Cell Cardiol, 2018. **114**: p. 220-233.
97. Suzuki, Y., et al., *HAX-1, a novel intracellular protein, localized on mitochondria, directly associates with HS1, a substrate of Src family tyrosine kinases.* J Immunol, 1997. **158**(6): p. 2736-44.

98. Hirasaka, K., et al., *UCP3 is associated with Hax-1 in mitochondria in the presence of calcium ion.* Biochem Biophys Res Commun, 2016. **472**(1): p. 108-13.
99. Balcerak, A., et al., *The calcium binding properties and structure prediction of the Hax-1 protein.* Acta Biochim Pol, 2017. **64**(3): p. 537-542.
100. Larsen, E.K., et al., *Intrinsically disordered HAX-1 regulates Ca(2+) cycling by interacting with lipid membranes and the phospholamban cytoplasmic region.* Biochim Biophys Acta Biomembr, 2020. **1862**(1): p. 183034.
101. Halestrap, A.P., S.J. Clarke, and S.A. Javadov, *Mitochondrial permeability transition pore opening during myocardial reperfusion--a target for cardioprotection.* Cardiovasc Res, 2004. **61**(3): p. 372-85.
102. Yedavalli, V.S., et al., *Human immunodeficiency virus type 1 Vpr interacts with antiapoptotic mitochondrial protein HAX-1.* J Virol, 2005. **79**(21): p. 13735-46.
103. Brenner, C. and G. Kroemer, *Apoptosis. Mitochondria--the death signal integrators.* Science, 2000. **289**(5482): p. 1150-1.
104. Cilenti, L., et al., *Regulation of HAX-1 anti-apoptotic protein by Omi/HtrA2 protease during cell death.* J Biol Chem, 2004. **279**(48): p. 50295-301.
105. Green, D. and G. Kroemer, *The central executioners of apoptosis: caspases or mitochondria?* Trends Cell Biol, 1998. **8**(7): p. 267-71.
106. Green, D.R. and J.C. Reed, *Mitochondria and apoptosis.* Science, 1998. **281**(5381): p. 1309-12.
107. Ramsay, A.G., et al., *HS1-associated protein X-1 regulates carcinoma cell migration and invasion via clathrin-mediated endocytosis of integrin alphavbeta6.* Cancer Res, 2007. **67**(11): p. 5275-84.
108. Cheng, C.F., et al., *Pravastatin attenuates carboplatin-induced cardiotoxicity via inhibition of oxidative stress associated apoptosis.* Apoptosis, 2008. **13**(7): p. 883-94.
109. Li, W.B., et al., *Induction of apoptosis by Hax-1 siRNA in melanoma cells.* Cell Biol Int, 2009. **33**(4): p. 548-54.
110. Trebinska, A., et al., *HAX-1 overexpression, splicing and cellular localization in tumors.* BMC Cancer, 2010. **10**: p. 76.
111. Siamakpour-Reihani, S., et al., *Grb7 binds to Hax-1 and undergoes an intramolecular domain association that offers a model for Grb7 regulation.* J Mol Recognit, 2011. **24**(2): p. 314-21.
112. Yap, S.V., J.M. Koontz, and A. Kontrogianni-Konstantopoulos, *HAX-1: a family of apoptotic regulators in health and disease.* J Cell Physiol, 2011. **226**(11): p. 2752-61.
113. Simmen, T., *Hax-1: a regulator of calcium signaling and apoptosis progression with multiple roles in human disease.* Expert Opin Ther Targets, 2011. **15**(6): p. 741-51.
114. Wei, X.J., et al., *Expression of HAX-1 in human colorectal cancer and its clinical significance.* Tumour Biol, 2014. **35**(2): p. 1411-5.
115. Baumann, U., et al., *Disruption of the PRKCD-FBXO25-HAX-1 axis attenuates the apoptotic response and drives lymphomagenesis.* Nat Med, 2014. **20**(12): p. 1401-9.
116. Li, X., et al., *Expression and Function of HAX-1 in Human Cutaneous Squamous Cell Carcinoma.* J Cancer, 2015. **6**(4): p. 351-9.
117. Li, X., et al., *Expression of HAX-1 in colorectal cancer and its role in cancer cell growth.* Mol Med Rep, 2015. **12**(3): p. 4071-4078.

118. Yan, J., et al., *HAX-1 inhibits apoptosis in prostate cancer through the suppression of caspase-9 activation.* Oncol Rep, 2015. **34**(5): p. 2776-81.
119. You, B., et al., *Clinical and biological significance of HAX-1 overexpression in nasopharyngeal carcinoma.* Oncotarget, 2016. **7**(11): p. 12505-24.
120. Sheng, C. and Q. Ni, *Expression of HAX1 and Ki-67 in breast cancer and its correlations with patient's clinicopathological characteristics and prognosis.* Int J Clin Exp Med, 2015. **8**(11): p. 20904-10.
121. Sun, X., et al., *MicroRNA-223 Increases the Sensitivity of Triple-Negative Breast Cancer Stem Cells to TRAIL-Induced Apoptosis by Targeting HAX-1.* PLoS One, 2016. **11**(9): p. e0162754.
122. Liu, J., et al., *Inhibition of HAX-1 by miR-125a reverses cisplatin resistance in laryngeal cancer stem cells.* Oncotarget, 2016. **7**(52): p. 86446-86456.
123. Wang, Y., et al., *High expression of HAX-1 protein is associated with tumor growth in papillary thyroid carcinoma.* Int J Clin Exp Pathol, 2018. **11**(4): p. 2080-2087.
124. Feng, X., et al., *HAX-1 overexpression in multiple myeloma is associated with poor survival.* Br J Haematol, 2019. **185**(1): p. 179-183.
125. Qian, B., et al., *Role of the tumour protein P53 gene in human cervical squamous carcinoma cells: Discussing haematopoietic cell-specific protein 1-associated protein X-1-induced survival, migration and proliferation.* Oncol Lett, 2018. **16**(2): p. 2629-2637.
126. Wu, Z., et al., *Hematopoietic-substrate-1 associated protein X-1 (HAX-1) regulates liver cancer cells growth, metastasis, and angiogenesis through Akt.* Cancer Biol Ther, 2019. **20**(9): p. 1223-1233.
127. Li, F., et al., *Expression of Integrin beta6 and HAX-1 Correlates with Aggressive Features and Poor Prognosis in Esophageal Squamous Cell Carcinoma.* Cancer Manag Res, 2020. **12**: p. 9599-9608.
128. Yang, J., et al., *Chemoresistance is associated with overexpression of HAX-1, inhibition of which resensitizes drug-resistant breast cancer cells to chemotherapy.* Tumour Biol, 2017. **39**(3): p. 1010428317692228.
129. Hu, G., et al., *miR-125b regulates the drug-resistance of breast cancer cells to doxorubicin by targeting HAX-1.* Oncol Lett, 2018. **15**(2): p. 1621-1629.
130. Wu, G., et al., *miR-100 Reverses Cisplatin Resistance in Breast Cancer by Suppressing HAX-1.* Cell Physiol Biochem, 2018. **47**(5): p. 2077-2087.
131. Yu, Z., et al., *miR-125b suppresses cell proliferation and metastasis by targeting HAX-1 in esophageal squamous cell carcinoma.* Pathol Res Pract, 2020. **216**(2): p. 152792.
132. Huang, F., et al., *miR-654-5p Targets HAX-1 to Regulate the Malignancy Behaviors of Colorectal Cancer Cells.* Biomed Res Int, 2020. **2020**: p. 4914707.
133. Li, R., J.Z. Zheng, and X. Huang, *Suppression of HAX-1 induced by miR-325 resensitizes bladder cancer cells to cisplatin-induced apoptosis.* Eur Rev Med Pharmacol Sci, 2020. **24**(18): p. 9303-9314.
134. Bassani, R.A., J.W. Bassani, and D.M. Bers, *Mitochondrial and sarcolemmal Ca2+ transport reduce [Ca2+]i during caffeine contractures in rabbit cardiac myocytes.* J Physiol, 1992. **453**: p. 591-608.
135. Keeler, J., *Understanding NMR spectroscopy*. 2nd ed. 2010, Chichester, U.K.: John Wiley and Sons. xiii, 511 p.
136. Levitt, M.H., *Spin dynamics : basics of nuclear magnetic resonance*. 2nd ed. 2008, Chichester, England ; Hoboken, NJ: John Wiley & Sons. xxv, 714 p., 7 p. of plates.

137. Pauli, W., *Zur Quantenmechanik des magnetischen Elektrons.* Zeitschrift für Physik, 1927. **43**(9): p. 601-623.
138. Fermi, E., *Zur Quantelung des idealen einatomigen Gases.* Zeitschrift für Physik, 1926. **36**(11): p. 902-912.
139. Cavanagh, J., *Protein NMR spectroscopy : principles and practice*. 2nd ed. 2007, Amsterdam ; Boston: Academic Press. xxv, 885 p.
140. Duer, M.J., *Solid-state NMR spectroscopy : principles and applications*. 2002, Malden, MA: Blackwell Science. xvii, 567 p.
141. *Encyclopedia of spectroscopy and spectrometry.* Choice: Current Reviews for Academic Libraries, 2011. **48**(10): p. 1880-1880.
142. Ernst, R.R., G. Bodenhausen, and A. Wokaun, *Principles of nuclear magnetic resonance in one and two dimensions*. The International series of monographs on chemistry. 1987, Oxford Oxfordshire

New York: Clarendon Press ;

Oxford University Press. xxiv, 610 p.
143. Lipari, G. and A. Szabo, *Model-Free Approach to the Interpretation of Nuclear Magnetic-Resonance Relaxation in Macromolecules .2. Analysis of Experimental Results.* Journal of the American Chemical Society, 1982. **104**(17): p. 4559-4570.
144. Pu, M., et al., *Correlation of vesicle binding and phospholipid dynamics with phospholipase C activity: insights into phosphatidylcholine activation and surface dilution inhibition.* J Biol Chem, 2009. **284**(24): p. 16099-16107.
145. Marassi, F.M. and S.J. Opella, *A Solid-State NMR Index of Helical Membrane Protein Structure and Topology.* Journal of Magnetic Resonance, 2000. **144**(1): p. 150-155.
146. Ramamoorthy, A. and K. Yamamoto, *A Family of PISEMA Experiments for Structural Studies of Biological Solids*. 2007, Springer Netherlands: Dordrecht. p. 703-709.
147. Ramamoorthy, A., Y.F. Wei, and D.K. Lee, *PISEMA solid-state NMR spectroscopy.* Advances in Solid State Nmr Studies of Materials and Polymers: A Special Volume Dedicated to Isao Ando, 2004. **52**: p. 1-52.
148. Gopinath, T., et al., *Solid-State NMR of Membrane Proteins in Lipid Bilayers: To Spin or Not To Spin?* Acc Chem Res, 2021. **54**(6): p. 1430-1439.
149. *The Structure of Biological Membranes*. Second ed. 2005: CRC Press.
150. Chipot, C., et al., *Perturbations of Native Membrane Protein Structure in Alkyl Phosphocholine Detergents: A Critical Assessment of NMR and Biophysical Studies.* Chem Rev, 2018. **118**(7): p. 3559-3607.
151. Zhou, H.X. and T.A. Cross, *Influences of membrane mimetic environments on membrane protein structures.* Annu Rev Biophys, 2013. **42**: p. 361-92.
152. Ognjenovic, J., R. Grisshammer, and S. Subramaniam, *Frontiers in Cryo Electron Microscopy of Complex Macromolecular Assemblies.* Annu Rev Biomed Eng, 2019.
153. Ladizhansky, V., *Applications of solid-state NMR to membrane proteins.* Biochim Biophys Acta Proteins Proteom, 2017. **1865**(11 Pt B): p. 1577-1586.
154. McDermott, A., *Structure and dynamics of membrane proteins by magic angle spinning solid-state NMR.* Annu Rev Biophys, 2009. **38**: p. 385-403.
155. Gong, X.M., et al., *Nuclear magnetic resonance structural studies of membrane proteins in micelles and bilayers.* Methods Mol Biol, 2007. **400**: p. 515-29.

156. Griffin, R.G., *Dipolar recoupling in MAS spectra of biological solids.* Nat Struct Biol, 1998. **5 Suppl**: p. 508-12.
157. Opella, S.J. and F.M. Marassi, *Structure determination of membrane proteins by NMR spectroscopy.* Chem Rev, 2004. **104**(8): p. 3587-606.
158. Mulder, F.A., et al., *Studying excited states of proteins by NMR spectroscopy.* Nat Struct Biol, 2001. **8**(11): p. 932-5.
159. Gopinath, T. and G. Veglia, *Probing membrane protein ground and conformationally excited states using dipolar- and J-coupling mediated MAS solid state NMR experiments.* Methods, 2018. **148**: p. 115-122.
160. Gustavsson, M., N.J. Traaseth, and G. Veglia, *Probing ground and excited states of phospholamban in model and native lipid membranes by magic angle spinning NMR spectroscopy.* Biochim Biophys Acta, 2012. **1818**(2): p. 146-53.
161. Traaseth, N.J. and G. Veglia, *Probing excited states and activation energy for the integral membrane protein phospholamban by NMR CPMG relaxation dispersion experiments.* Biochim Biophys Acta, 2010. **1798**(2): p. 77-81.
162. Das, N., D.T. Murray, and T.A. Cross, *Lipid bilayer preparations of membrane proteins for oriented and magic-angle spinning solid-state NMR samples.* Nat Protoc, 2013. **8**(11): p. 2256-70.
163. Durr, U.H., M. Gildenberg, and A. Ramamoorthy, *The magic of bicelles lights up membrane protein structure.* Chem Rev, 2012. **112**(11): p. 6054-74.
164. Radoicic, J., S.H. Park, and S.J. Opella, *Macrodiscs Comprising SMALPs for Oriented Sample Solid-State NMR Spectroscopy of Membrane Proteins.* Biophys J, 2018. **115**(1): p. 22-25.
165. Howard, K.P. and S.J. Opella, *High-resolution solid-state NMR spectra of integral membrane proteins reconstituted into magnetically oriented phospholipid bilayers.* Journal of Magnetic Resonance Series B, 1996. **112**(1): p. 91-94.
166. Durr, U.H.N., R. Soong, and A. Ramamoorthy, *When detergent meets bilayer: Birth and coming of age of lipid bicelles.* Progress in Nuclear Magnetic Resonance Spectroscopy, 2013. **69**: p. 1-22.
167. Yamamoto, K., R. Soong, and A. Ramamoorthy, *Comprehensive Analysis of Lipid Dynamics Variation with Lipid Composition and Hydration of Bicelles Using Nuclear Magnetic Resonance (NMR) Spectroscopy.* Langmuir, 2009. **25**(12): p. 7010-7018.
168. Veglia, G., et al., *The Hybrid Solution/Solid-State NMR Method for Membrane Protein Structure Determination.* Comprehensive Biophysics, Vol 1: Biophysical Techniques for Structural Characterization of Macromolecules, 2011: p. 182-198.
169. Hong, M., *Structure, topology, and dynamics of membrane peptides and proteins from solid-state NMR spectroscopy.* J Phys Chem B, 2007. **111**(35): p. 10340-51.
170. Hu, F., W. Luo, and M. Hong, *Mechanisms of proton conduction and gating in influenza M2 proton channels from solid-state NMR.* Science, 2010. **330**(6003): p. 505-8.
171. Sharma, M., et al., *Insight into the Mechanism of the Influenza A Proton Channel from a Structure in a Lipid Bilayer.* Science, 2010. **330**(6003): p. 509-512.
172. Traaseth, N.J., et al., *Structure and topology of monomeric phospholamban in lipid membranes determined by a hybrid solution and solid-state NMR approach.* Proc Natl Acad Sci U S A, 2009. **106**(25): p. 10165-70.
173. Verardi, R., et al., *Probing membrane topology of the antimicrobial peptide distinctin by solid-state NMR spectroscopy in zwitterionic and charged lipid bilayers.* Biochim Biophys Acta, 2011. **1808**(1): p. 34-40.

174. Vostrikov, V.V., et al., *Structural dynamics and topology of phosphorylated phospholamban homopentamer reveal its role in the regulation of calcium transport.* Structure, 2013. **21**(12): p. 2119-30.
175. Mote, K.R., T. Gopinath, and G. Veglia, *Determination of structural topology of a membrane protein in lipid bilayers using polarization optimized experiments (POE) for static and MAS solid state NMR spectroscopy.* J Biomol NMR, 2013. **57**(2): p. 91-102.
176. Hulko, M., et al., *The HAMP domain structure implies helix rotation in transmembrane signaling.* Cell, 2006. **126**(5): p. 929-40.
177. Matthews, E.E., M. Zoonens, and D.M. Engelman, *Dynamic helix interactions in transmembrane signaling.* Cell, 2006. **127**(3): p. 447-50.
178. Cady, S.D., et al., *Determining the orientation of uniaxially rotating membrane proteins using unoriented samples: A (2)H, (13)C, and (15)N solid-state NMR investigation of the dynamics and orientation of a transmembrane helical bundle.* Journal of the American Chemical Society, 2007. **129**(17): p. 5719-5729.
179. Das, B.B., et al., *Structure determination of a membrane protein in proteoliposomes.* J Am Chem Soc, 2012. **134**(4): p. 2047-56.
180. Su, Y., L. Andreas, and R.G. Griffin, *Magic angle spinning NMR of proteins: high-frequency dynamic nuclear polarization and (1)H detection.* Annu Rev Biochem, 2015. **84**: p. 465-97.
181. Ong, Y.S., et al., *Detecting substrates bound to the secondary multidrug efflux pump EmrE by DNP-enhanced solid-state NMR.* J Am Chem Soc, 2013. **135**(42): p. 15754-62.
182. Reif, B., *Deuterated peptides and proteins: structure and dynamics studies by MAS solid-state NMR.* Methods Mol Biol, 2012. **831**: p. 279-301.
183. Wickramasinghe, N.P., et al., *Nanomole-scale protein solid-state NMR by breaking intrinsic 1HT1 boundaries.* Nat Methods, 2009. **6**(3): p. 215-8.
184. Gustavsson, M., et al., *Allosteric regulation of SERCA by phosphorylation-mediated conformational shift of phospholamban.* Proceedings of the National Academy of Sciences, 2013. **110**(43): p. 17338-17343.
185. Gopinath, T. and G. Veglia, *Experimental Aspects of Polarization Optimized Experiments (POE) for Magic Angle Spinning Solid-State NMR of Microcrystalline and Membrane-Bound Proteins.* Methods Mol Biol, 2018. **1688**: p. 37-53.
186. Gopinath, T. and G. Veglia, *3D DUMAS: simultaneous acquisition of three-dimensional magic angle spinning solid-state NMR experiments of proteins.* J Magn Reson, 2012. **220**: p. 79-84.
187. Gopinath, T. and G. Veglia, *Dual acquisition magic-angle spinning solid-state NMR-spectroscopy: simultaneous acquisition of multidimensional spectra of biomacromolecules.* Angew Chem Int Ed Engl, 2012. **51**(11): p. 2731-5.
188. Gopinath, T., K.R. Mote, and G. Veglia, *Simultaneous acquisition of 2D and 3D solid-state NMR experiments for sequential assignment of oriented membrane protein samples.* J Biomol NMR, 2015. **62**(1): p. 53-61.
189. Gopinath, T., et al., *Hybridization of TEDOR and NCX MAS solid-state NMR experiments for simultaneous acquisition of heteronuclear correlation spectra and distance measurements.* J Biomol NMR, 2019.
190. Banigan, J.R. and N.J. Traaseth, *Utilizing afterglow magnetization from cross-polarization magic-angle-spinning solid-state NMR spectroscopy to obtain simultaneous heteronuclear multidimensional spectra.* J Phys Chem B, 2012. **116**(24): p. 7138-44.

191. Gopinath, T., D.K. Weber, and G. Veglia, *Multi-receiver solid-state NMR using polarization optimized experiments (POE) at ultrafast magic angle spinning.* J Biomol NMR, 2020. **74**(4-5): p. 267-285.
192. Gopinath, T. and G. Veglia, *Proton-detected polarization optimized experiments (POE) using ultrafast magic angle spinning solid-state NMR: Multi-acquisition of membrane protein spectra.* J Magn Reson, 2020. **310**: p. 106664.
193. Gopinath, T., et al., *Sensitivity enhanced heteronuclear correlation spectroscopy in multidimensional solid-state NMR of oriented systems via chemical shift coherences.* J Am Chem Soc, 2010. **132**(15): p. 5357-63.
194. Gopinath, T. and G. Veglia, *Sensitivity enhancement in static solid-state NMR experiments via single- and multiple-quantum dipolar coherences.* J Am Chem Soc, 2009. **131**(16): p. 5754-6.
195. Wang, S., T. Gopinath, and G. Veglia, *Application of paramagnetic relaxation enhancements to accelerate the acquisition of 2D and 3D solid-state NMR spectra of oriented membrane proteins.* Methods, 2018. **138-139**: p. 54-61.
196. Wang, S., T. Gopinath, and G. Veglia, *Improving the quality of oriented membrane protein spectra using heat-compensated separated local field experiments.* J Biomol NMR, 2019. **73**(10-11): p. 617-624.
197. Robustelli, P., et al., *Using NMR Chemical Shifts as Structural Restraints in Molecular Dynamics Simulations of Proteins.* Structure, 2010. **18**(8): p. 923-933.
198. Nevzorov, A.A. and S.J. Opella, *Structural fitting of PISEMA spectra of aligned proteins.* J Magn Reson, 2003. **160**(1): p. 33-9.
199. Tian, Y., et al., *A Practical Implicit Membrane Potential for NMR Structure Calculations of Membrane Proteins.* Biophys J, 2015. **109**(3): p. 574-85.
200. Verardi, R., et al., *Structural topology of phospholamban pentamer in lipid bilayers by a hybrid solution and solid-state NMR method.* Proc Natl Acad Sci U S A, 2011. **108**(22): p. 9101-6.
201. De Simone, A., K.R. Mote, and G. Veglia, *Structural Dynamics and Conformational Equilibria of SERCA Regulatory Proteins in Membranes by Solid-State NMR Restrained Simulations.* Biophysical Journal, 2014. **106**(12): p. 2566-2576.
202. Fusco, G., et al., *Structural Ensembles of Membrane-bound alpha-Synuclein Reveal the Molecular Determinants of Synaptic Vesicle Affinity.* Sci Rep, 2016. **6**: p. 27125.
203. Phillips, R., et al., *Emerging roles for lipids in shaping membrane-protein function.* Nature, 2009. **459**(7245): p. 379-385.
204. Popot, J.L., *Do Membrane Proteins Need to Fold in a "Membrane-Mimetic" Environment in Order to Reach a Functional 3D Structure?* Biophysical Journal, 2013. **104**(2): p. 194a-194a.
205. Lee, A.G., *Biological membranes: the importance of molecular detail.* Trends Biochem Sci, 2011. **36**(9): p. 493-500.
206. Gayen, A., J.R. Banigan, and N.J. Traaseth, *Ligand-induced conformational changes of the multidrug resistance transporter EmrE probed by oriented solid-state NMR spectroscopy.* Angew Chem Int Ed Engl, 2013. **52**(39): p. 10321-4.
207. Gustavsson, M., et al., *Allosteric regulation of SERCA by phosphorylation-mediated conformational shift of phospholamban.* Proc Natl Acad Sci U S A, 2013. **110**(43): p. 17338-43.
208. Weber, D.K., et al., *A Bitopic Miniprotein Regulates a Membrane-Embedded Enzyme via Topological Allostery.* Biorxv, 2020. **doi:** https://doi.org/10.1101/2020.08.28.271940.

209. Akin, B.L., et al., *The structural basis for phospholamban inhibition of the calcium pump in sarcoplasmic reticulum.* J Biol Chem, 2013. **288**(42): p. 30181-91.
210. Sekhar, A. and L.E. Kay, *An NMR View of Protein Dynamics in Health and Disease.* Annu Rev Biophys, 2019. **48**: p. 297-319.
211. Andronesi, O.C., et al., *Determination of membrane protein structure and dynamics by magic-angle-spinning solid-state NMR spectroscopy.* J Am Chem Soc, 2005. **127**(37): p. 12965-74.
212. Gopinath, T., S.E.D. Nelson, and G. Veglia, *(1)H-detected MAS solid-state NMR experiments enable the simultaneous mapping of rigid and dynamic domains of membrane proteins.* J Magn Reson, 2017. **285**: p. 101-107.
213. Gopinath, T., et al., *Probing the Conformationally Excited States of Membrane Proteins via (1)H-Detected MAS Solid-State NMR Spectroscopy.* J Phys Chem B, 2017. **121**(17): p. 4456-4465.
214. Fusco, G., et al., *Direct observation of the three regions in alpha-synuclein that determine its membrane-bound behaviour.* Nat Commun, 2014. **5**: p. 3827.
215. Fusco, G., et al., *Structural basis of synaptic vesicle assembly promoted by alpha-synuclein.* Nat Commun, 2016. **7**: p. 12563.
216. Bodner, C.R., et al., *Differential phospholipid binding of alpha-synuclein variants implicated in Parkinson's disease revealed by solution NMR spectroscopy.* Biochemistry, 2010. **49**(5): p. 862-71.
217. Robinson, C.V., A. Sali, and W. Baumeister, *The molecular sociology of the cell.* Nature, 2007. **450**(7172): p. 973-82.
218. Koukos, P.I. and A. Bonvin, *Integrative Modelling of Biomolecular Complexes.* J Mol Biol, 2019.
219. Larsen, E., et al., *Probing Protein-Protein Interactions Using Asymmetric Labeling and Carbonyl-Carbon Selective Heteronuclear NMR Spectroscopy.* Molecules, 2018. **23**(8): p. 1937-1937.
220. Marintchev, A., D. Frueh, and G. Wagner, *NMR Methods for Studying Protein–Protein Interactions Involved in Translation Initiation*, in *Methods in Enzymology*, J. Lorsch, Editor. 2007, Academic Press. p. 283-331.
221. Tord, B., L. Sara, and J. Peter, *Methods for the detection and analysis of protein–protein interactions.* PROTEOMICS, 2007. **7**(16): p. 2833-2842.
222. Ngounou Wetie, A.G., et al., *Investigation of stable and transient protein-protein interactions: past, present and future.* Proteomics, 2013. **13**(0): p. 10.1002/pmic.201200328.
223. Barile, E. and M. Pellecchia, *NMR-Based Approaches for the Identification and Optimization of Inhibitors of Protein–Protein Interactions.* Chemical Reviews, 2014. **114**(9): p. 4749-4763.
224. Zuiderweg, E.R.P., *Mapping Protein−Protein Interactions in Solution by NMR Spectroscopy.* Biochemistry, 2002. **41**(1): p. 1-7.
225. Nishida, N. and I. Shimada, *An NMR Method to Study Protein–Protein Interactions*, in *Integrin and Cell Adhesion Molecules: Methods and Protocols*, M. Shimaoka, Editor. 2012, Humana Press: Totowa, NJ. p. 129-137.
226. Ishima, R. and D.A. Torchia, *Protein dynamics from NMR.* Nature Structural Biology, 2000. **7**: p. 740.
227. Kay, L.E., *Protein dynamics from NMR.* Biochemistry and Cell Biology, 1998. **76**(2-3): p. 145-152.
228. Kempf, J.G. and J.P. Loria, *Protein dynamics from solution NMR.* Cell Biochemistry and Biophysics, 2002. **37**(3): p. 187-211.

229. Olivieri, C., et al., *Simultaneous detection of intra- and inter-molecular paramagnetic relaxation enhancements in protein complexes.* Journal of Biomolecular NMR, 2018. **70**(3): p. 133-140.
230. Park, S.H., et al., *Paramagnetic relaxation enhancement of membrane proteins by incorporation of the metal-chelating unnatural amino acid 2-amino-3-(8-hydroxyquinolin-3-yl)propanoic acid (HQA).* J Biomol NMR, 2015. **61**(3-4): p. 185-96.
231. Gong, Z., C.D. Schwieters, and C. Tang, *Theory and practice of using solvent paramagnetic relaxation enhancement to characterize protein conformational dynamics.* Methods, 2018.
232. Pervushin, K., et al., *Transverse Relaxation-Optimized Spectroscopy (TROSY) for NMR Studies of Aromatic Spin Systems in 13C-Labeled Proteins.* Journal of the American Chemical Society, 1998. **120**(25): p. 6394-6400.
233. Tugarinov, V., P.M. Hwang, and L.E. Kay, *Nuclear Magnetic Resonance Spectroscopy of High-Molecular-Weight Proteins.* Annual Review of Biochemistry, 2004. **73**(1): p. 107-146.
234. Gardner, K.H., et al., *Solution NMR Studies of a 42 KDa Escherichia Coli Maltose Binding Protein/β-Cyclodextrin Complex: Chemical Shift Assignments and Analysis.* Journal of the American Chemical Society, 1998. **120**(45): p. 11738-11748.
235. Walters, K.J., et al., *[11] - Characterizing Protein-Protein Complexes and Oligomers by Nuclear Magnetic Resonance Spectroscopy*, in *Methods in Enzymology*, T.L. James, V. Dötsch, and U. Schmitz, Editors. 2001, Academic Press. p. 238-258.
236. Göbl, C., et al., *NMR approaches for structural analysis of multidomain proteins and complexes in solution.* Progress in Nuclear Magnetic Resonance Spectroscopy, 2014. **80**: p. 26-63.
237. Keskin, O., N. Tuncbag, and A. Gursoy, *Predicting Protein-Protein Interactions from the Molecular to the Proteome Level.* Chem Rev, 2016. **116**(8): p. 4884-909.
238. Jones, S. and J.M. Thornton, *Principles of protein-protein interactions.* Proc Natl Acad Sci U S A, 1996. **93**(1): p. 13-20.
239. Zhang, X., et al., *Protein-protein interactions among signaling pathways may become new therapeutic targets in liver cancer.* Oncology Reports, 2016. **35**(2): p. 625-638.
240. Braun, P. and A.C. Gingras, *History of protein-protein interactions: from egg-white to complex networks.* Proteomics, 2012. **12**(10): p. 1478-98.
241. Andreani, J. and R. Guerois, *Evolution of protein interactions: from interactomes to interfaces.* Arch Biochem Biophys, 2014. **554**: p. 65-75.
242. Lage, K., *Protein-protein interactions and genetic diseases: The interactome.* Biochim Biophys Acta, 2014. **1842**(10): p. 1971-1980.
243. Bhattacharya, A., Y.C. Kim, and J. Mittal, *Protein-protein interactions in a crowded environment.* Biophys Rev, 2013. **5**(2): p. 99-108.
244. Vuister, G.W., A.C. Wang, and A. Bax, *Measurement of three-bond nitrogen-carbon J couplings in proteins uniformly enriched in nitrogen-15 and carbon-13.* Journal of the American Chemical Society, 1993. **115**(12): p. 5334-5335.
245. Montelione, G.T., et al., *Accurate measurements of long-range heteronuclear coupling constants from homonuclear 2D NMR spectra of isotope-enriched proteins.* Journal of Magnetic Resonance (1969), 1989. **82**(1): p. 198-204.

246. Wider, G., et al., *A heteronuclear three-dimensional NMR experiment for measurements of small heteronuclear coupling constants in biological macromolecules.* Journal of Magnetic Resonance (1969), 1989. **85**(2): p. 426-431.
247. Kurz, M., P. Schmieder, and H. Kessler, *HETLOC, an Efficient Method for Determining Heteronuclear Long-Range Couplings with Heteronuclei in Natural Abundance.* Angewandte Chemie International Edition in English, 1991. **30**(10): p. 1329-1331.
248. Edison, A.S., W.M. Westler, and J.L. Markley, *Elucidation of amino acid spin systems in proteins and determination of heteronuclear coupling constants by carbon-proton-proton three-dimensional NMR.* Journal of Magnetic Resonance (1969), 1991. **92**(2): p. 434-438.
249. Xu, R.X., E.T. Olejniczak, and S.W. Fesik, *Stereospecific assignments and χ1 rotamers for FKBP when bound to ascomycin from 3JHα,Hβ and 3JN,Hβ coupling constants.* FEBS Letters, 1992. **305**(2): p. 137-143.
250. Sattler, M., H. Schwalbe, and C. Griesinger, *Stereospecific assignment of leucine methyl groups with carbon-13 in natural abundance or with random 13C labeling.* Journal of the American Chemical Society, 1992. **114**(3): p. 1126-1127.
251. Tonelli, M., et al., *Carbonyl carbon label selective (CCLS) (1)H–(15)N HSQC experiment for improved detection of backbone (13)C–(15)N cross peaks in larger proteins.* Journal of biomolecular NMR, 2007. **39**(3): p. 177-185.
252. Taylor, S.S., et al., *PKA: a portrait of protein kinase dynamics.* Biochimica et biophysica acta, 2004. **1697**(1-2): p. 259-269.
253. Taylor, S.S., et al., *Dynamics of signaling by PKA.* Biochimica et Biophysica Acta (BBA) - Proteins and Proteomics, 2005. **1754**(1): p. 25-37.
254. Langer, T., et al., *NMR Backbone Assignment of a Protein Kinase Catalytic Domain by a Combination of Several Approaches: Application to the Catalytic Subunit of cAMP-Dependent Protein Kinase.* ChemBioChem, 2004. **5**(11): p. 1508-1516.
255. Langer, T., et al., *Folding and activity of cAMP-dependent protein kinase mutants.* FEBS Letters, 2005. **579**(19): p. 4049-4054.
256. Vogtherr, M., et al., *NMR backbone assignment of the mitogen-activated protein (MAP) kinase p38.* Journal of Biomolecular NMR, 2005. **32**(2): p. 175-175.
257. Vogtherr, M., et al., *NMR Characterization of Kinase p38 Dynamics in Free and Ligand-Bound Forms.* Angewandte Chemie International Edition, 2006. **45**(6): p. 993-997.
258. Masterson, L.R., et al., *Backbone NMR resonance assignment of the catalytic subunit of cAMP-dependent protein kinase A in complex with AMP-PNP.* Biomolecular NMR Assignments, 2009. **3**(1): p. 115-117.
259. Masterson, L.R., et al., *Dynamically committed, uncommitted, and quenched states encoded in protein kinase A revealed by NMR spectroscopy.* Proceedings of the National Academy of Sciences, 2011. **108**(17): p. 6969-6974.
260. Srivastava, Atul K., et al., *Synchronous Opening and Closing Motions Are Essential for cAMP-Dependent Protein Kinase A Signaling.* Structure, 2014. **22**(12): p. 1735-1743.
261. Kim, J., et al., *A dynamic hydrophobic core orchestrates allostery in protein kinases.* Science Advances, 2017. **3**(4).
262. Dalton, G.D. and W.L. Dewey, *Protein kinase inhibitor peptide (PKI): A family of endogenous neuropeptides that modulate neuronal cAMP-dependent protein kinase function.* Neuropeptides, 2006. **40**(1): p. 23-34.

263. Mori, S., et al., *Improved Sensitivity of HSQC Spectra of Exchanging Protons at Short Interscan Delays Using a New Fast HSQC (FHSQC) Detection Scheme That Avoids Water Saturation.* Journal of Magnetic Resonance, Series B, 1995. **108**(1): p. 94-98.
264. Masterson, L.R., et al., *Simultaneous Detection and Deconvolution of Congested NMR Spectra Containing Three Isotopically Labeled Species.* Journal of the American Chemical Society, 2008. **130**(25): p. 7818-7819.
265. Wirmer, J. and H. Schwalbe, *Angular dependence of 1J(Ni,Cα i) and 2J(Ni,Cα (i − 1)) coupling constants measured in J-modulated HSQCs.* Journal of Biomolecular NMR, 2002. **23**(1): p. 47-55.
266. Traaseth, N.J., R. Verardi, and G. Veglia, *Asymmetric methyl group labeling as a probe of membrane protein homo-oligomers by NMR spectroscopy.* J Am Chem Soc, 2008. **130**(8): p. 2400-1.
267. Verardi, R., et al., *Isotope labeling for solution and solid-state NMR spectroscopy of membrane proteins.* Adv Exp Med Biol, 2012. **992**: p. 35-62.
268. Walters, K.J., et al., *Characterizing protein-protein complexes and oligomers by nuclear magnetic resonance spectroscopy.* Methods Enzymol, 2001. **339**: p. 238-58.
269. Atreya, H.S., *Isotope labeling in biomolecular NMR*. Advances in experimental medicine and biology. 2012, Dordrecht ; New York: Springer. viii, 219 p.
270. Anglister, J., G. Srivastava, and F. Naider, *Detection of intermolecular NOE interactions in large protein complexes.* Prog Nucl Magn Reson Spectrosc, 2016. **97**: p. 40-56.
271. Anglister, J., R. Levy, and T. Scherf, *Interactions of antibody aromatic residues with a peptide of cholera toxin observed by two-dimensional transferred nuclear Overhauser effect difference spectroscopy.* Biochemistry, 1989. **28**(8): p. 3360-5.
272. Scherf, T. and J. Anglister, *A T1 rho-filtered two-dimensional transferred NOE spectrum for studying antibody interactions with peptide antigens.* Biophys J, 1993. **64**(3): p. 754-61.
273. Hansen, D.F., et al., *Probing Chemical Shifts of Invisible States of Proteins with Relaxation Dispersion NMR Spectroscopy: How Well Can We Do?* Journal of the American Chemical Society, 2008. **130**(8): p. 2667-2675.
274. Lundström, P., et al., *Fractional 13C enrichment of isolated carbons using [1-13C]- or [2-13C]-glucose facilitates the accurate measurement of dynamics at backbone Cα and side-chain methyl positions in proteins.* Journal of Biomolecular NMR, 2007. **38**(3): p. 199-212.
275. LeMaster, D.M. and D.M. Kushlan, *Dynamical Mapping of E. coli Thioredoxin via 13C NMR Relaxation Analysis.* Journal of the American Chemical Society, 1996. **118**(39): p. 9255-9264.
276. Takeuchi, K., et al., *1-13C amino acid selective labeling in a 2H15N background for NMR studies of large proteins.* Journal of Biomolecular NMR, 2007. **38**(1): p. 89-98.
277. Takeuchi, K., Z.-Y.J. Sun, and G. Wagner, *Alternate 13C−12C Labeling for Complete Mainchain Resonance Assignments using Cα Direct-Detection with Applicability Toward Fast Relaxing Protein Systems.* Journal of the American Chemical Society, 2008. **130**(51): p. 17210-17211.
278. Prestegard, J.H., C.M. Bougault, and A.I. Kishore, *Residual Dipolar Couplings in Structure Determination of Biomolecules.* Chemical Reviews, 2004. **104**(8): p. 3519-3540.

279. Lipsitz, R.S. and N. Tjandra, *Residual Dipolar Couplings in NMR Structure Analysis.* Annual Review of Biophysics and Biomolecular Structure, 2004. **33**(1): p. 387-413.
280. Bax, A. and A. Grishaev, *Weak alignment NMR: a hawk-eyed view of biomolecular structure.* Current Opinion in Structural Biology, 2005. **15**(5): p. 563-570.
281. Tolman, J.R. and K. Ruan, *NMR Residual Dipolar Couplings as Probes of Biomolecular Dynamics.* Chemical Reviews, 2006. **106**(5): p. 1720-1736.
282. Ottiger, M., F. Delaglio, and A. Bax, *Measurement ofJand Dipolar Couplings from Simplified Two-Dimensional NMR Spectra.* Journal of Magnetic Resonance, 1998. **131**(2): p. 373-378.
283. Ding, K. and A.M. Gronenborn, *Sensitivity-enhanced 2D IPAP, TROSY–anti-TROSY, and E.COSY experiments: alternatives for measuring dipolar 15N–1HN couplings.* Journal of Magnetic Resonance, 2003. **163**(2): p. 208-214.
284. Tonelli, M., et al., *One-Sample Approach to Determine the Relative Orientations of Proteins in Ternary and Binary Complexes from Residual Dipolar Coupling Measurements.* Journal of the American Chemical Society, 2009. **131**(40): p. 14138-14139.
285. Sharff, A.J., et al., *Crystallographic evidence of a large ligand-induced hinge-twist motion between the two domains of the maltodextrin binding protein involved in active transport and chemotaxis.* Biochemistry, 1992. **31**(44): p. 10657-10663.
286. Vijay-Kumar, S., C.E. Bugg, and W.J. Cook, *Structure of ubiquitin refined at 1.8Åresolution.* Journal of Molecular Biology, 1987. **194**(3): p. 531-544.
287. Clore, G.M. and J. Iwahara, *Theory, Practice, and Applications of Paramagnetic Relaxation Enhancement for the Characterization of Transient Low-Population States of Biological Macromolecules and Their Complexes.* Chemical Reviews, 2009. **109**(9): p. 4108-4139.
288. Solomon, I., *Relaxation Processes in a System of Two Spins.* Physical Review, 1955. **99**(2): p. 559-565.
289. Iwahara, J., C. Tang, and G.M. Clore, *Practical Aspects of (1)H Transverse Paramagnetic Relaxation Enhancement Measurements on Macromolecules.* Journal of magnetic resonance (San Diego, Calif. : 1997), 2007. **184**(2): p. 185-195.
290. Janowska, M.K. and J. Baum, *Intermolecular Paramagnetic Relaxation Enhancement (PRE) Studies of Transient Complexes in Intrinsically Disordered Proteins.* Methods Mol Biol, 2016. **1345**: p. 45-53.
291. Newby, F.N., et al., *Structure-Free Validation of Residual Dipolar Coupling and Paramagnetic Relaxation Enhancement Measurements of Disordered Proteins.* Biochemistry, 2015. **54**(46): p. 6876-86.
292. Eliezer, D., *Distance information for disordered proteins from NMR and ESR measurements using paramagnetic spin labels.* Methods Mol Biol, 2012. **895**: p. 127-38.
293. Mainz, A., et al., *NMR Spectroscopy of Soluble Protein Complexes at One Mega-Dalton and Beyond.* Angewandte Chemie International Edition, 2013. **52**(33): p. 8746-8751.
294. Tzakos, A.G., et al., *NMR TECHNIQUES FOR VERY LARGE PROTEINS AND RNAS IN SOLUTION.* Annual Review of Biophysics and Biomolecular Structure, 2006. **35**(1): p. 319-342.

295. Manu, V.S. and G. Veglia, *Genetic algorithm optimized triply compensated pulses in NMR spectroscopy.* Journal of Magnetic Resonance, 2015. **260**: p. 136-143.
296. Xia, Y., et al., *Enhancing the sensitivity of multidimensional NMR experiments by using triply-compensated pi pulses.* J Biomol NMR, 2017. **69**(4): p. 237-243.
297. Weber, D.K., et al., *Cysteine-ethylation of tissue-extracted membrane proteins as a tool to detect conformational states by solid-state NMR spectroscopy*. 2019, Elsevier Inc. p. 281-304.
298. Chipot, C., et al., *Perturbations of Native Membrane Protein Structure in Alkyl Phosphocholine Detergents: A Critical Assessment of NMR and Biophysical Studies.* Chemical Reviews, 2018. **118**(7): p. 3559-3607.
299. Verardi, R., et al., *Isotope Labeling for Solution and Solid-State NMR Spectroscopy of Membrane Proteins*, in *Isotope labeling in Biomolecular NMR*, H.S. Atreya, Editor. 2012, Springer Netherlands: Dordrecht. p. 35-62.
300. Iwai, H. and S. Züger, *Protein Ligation: Applications in NMR Studies of Proteins.* Biotechnology and Genetic Engineering Reviews, 2007. **24**(1): p. 129-146.
301. Prestegard, J.H., et al., *Sparse labeling of proteins: Structural characterization from long range constraints.* Journal of Magnetic Resonance, 2014. **241**(1): p. 32-40.
302. Walters, K.J., et al., *Characterizing Protein-Protein Complexes and Oligomers by Nuclear Magnetic Resonance Spectroscopy*, in *Nuclear Magnetic Resonance of Biological Macromolecules - Part B*, V.D. Thomas L. James, Uli Schmitz, Editor. 2001, Elsevier Masson SAS. p. 238-258.
303. Xu, R., et al., *Chemical ligation of folded recombinant proteins: Segmental isotopic labeling of domains for NMR studies.* Proceedings of the National Academy of Sciences, 1999. **96**(2): p. 388-393.
304. Debelouchina, G.T. and T.W. Muir, *A molecular engineering toolbox for the structural biologist.* Quarterly Reviews of Biophysics, 2017. **50**: p. e7-e7.
305. Boutureira, O. and G.J.L. Bernardes, *Advances in Chemical Protein Modification.* Chemical Reviews, 2015. **115**(5): p. 2174-2195.
306. Vostrikov, V.V., et al., *Ca(2+) ATPase Conformational Transitions in Lipid Bilayers Mapped by Site-directed Ethylation and Solid-State NMR.* ACS chemical biology, 2016. **11**(2): p. 329-34.
307. Religa, T.L., et al., *Site-Directed Methyl Group Labeling as an NMR Probe of Structure and Dynamics in Supramolecular Protein Systems: Applications to the Proteasome and to the ClpP Protease.* Journal of the American Chemical Society, 2011. **133**(23): p. 9063-9068.
308. Takegoshi, K., S. Nakamura, and T. Terao, *^{13}C-^{1}H dipolar-assisted rotational resonance in magic-angle spinning NMR.* Chemical Physics Letters, 2001. **344**(5-6): p. 631-637.
309. Kenyon, G.L. and T.W. Bruice, *Novel Sulfhydryl Reagents*, in *Methods in Enzymology*. 1977. p. 407-430.
310. Toyoshima, C., *Structural aspects of ion pumping by Ca^{2+}-ATPase of sarcoplasmic reticulum.* Archives of Biochemistry and Biophysics, 2008. **476**(1): p. 3-11.
311. Hayashi, S., et al., *Studies on Antitumor Substances. III. Syntheses of Bis(methanesulphonylthio)alkanes.* Chemical & Pharmaceutical Bulletin, 1964. **12**(11): p. 1271-1276.
312. Pachter, I.J. and M.L. Scheinbaum, *Trimethylene dithiotosylate and ethylene dithiotosylate.* Organic Syntheses, 1974. **54**(September): p. 33-33.

313. Weidner, J.P. and S.S. Block, *Alkyl and Aryl Thiolsulfonates.* Journal of Medicinal Chemistry, 1964. **7**(5): p. 671-673.
314. Gottlieb, H.E., V. Kotlyar, and A. Nudelman, *NMR chemical shifts of common laboratory solvents as trace impurities.* Journal of Organic Chemistry, 1997. **62**(21): p. 7512-7515.
315. Fernandez, J., M. Rosemblatt, and C. Hidalgo, *Highly purified sarcoplasmic reticulum vesicles are devoid of $^{Ca2+}$-independent ('basal') ATPase activity.* Biochimica et Biophysica Acta (BBA) - Biomembranes, 1980. **599**(2): p. 552-568.
316. Stokes, D.L. and N. Michael Green, *Structure of CaATPase: Electron microscopy of frozen-hydrated crystals at 6 Å resolution in projection.* Journal of Molecular Biology, 1990. **213**(3): p. 529-538.
317. Reddy, L.G., et al., *Defining the Molecular Components of Calcium Transport Regulation in a Reconstituted Membrane System.* Biochemistry, 2003. **42**(15): p. 4585-4592.
318. Le Maire, M., et al., *Mode of Interaction of Polyoxyethyleneglycol Detergents with Membrane Proteins.* European Journal of Biochemistry, 1983. **129**(3): p. 525-532.
319. Rigaud, J.L., et al., *Detergent removal by non-polar polystyrene beads: Applications to membrane protein reconstitution and two-dimensional crystallization.* European Biophysics Journal, 1998. **27**(4): p. 305-319.
320. Morcombe, C.R. and K.W. Zilm, *Chemical shift referencing in MAS solid state NMR.* Journal of Magnetic Resonance, 2003. **162**(2): p. 479-486.
321. Delaglio, F., et al., *NMRPipe: A multidimensional spectral processing system based on UNIX pipes.* Journal of Biomolecular NMR, 1995. **6**(3): p. 277-293.
322. Hartmann, S.R. and E.L. Hahn, *Nuclear Double Resonance in the Rotating Frame.* Physical Review, 1962. **128**(5): p. 2042-2053.
323. Michaeli, S., et al., *Transverse relaxation in the rotating frame induced by chemical exchange.* Journal of Magnetic Resonance, 2004. **169**(2): p. 293-299.
324. Metz, G., X.L. Wu, and S.O. Smith, *Ramped-Amplitude Cross Polarization in Magic-Angle-Spinning NMR.* Journal of Magnetic Resonance, Series A, 1994. **110**(2): p. 219-227.
325. Hediger, S., B.H. Meier, and R.R. Ernst, *Adiabatic passage Hartmann-Hahn cross polarization in NMR under magic angle sample spinning.* Chemical Physics Letters, 1995. **240**(5-6): p. 449-456.
326. Hediger, S., et al., *NMR cross polarization by adiabatic passage through the Hartmann-Hahn condition (APHH).* Chemical Physics Letters, 1994. **223**(4): p. 283-288.
327. Fung, B.M., A.K. Khitrin, and K. Ermolaev, *An Improved Broadband Decoupling Sequence for Liquid Crystals and Solids.* Journal of Magnetic Resonance, 2000. **142**(1): p. 97-101.
328. Bennett, A.E., et al., *Heteronuclear decoupling in rotating solids.* The Journal of Chemical Physics, 1995. **103**(16): p. 6951-6958.
329. Wickramasinghe, N.P., et al., *Sensitivity enhancement in ^{13}C solid-state NMR of protein microcrystals by use of paramagnetic metal ions for optimizing ^{1}H T_1 relaxation.* Journal of Magnetic Resonance, 2007. **184**(2): p. 350-356.
330. Ishii, Y., et al., *Progress in proton-detected solid-state NMR (SSNMR): Super-fast 2D SSNMR collection for nano-mole-scale proteins.* Journal of Magnetic Resonance, 2018. **286**: p. 99-109.

331. Morris, G.A. and R. Freeman, *Enhancement of nuclear magnetic resonance signals by polarization transfer.* Journal of the American Chemical Society, 1979. **101**(3): p. 760-762.
332. Gopinath, T., et al., *Probing the Conformationally Excited States of Membrane Proteins via ^{1}H-Detected MAS Solid-State NMR Spectroscopy.* The Journal of Physical Chemistry B, 2017. **121**(17): p. 4456-4465.
333. Andronesi, O.C., et al., *Determination of Membrane Protein Structure and Dynamics by Magic-Angle-Spinning Solid-State NMR Spectroscopy.* Journal of the American Chemical Society, 2005. **127**(37): p. 12965-12974.
334. van Rossum, B.J., H. Förster, and H.J.M. de Groot, *High-Field and High-Speed CP-MAS ^{13}C NMR Heteronuclear Dipolar-Correlation Spectroscopy of Solids with Frequency-Switched Lee–Goldburg Homonuclear Decoupling.* Journal of Magnetic Resonance, 1997. **124**(2): p. 516-519.
335. Lee, M. and W.I. Goldburg, *Nuclear-magnetic-resonance line narrowing by a rotating rf field.* Physical Review, 1965. **140**(4A): p. A1261-A1271.
336. Szeverenyi, N.M., M.J. Sullivan, and G.E. Maciel, *Observation of spin exchange by two-dimensional fourier transform 13C cross polarization-magic-angle spinning.* Journal of Magnetic Resonance (1969), 1982. **47**(3): p. 462-475.
337. Weingarth, M., et al., *Improved magnetization transfer in solid-state NMR with fast magic angle spinning.* Chemical Physics Letters, 2009. **469**(4-6): p. 342-348.
338. Hu, B., et al., *Broad-band homo-nuclear correlations assisted by ^{1}H irradiation for bio-molecules in very high magnetic field at fast and ultra-fast MAS frequencies.* Journal of Magnetic Resonance, 2011. **212**(2): p. 320-329.
339. Chen, L., et al., *Constant-Time Through-Bond ^{13}C Correlation Spectroscopy for Assigning Protein Resonances with Solid-State NMR Spectroscopy.* Journal of the American Chemical Society, 2006. **128**(31): p. 9992-9993.
340. Wawrzynow, A., J.H. Collins, and C. Coan, *An iodoacetamide spin-label selectively labels a cysteine side chain in an occluded site on the sarcoplasmic reticulum calcium-ATPase.* Biochemistry, 1993. **32**(40): p. 10803-10811.
341. Abraham, S.J., et al., *^{13}C NMR detects conformational change in the 100-kDa membrane transporter ClC-ec1.* Journal of Biomolecular NMR, 2015. **61**(3-4): p. 209-226.
342. Galiakhmetov, A.R., et al., *Application of methyl-TROSY to a large paramagnetic membrane protein without perdeuteration: ^{13}C-MMTS-labeled NADPH-cytochrome P450 oxidoreductase.* Journal of Biomolecular NMR, 2018. **70**(1): p. 21-31.
343. Larda, S.T., et al., *Lysine methylation strategies for characterizing protein conformations by NMR.* Journal of Biomolecular NMR, 2012. **54**(2): p. 199-209.
344. Cady, S.D., et al., *Determining the orientation of uniaxially rotating membrane proteins using unoriented samples: A 2H, 13C, and 15N solid-state NMR investigation of the dynamics and orientation of a transmembrane helical bundle.* Journal of the American Chemical Society, 2007. **129**(17): p. 5719-5729.
345. Tugarinov, V., J.E. Ollerenshaw, and L.E. Kay, *Probing Side-Chain Dynamics in High Molecular Weight Proteins by Deuterium NMR Spin Relaxation: An Application to an 82-kDa Enzyme.* Journal of the American Chemical Society, 2005. **127**(22): p. 8214-8225.
346. Strandberg, E., et al., *Orientation and dynamics of peptides in membranes calculated from ^{2}H-NMR data.* Biophysical Journal, 2009. **96**(8): p. 3223-3232.
347. Galan, S.R.G., et al., *Post-translational site-selective protein backbone α-deuteration.* Nature Chemical Biology, 2018. **14**(10): p. 955-963.

348. Wang, M., et al., *Fast Magic-Angle Spinning ^{19}F NMR Spectroscopy of HIV-1 Capsid Protein Assemblies.* Angewandte Chemie International Edition, 2018: p. 5-10.
349. Prosser, R.S. and T.H. Kim, *Nuts and Bolts of CF_3 and CH_3 NMR Toward the Understanding of Conformational Exchange of GPCRs*, in *G Protein-Coupled Receptors in Drug Discovery*, M. Filizola, Editor. 2015. p. 39-51.
350. Kalbitzer, H.R., et al., *A new high sensitivity ^{19}F probe for labeling cysteine groups of proteins.* NMR in Biomedicine, 1992. **5**(6): p. 347-350.
351. Liu, J.J., et al., *Biased signaling pathways in β2-adrenergic receptor characterized by ^{19}F-NMR.* Science, 2012. **335**(6072): p. 1106-1110.
352. Manglik, A., et al., *Structural Insights into the Dynamic Process of β2-Adrenergic Receptor Signaling.* Cell, 2015. **161**(5): p. 1101-1111.
353. Shekhawat, S.S., et al., *Simultaneous Detection of Distinct Ubiquitin Chain Topologies by ^{19}F NMR.* ACS Chemical Biology, 2014. **9**(10): p. 2229-2236.
354. Ye, L., et al., *A comparison of chemical shift sensitivity of trifluoromethyl tags: optimizing resolution in ^{19}F NMR studies of proteins.* Journal of Biomolecular NMR, 2015. **62**(1): p. 97-103.
355. Richards, P.G., et al., *Electrochemical modification of lysozyme: Anodic reaction of tyrosine residues.* Enzyme and Microbial Technology, 1994. **16**(9): p. 795-801.
356. Jeuken, L.J.C., *Electrodes for integral membrane enzymes.* Natural Product Reports, 2009. **26**(10): p. 1234-1240.
357. Hebel, D., et al., *First direct fluorination of tyrosine-containing biologically active peptides.* Tetrahedron Letters, 1990. **31**(5): p. 619-622.
358. Hattori, Y., et al., *Protein ^{19}F-labeling using transglutaminase for the NMR study of intermolecular interactions.* Journal of Biomolecular NMR, 2017. **68**(4): p. 271-279.
359. Larda, S.T., D. Pichugin, and R.S. Prosser, *Site-Specific Labeling of Protein Lysine Residues and N-Terminal Amino Groups with Indoles and Indole-Derivatives.* Bioconjugate Chemistry, 2015. **26**(12): p. 2376-2383.
360. Mehta, V.D., et al., *Fluorinated Proteins as Potential ^{19}F Magnetic Resonance Imaging and Spectroscopy Agents.* Bioconjugate Chemistry, 1994. **5**(3): p. 257-261.
361. Abraham, S.J., S. Hoheisel, and V. Gaponenko, *Detection of protein–ligand interactions by NMR using reductive methylation of lysine residues.* Journal of Biomolecular NMR, 2008. **42**(2): p. 143-148.
362. Xie, Q., D.B. Fulton, and A.H. Andreotti, *A selective NMR probe to monitor the conformational transition from inactive to active kinase.* ACS Chemical Biology, 2015. **10**(1): p. 262-268.
363. Yokoyama, S., *Protein expression systems for structural genomics and proteomics.* Current Opinion in Chemical Biology, 2003. **7**(1): p. 39-43.
364. Zhang, M., E. Thulin, and H.J. Vogel, *Reductive methylation and pKa determination of the lysine side chains in calbindin D9k.* Journal of Protein Chemistry, 1994. **13**(6): p. 527-535.
365. Moore, G.R., et al., *Nε,Nε-dimethyl-lysine cytochrome c as an NMR probe for lysine involvement in protein-protein complex formation.* Biochemical Journal, 1998. **332**(Pt 2): p. 439-449.
366. Rayment, I., *Reductive alkylation of lysine residues to alter crystallization properties of proteins*, in *Methods in Enzymology*. 1997. p. 171-179.

367. Rypniewski, W.R., H.M. Holden, and I. Rayment, *Structural Consequences of Reductive Methylation of Lysine Residues in Hen Egg White Lysozyme: An X-ray Analysis at 1.8-Å Resolution.* Biochemistry, 1993. **32**(37): p. 9851-9858.
368. White, H.D. and I. Rayment, *Kinetic Characterization of Reductively Methylated Myosin Subfragment.* Biochemistry, 1993. **32**(37): p. 9859-9865.
369. Andrews, S.J. and J.A. Rothnagel, *Emerging evidence for functional peptides encoded by short open reading frames.* Nature Reviews: Genetics, 2014. **15**(3): p. 193-204.
370. Anderson, D.M., et al., *Widespread control of calcium signaling by a family of SERCA-inhibiting micropeptides.* Science Signaling, 2016. **9**(457): p. ra119-ra119.
371. Ma, J., et al., *Discovery of human sORF-encoded polypeptides (SEPs) in cell lines and tissue.* Journal of Proteome Research, 2014. **13**(3): p. 1757-1765.
372. Slavoff, S.A., et al., *Peptidomic discovery of short open reading frame–encoded peptides in human cells.* Nature Chemical Biology, 2013. **9**(1): p. 59-64.
373. Tada, M., et al., *Mechanism of the stimulation of Ca2+-dependent ATPase of cardiac sarcoplasmic reticulum by adenosine 3':5'-monophosphate-dependent protein kinase. Role of the 22,000-dalton protein.* Journal of Biological Chemistry, 1979. **254**(2): p. 319-326.
374. Bers, D.M., *Cardiac excitation–contraction coupling.* Nature, 2002. **415**(6868): p. 198-205.
375. Dyla, M., et al., *Structure and Mechanism of P-Type ATPase Ion Pumps.* Annual Review of Biochemistry, 2020. **89**(1): p. 583-603.
376. Ferrington, D.A., et al., *Comparable levels of Ca-ATPase inhibition by phospholamban in slow-twitch skeletal and cardiac sarcoplasmic reticulum.* Biochemistry, 2002. **41**(44): p. 13289-13296.
377. MacLennan, D.H. and E.G. Kranias, *Phospholamban: a crucial regulator of cardiac contractility.* Nature reviews: Molecular cell biology, 2003. **4**(7): p. 566-577.
378. Chu, G., et al., *A single site (Ser16) phosphorylation in phospholamban is sufficient in mediating its maximal cardiac responses to β-agonists.* Journal of Biological Chemistry, 2000. **275**(49): p. 38938-38943.
379. Segrest, J.P., et al., *Amphipathic helix motif: Classes and properties.* Proteins: Structure, Function, and Bioinformatics, 1990. **8**(2): p. 103-117.
380. James, Z.M., et al., *Protein-protein interactions in calcium transport regulation probed by saturation transfer electron paramagnetic resonance.* Biophysical Journal, 2012. **103**(6): p. 1370-1378.
381. Karim, C.B., et al., *Phosphorylation-dependent Conformational Switch in Spin-labeled Phospholamban Bound to SERCA.* Journal of Molecular Biology, 2006. **358**(4): p. 1032-1040.
382. Toyoshima, C., et al., *Modeling of the inhibitory interaction of phospholamban with the Ca2+ ATPase.* Proceedings of the National Academy of Sciences, 2003. **100**(2): p. 467-472.
383. Seidel, K., et al., *Structural characterization of Ca2+-ATPase-bound phospholamban in lipid bilayers by solid-state nuclear magnetic resonance (NMR) spectroscopy.* Biochemistry, 2008. **47**(15): p. 4369-4376.
384. Akin, B.L., et al., *The Structural Basis for Phospholamban Inhibition of the Calcium Pump in Sarcoplasmic Reticulum.* Journal of Biological Chemistry, 2013. **288**(42): p. 30181-30191.

385. Sanz-Hernández, M., et al., *Accurate Determination of Conformational Transitions in Oligomeric Membrane Proteins.* Scientific Reports, 2016. **6**(1): p. 23063-23063.
386. Traaseth, N.J., et al., *Structure and topology of monomeric phospholamban in lipid membranes determined by a hybrid solution and solid-state NMR approach.* Proceedings of the National Academy of Sciences, USA, 2009. **106**(25): p. 10165-10170.
387. Verardi, R., et al., *Structural topology of phospholamban pentamer in lipid bilayers by a hybrid solution and solid-state NMR method.* Proceedings of the National Academy of Sciences, 2011. **108**(22): p. 9101-9106.
388. Vostrikov, V.V., et al., *Structural dynamics and topology of phosphorylated phospholamban homopentamer reveal its role in the regulation of calcium transport.* Structure, 2013. **21**(12): p. 2119-2130.
389. Mravic, M., et al., *Packing of apolar side chains enables accurate design of highly stable membrane proteins.* Science, 2019. **363**(6434): p. 1418-1423.
390. Gustavsson, M., N.J. Traaseth, and G. Veglia, *Probing ground and excited states of phospholamban in model and native lipid membranes by magic angle spinning NMR spectroscopy.* Biochimica et Biophysica Acta (BBA) - Biomembranes, 2012. **1818**(2): p. 146-153.
391. Opella, S.J. and F.M. Marassi, *Structure Determination of Membrane Proteins by NMR Spectroscopy.* Chemical Reviews, 2004. **104**(8): p. 3587-3606.
392. Das, N., D.T. Murray, and T.A. Cross, *Lipid bilayer preparations of membrane proteins for oriented and magic-angle spinning solid-state NMR samples.* Nature Protocols, 2013. **8**(11): p. 2256-2270.
393. Sanders, C.R. and G.C. Landis, *Reconstitution of Membrane Proteins into Lipid-Rich Bilayered Mixed Micelles for NMR Studies.* Biochemistry, 1995. **34**(12): p. 4030-4040.
394. De Simone, A., et al., *Structures of the Excited States of Phospholamban and Shifts in Their Populations upon Phosphorylation.* Biochemistry, 2013. **52**(38): p. 6684-6694.
395. Zvaritch, E., et al., *The Transgenic Expression of Highly Inhibitory Monomeric Forms of Phospholamban in Mouse Heart Impairs Cardiac Contractility.* Journal of Biological Chemistry, 2000. **275**(20): p. 14985-14991.
396. Karim, C.B., et al., *Synthetic null-cysteine phospholamban analogue and the corresponding transmembrane domain inhibit the Ca-ATPase.* Biochemistry, 2000. **39**(35): p. 10892-10897.
397. Stokes, D.L. and N.M. Green, *Three-dimensional crystals of CaATPase from sarcoplasmic reticulum. Symmetry and molecular packing.* Biophysical Journal, 1990. **57**(1): p. 1-14.
398. Prosser, R.S., et al., *Magnetically Aligned Membrane Model Systems with Positive Order Parameter: Switching the Sign of S_{zz} with Paramagnetic Ions.* Journal of the American Chemical Society, 1996. **118**(1): p. 269-270.
399. Prosser, R.S., V.B. Volkov, and I.V. Shiyanovskaya, *Novel Chelate-Induced Magnetic Alignment of Biological Membranes.* Biophysical Journal, 1998. **75**(5): p. 2163-2169.
400. Gopinath, T. and G. Veglia, *Sensitivity enhancement in static solid-state NMR experiments via singleand multiple-quantum dipolar coherences.* Journal of the American Chemical Society, 2009. **131**(16): p. 5754-5756.
401. Mote, K.R., et al., *Multidimensional oriented solid-state NMR experiments enable the sequential assignment of uniformly ^{15}N labeled integral membrane proteins in*

magnetically aligned lipid bilayers. Journal of Biomolecular NMR, 2011. **51**(3): p. 339-346.
402. Weber, D.K. and G. Veglia, *A Theoretical Assessment of the Structure Determination of Multi-Span Membrane Proteins by Oriented Sample Solid-State NMR Spectroscopy.* Australian Journal of Chemistry, 2019. **73**: p. 246-251.
403. Denny, J.K., et al., *PISEMA powder patterns and PISA wheels.* Journal of Magnetic Resonance, 2001. **152**(2): p. 217-226.
404. Glaser, R.W., et al., *Orientation of the antimicrobial peptide PGLa in lipid membranes determined from 19F-NMR dipolar couplings of 4-CF3-phenylglycine labels.* Journal of Magnetic Resonance, 2004. **168**(1): p. 153-163.
405. Dong, X. and D.D. Thomas, *Time-resolved FRET reveals the structural mechanism of SERCA-PLB regulation.* Biochemical and Biophysical Research Communications, 2014. **449**(2): p. 196-201.
406. Bidwell, P., et al., *Phospholamban binds with differential affinity to calcium pump conformers.* Journal of Biological Chemistry, 2011. **286**(40): p. 35044-35050.
407. Chen, Z., et al., *Cross-linking of C-terminal residues of phospholamban to the Ca2+ pump of cardiac sarcoplasmic reticulum to probe spatial and functional interactions within the transmembrane domain.* Journal of Biological Chemistry, 2006. **281**(20): p. 14163-14172.
408. Chen, Z., et al., *Spatial and Dynamic Interactions between Phospholamban and the Canine Cardiac Ca2+ Pump Revealed with Use of Heterobifunctional Cross-linking Agents.* Journal of Biological Chemistry, 2003. **278**(48): p. 48348-48356.
409. Toyoshima, C. and T. Mizutani, *Crystal structure of the calcium pump with a bound ATP analogue.* Nature, 2004. **430**(6999): p. 529-535.
410. Sorensen, T.L., J.V. Moller, and P. Nissen, *Phosphoryl transfer and calcium ion occlusion in the calcium pump.* Science, 2004. **304**(5677): p. 1672-1675.
411. Olesen, C., et al., *The structural basis of calcium transport by the calcium pump.* Nature, 2007. **450**(7172): p. 1036-1042.
412. Toyoshima, C., H. Nomura, and T. Tsuda, *Lumenal gating mechanism revealed in calcium pump crystal structures with phosphate analogues.* Nature, 2004. **432**(7015): p. 361-368.
413. Winther, A.-M.L., et al., *The sarcolipin-bound calcium pump stabilizes calcium sites exposed to the cytoplasm.* Nature, 2013. **495**(7440): p. 265-9.
414. Toyoshima, C., et al., *How processing of aspartylphosphate is coupled to lumenal gating of the ion pathway in the calcium pump.* Proceedings of the National Academy of Sciences, 2007. **104**(50): p. 19831-19836.
415. Bublitz, M., et al., *Ion pathways in the sarcoplasmic reticulum Ca2+-ATPase.* Journal of Biological Chemistry, 2013. **288**(15): p. 10759-10765.
416. Toyoshima, C. and H. Nomura, *Structural changes in the calcium pump accompanying the dissociation of calcium.* Nature, 2002. **418**(6898): p. 605-611.
417. Jones, L.R., R.L. Cornea, and Z. Chen, *Close Proximity between Residue 30 of Phospholamban and Cysteine 318 of the Cardiac Ca2+ Pump Revealed by Intermolecular Thiol Cross-linking.* Journal of Biological Chemistry, 2002. **277**(31): p. 28319-28329.
418. James, P., et al., *Nature and site of phospholamban regulation of the Ca2+ pump of sarcoplasmic reticulum.* Nature, 1989. **342**(6245): p. 90-92.
419. Jensen, A.M., et al., *Modulatory and catalytic modes of ATP binding by the calcium pump.* EMBO Journal, 2006. **25**(11): p. 2305-2314.
420. Olivieri, C., et al., *Multi-state recognition pathway of the intrinsically disordered protein kinase inhibitor by protein kinase A.* eLife, 2020. **9**: p. 1-28.

421. Li, J., D.J. Bigelow, and T.C. Squier, *Phosphorylation by cAMP-Dependent Protein Kinase Modulates the Structural Coupling between the Transmembrane and Cytosolic Domains of Phospholamban.* Biochemistry, 2003. **42**(36): p. 10674-10682.
422. Li, J., et al., *Phospholamban Binds in a Compact and Ordered Conformation to the Ca-ATPase.* Biochemistry, 2004. **43**(2): p. 455-463.
423. Kimura, Y., et al., *Phospholamban Domain Ib Mutations Influence Functional Interactions with the Ca2+-ATPase Isoform of Cardiac Sarcoplasmic Reticulum.* Journal of Biological Chemistry, 1998. **273**(23): p. 14238-14241.
424. Akin, B.L., Z. Chen, and L.R. Jones, *Superinhibitory Phospholamban Mutants Compete with Ca2+ for Binding to SERCA2a by Stabilizing a Unique Nucleotide-dependent Conformational State.* Journal of Biological Chemistry, 2010. **285**(37): p. 28540-28552.
425. Gustavsson, M., et al., *Lipid-mediated folding/unfolding of phospholamban as a regulatory mechanism for the sarcoplasmic reticulum Ca2+-ATPase.* Journal of Molecular Biology, 2011. **408**(4): p. 755-765.
426. Norimatsu, Y., et al., *Protein–phospholipid interplay revealed with crystals of a calcium pump.* Nature, 2017. **545**(7653): p. 193-198.
427. Das, A., et al., *Conformational Transitions and Alternating-Access Mechanism in the Sarcoplasmic Reticulum Calcium Pump.* Journal of Molecular Biology, 2017. **429**(5): p. 647-666.
428. Rui, H., et al., *Proton Countertransport and Coupled Gating in the Sarcoplasmic Reticulum Calcium Pump.* Journal of Molecular Biology, 2018. **430**(24): p. 5050-5065.
429. Yokoe, S., et al., *Inhibition of phospholamban phosphorylation by O-GlcNAcylation: implications for diabetic cardiomyopathy.* Glycobiology, 2010. **20**(10): p. 1217-1226.
430. Kranias, E.G. and R.J. Hajjar, *The Phospholamban Journey 4 Decades After Setting Out for Ithaka.* Circulation Research, 2017. **120**(5): p. 781-783.
431. Menzel, J., et al., *14-3-3 Binding Creates a Memory of Kinase Action By Stabilizing the Modified State of Phospholamban.* Science signaling, 2020. **13**(647): p. eaaz1436-eaaz1436.
432. Mueller, B., et al., *Direct Detection of Phospholamban and Sarcoplasmic Reticulum Ca-ATPase Interaction in Membranes Using Fluorescence Resonance Energy Transfer.* Biochemistry, 2004. **43**(27): p. 8754-8765.
433. Martin, P.D., Z.M. James, and D.D. Thomas, *Effect of Phosphorylation on Interactions between Transmembrane Domains of SERCA and Phospholamban.* Biophysical Journal, 2018. **114**(11): p. 2573-2583.
434. Masterson, L.R., et al., *cAMP-dependent protein kinase A selects the excited state of the membrane substrate phospholamban.* J Mol Biol, 2011. **412**(2): p. 155-64.
435. Fujii, J., et al., *Expression and site-specific mutagenesis of phospholamban. Studies of residues involved in phosphorylation and pentamer formation.* Journal of biological chemistry, 1989. **264**(22): p. 12950-5.
436. Toyofuku, T., et al., *Amino Acids Glu2 to Ile18 in the Cytoplasmic Domain of Phospholamban Are Essential for Functional Association with the Ca2+-ATPase of Sarcoplasmic Reticulum.* Journal of Biological Chemistry, 1994. **269**(4): p. 3088-3094.

437. Bocharov, E.V., et al., *Helix-helix interactions in membrane domains of bitopic proteins: Specificity and role of lipid environment.* Biochimica et Biophysica Acta (BBA) - Biomembranes, 2017. **1859**(4): p. 561-576.
438. Presti, C.F., L.R. Jones, and J.P. Lindemann, *Isoproterenol-induced phosphorylation of a 15-kilodalton sarcolemmal protein in intact myocardium.* Journal of Biological Chemistry, 1985. **260**(6): p. 3860-3867.
439. Bers, D.M., S. Despa, and J. Bossuyt, *Regulation of Ca2+ and Na+ in normal and failing cardiac myocytes.* Annals of the New York Academy of Sciences, 2006. **1080**(1): p. 165-177.
440. Teriete, P., et al., *Effects of PKA phosphorylation on the conformation of the Na,K-ATPase regulatory protein FXYD1.* Biochimica et Biophysica Acta - Biomembranes, 2009. **1788**(11): p. 2462-2470.
441. Singh, D.R., et al., *Newly Discovered Micropeptide Regulators of SERCA Form Oligomers but Bind to the Pump as Monomers.* Journal of Molecular Biology, 2019. **431**(22): p. 4429-4443.
442. Makarewich, C.A., *The hidden world of membrane microproteins.* Experimental Cell Research, 2020. **388**(2): p. 111853-111853.
443. Buck, B., et al., *Overexpression, purification, and characterization of recombinant Ca-ATPase regulators for high-resolution solution and solid-state NMR studies.* Protein Expression and Purification, 2003. **30**(2): p. 253-261.
444. Lacabanne, D., B.H. Meier, and A. Böckmann, *Selective labeling and unlabeling strategies in protein solid-state NMR spectroscopy.* Journal of Biomolecular NMR, 2018. **71**(3): p. 141-150.
445. Weber, D.K., et al., *Cysteine-ethylation of tissue-extracted membrane proteins as a tool to detect conformational states by solid-state NMR spectroscopy.* Methods in Enzymology, 2019. **621**: p. 281-304.
446. Gor'kov, P.L., et al., *Using low-E resonators to reduce RF heating in biological samples for static solid-state NMR up to 900 MHz.* Journal of Magnetic Resonance, 2007. **185**(1): p. 77-93.
447. Bertani, P., J. Raya, and B. Bechinger, *15N chemical shift referencing in solid state NMR.* Solid State Nuclear Magnetic Resonance, 2014. **61–62**(0): p. 15-18.
448. Gopinath, T., et al., *Sensitivity enhancement of separated local field experiments: Application to membrane proteins.* Journal of Physical Chemistry B, 2010. **114**(15): p. 5089-5095.
449. Nevzorov, A.A. and S.J. Opella, *Selective averaging for high-resolution solid-state NMR spectroscopy of aligned samples.* Journal of Magnetic Resonance, 2007. **185**(1): p. 59-70.
450. Vinogradov, E., P.K. Madhu, and S. Vega, *High-resolution proton solid-state NMR spectroscopy by phase-modulated Lee-Goldburg experiment.* Chemical Physics Letters, 1999. **314**(5-6): p. 443-450.
451. Traaseth, N.J., T. Gopinath, and G. Veglia, *On the performance of spin diffusion NMR techniques in oriented solids: Prospects for resonance assignments and distance measurements from separated local field experiments.* Journal of Physical Chemistry B, 2010. **114**(43): p. 13872-13880.
452. Lee, W., M. Tonelli, and J.L. Markley, *NMRFAM-SPARKY: enhanced software for biomolecular NMR spectroscopy.* Bioinformatics, 2015. **31**(8): p. 1325-1327.
453. Helmus, J.J. and C.P. Jaroniec, *Nmrglue: an open source Python package for the analysis of multidimensional NMR data.* Journal of Biomolecular NMR, 2013. **55**(4): p. 355-367.

454. Weber, D.K., et al., *PISA-SPARKY: an interactive SPARKY plugin to analyze oriented solid-state NMR spectra of helical membrane proteins.* Bioinformatics, 2020(January): p. 1-2.
455. Weber, D.K., et al., *Hybridizing isotropic and anisotropic solid-state NMR restraints for membrane protein structure determination*, in *Solid-State NMR*. 2020, IOP Publishing. p. 12-1-12-21.
456. Huang, J. and A.D. MacKerell, *CHARMM36 all-atom additive protein force field: Validation based on comparison to NMR data.* Journal of Computational Chemistry, 2013. **34**(25): p. 2135-2145.
457. Case, D.A., et al., *AMBER18*. 2018, University of California: San Francisco.
458. Crowley, M.F., M.J. Williamson, and R.C. Walker, *CHAMBER: Comprehensive support for CHARMM force fields within the AMBER software.* International Journal of Quantum Chemistry, 2009. **109**(15): p. 3767-3772.
459. Loncharich, R.J., B.R. Brooks, and R.W. Pastor, *Langevin dynamics of peptides: The frictional dependence of isomerization rates of N-acetylalanyl-N'-methylamide.* Biopolymers, 1992. **32**(5): p. 523-535.
460. Faller, R. and J.J. de Pablo, *Constant pressure hybrid Molecular Dynamics–Monte Carlo simulations.* The Journal of Chemical Physics, 2002. **116**(1): p. 55-55.
461. Miyamoto, S. and P.A. Kollman, *Settle: An analytical version of the SHAKE and RATTLE algorithm for rigid water models.* Journal of Computational Chemistry, 1992. **13**(8): p. 952-962.
462. Webb, B. and A. Sali, *Comparative Protein Structure Modeling Using MODELLER.* Current Protocols in Protein Science, 2016. **86**(1): p. 2.9.1-2.9.37.
463. Jorgensen, W.L., et al., *Comparison of simple potential functions for simulating liquid water.* Journal of Chemical Physics, 1983. **79**(2): p. 926-935.
464. Marrink, S.J., et al., *The MARTINI Force Field: Coarse Grained Model for Biomolecular Simulations.* Journal of Physical Chemistry B, 2007. **111**(27): p. 7812-7824.
465. Wassenaar, T.A., et al., *Going Backward: A Flexible Geometric Approach to Reverse Transformation from Coarse Grained to Atomistic Models.* Journal of Chemical Theory and Computation, 2014. **10**(2): p. 676-690.
466. Pronk, S., et al., *GROMACS 4.5: A high-throughput and highly parallel open source molecular simulation toolkit.* Bioinformatics, 2013. **29**(7): p. 845-854.
467. Bussi, G., D. Donadio, and M. Parrinello, *Canonical sampling through velocity rescaling.* Journal of Chemical Physics, 2007. **126**(1): p. 014101-014101.
468. Berendsen, H.J.C., et al., *Molecular dynamics with coupling to an external bath.* Journal of Chemical Physics, 1984. **81**(8): p. 3684-3690.
469. Hess, B., et al., *LINCS: A linear constraint solver for molecular simulations.* Journal of Computational Chemistry, 1997. **18**(12): p. 1463-1472.
470. Darden, T., D. York, and L. Pedersen, *Particle mesh Ewald: An N·log(N) method for Ewald sums in large systems.* Journal of Chemical Physics, 1993. **98**(12): p. 10089-10092.
471. Roe, D.R. and T.E. Cheatham, *PTRAJ and CPPTRAJ: Software for Processing and Analysis of Molecular Dynamics Trajectory Data.* Journal of Chemical Theory and Computation, 2013. **9**(7): p. 3084-3095.
472. Humphrey, W., A. Dalke, and K. Schulten, *VMD: Visual molecular dynamics.* Journal of Molecular Graphics, 1996. **14**(1): p. 33-38.

473. Kasashima, K., et al., *Mitochondrial functions and estrogen receptor-dependent nuclear translocation of pleiotropic human prohibitin 2.* J Biol Chem, 2006. **281**(47): p. 36401-10.
474. Lee, A.Y., et al., *HS 1-associated protein X-1 is cleaved by caspase-3 during apoptosis.* Mol Cells, 2008. **25**(1): p. 86-90.
475. Han, Y., et al., *Overexpression of HAX-1 protects cardiac myocytes from apoptosis through caspase-9 inhibition.* Circ Res, 2006. **99**(4): p. 415-23.
476. Kang, Y.J., et al., *Molecular interaction between HAX-1 and XIAP inhibits apoptosis.* Biochem Biophys Res Commun, 2010. **393**(4): p. 794-9.
477. Dobreva, I., et al., *Mapping the integrin-linked kinase interactome using SILAC.* J Proteome Res, 2008. **7**(4): p. 1740-9.
478. Jing, Y.Y., et al., *A novel PrP partner HS-1 associated protein X-1 (HAX-1) protected the cultured cells against the challenge of H(2)O(2).* J Mol Neurosci, 2011. **45**(2): p. 216-28.
479. Zhang, Y., et al., *Kv3.3 Channels Bind Hax-1 and Arp2/3 to Assemble a Stable Local Actin Network that Regulates Channel Gating.* Cell, 2016. **165**(2): p. 434-448.
480. Radhika, V., et al., *Galpha13 stimulates cell migration through cortactin-interacting protein Hax-1.* J Biol Chem, 2004. **279**(47): p. 49406-13.
481. Han, D.C., T.L. Shen, and J.L. Guan, *The Grb7 family proteins: structure, interactions with other signaling molecules and potential cellular functions.* Oncogene, 2001. **20**(44): p. 6315-21.
482. Szwarc, M., E. Sarnowska, and E.A. Grzybowska, *[HAX-1 protein: multifunctional factor involved in apoptosis, cell migration, endocytosis and mRNA transport].* Postepy Biochem, 2007. **53**(3): p. 218-27.
483. Fadeel, B. and E. Grzybowska, *HAX-1: a multifunctional protein with emerging roles in human disease.* Biochim Biophys Acta, 2009. **1790**(10): p. 1139-48.
484. Sarnowska, E., et al., *Hairpin structure within the 3'UTR of DNA polymerase beta mRNA acts as a post-transcriptional regulatory element and interacts with Hax-1.* Nucleic Acids Res, 2007. **35**(16): p. 5499-510.
485. Grzybowska, E.A., et al., *HAX-1 is a nucleocytoplasmic shuttling protein with a possible role in mRNA processing.* FEBS J, 2013. **280**(1): p. 256-72.
486. Zayat, V., et al., *HAX-1: a novel p-body protein.* DNA Cell Biol, 2015. **34**(1): p. 43-54.
487. Banerjee, A., et al., *Hepatitis C virus core protein and cellular protein HAX-1 promote 5-fluorouracil-mediated hepatocyte growth inhibition.* J Virol, 2009. **83**(19): p. 9663-71.
488. Sharp, T.V., et al., *K15 protein of Kaposi's sarcoma-associated herpesvirus is latently expressed and binds to HAX-1, a protein with antiapoptotic function.* J Virol, 2002. **76**(2): p. 802-16.
489. Kawaguchi, Y., et al., *Interaction of Epstein-Barr virus nuclear antigen leader protein (EBNA-LP) with HS1-associated protein X-1: implication of cytoplasmic function of EBNA-LP.* J Virol, 2000. **74**(21): p. 10104-11.
490. Modem, S. and T.R. Reddy, *An anti-apoptotic protein, Hax-1, inhibits the HIV-1 rev function by altering its sub-cellular localization.* J Cell Physiol, 2008. **214**(1): p. 14-9.
491. Ortiz, D.F., et al., *Identification of HAX-1 as a protein that binds bile salt export protein and regulates its abundance in the apical membrane of Madin-Darby canine kidney cells.* J Biol Chem, 2004. **279**(31): p. 32761-70.

492. Sormanni, P., et al., *The s2D method: simultaneous sequence-based prediction of the statistical populations of ordered and disordered regions in proteins.* J Mol Biol, 2015. **427**(4): p. 982-996.
493. MacLennan, D.H. and E.G. Kranias, *Phospholamban: a crucial regulator of cardiac contractility.* Nat Rev Mol Cell Biol, 2003. **4**(7): p. 566-77.
494. Benjamin, E.J., et al., *Heart Disease and Stroke Statistics-2018 Update: A Report From the American Heart Association.* Circulation, 2018. **137**(12): p. e67-e492.
495. Hof, I.E., et al., *Prevalence and cardiac phenotype of patients with a phospholamban mutation.* Neth Heart J, 2018.
496. Ogawa, H., et al., *Structure of the Ca2+ pump of sarcoplasmic reticulum: a view along the lipid bilayer at 9-A resolution.* Biophys J, 1998. **75**(1): p. 41-52.
497. Tada, M., T. Yamamoto, and Y. Tonomura, *Molecular mechanism of active calcium transport by sarcoplasmic reticulum.* Physiol Rev, 1978. **58**(1): p. 1-79.
498. Tada, M., M.A. Kirchberger, and A.M. Katz, *Phosphorylation of a 22,000-dalton component of the cardiac sarcoplasmic reticulum by adenosine 3':5'-monophosphate-dependent protein kinase.* J Biol Chem, 1975. **250**(7): p. 2640-7.
499. Vandecaetsbeek, I., et al., *Factors controlling the activity of the SERCA2a pump in the normal and failing heart.* Biofactors, 2009. **35**(6): p. 484-99.
500. Buck, B., et al., *Overexpression, purification, and characterization of recombinant Ca-ATPase regulators for high-resolution solution and solid-state NMR studies.* Protein Expr Purif, 2003. **30**(2): p. 253-61.
501. Sitsel, A., et al., *Structures of the heart specific SERCA2a Ca(2+)-ATPase.* EMBO J, 2019. **38**(5).
502. Stokes, D.L. and N.M. Green, *Three-dimensional crystals of CaATPase from sarcoplasmic reticulum. Symmetry and molecular packing.* Biophys J, 1990. **57**(1): p. 1-14.
503. Reddy, L.G., et al., *Defining the molecular components of calcium transport regulation in a reconstituted membrane system.* Biochemistry, 2003. **42**(15): p. 4585-92.
504. Fernandez-Vidal, M., S.H. White, and A.S. Ladokhin, *Membrane partitioning: "classical" and "nonclassical" hydrophobic effects.* J Membr Biol, 2011. **239**(1-2): p. 5-14.
505. White, S.H., et al., *Protein folding in membranes: determining energetics of peptide-bilayer interactions.* Methods Enzymol, 1998. **295**: p. 62-87.
506. Olivieri, C., et al., *Design and characterization of chionodracine-derived antimicrobial peptides with enhanced activity against drug-resistant human pathogens.* Rsc Advances, 2018. **8**(72): p. 41331-41346.
507. Lee, D., et al., *Effective rotational correlation times of proteins from NMR relaxation interference.* J Magn Reson, 2006. **178**(1): p. 72-6.
508. Delaglio, F., et al., *NMRPipe: a multidimensional spectral processing system based on UNIX pipes.* J Biomol NMR, 1995. **6**(3): p. 277-93.
509. Lee, W., M. Tonelli, and J.L. Markley, *NMRFAM-SPARKY: enhanced software for biomolecular NMR spectroscopy.* Bioinformatics, 2015. **31**(8): p. 1325-7.
510. Youvan, D.C., et al., *Calibration of fluorescence resonance energy transfer in microscopy using genetically engineered GFP derivatives on nickel chelating beads.* Biotechnology et alia, 1997. **3**: p. 1-18.
511. Kelly, E.M., et al., *Phospholamban oligomerization, quaternary structure, and sarco(endo)plasmic reticulum calcium ATPase binding measured by*

fluorescence resonance energy transfer in living cells. J Biol Chem, 2008. **283**(18): p. 12202-11.
512. Eliezer, D., et al., *Conformational properties of alpha-synuclein in its free and lipid-associated states.* J Mol Biol, 2001. **307**(4): p. 1061-73.
513. Redfield, C., *NMR studies of partially folded molten-globule states.* Methods Mol Biol, 2004. **278**: p. 233-54.
514. Cavanagh, J., *Protein nmr spectroscopy : principles and practice*. 1st edition. ed. 2018, Waltham, MA: Elsevier. pages cm.
515. Janes, R.W., *PDB2CD visualises dynamics within protein structures.* European Biophysics Journal with Biophysics Letters, 2017. **46**(7): p. 607-616.
516. Chao, J.R., et al., *Hax1-mediated processing of HtrA2 by Parl allows survival of lymphocytes and neurons.* Nature, 2008. **452**(7183): p. 98-102.
517. Jeyaraju, D.V., et al., *Hax1 lacks BH modules and is peripherally associated to heavy membranes: implications for Omi/HtrA2 and PARL activity in the regulation of mitochondrial stress and apoptosis.* Cell Death and Differentiation, 2009. **16**(12): p. 1622-1629.
518. Qian, L., et al., *Grb7 and Hax1 may colocalize partially to mitochondria in EGF-treated SKBR3 cells and their interaction can affect Caspase3 cleavage of Hax1.* Journal of Molecular Recognition, 2016. **29**(7): p. 318-333.
519. Caldwell, T.A., et al., *Low- q Bicelles Are Mixed Micelles.* J Phys Chem Lett, 2018. **9**(15): p. 4469-4473.
520. Kashefi, M. and L.K. Thompson, *Signaling-Related Mobility Changes in Bacterial Chemotaxis Receptors Revealed by Solid-State NMR.* J Phys Chem B, 2017. **121**(37): p. 8693-8705.
521. Ha, K.N., M. Gustavsson, and G. Veglia, *Tuning the structural coupling between the transmembrane and cytoplasmic domains of phospholamban to control sarcoplasmic reticulum Ca(2+)-ATPase (SERCA) function.* J Muscle Res Cell Motil, 2012. **33**(6): p. 485-92.
522. Karim, C.B., et al., *Phosphorylation-dependent conformational switch in spin-labeled phospholamban bound to SERCA.* J Mol Biol, 2006. **358**(4): p. 1032-40.
523. Abu-Baker, S. and G.A. Lorigan, *Phospholamban and its phosphorylated form interact differently with lipid bilayers: a 31P, 2H, and 13C solid-state NMR spectroscopic study.* Biochemistry, 2006. **45**(44): p. 13312-22.
524. Abu-Baker, S., et al., *Side chain and backbone dynamics of phospholamban in phospholipid bilayers utilizing 2H and 15N solid-state NMR spectroscopy.* Biochemistry, 2007. **46**(42): p. 11695-706.
525. Yu, X. and G.A. Lorigan, *Secondary structure, backbone dynamics, and structural topology of phospholamban and its phosphorylated and Arg9Cys-mutated forms in phospholipid bilayers utilizing 13C and 15N solid-state NMR spectroscopy.* J Phys Chem B, 2014. **118**(8): p. 2124-33.
526. Soller, K.J., et al., *Rheostatic Regulation of the SERCA/Phospholamban Membrane Protein Complex Using Non-Coding RNA and Single-Stranded DNA oligonucleotides.* Sci Rep, 2015. **5**: p. 13000.
527. Reddy, L.G., L.R. Jones, and D.D. Thomas, *Depolymerization of phospholamban in the presence of calcium pump: a fluorescence energy transfer study.* Biochemistry, 1999. **38**(13): p. 3954-62.
528. Klein, C., *Congenital Neutropenia*. Steihm's Immune Deficiencies. 2014. 605-618.